Dissertation zur Erlangung des Doktorgrades
der Fakultät für Chemie und Pharmazie
der Ludwig-Maximilians-Universität München

# Application of Advanced Fluorescence Microscopy and Spectroscopy in Live-Cell Imaging

Chen Qian

aus

Shanghai, China

2022

## Erklärung

Diese Dissertation wurde im Sinne von § 7 der Promotionsordnung vom 28. November 2011 von Herrn Prof. Dr. Don C. Lamb betreut.

## Eidesstattliche Versicherung

Diese Dissertation wurde eigenständig und ohne unerlaubte Hilfe erarbeitet.

München, 11.01.2022

Chen Qian

Dissertation eingereicht am: 13.01.2022

1. Gutachter: Prof. Dr. Don C. Lamb

2. Gutachter: Prof. Dr. Philip Tinnefeld

Mündliche Prüfung am: 15.02.2022

# Abstract

Since its inception, fluorescence microscopy has been a key source of discoveries in cell biology. Advancements in fluorophores, labeling techniques and instrumentation have made fluorescence microscopy a versatile quantitative tool for studying dynamic processes and interactions both *in vitro* and in live-cells. In this thesis, I apply quantitative fluorescence microscopy techniques in live-cell environments to investigate several biological processes. To study Gag processing in HIV-1 particles, fluorescence lifetime imaging microscopy and single particle tracking are combined to follow nascent HIV-1 virus particles during assembly and release on the plasma membrane of living cells. Proteolytic release of eCFP embedded in the Gag lattice of immature HIV-1 virus particles results in a characteristic increase in its fluorescence lifetime. Gag processing and rearrangement can be detected in individual virus particles using this approach. In another project, a robust method for quantifying Förster resonance energy transfer in live-cells is developed to allow direct comparison of live-cell FRET experiments between laboratories. Finally, I apply image fluctuation spectroscopy to study protein behavior in a variety of cellular environments. Image cross-correlation spectroscopy is used to study the oligomerization of CXCR4, a G-protein coupled receptor on the plasma membrane. With raster image correlation spectroscopy, I measure the diffusion of histones in the nucleoplasm and heterochromatin domains of the nuclei of early mouse embryos. The lower diffusion coefficient of histones in the heterochromatin domain supports the conclusion that heterochromatin forms a liquid phase-separated domain. The wide range of topics covered in this thesis demonstrate that fluorescence microscopy is more than just an imaging tool but also a powerful instrument for the quantification and elucidation of dynamic cellular processes.

# Table of Contents

| | |
|---|---|
| Appendix I: | Published paper: Dynamics of HIV-1 Gag Processing as Revealed by Fluorescence Lifetime Imaging Microscopy and Single Virus Tracking |
| Appendix II: | Published paper: QuanTI-FRET: a framework for quantitative FRET measurements in living cells |
| Appendix III: | Submitted manuscript: A phase transition accompanies heterochromatin formation in mouse embryos |

# 1. Introduction

The use of microscopy is instrumental to our modern understanding of the structure and organization of cells. The development of the light microscope opened up a new world on the cellular and sub-cellular level, making possible the discovery and observation of cells by Robert Hook [1] and Antoni Van Leeuwenhoek in the 17th century [2]. This eventually led to the formulation of cell theory, the idea that cells formed the basic unit of structure and organization in all living organisms, by Schwann and Schleiden in 1838 [3, 4]. This remains a central concept in cell biology. Since then, advances in microscopy has continually enabled the observation of previously unobservable structures and phenomena in cells and microorganisms, whether it is by staining otherwise transparent structures or improving the resolving power of the microscope. More recently, the application of computational analysis has even allowed us to overcome the optical resolution limit or extract information that is not readily apparent in the raw image.

The advent of fluorescence microscopy marked a change in how light microscopy is performed, as it involved a switch from observing transmitted light to measuring photon emission from fluorescent molecules. Although fluorescence is an ubiquitous phenomenon, most molecules in the cell have very low absorption and emission efficiencies in the visible spectrum. The emission from fluorophores - compounds with high fluorescence quantum yields - appear very 'bright' in comparison. Fluorescently-labeled structures can therefore be imaged with much higher contrast than what is possible with traditional light microscopy. Over the years, the concurrent development of new fluorophores, labeling techniques and instrumentation mean that we now have access to a wide repertoire of tools for visualizing proteins and other biomolecules with high specificity and sensitivity. Many of these methods can also be performed in living cells or organisms, allowing for the visualization of dynamic biological processes with high spatial and temporal resolution.

In this work, I apply several advanced fluorescence microscopy techniques in live-cells, with a focus on the observation and quantification of dynamic biological processes. In Chapter 2, I start with a short introduction to fluorescence and the types of fluorescence microscopy used in this work. In Chapter 3, I introduce several methods used to analyze fluorescence emission, with an emphasis on the methods used in this work, such as fluorescence fluctuation spectroscopy, image fluctuation spectroscopy, fluorescence lifetime analysis and single particle tracking. The subsequent chapters describe the application of these methods in live-cell environments, with a focus on the observation and quantification of dynamic processes.

The measurement of fluorescence emission is not limited to that of the signal intensity alone. Other intrinsic parameters of fluorescence such as the fluorescence polarization and the fluorescence lifetime can be measured with specialized instruments. In particular, the fluorescence lifetime of certain fluorophores is sensitive to the local microenvironment including pH, charge and its proximity to other molecules. One such fluorophore is the fluorescent protein eCFP, whose fluorescence lifetime decreases when in close proximity to other eCFPs or proteins. In Chapter 4, this is used to follow the dynamics of Gag processing in nascent HIV-1 particles through a combination of fluorescence lifetime imaging (FLIM) and single particle tracking (SPT).

The fluorescence intensity can also encode additional information that is not immediately apparent in an image. The analysis of fluorescence intensity can be used to measure Förster resonance energy transfer (FRET), in which, instead of emitting a photon, an excited donor fluorophore transfers its energy to a nearby acceptor fluorophore, resulting in fluorescence emission from the acceptor instead. Because of the sensitivity of FRET to the donor-acceptor proximity, it is frequently used as a tool for detecting protein-protein interactions and measuring distances on the nanometer scale. In Chapter 5, a new, robust method for quantitative FRET in live-cell imaging is described based on concepts first developed in single-molecule FRET analysis.

Fluctuations in fluorescence intensity, both temporally and spatially, can also be used to extract information about the labeled species including its concentration, diffusion and interaction with other labeled molecules. Unlike traditional biochemical methods, fluorescence fluctuation spectroscopy and its imaging derivatives can be performed directly in living cells, without the need to lyse or fix the cells. This is demonstrated in Chapters 6 and 7, where I apply image fluctuation spectroscopy to study the behavior and interaction of proteins in various cellular compartments. In Chapter 6, I look at the oligomerization of a G-protein coupled receptor (GPCR) on the plasma membrane with image cross-correlation spectroscopy (ICCS) and FLIM. Finally, in Chapter 7, the diffusion of histones in the nuclei of mouse embryos is measured by raster image correlation spectroscopy (RICS), revealing the liquid-liquid phase separation that accompanies heterochromatin formation in early mouse embryonic development. The wide-ranging nature of these projects demonstrate the power and flexibility of fluorescence microscopy for quantitative biological experiments.

# 2. Fluorescence Microscopy

Advances in fluorescence microscopy have enabled the detection of weak fluorescence signals with single molecule sensitivity. The development of a wide range of organic fluorescent dyes and fluorescent proteins, in combination with highly specific methods of labelling biomolecules, has led to the widespread application of fluorescence as a sensitive, selective and accessible readout for biological and medical measurements. In this chapter, I will begin by giving a brief introduction to the phenomenon of fluorescence, followed by a description of the microscopy techniques and some of the more advanced technologies relevant to the quantitative imaging carried out in this work.

## 2.1. Introduction to Fluorescence

Fluorescence is the emission of light from a substance after excitation by light or other electromagnetic radiation. When a molecule absorbs light, it can enter a short-lived excited electronic singlet state, which has a chance to emit a photon when returning to the ground state. Molecules with high probability of photon emission are known as fluorophores.

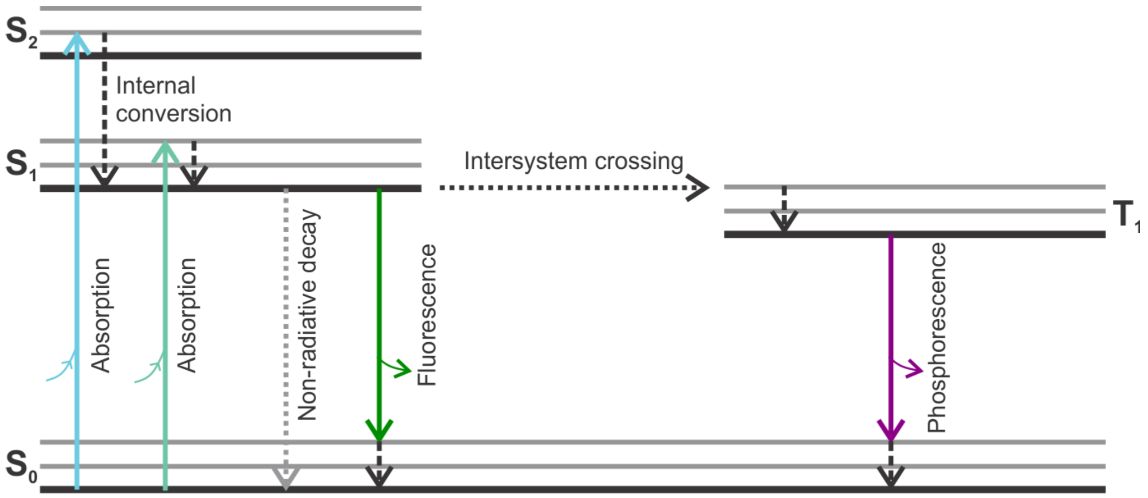

Figure 2.1. Jablonski diagram showing the common excitation and relaxation pathways of a fluorophore.

The process of fluorescence is often described by the Jablonski diagram (Figure 2.1). $S_0$, $S_1$ and $S_2$ are the singlet ground state and the first and second electronic excited states respectively. Within each electronic state, the fluorophore can also exist in one of a number of vibrational energy levels, denoted as 0, 1, 2, etc. Furthermore, every vibrational sublevel has a number of rotational states, creating a quasi-continuum of states within every electronic state. Upon absorbing a photon of a specific wavelength (or energy), the fluorophore undergoes a transition from ground state $S_0$ to an excited state $S_1$ or $S_2$. The transition occurs on the femtosecond timescale and therefore the nuclear coordinates remain unchanged. As a result, the transition probabilities from the vibronic ground state of $S_0$ to the different vibronic states of $S_1$ or $S_2$ are determined by the overlap of the vibronic wave functions (Franck-Condon principle) [5-7]. The excited fluorophore quickly ($10^{-12}$ s or less) relaxes to the vibronic ground state of $S_1$ in a process called internal conversion. The transition back to $S_0$ occurs from the vibronic ground state of $S_1$ and therefore the fluorescence emission spectrum is independent of the excitation wavelength (Kasha's rule) [8]. As the vibronic wave functions of $S_1$ and $S_0$ are similar, the fluorophore transitions back to excited vibronic states of $S_0$ ($10^{-9}$ to $10^{-8}$ s) with similar transition probabilities as for absorption. As a result of the above transitions, the fluorescence emission spectrum is mostly symmetrical to the absorption spectrum, and the energy of the emitted photon is reduced leading to a shift of the emission spectrum to longer wavelengths (Stokes shift, Figure 2.2) [9]. This property is exploited in fluorescence microscopy to separate excitation light from fluorescence emission by using special filters and polychroic mirrors, which transmit certain wavelengths but reflect or absorb others.

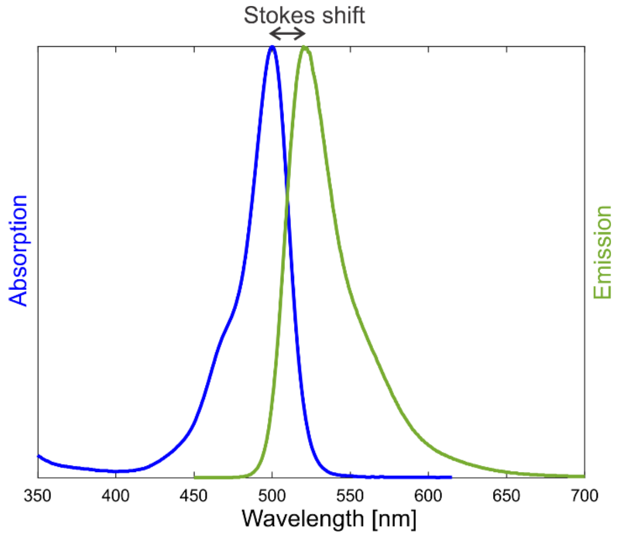

Figure 2.2. The absorption (*blue*) and emission (*green*) spectra of Atto 488 with ~20 nm Stokes shift.

Several additional pathways exist for the transition from $S_1$ to $S_0$. Non-radiative pathways include, for example, internal conversion followed by vibrational relaxation to the ground state, dynamic quenching by collision with another molecule (the quencher), as well as static quenching by the formation of a non-fluorescent complex. Additionally, molecules in $S_1$ can also undergo an intersystem conversion to the triplet state $T_1$, from which decay to the ground state can occur with emission at longer wavelengths (lower energy). This conversion requires the inversion of the spin of the excited state electron and is theoretically forbidden, but becomes more likely if the vibrational levels of the two states overlap. As both the $S_1$-$T_1$ and $T_1$-$S_0$ transitions are spin forbidden, emission via this pathway, known as phosphorescence, occurs at much slower rates ($10^3$ to $10^0$ $s^{-1}$) compared to fluorescence.

Two additional characteristics of a fluorophore are of particular interest in fluorescence microscopy: the fluorescence quantum yield and the fluorescence lifetime. The fluorescence quantum yield is the ratio of the number of photons emitted to the number of photons absorbed. The fluorescence lifetime is the average time a fluorophore spends in the excited state before decaying to the ground state. As the internal conversions take place on a much faster timescale ($10^{-12}$ s or less) than the $S_1$ to $S_0$ transition ($10^{-9}$ to $10^{-8}$ s), fluorescent decay can be simplified into a first-order process, where the quantum yield $Q$ and fluorescence lifetime $\tau$ are defined as:

$$Q = \frac{\Gamma}{\Gamma + k_{nr}} \tag{1}$$

$$\tau = \frac{1}{\Gamma + k_{nr}} \tag{2}$$

where $\Gamma$ is the radiative decay rate and $k_{nr}$ is the sum of the non-radiative decay rates. The measurement of fluorescence lifetime is discussed further in Chapter 3.4.

One phenomenon of particular importance to the application of fluorescence as a quantitative tool is Förster resonance energy transfer (FRET) [10]. It is a mechanism of energy transfer between two light-sensitive molecules, a donor and an acceptor, through non-radiative dipole-dipole interactions (Figure 2.3). The efficiency of this process depends on the distance separating the donor and acceptor, the spectral overlap of the donor emission spectrum and the acceptor absorption spectrum and the relative orientation of the donor and acceptor dipole moments.

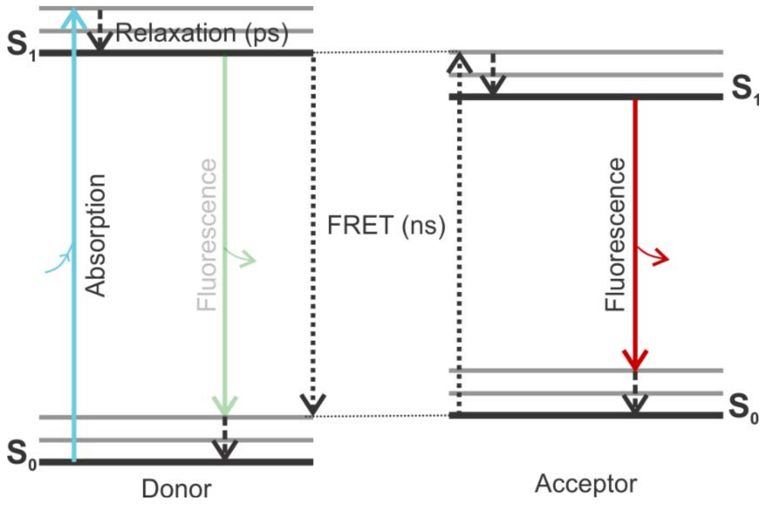

Figure 2.3. Jablonski diagram of the FRET process. When an excited donor fluorophore is in close proximity to an acceptor, there is a probability that, instead of emitting a photon, the energy released from the relaxation of the donor is transferred to the acceptor through dipole-dipole interactions. The acceptor becomes excited and can subsequently emit a photon.

FRET efficiency, $E$, can be expressed as the ratio of the FRET rate and the total decay rate (radiative, FRET and other non-radiative processes):

$$E = \frac{k_{FRET}}{k_{FRET} + \Gamma + \sum k_{others}} \tag{3}$$

$E$ also shows a power of six dependence on the separation distance, $r$, between the donor and acceptor:

$$E = \frac{R_0^6}{R_0^6 + r^6} \tag{4}$$

where $R_0$ is the Förster radius, which is the distance at which the probability of FRET is 50%. The Förster radius is specific to each donor-acceptor pair and is given by:

$$R_0 = \left( \frac{9000(\ln 10)\kappa^2 \phi_D}{128\pi^5 N_A n^4} J(\lambda) \right)^{\frac{1}{6}} \tag{5}$$

where $\kappa^2$ is an orientation factor that depends on the relative orientation of the donor and acceptor transition dipoles, $\phi_D$ is the quantum yield of the donor, $N_A$ is Avogadro's number, $n$ is the refractive index of the medium, and $J(\lambda)$ is the overlap integral of the donor emission and acceptor absorption spectra. The orientation factor, $\kappa^2$, is defined as:

$$\kappa^2 = (\cos\theta_T - 3\cos\theta_D \cos\theta_A)^2 \tag{6}$$

where $\theta_T$ is the angle between the donor emission dipole moment and the acceptor absorption dipole moment, and $\theta_D$ and $\theta_A$ are the angles between the respective dipoles and the vector joining the donor and acceptor. For freely rotating dyes with rotation times below 1 ns and lifetimes of around 4 ns, $\kappa^2$ is usually averaged over all possible values to 2/3.

$J(\lambda)$ depends on the normalized emission spectrum of the donor $\int_0^\infty F_D(\lambda) d\lambda = 1$ and the absorption spectrum of the acceptor expressed in terms of the extinction coefficient $\epsilon_A(\lambda)$:

$$J(\lambda) = \int_0^\infty F_D(\lambda)\epsilon_A(\lambda)\lambda^4 d\lambda \tag{7}$$

A dye pair with a known Förster radius can be used as a molecular ruler as we can determine the distance separation between the donor and acceptor by measuring its FRET efficiency in a sample. This can be done through two main approaches: one based on measuring the donor fluorescence lifetime (see Chapter 3.3) and the other based on measuring changes in donor and acceptor fluorescence intensity (see Chapter 5.1).

The measurement of fluorescence emissions is frequently carried out on a microscope. In the following sections, I will give an overview of the microscopy techniques used in this work.

## 2.2. Widefield Fluorescence Microscopy

One of the most common and basic forms of fluorescence microscopy is widefield fluorescence microscopy, in which the entire field of view is illuminated by the light source. The resulting image could be viewed through the eyepiece or captured on a camera. Most widefield fluorescence microscopes are built so that the excitation light travels through the objective lens to illuminate the sample, and the fluorescence emission is collected by the same objective. This type of microscopy is known as epifluorescence microscopy (Figure 2.4). Typically, the excitation beam is focused at the back focal plane of the objective to produce a large collimated beam with a gaussian intensity profile. For quantitative analyses that require even illumination, the usable field of view is restricted to around 40 µm in diameter around the center of the illumination beam. This is sufficient for typical applications but newer methods have been developed to meet the demands of cameras and quantitative imaging applications with larger fields of view [11].

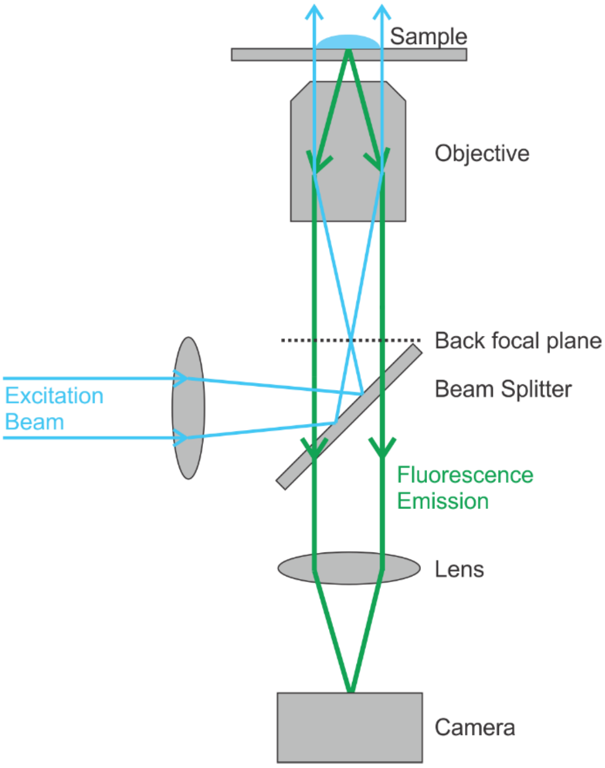

Figure 2.4. Principle of a widefield epifluorescence microscope. A collimated excitation beam (*cyan*) is focused onto the back focal plane of the objective, which results a collimated beam exiting the objective lens to illuminate the sample. Fluorescence emission (*green*) is collected by the same objective, passes through the beam splitter and is projected onto a camera to collect the image.

One important drawback of widefield fluorescence is the illumination of out-of-focus planes, resulting in high background, obfuscation of in-focus features, and low axial resolution. The microscopy methods in the following sections, as well as methods outside the scope of this work (such as light sheet microscopy [12-14]), primarily address the problem of out-of-focus illumination, either by restricting illumination to a certain plane, or by filtering out the out-of-focus emission.

## 2.3. Total internal reflection fluorescence microscopy

Total internal reflection fluorescence microscopy (TIRFM) uses the phenomenon of total internal fluorescence to illuminate only the fluorophores close to the surface of the coverslip [15, 16]. When light travels from a medium with high refractive index ($n_1$) to a medium of low refractive index ($n_2$), it is either refracted in the second medium or reflected at the interface depending on the incidence angle (Figure 2.5). For refraction, the relationship between the refractive indices and angles is given by Snell's law:

$$n_1 \sin\theta_1 = n_2 \sin\theta_2 \tag{8}$$

When the incidence angle is equal to the critical angle $\theta_c$, the refracted beam travels parallel to the interface between the two media ($\theta_2 = 90°$). The critical angle can be calculated from Snell's law:

$$\theta_c = \sin^{-1}\frac{n_2}{n_1} \tag{9}$$

For incidence angles above $\theta_c$, Snell's law cannot be fulfilled and the beam is completely reflected at the interface. This phenomenon is known as total internal reflection. However, a portion of the energy of the incident light is converted into an evanescent wave that penetrates into the second medium perpendicular to the interface. The evanescent wave has the same frequency as the incident light and its amplitude $I$ decays exponentially with distance $z$ from the interface:

$$I(z) = I_0 \exp\left(-\frac{z}{d}\right) \tag{10}$$

where $I_0$ is the intensity of the wave at the interface ($z = 0$) and the penetration depth $d$ is defined by

$$d = \frac{\lambda_0}{4\pi\sqrt{{n_1}^2 \sin\theta_1 - {n_2}^2}} \tag{11}$$

where $\lambda_0$ is the wavelength of the incident beam in vacuum. The penetration depth of this evanescent wave is typically in the range of ~100-200 nm [16].

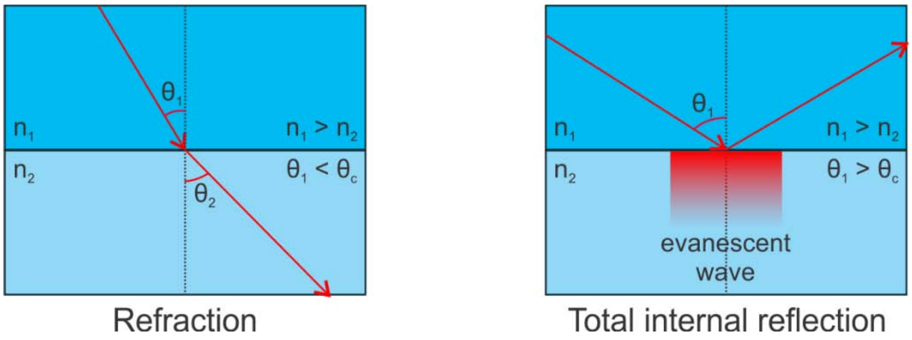

Figure 2.5. Behaviour of light at the interface of two media with different refractive indices $n_1$ and $n_2$. In both cases, $n_1 > n_2$. Refraction (*left*) occurs when the incidence angle $\theta_1$ is smaller than the critical angle $\theta_c$, and total internal reflection (*right*) occurs when $\theta_1$ is larger than $\theta_c$.

Therefore, by illuminating the sample such that the incidence angle of the excitation beam at the coverslip-sample boundary, TIRFM restricts illumination to the sample surface immediately adjacent to the coverslip. There are two main microscopy configurations to achieve total internal reflection: prism-type and objective-type TIRFM [17, 18]. For prism-type TIRFM (Figure 2.6A), the excitation beam is directed into a quartz prism so that it strikes the prism-sample interface at an incidence angle above the critical angle. The total internal reflection of the beam generates an evanescent field below the prism where the sample is located. The fluorescence emission is collected by an objective placed on the opposite side of the coverslip with respect to the prism. For objective-type TIRFM (Figure 2.6B), the excitation beam is focused off-axis on the back focal plane of a high numerical aperture objective (NA 1.4 or higher). The beam exits the objective at an angle sufficient for total internal reflection to occur at the coverslip-sample interface. The evanescent wave is generated above the coverslip and the same objective collects the fluorescence emission. In this work, objective-type TIRFM is used as it allows easy access and manipulation of the live-cell samples. Additionally, with the use of a translational stage, one can also switch between TIRF and widefield illumination modalities.

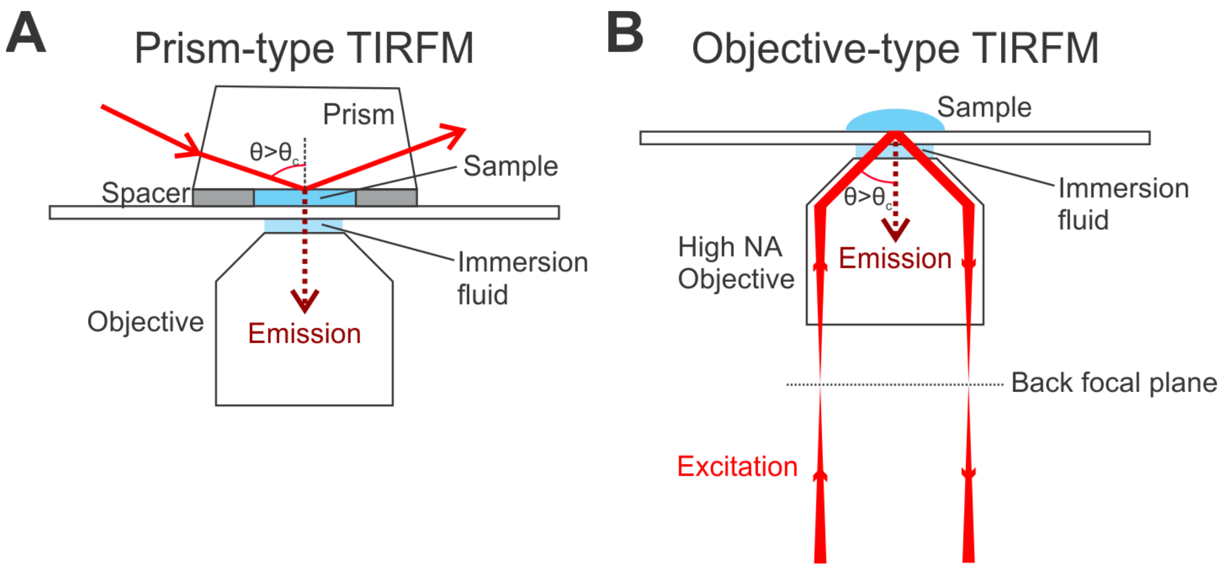

Figure 2.6. TIRFM excitation modes. (A) A schematic of prism-type TIRFM. The excitation beam is reflected at the prism-sample interface. (B) A schematic of objective-type TIRFM. The excitation beam is focused off-axis on the back focal plane of the objective, creating a collimated beam that exits the objective at an angle. The beam is then reflected at the coverslip-sample interface.

TIRFM is therefore suitable for experiments where the focal plane of interest lies close to the reflection interface, such as when the fluorophores are immobilized on the surface [19, 20], or when imaging the plasma membrane of cells attached to the surface of the coverslip [21]. It is highly effective at minimizing the background signal from out-of-focus planes as they are simply not illuminated. This also greatly reduces phototoxicity in the case of live-cell imaging. However, the shallow penetration depth of the evanescent wave also means TIRFM cannot be used to image objects further away from the coverslip surface.

A Nikon Eclipse Ti microscope with homebuilt excitation and detection pathways [22] was used for the widefield and TIRF imaging in this work. The setup features 6 continuous wave laser diodes (445 nm, 488 nm, 514 nm, 561 nm, 594 nm, 642 nm) and 3 EMCCD cameras (DU-897, Andor). The lasers are coupled to an acousto-optic tunable filter (AOTF, PCAOM LFVIS5, Gooch & Housego) controlled by a field programmable gate array (FPGA, cRIO-9074, National Instruments). This enabled laser switching on the millisecond timescale and also allowed camera exposure to be synchronized to the laser excitation. The image acquisition parameters for each project are explained in the respective chapters and publications.

## 2.4. Confocal Microscopy

Another microscopy method aimed at reducing out-of-focus signal is confocal microscopy, invented in 1957 by Marvin Minsky [23]. Instead of illuminating the entire sample as in wide-field microscopy, a confocal microscope focuses light to a small spot in the focal plane. In the original prototype, Minsky achieved this by placing a pinhole in the path of the light source. Modern confocal microscopes generally use a collimated light beam for excitation. A second pinhole is placed in the conjugate focal plane (hence the term 'confocal') in front of the detector to eliminate out-of-focus signal, which arises from illumination of the sample by light cones before and after the focal plane (Figure 2.7). The result is that a small observation volume is achieved. This confocal observation volume is often described as a point spread function (PSF), which describes how a point emitter is seen in an imaging system. The confocal PSF is the product of the excitation and detection PSFs and is commonly approximated as a 3D Gaussian function:

$$PSF(x,y,z) \propto exp\left[-2\left(\frac{x^2+y^2}{\omega_r^2}+\frac{z^2}{\omega_z^2}\right)\right] \tag{12}$$

where $\omega_r$ and $\omega_z$ are respectively defined as the lateral and axial distances from the center at which the intensity decreases to $1/e^2$ of the maximum.

The diffraction image of a point emitter is described by the Airy disk [24]. The lateral resolution limit *r* according to the Rayleigh criterion can be given as:

$$r = \frac{0.61\lambda}{NA} \tag{13}$$

$$NA = n\sin\alpha \tag{14}$$

where $\lambda$ is the excitation wavelength and $NA$ is the numerical aperture of the objective, which is in turn defined by the refractive index $n$ and the maximum half-opening angle of the objective $\alpha$. The resolution limit given here describes the minimum distance at which two point emitters can be distinguished by the microscope. The Rayleigh criterion [25] defines this as the distance where the maximum of the Airy disk of the first emitter overlaps with the first minimum of that of the second emitter.

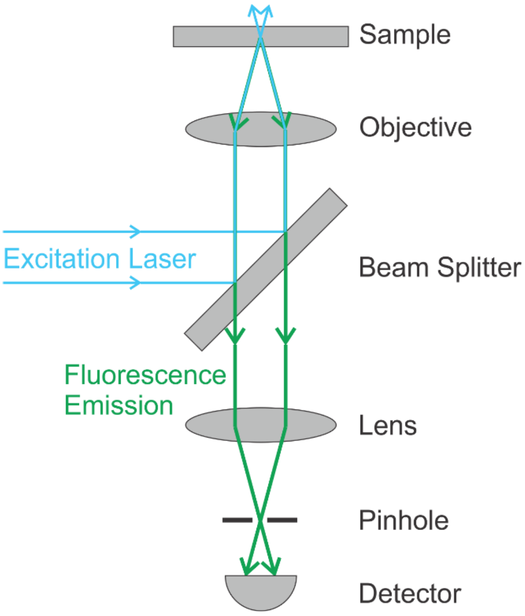

Figure 2.7. Principle of a confocal microscope. A diffraction-limited collimated laser beam is focused onto the sample by the microscope objective. Fluorescence emission from the focal point passes through the pinhole in the conjugate focal plane. Out-of-focus light is blocked by the pinhole.

As a confocal microscope collects fluorescence from only one focal point at a time, either the sample or the focus needs to be moved to generate an image. Moving the sample can be implemented via a motorized stage, such as a piezoelectric scanning stage, but this results in relatively slow scan speeds. Alternatively, the focus can be moved by using scanning mirrors to change the incident angle at the back focal plane, as is done in confocal laser scanning microscopes (CLSM). To avoid changing the position of the beam at the objective during the scan, a relay system, such as telescope lenses, is set up between the scanning mirror and the objective (Figure 2.8). If the focal planes of the lenses coincide, tilting the scanning mirror only changes the angle but not the position of the incident beam at the back focal plane of the objective. Additionally, the scanning mirror and relay system are placed after the excitation-emission dichroic, such that the fluorescence emission collected from the sample travels in the same path as the excitation beam to reach the dichroic mirror in a process known as descanning. The emission will always reach the pinhole in the same position regardless of the position of the scanning mirror.

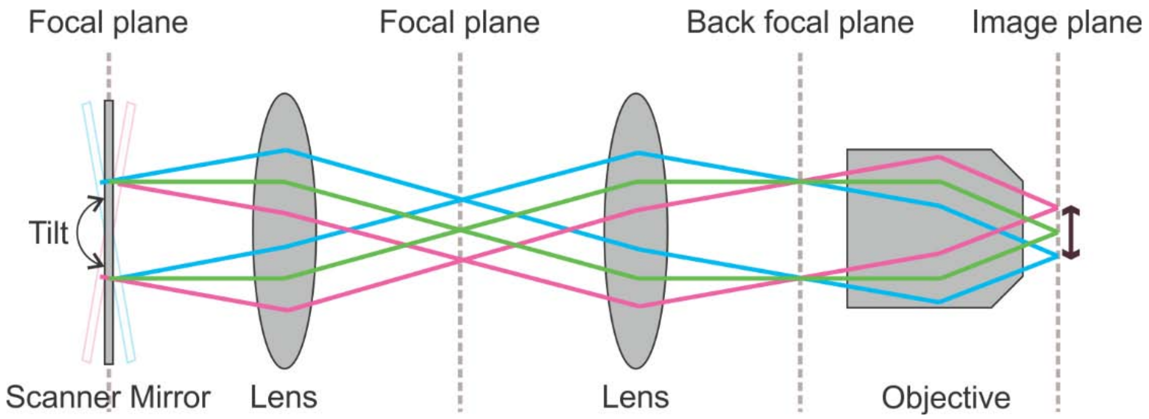

Figure 2.8. Schematic of confocal laser scanning. The scanner mirror and a telescope relay system are setup so that the focal planes of the lenses coincide with the mirror and the back focal plane of the objective. When the scanner mirror is tilted, the focus is translated only along the image plane.

The mechanism by which the mirrors are tilted largely determines the maximum scanning speed. Piezoelectric mirrors can tilt in both axes, but are quite slow and do not significantly improve scanning speed compared to piezoelectric stages. Instead, most CLSMs use a pair of galvanometric mirrors positioned very close to each other, with each mirror controlling tilt in one axis [26, 27]. Such systems can achieve line scan frequencies of around 1kHz, corresponding to a maximum frame rate of 1-10 frames per second, depending on the number of lines scanned per image.

## 2.5. Time correlated single photon counting

The measurement of photon arrival time with high temporal resolution is essential for many of the methods described in this work, such as pulsed interleaved excitation (Chapter 2.6) and the measurement of fluorescence lifetime (Chapter 3.3). This can be achieved with time correlated single photon counting (TCSPC), a detection method that enables the measurement of the arrival time of single photons with picosecond accuracy [28]. The method measures the time between a synchronization signal, which is used to drive the lasers, and a photon detection event, which is an electronic pulse from counting detectors such as photomultiplier tubes (PMTs) or avalanche photodiodes (APDs). It is commonly paired with confocal microscopy, where the small observation volume facilitates the detection of single photon events even at relatively high fluorophore concentrations, and where the use of counting detectors is also common.

The TCSPC timing information is split into two parts, the macro-time and micro-time. The macro-time is measured as the number of synchronization periods that have passed since the start of the measurement, whereas the micro-time is the delay between the last synchronization signal and photon detection event. The sum of the macro- and micro-time gives the exact arrival time of the photon. The micro-time is measured to picosecond accuracy by the time-to-amplitude converter (TAC). The TAC is a linear voltage ramp generator that can be started by one signal and stopped by another. In most cases, the photon signal is used as the start signal and the synchronization signal is used as the termination signal, as photon events are generally much rarer than synchronization ticks and this setup reduces the effects of the dead time of TACs thereby allowing for higher measurement frequencies. The arrival time of the signals is measured using a constant-fraction discriminator (CFD) that provides an intensity-independent timing of the detected pulse. The voltage from the TAC is digitized by an analog-to-digital converter (ADC) that determines the maximum obtainable timing resolution.

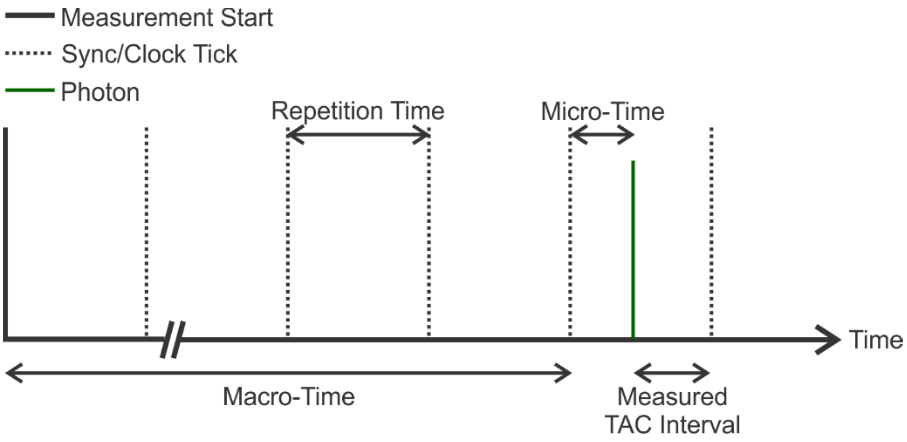

Figure 2.9. TCSPC detection scheme. The TCSPC card is synchronized with the pulsed laser via the synchronization pulses. The timing between the laser pulse and detected photon is measured with picosecond resolution, referred to as the micro-time. The precise photon arrival time is the sum of the macro-time and micro-time.

## 2.6. Pulsed interleaved excitation

An application of TCSPC in multi-color fluorescence microscopy is pulsed interleaved excitation (PIE), in which laser excitation pulses are interleaved within a single TCSPC synchronization period [29-31]. Two or more pulsed lasers, usually of different colors, are triggered at an identical frequency by the synchronization signal. However, one or more lasers are delayed with respect to the first one, such that the fluorescence emission generated by each pulse is complete before the next excitation pulse arrives. In this way, in addition to sorting the photons by the detection channel (using dichroic mirrors and filters to direct them to a specific detector), one can use the micro-time information to assign photons to their excitation source (Figure 2.10).

In a two-color PIE experiment, three PIE channels can be defined based on the detection channel and the micro-time information: green emission after green excitation ($GG$), red emission after green excitation ($GR$) and red emission after red excitation ($RR$). Usually, no signal is detected in the green channel after red excitation as the emission spectrum of the red fluorophore generally has negligible overlap with the emission filter of the green detector. Hence the PIE channel $RG$ can be omitted. The PIE channels $GG$ and $RR$ contain the fluorescence of the green and red fluorophores after direct excitation by their respective lasers. *GR*, on the other hand, contains signal from the spectral crosstalk of the green dye, direct excitation of the red dye by the green laser, as well as FRET-sensitized acceptor emission from the red dye.

The use of PIE greatly increases the sensitivity of fluorescence cross-correlation methods (described in Chapter 3.1.2) [32]. Separation of the emissions in *GR* from those in *RR* makes fluorescence cross-correlation spectroscopy (FCCS) and its imaging derivatives more sensitive to weaker interactions and allows quantitative cross-correlation analysis of complexes that undergo FRET.

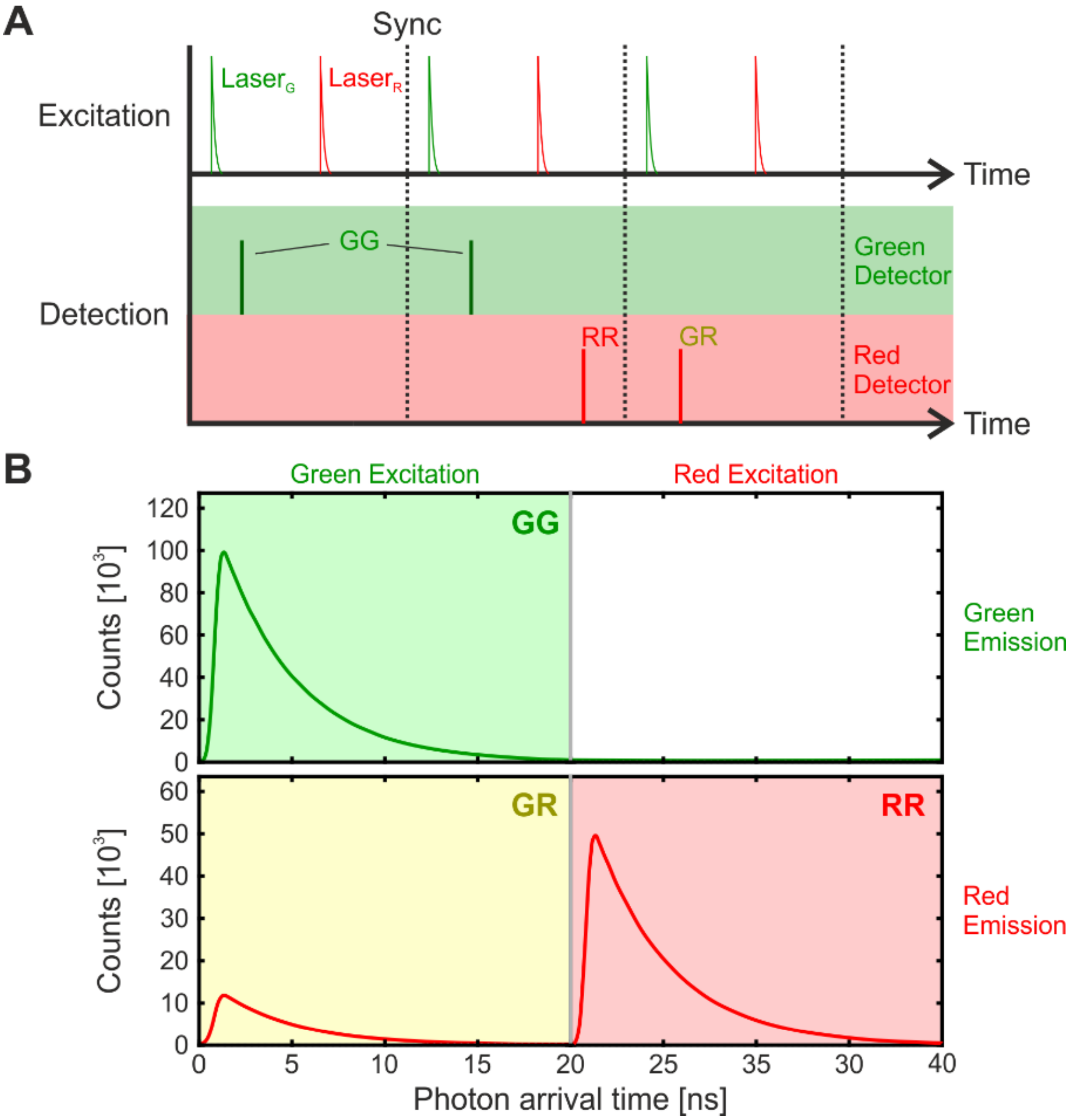

Figure 2.10. Pulsed interleaved excitation (PIE). (A) The excitation and detection scheme of two-color PIE. In each synchronization period, two lasers (green and red) are triggered with a delay with respect to the synchronization signal. The delay for the red laser is longer compared to that for the green laser, so that the emission after green excitation is complete before the red excitation pulse arrives. The emissions are detected by two detectors. Three types of detection events are illustrated: green emission after green excitation (*GG*), red emission after green excitation (*GR*) and red emission after red excitation (*RR*). (B) Micro-time histograms of a two-color PIE measurement showing the fluorescence decays in the PIE channels *GG*, *GR* and *RR*.

PIE is conceptually related to a method known as alternating laser excitation (ALEX) [33], which achieves alternating excitation on the microsecond to millisecond timescales using continuous wave lasers. The method was initially developed for single-molecule FRET analysis [33-35] and involves the rapid switching between two excitation lasers using fast shutters and capturing the resulting emission in both channels after each laser is triggered (for an example see Chapter 6.2.1 and Figure 6.2A, top panel). This produces four emission channels that are equivalent to the PIE channels described earlier. PIE allows the calculation of fluorescence correlation functions down to the sub-microsecond regime, whereas in ALEX this would be limited to the timescale of the alternation period. Like ALEX, PIE can also be applied to single molecule FRET experiments [30], where, by virtue of being an extension of TCSPC, it is also able to provide fluorescence lifetime information not available using ALEX. However, the pulsed excitation of PIE results in higher peak power densities of the lasers and therefore higher photostress and bleaching rates compared to ALEX.

A home-built CLSM with PIE and TCSPC was used for the FLIM and RICS experiments in this work. The setup has been previously described [31, 36] and has been recently rebuilt with newer optical and electronic components [37]. The confocal excitation pathway features 5 pulsed diode lasers (LDH series, Picoquant) driven by a laser driver (PDL 828 Sepia II, Picoquant). Up to 3 lasers can be simultaneously driven at up to 80 MHz in a synchronized manner for PIE. However, a synchronization frequency of 40 MHz or lower is normally used for dual-color PIE so that there is sufficient temporal range to separate the fluorescence decay from each excitation pulse on the photon arrival microtimes. The fluorescence emission is focused on a 80 μm pinhole and recollimated with an identical achromatic lens (AC254-100-A, Thorlabs) before being spectrally separated by beamsplitters for detection on single photon avalanche diodes (PDM series, PicoQuant) or APDs (Count® Blue and Count® Series, Laser Components). Each detector is connected to a separate TCSPC card (SPC-140, Becker & Hickel). Detailed image acquisition parameters for FLIM (Chapter 4) and RICS (Chapter 7) are explained in the respective publications of each project (Appendices I and III respectively).

# 3. Fluorescence Microscopy and Spectroscopy Methods

With the development of highly sensitive and accurate electronic equipment and advanced data analysis techniques, fluorescence microscopy has developed into a versatile tool for investigating a wide variety of physical and chemical properties. In this chapter, I introduce the techniques used in this work for the analysis of live-cell fluorescence data, including fluorescence fluctuation spectroscopy, fluorescence lifetime imaging, and single particle tracking.

## 3.1. Fluorescence Fluctuation Spectroscopy

Fluorescence fluctuation spectroscopy (FFS) is a collection of techniques that analyzes the intensity fluctuations of a fluorescence signal [38, 39]. By measuring the fluorescence signal from a sufficiently small volume containing only a few molecules, one can extract information about the distribution and kinetic parameters of the species present. In experiments with much larger observation volumes (such as in a cuvette), the fluctuations are averaged out and this information is lost. Therefore, confocal and two-photon microscopy are ideal signal acquisition methods for FFS, as they can achieve the small observation volumes below 1 $\mu m^3$. In the following section, I will focus on fluorescence correlation spectroscopy, which analyzes the temporal aspects of the fluctuations.

### 3.1.1. Fluorescence Correlation Spectroscopy

Fluorescence correlation spectroscopy (FCS) is an analysis of the temporal fluctuations of fluorescence intensity [40-42]. The temporal self-similarity of the fluorescence signal as a function of the time lag, $\tau$, can be accessed by calculating the auto-correlation function (ACF). From the ACF, information regarding the photophysics, diffusion and binding kinetics of a fluorescent species in solution can then be extracted.

The temporal ACF can be expressed as:

$$G(\tau) = \frac{\langle I(t) \cdot I(t+\tau) \rangle}{\langle I(t) \rangle^2} - 1 = \frac{\langle \delta I(t) \cdot \delta I(t+\tau) \rangle}{\langle I(t) \rangle^2} \tag{15}$$

where $G(\tau)$ is the correlation amplitude at time lag $\tau$, $I(t)$ and $I(t+\tau)$ is the fluorescence intensity at a certain time point $t$ or $t+\tau$ respectively, and the angled brackets represent the average over all possible time points t. Alternatively, the equation can be expressed as a function of intensity fluctuations ($dI(t) = I(t) - \langle I(t) \rangle$).

Fluctuations in fluorescence intensity can occur due to a combination of factors. At extremely short timescales ($10^{-10}$ to $10^{-8}$ s), we observe antibunching (I in Figure 3.1) [43, 44], where the emission of a second photon is delayed due to fluorescence lifetime, which is 1-4 ns for most fluorophores. This results in sub-Poissonian statistics and thus decreases the auto-correlation amplitude. A second fast process observable in FCS is molecular rotation (II in Figure 3.1) [45, 46], which can range from a few hundred picoseconds for small fluorophores [47] to about 50 ns for fluorescent proteins [48]. The rotation of the fluorophore results in intensity fluctuations because the probability of excitation depends on the alignment of the polarization of the excitation light with the fluorophore's dipole moment. At timescales of $10^{-7}$ to $10^{-6}$ s, photophysical effects, such as blinking from intersystem crossing to a triplet state, dominate as the cause of intensity fluctuations (III in Figure 3.1) [49-52].

At slower timescales of $10^{-5}$ to $10^{-1}$ s, fluorophores diffusing in and out of the observation volume are mainly responsible for the intensity fluctuations (IV in Figure 3.1) [40]. At these timescales, FCS is sensitive to the fluctuations in the number of fluorescent particles within the observation volume. As the time lag, $\tau$, increases, it becomes more and more likely that molecules would diffuse into or out of the observation volume, resulting in fluctuations in the fluorescence signal relative to the original time point ($\tau = 0$) and thus a decrease in the ACF amplitude. Eventually, enough time passes that the intensity fluctuations relative to the original time point become essentially random and the correlation amplitude decays to zero. The faster the molecule diffuses, the more quickly the ACF decays.

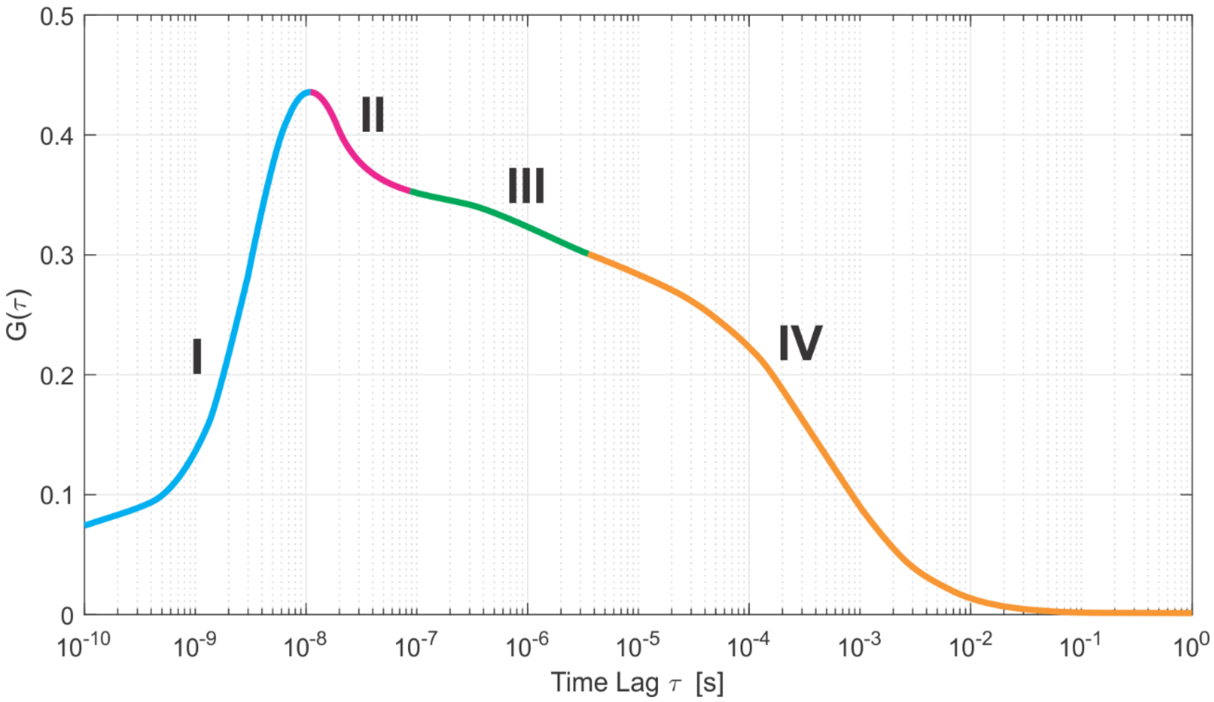

Figure 3.1. Sketch of an autocorrelation curve depicting the fluctuation sources at different timescales. I: antibunching. II: molecular rotation. III: photophysical effects. IV: translational fluctuations.

The decay of the ACF at the microsecond and slower timescales can be modeled as a function of the diffusion coefficient of the fluorescent species and the size of the observation volume (Figure 3.2). For free diffusion through a 3D Gaussian volume (which approximates the confocal detection volume), the ACF can be modelled as [40]:

$$G(\tau) = \frac{\gamma}{N} \cdot \left( \frac{1}{1 + \frac{4D\tau}{\omega_r^2}} \right) \cdot \left( \frac{1}{1 + \frac{4D\tau}{\omega_z^2}} \right)^{\frac{1}{2}} \tag{16}$$

where N is the average number of particles in the detection volume, D is the diffusion coefficient and $\omega_r$ and $\omega_z$ respectively define the lateral and axial sizes of the Gaussian volume (see Chapter 2.4). The shape factor, γ, accounts for the fact that the Gaussian volume is not a step function with clear borders, but gradually decreases in intensity from the center. For a 3D Gaussian, $\gamma$ is equal to $2^{-\frac{3}{2}}$.

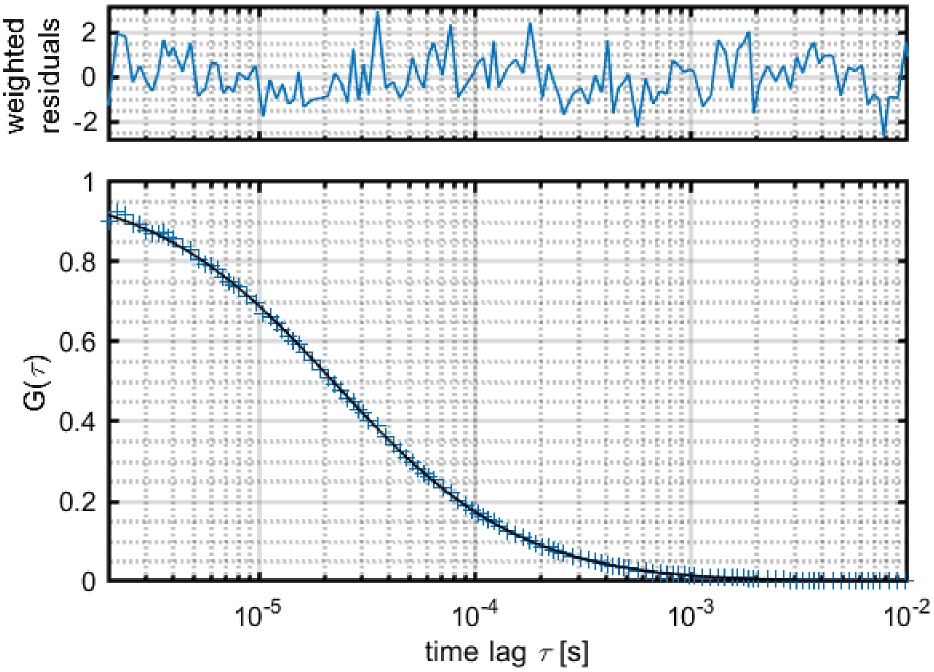

Figure 3.2. An FCS curve of Atto488-COOH at 23 °C acquired on a confocal microscope with a 60x water-immersion objective. Pluses (*blue*) represent the calculated ACF using the measured data and the solid line (*black*) is a fit using equation (16). The weighted residuals are shown in the upper plot.

FCS has been widely applied to measure diffusion changes as a result of structural and size changes of the labeled molecule, both *in vitro* [53-55] and in live-cell experiments [56, 57]. However, this approach has limited sensitivity for detecting changes in molecular weight. The diffusion coefficient for spherical particles is directly proportional to the hydrodynamic radius, which in turn scales with the cube root of molecular mass. Therefore, a doubling of molecular mass (such as when binding to an interaction partner) would only result in a 26% change in diffusion time. While such a change can still be detected by FCS, it would be harder to quantify interactions that result in a mixture of bound and unbound species, or interactions that produce even smaller changes in molecular mass. Fluorescence cross-correlation spectroscopy (FCCS), introduced in the next section, can be very helpful in overcoming the limitations of FCS when measuring interactions between two species.

### 3.1.2. Fluorescence Cross-Correlation Spectroscopy

Fluorescence cross-correlation spectroscopy (FCCS) is an extension of FCS from correlating a signal with itself to the correlation of two different signals. The temporal cross-correlation function (CCF) for two signals $i$ and $j$ can be written as:

$$G_{ij}(\tau) = \frac{\langle \delta I_i(t) \cdot \delta I_j(t+\tau) \rangle}{\langle I_i(t) \rangle \cdot \langle I_j(t) \rangle} \tag{17}$$

The fluorescence signal from a sample could be separated in a variety of ways to obtain the two fluorescence signals used for FCCS. One can discriminate the signal based on parameters such as fluorescence lifetime [58] or polarization [59, 60]. Most commonly, the fluorescence signal is spectrally separated in what is known as dual-color FCCS [61-63].

Dual-color FCCS is useful for detecting interactions between two differently labeled species. When correlating the fluorescence signals of two spectrally-separated fluorescent dyes, the CCF will only show a non-vanishing amplitude in the case of conjoined movement of both dyes, i.e. interaction between the two species. It is important that there is little to no spectral crosstalk between the two signals, as such crosstalk would be correlated. With conventional excitation methods, it can be difficult to completely eliminate spectral crosstalk for dyes with significant spectral overlap. However, when measuring fluorescence with PIE (Chapter 2.6), spectral crosstalk and the primary fluorescence emissions can be separated into different channels based on photon arrival time. With PIE, one can obtain fluorescence signals containing only the emissions after direct excitation by the respective laser. The CCF of such fluorescence signals gives an unambiguous and quantifiable readout for interaction. The CCF amplitude at $\tau = 0$ is directly proportional to the concentration of dual-color species, but is inversely proportional to the average particle concentration in each individual channel. We can extract the fraction of dual-color species by taking the ratio of the cross-correlation to auto-correlation amplitude [64].

$$G_{ij,CCF}(0) = \gamma \cdot \frac{N_{ij}}{(N_i + N_{ij}) \cdot (N_j + N_{ij})} \tag{18}$$

$$G_{i,ACF}(0) = \frac{\gamma}{N_i + N_{ij}} \tag{19}$$

$$\frac{G_{ij,CCF}(0)}{G_{i,ACF}(0)} = \frac{N_{ij}}{N_j + N_{ij}} \tag{20}$$

where $N_i$ and $N_j$ are the average number of particles in the detection volume for the non-interacting fractions of the species $i$ and $j$, and $N_{ij}$ is the average number of interacting molecules. Note that this is also applicable to the spatial correlation methods discussed later.

## 3.2. Image Fluctuation Spectroscopy

The techniques discussed so far in this chapter use temporal correlations to extract information from fluorescence signals. Similar correlation techniques can be applied to images, which consist of fluctuations of the fluorescence signal in space, giving rise to image correlation spectroscopy and its derivative methods. By correlating the signal spatially, we can extract information about the spatial distribution of the fluorescent species and thereby infer its concentration within the sample.

### 3.2.1. Image Correlation Spectroscopy

Image correlation spectroscopy (ICS) [65-68] is the spatial equivalent to FCS. Instead of correlating the signal temporally, the correlation is performed in the two spatial dimensions of the image:

$$G(\xi,\psi) = \frac{\langle I_i(x,y) \cdot I_j(x+\xi, y+\psi)\rangle}{\langle I_i(x,y)\rangle \cdot \langle I_j(x,y)\rangle} - 1 = \frac{\langle \delta I_i(x,y) \cdot \delta I_j(x+\xi, y+\psi)\rangle}{\langle I_i(x,y)\rangle \cdot \langle I_j(x,y)\rangle} \tag{21}$$

, where $x$ and $y$ are the dimensional coordinates of the image, and $\xi$ and $\psi$ are the corresponding spatial lags in pixels. $I$ denotes the intensity of the signal at the corresponding pixel coordinate. The angled brackets indicate an average over all spatial position of the image.

For images that contain randomly distributed particles that are significantly smaller than the size of the focus, the spatial ACF can be fit by a 2D Gaussian function:

$$G(\xi,\psi) = \frac{\gamma}{N} \cdot \exp\left(-\frac{\delta r^2 \cdot (\xi^2 + \psi^2)}{\omega_r^2}\right) \tag{22}$$

where $\omega_r$ is the distance at which the PSF amplitude decays to $e^{-2}$ of the maximum value, $N$ is the average number of particles in the focus, $\gamma$ is the shape factor ($2^{-3/2}$ for 3D and $2^{-1}$ for 2D Gaussian focus profile) and $\delta r$ is the pixel size. Figure 3.3 shows an example of a spatial ACF and the fitted Gaussian function.

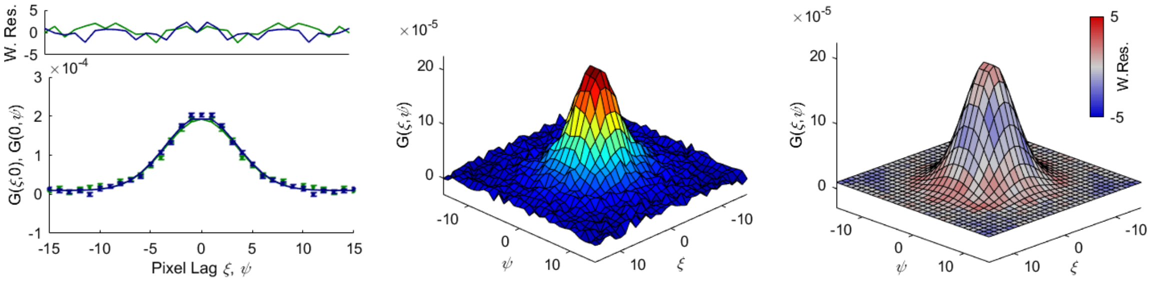

**Figure 3.3.** ICS of palmitoylated-GFP-mCherry in HEK293T cells. On-axis (left) and surface (middle) of the spatial ACF for GFP, as well as the surface plot of the fit to the ACF (right) using equation (22), colored according to the weighted residuals of the fit.

The spatial autocorrelation function represents the average size and concentration of the observed particles. Thus, sufficient sampling is necessary to obtain a correlation function that is representative of the underlying distributions. In a single image, the number of pixels available for correlation is limited by the pixel density of the cameras as well as the size of the sample. This would often result in under-sampling of the statistics and therefore introduce noise or artefacts in the spatial correlation function. To overcome this problem, multiple frames of the same sample would be taken and their individual spatial correlation functions are averaged to produce the final correlation function.

As the correlation amplitude is inversely proportional to the average number of fluorophores in the focus, we can extract the density or concentration of particles from the spatial ACF (SACF). In addition, using the average intensity $\langle I \rangle$, we can determine the molecular brightness $\epsilon$:

$$\epsilon = \frac{\langle I \rangle}{N} \tag{23}$$

When the shape factor $\gamma$ is accounted for and when all emitters are of the same brightness, $\epsilon$ represents the intensity of a single emitter at the center of the focus. We can then use the molecular brightness to determine the fluorophore stoichiometry and by extension the oligomerization state of the sample.

When the particle size exceeds that of the focus, $\omega_r$ becomes the convolution of the focus and particle dimensions. This, in turn, enables the measurement of particle size through ICS.

Similar to FCS and FCCS, ICS can be extended to two different images in image cross-correlation spectroscopy [69]. The resulting spatial CCF (SCCF) has a non-vanishing amplitude when there are similarities in the spatial fluctuations of the two images. Most commonly this can be applied to images of differently labeled species, where a cross-correlation would only occur when they colocalize.

### 3.2.2. Raster Image Correlation Spectroscopy

Raster image correlation spectroscopy (RICS) is an extension of ICS that is specifically applied to images recorded with a confocal laser scanning microscope [70-73]. Unlike widefield microscopy images recorded with a camera, the confocal microscope generates an image by performing a raster scan to create the image. In such a scan, the focus is moved along the x-axis (continuously or stepwise for each pixel) until the end of the line, upon which the focus is retracted to the starting position, shifted one pixel in the y-direction, and a new line is scanned. This is repeated until a complete image is formed. This method of imaging introduces a time delay in the acquisition of each pixel, which encodes temporal information in the resulting spatial correlation. Additionally, the time delay differs depending on the direction of the spatial pixel lag – the pixel-to-pixel time lag in the x-axis is determined by the pixel dwell time $\tau_p$ and is several orders of magnitude smaller than the corresponding time lag for the y-axis, which is determined by the line time $\tau_l$. RICS extracts information from this temporal component to investigate processes that occur on the timescale of image acquisition.

The correlation algorithm for RICS is the same as for ICS, but the fit function has to be adjusted to account for the temporal component. For free diffusion in a 3D Gaussian focus, the spatial correlation function can be written as:

$$G(\xi,\psi) = \frac{\gamma}{N} \cdot \left(1 + \frac{4D \cdot (\tau_p \xi + \tau_l \psi)}{\omega_r^2}\right)^{-1} \cdot \left(1 + \frac{4D \cdot (\tau_p \xi + \tau_l \psi)}{\omega_z^2}\right)^{-\frac{1}{2}} \cdot \exp\left(-\frac{\delta r^2 \cdot (\xi^2 + \psi^2)}{\omega_r^2 + \left(4D \cdot (\tau_p \xi + \tau_l \psi)\right)}\right) \tag{24}$$

where $N$ is the average number of particles in the focal volume, $D$ is the diffusion coefficient and $\gamma$ is the shape factor, $\omega_r$ and $\omega_z$ define the size of the focus in the lateral and axial dimensions respectively (see Chapter 2.4, equation (12)), $\delta r$ is the pixel size, $\tau_p$ and $\tau_l$ represent the pixel and line times respectively.

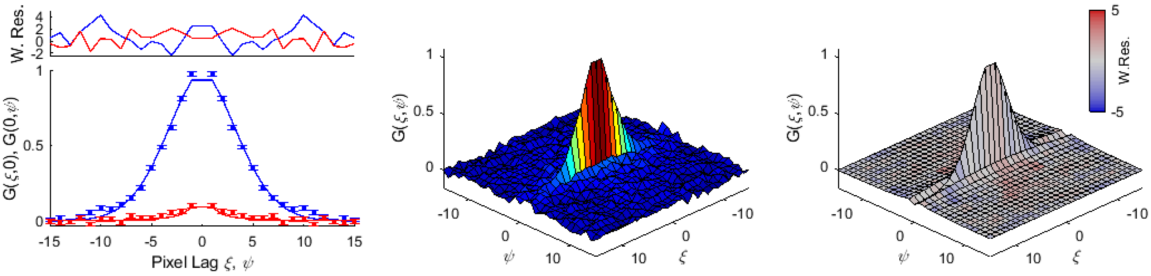

**Figure 3.4.** EGFP diffusion in a HEK293T cell as measured by RICS. Slices along the $\xi$ and $\psi$ spatial lag axes (left) and surface plot (middle) of the SACF. Surface plot of the fit to the SACF using equation (24) is shown on the right, colored according to the weighted residuals of the fit.

Cross correlation experiments can be performed using RICS based on the same principles to FCCS and ICCS [73, 74]. An amplitude for the SCCF is only observed when the two measured species show concerted movement, such as when they bind to each other. This enables the detection and quantification of molecular interactions by simply imaging a sample in which each potential interaction partner is tagged by a different fluorophore. An example of cross-correlation RICS performed on samples where EGFP and mCherry are in a tandem construct (palmitoylated-EGFP-mCherry) or diffusing separately (CD86-EGFP/CD86-mCherry) is shown in Figure 3.5.

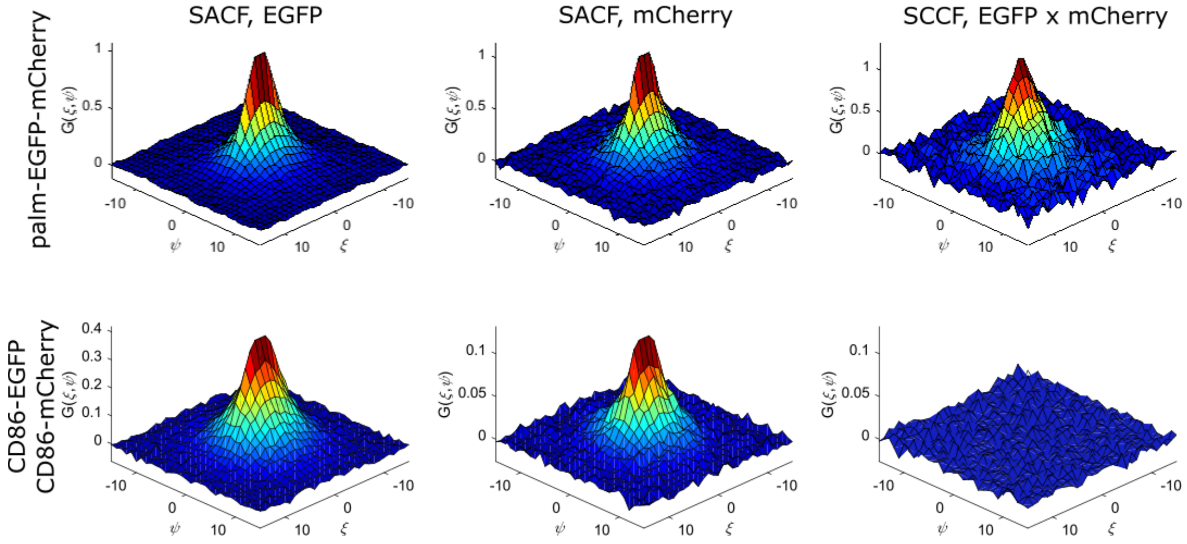

Figure 3.5. 2-color RICS on HEK293T cells expressing palmitoylated-EGFP-mCherry tandem construct (top row) and CD86-EGFP/CD86-mCherry (bottom row), which is a monomeric membrane associated protein. The data was averaged over 150 frames.

Wavelength dependent lateral focus shift, which is noticeable in the SCCF of the EGFP-mCherry tandem construct, can be accounted for by adapting the fit equation. The addition of shift parameters $\delta x$ and $\delta y$ accounts for the spatial shift of the observation volume while leaving the temporal correlation untouched:

$$G(\xi,\psi) = \frac{\gamma}{N} \cdot \left(1 + \frac{4D \cdot (\tau_p \xi + \tau_l \psi)}{\omega_r^2}\right)^{-1} \cdot \left(1 + \frac{4D \cdot (\tau_p \xi + \tau_l \psi)}{\omega_z^2}\right)^{-\frac{1}{2}} \cdot \exp\left(-\frac{\delta r^2 \cdot ((\xi - \delta x)^2 + (\psi - \delta y)^2)}{\omega_r^2 + \left(4D \cdot (\tau_p \xi + \tau_l \psi)\right)}\right) \tag{25}$$

Note that the use of achromatic lenses can largely correct this focus shift. For the CLSM used in this work, this was implemented in a recent upgrade of the setup [37].

### 3.2.3. Arbitrary Region RICS

The classical algorithm used for RICS and ICS analyses as discussed up to this point requires a square region-of-interest (ROI) and only performs well when there is a relatively high homogeneity within the ROI. These requirements pose significant limitations when dealing with images from live-cell imaging experiments, as living cells contain many complex and inhomogeneous structures. While one could decrease the size of the ROI and position it over a relatively homogenous area, it can be difficult to find such an area while still having a sufficiently large ROI for an accurate spatial correlation analysis, as limited statistics reduce the accuracy of the spatial correlation analysis below n ≈ 64 [75]. Moreover, many cellular structures, such as the endoplasmic reticulum (ER) or mitochrondria, have complex and dynamic shapes that are not satisfactorily handled by a square ROI.

An adapted version of the RICS algorithm, known as arbitrary-region RICS (ARICS), has been developed so that ROIs of any shape can be accepted for the spatial correlation analysis [75]. An arbitrarily shaped binary mask, $R(x, y)$, is generated, for which pixels inside the ROI have a value of 1 and those outside have a values of 0:

$$R(x,y) = \begin{cases} 1\ (inside) \\ 0\ (outside) \end{cases} \tag{26}$$

The image is then masked by an elementwise multiplication with R:

$$I_R(x,y) = R(x,y)I(x,y) \tag{27}$$

The fluctuation image is then defined as:

$$\delta I_R(x,y) = R(x,y)\{I_R(x,y) - \langle I_R(x,y)\rangle_{ROI}\} \tag{28}$$

where $\langle I_R(x,y)\rangle_{ROI}$ is the mean intensity of all pixels included in the ROI. Then the unnormalized SACF can be written as:

$$G(\xi,\psi) = \frac{\langle \delta I_R(x,y) \cdot \delta I_R(x+\xi, y+\psi)\rangle}{\langle R(x,y) \cdot R(x+\xi, y+\psi)\rangle} \tag{29}$$

where the correlation in the denominator represents the number of times a particular spatial lag has been sampled, so that each pixel lag in the SACF is averaged by the number of times it was observed in the ROI. The SACF is then normalized by the averaged intensity of all pixels in the ROI, $\langle I_R(x,y)\rangle^2$ and averaged over all frames.

The ROI can be generated in several ways. It can be generated by manually drawing over the image to specify an area to be included or excluded. Alternatively, certain pixel characteristics can be used for defining the ROI, such as the absolute or relative intensity or intensity variance. By setting a threshold for such parameters, one could for example filter out large bright aggregates or dark vesicles moving through the imaged area. In addition, the ROI could also be generated from another color channel of the same image series, where a particular structure could be labelled. Overall, there is a lot of flexibility in the generation of the ROI and this could be adapted according to the needs of the experiment.

For live-cells, it is often necessary to remove slow fluctuations and spatial inhomogeneities from the raw image data before performing a RICS analysis. This can be achieved by subtracting a moving average of the pixel intensities:

$$I_{RICS}(x,y,f) = I(x,y,f) - \langle I(x,y,f)\rangle_{\Delta F} + \langle I(x,y,f)\rangle \tag{30}$$

Here, $I(x, y, f)$ is the intensity of pixel $(x, y)$ in frame $f$, $\langle I(x,y,f)\rangle_{\Delta F}$ is a moving average of the pixel intensities from frames $(f-\Delta F)$ to $(f+\Delta F)$. $\langle I(x,y,f)\rangle$ is the mean intensity of all pixels in all frames. For images acquired on a CLSM, a value of 1 is usually used for ΔF to generate a moving average over 3 frames. Additionally, when performing the temporal average, pixels that were excluded from the ROI in the time window $(f \pm \Delta F)$ must also be excluded from the ROI of frame $f$. The moving average decreases the amplitude of fluctuations in the original image, as this image itself is also included in the moving average and subtracted from the original data. This decreases the amplitude of the resulting SACF. It is therefore necessary to correct the SACF by rescaling it:

$$G_{corr}(\xi,\psi) = \frac{2\Delta F + 1}{2\Delta F} G(\xi,\psi) \qquad (31)$$

## 3.3. Fluorescence Lifetime Analysis

The signal intensity is not the only parameter that can be measured in a fluorescence experiment. The fluorescence lifetime can provide information about the fluorophore or its surroundings that are unavailable from intensity measurements alone. Fluorescence lifetime is not only determined by the intrinsic properties of the fluorophore but also dependent on its local microenvironment and can be affected by factors such as pH, charge, FRET, and so on. Additionally, we can perform spatially resolved fluorescence lifetime measurements. In fluorescence lifetime imaging microscopy (FLIM), the lifetime of each individual pixel of an image is determined, revealing the spatial distribution of parameters affecting the fluorescence lifetime [76-80].

As described in Chapter 2.1, fluorescence is a first-order process. This in turn means that the fluorescence decay of a single fluorescent species is a single exponential. Multiple exponentials are observed only when the sample contains multiple fluorescent species. This could be caused by different fractions of the sample being quenched to a different degree, which is a parameter of interest in many measurements such as FRET measurements. Some fluorophores, such as EGFP, may also naturally exhibit and transition between multiple states with different fluorescent properties. These fluorophores will always exhibit a multi-exponential decay.

From Equation (2), we know that the fluorescence lifetime depends on the radiative and non-radiative decay rates. For a given fluorophore and solvent, the radiative decay rate Γ is relatively stable and depends on the excitation and emission spectra. The local microenvironment, however, can heavily influence the non-radiative decay rates. A common example of this is Förster resonance energy transfer (FRET), which is a form of quenching in a donor-acceptor system. In FRET, energy can be transferred from a donor fluorophore to an acceptor via dipole-dipole interactions. This creates a non-radiative decay pathway and reduces the fluorescence lifetime by increasing $\mathrm{k}_{nr}$. As FRET requires the acceptor to be in close proximity to the donor (within 10 nm), when the donor and acceptor are placed on different molecules or different parts of a larger molecule, we can resolve interactions or conformational changes using the donor lifetime as a readout for the distance between the donor and acceptor.

The distance dependence of the efficiency of energy transfer in FRET can be used to accurately measure the distance between a donor-acceptor fluorophore pair. From Equations (2) and (3) we can derive FRET efficiency, $E$, as an expression of donor fluorescence lifetime:

$$E = 1 - \frac{\tau_{FRET}}{\tau_0} \tag{32}$$

where $\tau_0$ is the native fluorescence lifetime of the donor in the absence of the acceptor and $\tau_{FRET}$ is the lifetime measured in the presence of the acceptor.

### 3.3.1. Fluorescence lifetime measurements

Two approaches for measuring fluorescence lifetime are in widespread use: time-domain measurements and frequency-domain measurements.

In time-domain measurements, the sample is excited with a pulse of light, whose width is made as short as possible and ideally much shorter than the fluorescence lifetime $\tau$ of the sample. The time dependent intensity $I(t)$ is measured following the excitation pulse, and the fluorescence lifetime of the sample can be extracted by fitting the intensity decay (Figure 3.6). The intensity decays are often measured through a polarizer oriented at the magic angle of 54.7° from the vertical axis in order to avoid the effects of rotational diffusion and anisotropy on the intensity decay.

In a confocal microscope, a single pulse is not enough to measure the fluorescence lifetime. The small focal volume includes only a few fluorophores that could be excited at a time. Since each fluorophore only emits a maximum of one photon per excitation pulse, the number of photons detectable per pulse is too low for an accurate determination of the fluorescence lifetime. To overcome this problem, TCSPC detection is used in modern confocal microscopes (Chapter 2.5). By synchronizing the detectors to the excitation pulse and registering the precise arrival time (down to a few picoseconds) of each photon relative to the pulse, we can reconstruct the fluorescence decay by building a histogram of the photon arrival times over many excitation cycles.

Accurate analysis of the fluorescence decay data recorded by TCSPC detection must also consider the instrument response function (IRF). Ideally, the sample is excited by an instantaneous laser pulse resulting in a sharp increase in emitted photons followed by a gradual decay (Figure 3.6, cyan dashed line). However, in practice, laser pulses have a non-vanishing pulse width, and the electronics involved in photon detection and timing exhibit a small amount of temporal jitter. These cause even infinitely short signals to be detected with some temporal width, known as the instrument response function (IRF, Figure 3.6, magenta dotted line). The measured photon signal (Figure 3.6, blue solid line) is therefore always a convolution of the actual decay by the IRF.

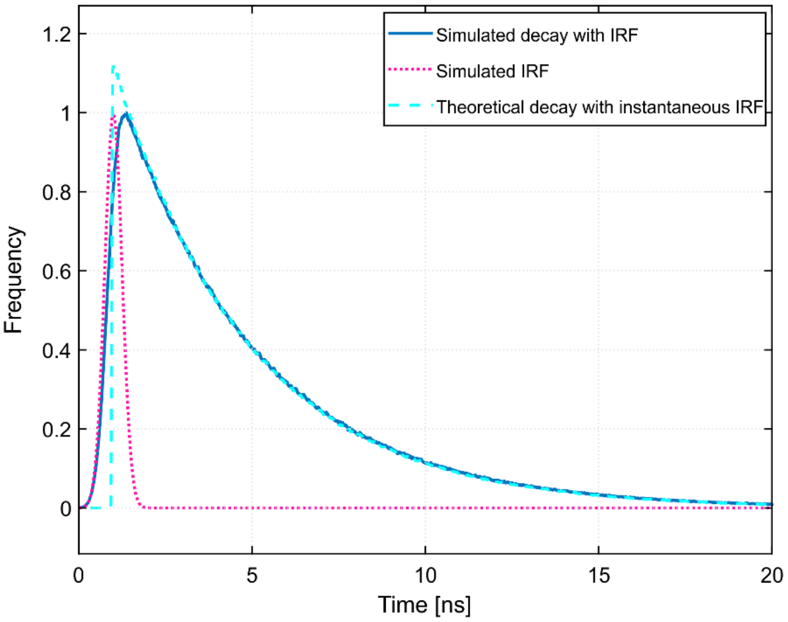

Figure 3.6. Simulated TCSPC data for the fluorescence decay of a fluorophore with a 4 ns lifetime. The simulated decay (blue solid line) with an IRF of 250 ps full-width half maximum (magenta dotted line) are shown normalized to their individual maximums. The theoretical decay for an instantaneous IRF (cyan dashed line) is scaled so that the tail matches the simulated decay.

Alternatively, fluorescence lifetime can be measured using the frequency-domain or phase-modulation method. Here, the sample is excited with intensity-modulated light, typically with a sine-wave. The intensity of the excitation light is modulated at high frequency (typically near 100 MHz) so its reciprocal frequency is comparable to the fluorescence lifetime. When a fluorophore is excited in this way, the emission responds with the same modulation frequency. The lifetime of the fluorophore causes the emission to be delayed with a decrease in amplitude compared to the excitation modulation (Figure 3.7).

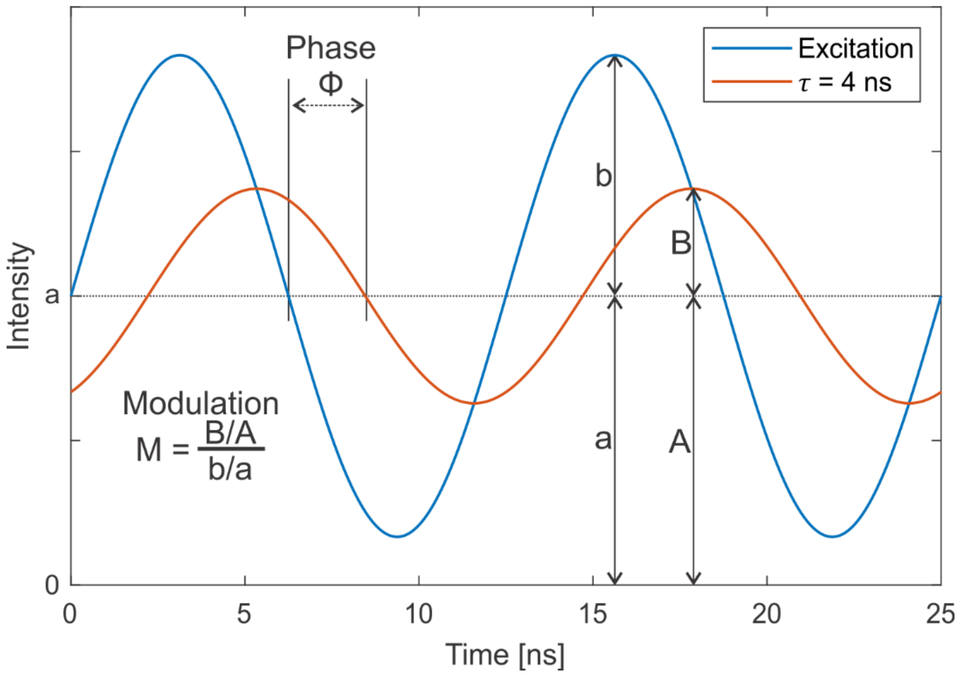

Figure 3.7. Schematic illustration of a frequency-domain fluorescence lifetime measurement. The definitions of phase shift and modulation are shown. The modulation frequency is 80 MHz and the simulated lifetime of the fluorophore is 4 ns.

The phase shift $\Phi_\omega$ and modulation $M_\omega$ depend on the circular modulation frequency ω and the fluorescence lifetime τ:

$$\tan \Phi_\omega = \omega \tau_\Phi \tag{33}$$

$$M_\omega = (1 + \omega^2 \tau_m^2)^{-\frac{1}{2}} \tag{34}$$

From the phase shift and demodulation, two apparent lifetimes $\tau_\Phi$ and $\tau_\mathrm{m}$ can be calculated. In the case of a mono-exponential decay, the two values will be equal. When the signal contains more than one exponential decay, the phase- and modulation-lifetimes will differ depending on the modulation frequency, the lifetimes of the fluorescent species and their fractional intensities.

### 3.3.2. Phasor FLIM

A phasor plot is a graphical way of analyzing fluorescence lifetime decays [81, 82]. For frequency-domain lifetime measurements, each lifetime measurement can be represented as a vector whose angle to the abscissa corresponds to the phase shift $\Phi_\omega$ and whose length corresponds to the modulation $M_\omega$. The Cartesian coordinates s and g of the phasor (a contraction of the term phase vector) represent, respectively, the first sine and cosine Fourier coefficients of the signal:

$$s_\omega = M_\omega \cdot \sin \Phi_\omega = \int_0^\infty I(t) \cdot \sin(\omega t) dt \bigg/ \int_0^\infty I(t) dt \tag{35}$$

$$g_\omega = M_\omega \cdot \cos \Phi_\omega = \int_0^\infty I(t) \cdot \cos(\omega t) dt \bigg/ \int_0^\infty I(t) dt \tag{36}$$

where $I(t)$ represents the fluorescence intensity at time $t$ and $\omega$ is the angular modulation frequency. Each phasor is specific to the frequency at which it was measured.

The shift to Fourier space simplifies the analysis and representation of lifetime data as certain complicated mathematical relationships in regular time space are simplified in Fourier space. Most importantly, phasors show the following behavior:

1. Mono-exponential decays lie on the universal circle centered at (0.5, 0) with radius 0.5.
2. The phasor of a mixture is the sum of the phasors of the components of the pure species, weighted by their fluorescence fraction in the mixture.
3. A convolution in time space leads to a change of base in Fourier space. This results in a rotation and rescaling of the coordinate system.

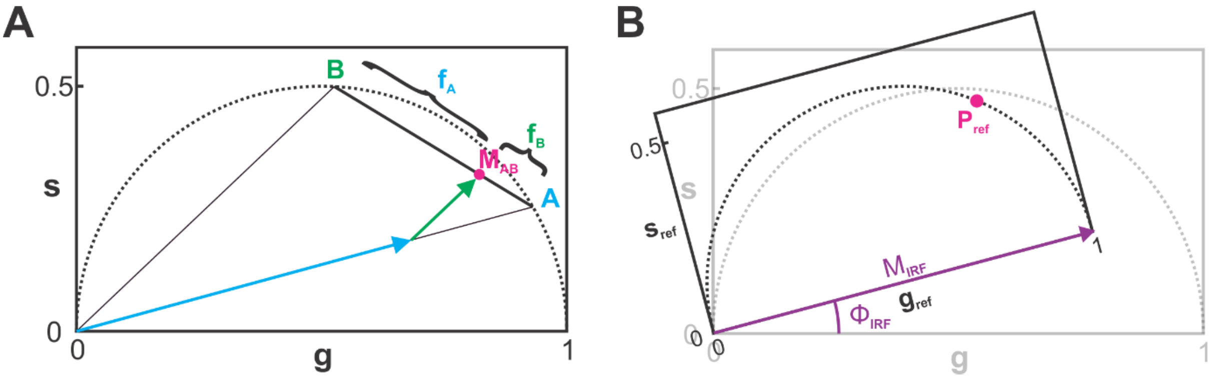

Figure 3.8. Behavior of fluorescence lifetime decays on the phasor plot. (A) The lifetimes of the species A and B with mono-exponential decays lie on the universal circle indicated by the dotted line. The lifetime of a mixture of A and B, $M_{AB}$, is the fractional sum of the phasors for A and B and therefore lie on the line connecting the phasors. (B) To account for the IRF, a new reference base ($s_{ref}$, $g_{ref}$) is chosen for the measured phasor $P_{ref}$ such that it is at the expected position in the new base.

Although the phasor approach is based on principles rooted in frequency-domain analysis, it can also be applied to time-domain data using pulsed excitation, as repeated excitation pulses at a specific frequency is also a form of (non-sinusoidal) modulation. The only difference is that the IRF needs to be corrected for. As the IRF is a convolution of the time-domain signal in time space, it essentially results in a change of base or axes in Fourier space. The measured phase shift and demodulation can be expressed as:

$$M_\omega = \Phi_{IRF} \cdot \Phi_{sample} \tag{37}$$

$$\Phi_\omega = \Phi_{IRF} + \Phi_{sample} \tag{38}$$

Therefore, accounting for the IRF becomes simple as long as the phase shift $\Phi_{IRF}$ and demodulation $M_{IRF}$ caused by the instrument is known:

$$s_{sample} = \frac{M_\omega}{M_{IRF}} \cdot \sin(\Phi_\omega - \Phi_{IRF}) = \frac{1}{M_{IRF}} \cdot \int_0^\infty I(t) \cdot \sin(\omega t - \Phi_{IRF}) dt \bigg/ \int_0^\infty I(t) dt \tag{39}$$

$$g_{sample} = \frac{M_\omega}{M_{IRF}} \cdot \cos(\Phi_\omega - \Phi_{IRF}) = \frac{1}{M_{IRF}} \cdot \int_0^\infty I(t) \cdot \cos(\omega t - \Phi_{IRF}) dt \bigg/ \int_0^\infty I(t) dt \tag{40}$$

For TCSPC data, which is not continuous but binned, the above equations need to be adjusted for the calculations at each pixel:

$$s_{sample} = \frac{1}{M_{IRF}} \cdot \sum_{n=1}^{N} \sin\left(\frac{2\pi n}{N} - \Phi_{IRF}\right) \tag{41}$$

$$g_{sample} = \frac{1}{M_{IRF}} \cdot \sum_{n=1}^{N} \cos\left(\frac{2\pi n}{N} - \Phi_{IRF}\right) \tag{42}$$

In practice, the base change induced by the IRF can be mapped by measuring a sample with known lifetime and choosing a new base such that the measured phasor is mapped onto its expected position in the new coordinate system (Figure 3.8B).

Compared to fitting the fluorescence decay with a model decay function, the phasor analysis has several advantages, particularly for live-cell imaging experiments. First, the phasor analysis does not require prior knowledge or assumptions regarding the decay characteristics (e.g. single or double exponential decay) of the sample. It is common for fluorescent proteins used in live-cell experiments to exhibit complex decay behavior. This may also change depending on the cellular microenvironment around the protein. In such situations, choosing the appropriate fit function without over-fitting the data can be difficult. Additionally, relatively few photons (~1000 or less) are collected per-pixel, making it difficult to even distinguish a single exponential decay from a double exponential decay by fitting. Second, fitting each pixel of an image is computationally taxing, as there are $10^5$~$10^6$ pixels in one frame and potentially hundreds or even thousands of frames. Comparatively, the requirements for computing a phasor plot is much lower per pixel as it is directly calculated from the data and does not require iterative regression fitting. Therefore, the phasor analysis is well-suited for large FLIM datasets.

## 3.4. Particle tracking methods

Advances in fluorescence microscopy has made it possible to observe a wide range of dynamic processes at the cellular and molecular level. The imaging of living organisms and cells generates a wealth of spatial and temporal information. The increase in the amount and complexity of image data has necessitated the development of automated object tracking methods as it is practically impossible to manually follow hundreds to thousands of cells or particles through hundreds to thousands of frames. These methods generally involve two steps: 1) the identification and separation of objects of interest from the background (the detection step) and 2) the association of detected objects in a series of image frames to form tracks (the linking step).

### 3.4.1. Particle detection

Particle tracking focuses on tracking objects that are much smaller than the resolution of optical microscopy (typically 200 nm or higher). These objects would appear as diffraction-limited spots (foci) in the images. When there is sufficient contrast between these foci and the background, they can be detected simply by intensity thresholding and their position can be localized to nanometer precision by computing the centroid position of the spot or by fitting it to a model of the point spread function. However, in live-cell imaging, the contrast is often poor and the background often non-uniform, necessitating the use of more sophisticated methods for accurate particle detection.

The particle detection framework can be divided into three general steps: 1) noise reduction, 2) signal enhancement, and 3) signal thresholding [83]. In practice some of the steps are optional or can be combined. In the first step, the input image is pre-processed by noise reduction techniques such as Gaussian smoothing to increase the signal-to-noise ratio (SNR) and improve image quality and object visibility. Subsequently, signal processing techniques are used to enhance the denoised fluorescence signal only in the regions where the actual particles are, as well as simultaneously suppress the signal from background structures. Lastly, the filtered and enhanced image is thresholded on signal magnitude to obtain a binary map of disjoint clusters of connected pixels, which corresponds to the detected objects and can be mapped to pixels in the original image for subsequent analysis. A second threshold may also be applied to the size and/or shape of the clusters to further filter the detected objects.

The particle tracking implementation in PAM uses wavelet decomposition for particle detection [84, 85]. In this method, the image is first denoised using an isotropic undecimated wavelet transform (IUWT). Specifically, the B3-spline version of an à trous algorithm is applied [84, 86]. The algorithm decomposes the original image into $K$ wavelet planes (also known as detail images) and a smoothed image, all with the same size as the original image. In the first step ($k$ = 1), the original image $I_0(i, j)$ is convolved row by row and then column by column with the kernel [1/16, 1/4, 3/8, 1/4, 1/16] to produce the smoothed image $I_1(i, j)$. The wavelet plane $W_1(i, j)$ (also termed detail image) is computed as $W_1(i,j) = I_0(i,j) - I_1(i,j)$. The same process is repeated recursively from the smoothed images at each scale k by inserting $2^{k-1}$-1 zeros between every two taps of the convolution kernel. For example, at $k$ = 2, the convolution kernel becomes [1/16, 0, 1/4, 0, 3/8, 0, 1/4, 0, 1/16]. We thus generate a set of $K$ wavelet planes, $W = W_1, \ldots, W_K$, and the final smoothed image $I_K$. The general decomposition formula can thus be written as:

$$W_k(i,j) = I_k(i,j) - I_{k-1}(i,j) \quad 0 < k \leq K \tag{43}$$

The reconstruction can be performed by summing the wavelet planes and the smoothed image:

$$I_0(i,j) = I_j(i,j) + \sum_{k=1}^{K} W_k(i,j) \tag{44}$$

The wavelet decomposition allows separation of the components of an image according to their size. The wavelet planes correspond to objects and structures at larger values of $k$ ($k \geq 3$, with larger values corresponding to larger structures) while at small values of $k$ they correspond to noise. A denoising step can be performed by applying a threshold $T_d$ to each wavelet plane and using the modified images $\widetilde{W}_k(i,j) = T_d(W_k)$ in the reconstruction.

In the original wavelet multiscale product algorithm [84], a signal enhancement step can be performed after image decomposition. Instead of summing the images, the detail images are multiplied to produce the multiscale product image:

$$P_K(i,j) = \prod_{k=1}^{K} W_k(i,j) \tag{45}$$

This exploits the fact that real objects are represented by wavelet coefficients that are correlated across multiple resolution levels (scales), whereas the wavelet coefficients of noise do not correlate. To improve detection performance, the algorithm also applies a threshold to each detail image before multiplication:

$$T_d\big(W_k(i,j)\big) = \begin{cases} 0, & W_k(i,j) < k_d\sigma_k \\ W_k(i,j), & W_k(i,j) \geq k_d\sigma_k \end{cases} \tag{46}$$

where $\sigma_k$ is the standard deviation of the wavelet coefficients in the detail image and $k_d$ is a multiplication factor set to 3 by default. A separate, user-defined threshold is then applied to the product image $P_K$ to produce a binary image, where connected pixels are considered to be detected objects.

The detection approach implemented in PAM is a modified version of the wavelet multiscale product algorithm. Instead of computing the product of the wavelet planes, the user selects one of the wavelet planes and the binary image is directly computed from this plane by applying a user-defined threshold [85]. The appropriate wavelet plane depends on the size of the tracked objects on the image. This detection approach is able to efficiently detect objects with a consistent size. The detected objects can be further filtered based on properties such as size or eccentricity.

### 3.4.2. Particle linking

After objects are detected in each frame, the particle tracking algorithm must establish the correspondence between particles in consecutive frames to generate complete tracks. The simplest approach to link particles to each other is the nearest-neighbor approach [87]. Every detected particle in a given frame is linked to the nearest particle in the next frame. Although 'nearest' usually refers to spatial distance, other parameters such as differences in intensity, size, shape and other features may also be included in the calculation of assignment cost. The source particle is assigned to the particle with the lowest assignment cost in the next frame, and the target particle is then removed from the pool of potential assignments for all subsequent assignments. Thresholds may be applied to reject assignments that are considered too far apart to be correct. The procedure is then repeated for every detected particle in every frame. While the nearest neighbor approach is sufficient at low particle densities and uncomplicated tracking conditions, it has difficulties dealing with high particle densities, particle disappearance (caused by detection failure or particles moving out of focus), as well as track merging and splitting (due to the separation distance between two or more particles being below the resolution limit of the instrument). These are conditions that commonly occur in biological imaging. Therefore, the nearest neighbor approach often produces unreliable results and require additional input or manual intervention [88, 89].

Many algorithms have been developed to deal with high particle density and the issues of particle merging or splitting. A global solution to the tracking problem can be achieved through the multiple-hypothesis tracking (MHT) approach [90, 91]. In MHT, all particle positions for every frame are considered at the same time, constructing all possible particle paths that conform to the expected particle behavior. The optimal solution is the largest non-conflicting set of paths, i.e. no paths share the image of the same particle in any frame. This solution is globally optimal in both space and time. However, it is computationally prohibitive even for problems involving tens of particles in tens of frames. Therefore, most tracking algorithms attempt to approximate the MHT solution by taking a greedy approach, that is, they take a series of locally optimal solutions to reduce computational complexity [92-96]. particles in consecutive frames are linked step-by-step before seeking a globally optimal solution to the linking of the resulting track fragments.

The algorithm used in this work, developed by Jaqaman, *et al* [97], employs the mathematical framework of the linear assignment problem (LAP). The approach was shown to provide robust tracking when applied to live-cell time-lapse images with high particle density while remaining computationally feasible. In this framework, a cost matrix $C$ is computed, where $c(i, j)$ is the cost of assigning the detected particle $i$ in a given frame to the particle $j$ in the subsequent frame:

$$C = \begin{bmatrix} c_{1,1} & \cdots & c_{1,q} \\ \vdots & \vdots & \vdots \\ c_{p,1} & \cdots & c_{p,q} \end{bmatrix} \tag{47}$$

The cost of linking may depend not just on spatial distance but also other parameters such as differences in intensity, size, shape and other features. The optimal solution to the assignment problem is one in which the total cost of the assignments is minimized and is computed with the Hungarian algorithm [98]. In this way, the particles in consecutive frames are first linked step-by-step in a locally optimal, but temporally greedy manner. Gap closing, track merging and track splitting are not considered in the first step. A second pass links the ends of the resulting track fragments by generating a similar cost matrix containing the costs of assigning the end of each fragment to the start of another. Here, gap closing, merging, splitting and track termination events all have associated costs and are in competition with one another. Therefore, while the first assignment pass is temporally greedy, the second pass linking track fragments takes a globally optimal approach, but remains computationally feasible as it only considers the start and end of each fragment.

# 4. Dynamics of Gag Processing during HIV-1 Maturation

The polyprotein Gag is the primary structural protein of the human immunodeficiency virus (HIV-1). Proteolytic processing of Gag by the HIV protease triggers structural rearrangements within the virus particle that mark the transition from immature virions to mature, infectious viruses. This project uses the sensitivity of the fluorescence lifetime of eCFP to the environment along with single virus tracing to observe Gag processing in HIV-1 virus-like particles (VLPs). We established the fluorescence lifetime of eCFP as a marker for Gag processing and were able to directly observe and measure the kinetics of Gag rearrangements in individual HIV-1 particles during maturation. The published paper is included in Appendix I.

**Dynamics of HIV-1 Gag Processing as Revealed by Fluorescence Lifetime Imaging Microscopy and Single Virus Tracking** by Chen Qian, Annica Flemming, Barbara Müller and Don C. Lamb. *Viruses* **14**(2), 340 (2022).

## 4.1. Motivation

Assembly, release and maturation are critical steps in the late phase of the HIV-1 replication cycle. The viral structural polyprotein Gag plays an important role throughout the entire process. The various domains of Gag are required for membrane targeting (matrix, MA), protein-protein interactions (capsid, CA), packaging of the viral RNA genome (nucleocapsid, NC), and recruitment of ESCRT machinery components that facilitate virion release (p6) [99-101]. Gag also recruits the GagProPol polyprotein, which is expressed by ribosomal frameshifting and comprises the viral protease (PR), reverse transcriptase (RT) and integrase (IN) into the nascent particle. During or shortly after virus release, PR mediates proteolytic cleavage of GagProPol and Gag, triggering the morphological rearrangements that yields the characteristic conical capsid core of the mature virus (Figure 4.1) [102].

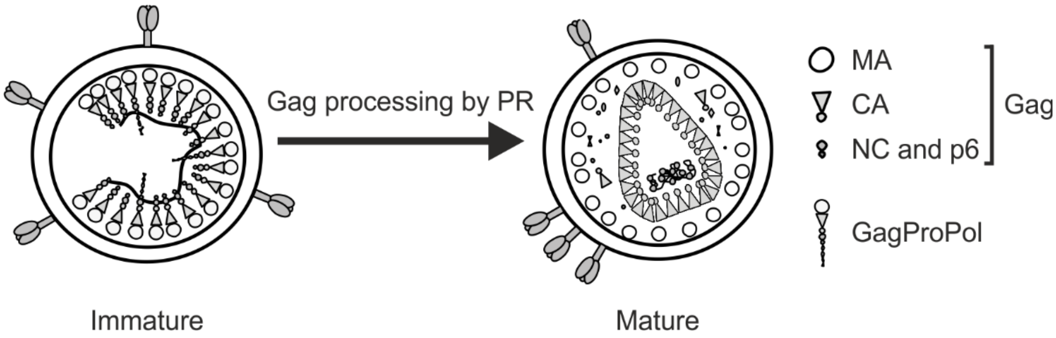

Figure 4.1 Schematic of immature and mature HIV-1. Proteolytic cleavage by PR triggers a rearrangement of Gag components leading to the formation of the conical capsid encapsulating the viral genetic material.

Productive maturation of HIV-1 relies on the coordination of Gag proteolysis and assembly and on the sequential cleavage of specific sites within Gag and GagProPol in an ordered processing cascade. The timing and kinetics of this process are not fully understood. Experiments involving *in vitro* processing of Gag or VLPs by purified PR identified the order of proteolytic events [103-105], but does not faithfully recapitulate processing by the endogenous viral PR *in situ*. Protease inhibitor (PI) wash out or the use of a photodestructible PI has been employed to synchronize Gag processing within the context of virus-like particles (VLPs) [106-108]. However, these approaches uncouple proteolytic maturation from assembly.

Here, I applied a combination of FLIM and single virus tracing (introduced in Chapters 3.3 and 3.4) to analyze the assembly and maturation of HIV-1. Using CLSM with TCSPC detection, I imaged eCFP-tagged HIV-1 VLPs both *in vitro* and in cells producing the VLPs. Individual virus particles were then tracked using a combination of approaches and the average lifetime of each tracked particle was extracted using the phasor approach. Proteolytic release of eCFP from the Gag lattice of the immature virion resulted in a change in its fluorescence lifetime, as the eCFP fluorescence lifetime is sensitive to the close proximity of other eCFP molecules [109-112]. This enabled the observation of asynchronous Gag processing in relation to the assembly process with high time resolution.

## 4.2. Key results

### 4.2.1. The fluorescent lifetime of eCFP as a marker for the maturation of HIV

We first established that the fluorescence lifetime of eCFP can be used as a marker for HIV-1 maturation. For this, I performed FLIM on HIV-1 derivatives ($HIV^{eCFP}$ [113] and $HIV^{ieCFP}$) carrying an eCFP moiety between the MA and CA domains. In $HIV^{eCFP}$, the fluorophore has a single PR cleavage site (amino acid sequence SQNY↓PIV) at its C-terminus, so it will remain attached to the envelope-bound MA domain post PR processing. $HIV^{ieCFP}$ carries an additional cleavage site at the N-terminus of the fluorophore, allowing for release of the free fluorophore after PR processing (Figure 4.2A). In both cases, proteolytic processing results in a change of the environment of the fluorophore from its packed arrangement within the immature shell. Since mature MA remains associated with the viral membrane and was recently observed to retain a modified lattice arrangement [114], the change in the local microenvironment of eCFP is expected to be less pronounced for $HIV^{eCFP}$ compared to $HIV^{ieCFP}$, where the released fluorophore would be able to distribute within the particle volume. eCFP-labelled VLPs were produced in the presence or absence of the PI lopinavir (LPV), the addition of which would block viral maturation by inhibiting PR activity. The VLPs were purified from the supernatant of transfected HEK293T cells and imaged at room temperature. Fluorescence lifetimes were extracted using the phasor approach [81] (see Chapter 3.3.2).

Two distinct populations were observed in the eCFP fluorescence lifetime distribution, corresponding to the mature and immature populations (Figure 4.2C-E). Immature particles showed comparable eCFP fluorescence lifetimes for both virus derivatives (2.21 ns for $HIV^{eCFP}$ and 2.18 ns for $HIV^{ieCFP}$). Mature $HIV^{ieCFP}$ particles in which the eCFP moiety should be completely released from Gag showed an average increase of 0.45 ns to 2.63 ns compared to immature particles. For the $HIV^{eCFP}$ variant, where the eCFP moiety remains associated with the MA layer, the difference between immature and mature particles was smaller (0.20 ns), with an average lifetime of 2.43 ns for mature particles (Figure 4.2F). The lifetime of eCFP in the HIV$^{ieCFP}$ particles is still lower than that of free eCFP (3.34 ns, Figure 4.2C), suggesting that the lifetime of eCFP is sensitive to the high density of protein within the mature virus (based on an average number of 2,400 Gag molecules per virion [115], the estimated concentration of eCFP is in the range of ~0.5 mM for an equimolar ratio of Gag and Gag.eCFP).

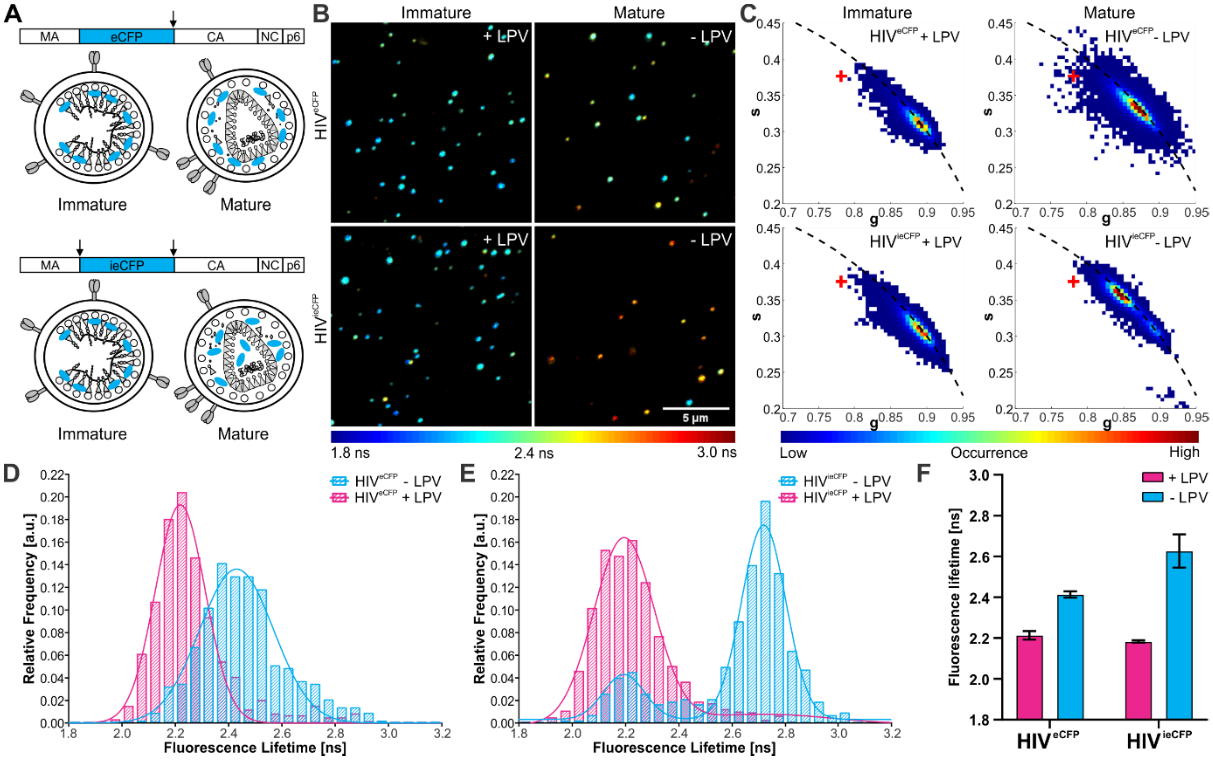

Figure 4.2. Fluorescence lifetime of eCFP in purified HIV-1 particles. (A) Scheme of the HIV-1 Gag polyprotein, with eCFP inserted between the MA and CA domains and flanked by one (Gag.eCFP, *top*) or two (Gag.ieCFP, *bottom*) PR cleavage sites. Arrows indicate PR cleavage sites flanking the eCFP domain. Schematic drawing of immature and mature HIV$^{eCFP}$ and HIV$^{ieCFP}$ particles. (B) Confocal images and (C) phasor plots of immature and mature HIVeCFP or HIVieCFP particles. A red '+' indicates the lifetime of free ECFP measured on the same setup. VLPs were produced in transfected HEK293T cells grown in the presence (immature) or absence (mature) of 2 µM LPV. Particles were adhered to borosilicate coverslips and imaged by CLSM using TCSPC detection. Measurements were conducted at 23°C. The lifetime determined for individual VLPs is represented according to the indicated color scale. Scale bar 5 µm. (D-E) Histograms of fluorescence lifetimes of the immature (*cyan*) and mature (*magenta*) particle populations extracted from the phasor analysis. Solid lines show the fitted Gaussian distribution function (sum of 2 Gaussians). The mean of each Gaussian component is shared between the corresponding pair of LPV-treated and untreated virus particles. n=500 particles each. (F) Mean and SD of the fluorescence lifetime distribution peak from three independent experiments.

To investigate why we have less contrast with Gag.eCFP, we measured the lifetime of eCFP alone and attached to MA in the cytosol of live cells at 37°C. Cytosolic MA-eCFP showed a lower lifetime (2.51 ± 0.04 ns) compared to cytosolic eCFP (2.70 ± 0.13 ns), suggesting that the presence of the MA domain influences the lifetime of eCFP. As the HIV$^{\text{ieCFP}}$ provided higher contrast in the lifetime changes between immature and mature virions, we proceeded to focus on this variant in subsequent live-cell experiments, where we followed Gag assembly and processing in individual HIV-1 particles. HeLa Kyoto cells were transfected with equimolar ratios of pCHIV/pCHIV$^{\text{ieCFP}}$ and imaged on the same CLSM setup at 37°C.

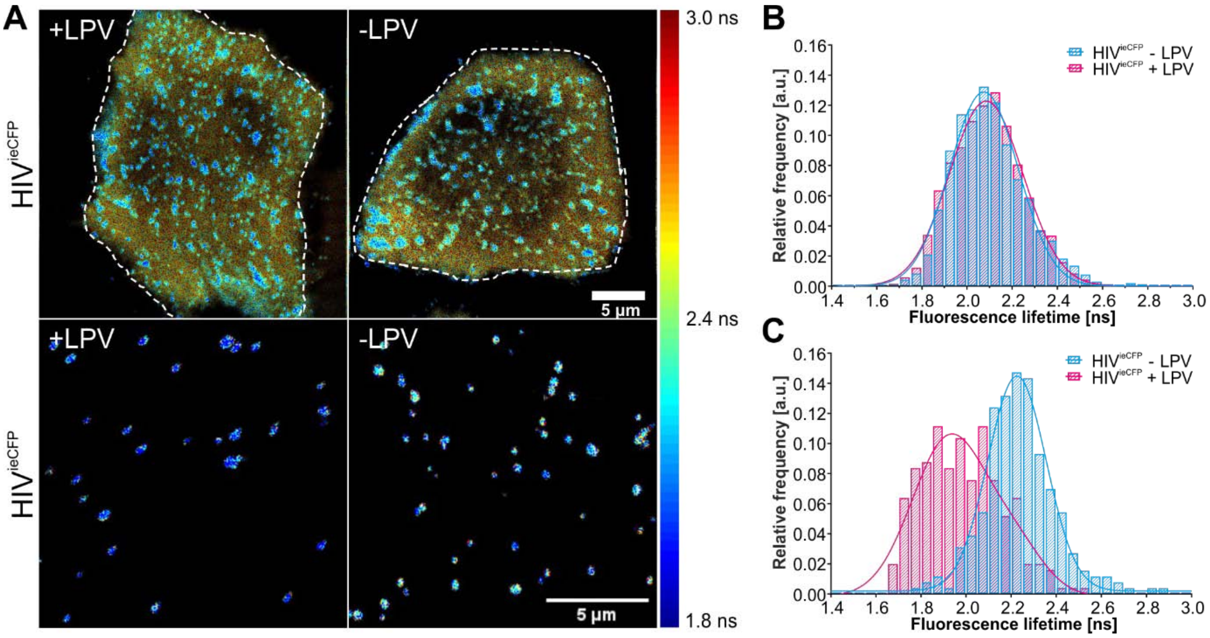

Figure 4.3. Measurements of the fluorescence lifetime of eCFP in HeLa Kyoto cells expressing HIVieCFP and grown in the presence or absence of 2 μm LPV. Cells were imaged 24 hpt at 37°C by CSLM. (A) Fluorescence lifetime images of assembly sites and trapped particles of HIVieCFP (*top panels*) and released HIVieCFP particles detected adjacent to transfected cells (*lower panels*). Measurements were performed in the absence or presence of LPV. Scale bar 5 μm. (B) Histogram of fluorescence lifetime of patches of trapped or cell-associated HIVieCFP particles and a fit to a single Gaussian distribution (solid lines). n=3196 particles from 7 cells treated with LPV and n=2999 particles from 9 non-treated cells. (C) Histogram of the fluorescence lifetime of cell-free HIVieCFP particles, fitted to a sum of two Gaussians (*solid lines*), where the mean of each Gaussian is shared between both fits. n=250 particles each from LPV-treated and non-treated cells.

We tracked individual VLPs and determined the fluorescence lifetime of the individual particles, as well as released VLPs adhered to the coverslip in the vicinity of these cells (Figure

4.3). The distribution of lifetimes of membrane localized assemblies in cells grown in the absence of LPV was not notably different from the LPV+ condition (Figure 4.3A, *top panels* and B). In contrast, cell-free particles observed in the vicinity of the particle producing cells did display the difference in average lifetime as expected for immature vs. mature VLPs (Figure 4.3A, *bottom panels* and C). This observation suggests that maturation occurs relatively late in the assembly process such that potential signals corresponding to maturing VLPs at the plasma membrane is obscured by the immature background of newly assembled immature VLPs. We therefore could not look at the population as a whole but rather have to analyze individual traces to look for assembly and maturation events.

### 4.2.2. Observation of Gag assembly and processing in individual HIV-1 particles

We then proceeded to analyze the intensity and lifetime changes of individual VLP traces as extracted by SPT from the FLIM images. Both incorporation of eCFP into the Gag lattice during assembly and its subsequent cleavage from the lattice during maturation resulted in measurable changes in the fluorescence lifetime of the fluorophore.

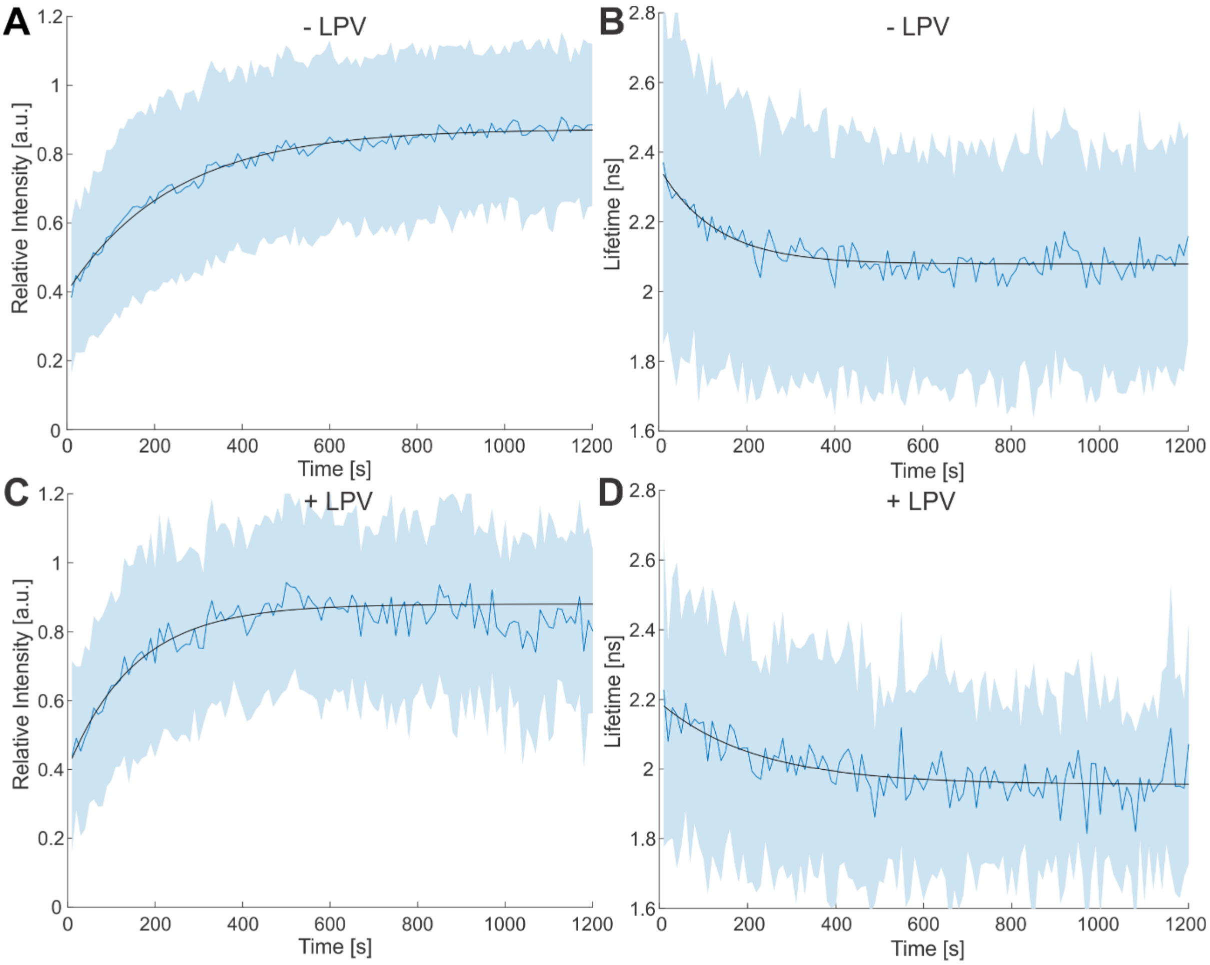

Figure 4.4. Gag assembly kinetics at the plasma membrane of HeLa Kyoto cells producing HIV$^{ieCFP}$ at 16 hpt. Plots of (A) fluorescence intensity and (B) fluorescence lifetime measured at individual assembly sites in cells grown in the absence of LPV. Mean values and SD are shown (n=170 sites from 4 cells). Plot of (C) fluorescence intensity and (D) fluorescence lifetime measured at individual assembly sites in cells grown in the presence of LPV. Mean values and SD are shown (n=51 sites from 2 cells). Black lines represent fits to single exponential equations.

From a set of 489 traces with a minimum length of 60 frames (corresponding to 10 min), 354 traces showed an increase in fluorescence intensity over time (Figure 4.4A), as expected for nascent assembly sites [22]. As the number of eCFP incorporated in a VLP increases, we anticipated a decrease in the fluorescence lifetime as observed for immature particles. Indeed, 170 out of the 354 traces displayed a decrease in fluorescence lifetime within the time window of observation (Figure 4.4B). To extract the rate of assembly, I aligned the traces to the onset of intensity increase and averaged the fluorescence intensities and lifetimes. The resulting averages could be fitted with a saturating exponential function. The same analysis procedure was applied to 105 traces from cells grown in the presence of LPV, of which 86 showed an intensity increase indicative of assembly (Figure 4.4C) and 51 showed an additional concomitant decrease in fluorescence lifetime (Figure 4.4D). The assembly kinetics measured here are consistent with previously reported values recorded using other microscopy techniques [22, 116, 117].

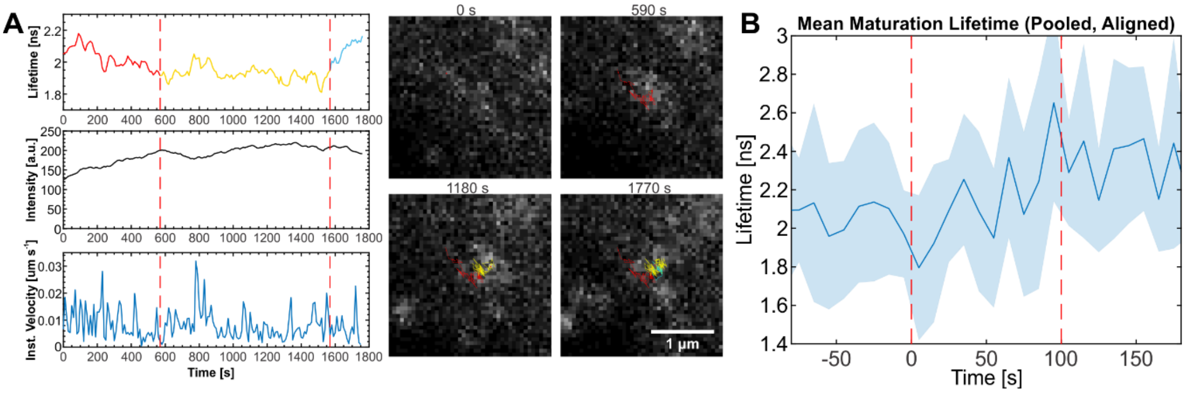

Figure 4.5. Particles showing eCFP lifetime changes indicative of maturation. (A) Lifetime, intensity, and velocity plots of an individual particle showing lifetime changes indicative of maturation following assembly. The lifetime plot is colored according to the state of the particle (red: assembly, yellow: plateau phase, blue: maturation). Images of the corresponding particle recorded at the indicated times are shown with an overlay of the particle trajectory up to that time point. (B) Mean and SD of fluorescence lifetime of maturing particles in pCHIV$^{ieCFP}$ transfected HeLa Kyoto cells. The lifetime of each particle was aligned at the start point of maturation (Time = 0 s) for each trace before averaging. Dotted lines indicate the apparent time range over which the lifetime change occurs. n=11 traces from 4 cells.

Among the 170 traces used for the analysis of assembly kinetics in cells grown in the absence of LPV, 11 traces (6.5%) showed an increase of ~0.4 ns after assembly was complete. This change was similar to the mean shift in lifetime observed between purified mature and immature HIV$^{ieCFP}$ particles. An exemplary trace is shown in Figure 4.5A. No such increase in fluorescence lifetime after assembly was observed for traces from cells grown in the presence of LPV (n=51). The same held true when we ignored assembly and looked at the full set of 105 LPV+ traces.

To estimate the timescale of Gag processing, the lifetime data for the 11 identified traces were aligned to the starting point of the lifetime increase and averaged (Figure 4.5B). On average, the lifetime increase indicative of Gag processing occurred over a period of ~100 s in an approximately sigmoidal fashion. The mean delay between the start of assembly and maturation as detected by FLIM was 837 (±542) s. However, it is likely that, for the majority of VLPs, Gag processing is further delayed with respect to viral assembly. The lifetime measurements on VLPs isolated from the tissue culture supernatant (Figure 4.2E) and recently released VLPs detected in the vicinity of particle producing cells (Figure 4.3C) indicated that the vast majority of VLPs produced eventually underwent Gag processing under the conditions of our experiments. Nevertheless, a distinct shift in lifetime indicative of processing was observed only for a minority of nascent assembly traces during the observation period in the live-cell measurements. Based on this, we can infer that, for most VLPs, Gag processing is delayed with respect to viral assembly and occurred beyond the period of observation in our SPT experiments.

## 4.3. Additional information: the particle tracking approach

Two particle tracking approaches were adopted in this study: a wavelet tracking approach developed in-house [85] (described in Chapter 3.4.1), and the Autoregressive Motion algorithm in the spot detection module of Imaris (Bitplane AG, Zurich, Switzerland). The wavelet tracking approach was initially applied to tracking virus particles *in vitro*. The Imaris algorithm was used to identify traces for the analysis of assembly and maturation kinetics, as it could apply a semi-automatic filter for traces that showed the appropriate intensity characteristics of nascent assembly sites. However, the overall Imaris tracking process was relatively time consuming and there was a possibility that the small number of control traces (LPV+) caused us to miss potential Gag processing events. We therefore applied the wavelet tracking approach to the live-cell data to generate additional traces to confirm the lack of maturation traces in LPV-treated cells.

The wavelet tracking algorithm performs an à trous wavelet decomposition on each image to denoise the fluorescence signal before detection of the VLPs by thresholding. The 3rd wavelet plane ($K = 3$) was used for particle detection as the spot size corresponded well to the size of the VLPs. The thresholded binary image was passed to the MATLAB function *regionprops* to extract information about the spot, including its intensity, eccentricity, and centroid. A filter was then applied to remove spots that do not fall under the specified intensity or eccentricity thresholds.

The centroid positions of the detected spots were used for the next step, particle linking. This was done over two stages. The first pass linked detected spots on each frame with those on the subsequent frame using the Hungarian algorithm [97, 98]. The second pass performed end-to-end joining for tracks generated by the first pass, where the end of each track was linked to the start of another track, provided the two ends were within the user-defined distance (< 5 pixels) and frame-skip (< 5 frames) thresholds. The tracks were then filtered so that only those of a sufficient length (≥ 30 frames) were selected for further analysis. The pixel positions of the generated tracks were used to extract the particle-wise phasor information using an intensity-weighted average.

## Outlook

In this project, we showed that the fluorescence lifetime of eCFP can be used in conjunction with SPT to detect Gag processing in an asynchronous virus population in a live-cell environment. Our approach can potentially be combined with other imaging and cell culture techniques. It is possible that FLIM in a microfluidic system can give a better picture of the overall kinetics of Gag processing post-release. Imaging particles at different distances from the cells in a microfluidic chamber where there is constant flow of the buffer in one direction would, in theory, provide a snapshot of their maturation status at the corresponding time-lags after release. Alternatively, a spheroid cell culture system could be used to trap the released particles and thus allow the tracking algorithm to follow them over a longer period of time. As fluorescence lifetime is sensitive to a wide range of physical properties, our approach of combining SPT with FLIM also has the potential for broader applications in studying other viral processes in addition to protease cascades.

# 5. Quantitative FRET measurements in live-cells

This project aims to adapt the analytical methods of single molecule FRET studies to live-cell imaging to facilitate the comparison of FRET efficiency values from datasets generated by different instruments in different laboratories. It defines the necessary correction factors for quantitative FRET imaging and establishes a single-step calibration method for obtaining these correction factors. To prove that the obtained FRET efficiencies are comparable between different setups, I performed quantitative live-cell imaging with widefield microscopy to provide independently acquired data for comparison against the data from the primary authors. The published paper is included in Appendix II.

**QuanTI-FRET: a framework for quantitative FRET measurements in living cells** by Alexis Coullomb, Cécile M. Bidan, Chen Qian, Fabian Wehnekamp, Christiane Oddou, Corinne Albigès-Rizo, Don. C. Lamb and Aurélie Dupont. *Sci Rep* **10**, 6504 (2020).

## 5.1. Motivation and Key Results

The development of FRET-based biosensors, along with advances in optics, has enabled the observation of biochemical activity in living cells with high spatial and temporal resolution. Two main approaches exist for measuring FRET in biological specimens. The first is based on measuring fluorescence intensity and the second is based on measuring the donor fluorescence lifetime. While fluorescence lifetime measurements are generally quantitative and relatively straightforward to calibrate, they require sophisticated instrumentation and analysis [118]. Among intensity-based methods for measuring FRET, the most widely applied strategy for quantitative FRET imaging in live-cells is sensitized acceptor emission, in which the fluorescence of the acceptor is measured after donor excitation and the FRET efficiency is calculated as the ratio of acceptor emission as a result of FRET to the sum of donor and acceptor emissions after donor excitation. However, the collected fluorescence intensity is heavily affected by instrumentation – the excitation wavelength and power, the filters used, the camera sensitivity, and so on can all affect the detected fluorescence intensity and therefore the calculated FRET efficiency. Numerous approaches have been developed to correct for them [119, 120]. In particular, the 3-cube strategy [119] was widely adopted to allow the correction for spectral crosstalk in the form of donor emission bleedthrough in the acceptor channel and direct excitation of the acceptor by the donor excitation light source. Despite this, the apparent FRET index varies with fluorophore concentration and direct comparison of independently obtained FRET values remains difficult even after normalization [121]. A number of other factors make FRET particularly challenging for fluorescent protein pairs, which are commonly used for live-cell FRET measurements. For example, some fluorescent proteins, such as mCherry, exhibit inefficient protein maturation leading to dark states [122, 123]. Fluorescent proteins also have inherently low FRET efficiency due to their relatively large size - the minimum center-to-center distance is ~5 nm for two fluorescent proteins, which is on par with the Förster radius of most fluorescent protein pairs used for FRET measurements. Fluorescent proteins also generally have much poorer brightness and photostability compared to organic dyes. Experimental determination of the correction factors pose further challenges as existing methods require known FRET efficiency [124], known concentration [125], or additional experiments using acceptor photobleaching [120].

In this work, the theory of single-molecule FRET studies [34] was adapted to live-cell imaging. The method, known as Quantitative Three-Image FRET (QuanTI-FRET), can determine all necessary correction factors after measuring at least 2 samples with known stoichiometry and varying FRET efficiencies. This can be achieved directly on the sample of interest or through the use of FRET standards. The stoichiometry additionally acts as an indicator for data quality, where pixels that deviate from the expected stoichiometry can be discarded. Two sets of independently acquired live-cell imaging data were analyzed using QuanTI-FRET and the results were compared to confirm the quantitative, instrument-independent nature of the method. I generated a second dataset (dataset [B]) for comparison against the primary dataset (dataset [A]) using independently acquired expression plasmids and separately cultured cell lines and imaging on a microscope with different instrumentation compared to the one used for dataset [A].

In the three-cube imaging approach, the sample sequentially illuminated at the donor and acceptor excitation wavelengths and the emission is split into two camera channels (Figure 5.1A). This results in the collection of four images:

$I_{DD}$: intensity in the donor channel after excitation at the donor wavelength.

$I_{DA}$: intensity in acceptor channel after excitation at the donor wavelength.

$I_{AA}$: intensity in acceptor channel after excitation at the acceptor wavelength.

$I_{AD}$: intensity in donor channel after excitation at the acceptor wavelength.

$I_{AD}$ is discarded as it generally contains no relevant information. $I_{DA}$ contains the FRET signal but it must be corrected for contributions from bleedthrough (or spectral crosstalk) and direct excitation:

$$I_{DA}^{corr} = I_{DA} - \alpha^{BT} I_{DD} - \delta^{DE} I_{AA} \tag{48}$$

The correction factors for bleedthrough $\alpha^{BT}$ and direct excitation $\delta^{DE}$ can be determined by measuring donor-only and acceptor-only cells.

The corrected FRET efficiency, $E$, and stoichiometry, $S$, can be written as:

$$E = \frac{I_{DA}^{corr}}{I_{DA}^{corr} + \gamma^{M} I_{DD}} \tag{49}$$

$$S = \frac{I_{DA}^{corr} + \gamma^M I_{DD}}{I_{DA}^{corr} + \gamma^M I_{DD} + I_{AA}/\beta^X} \tag{50}$$

where $\gamma^M$ is the correction factor for the differences in detection efficiencies and $\beta^X$ is correction factor for the excitation efficiencies.

To determine $\gamma^M$ and $\beta^X$, Equation (50) can be rewritten as

$$\beta^X \gamma^M I_{DD} + \beta^X I_{DA}^{corr} = \frac{S}{1 - S} I_{AA} \tag{51}$$

which is the equation of a plane in the 3D space with $I_{DD}$, $I_{DA}^{corr}$ and $I_{AA}$ as the principle axes. Therefore, one could obtain $\gamma^M$ and $\beta^X$ by fitting experimental data with known stoichiometry (Figure 5.1B). A sample with one FRET efficiency $E$ will form a straight line in the 3D space, so a minimum of two samples with sufficiently different FRET efficiencies are required to determine the correction factors. For this work, three FRET standards consisting of a pair of fluorescent proteins Cerulean (donor) and Venus (acceptor) separated by an amino acid linker sequence of varying length were used for calibration. The standard samples used were C5V, C17V and C32V [125, 126], which contained a linker of 5, 17 and 32 amino acids respectively, were used. FRET efficiency was expected to decrease as the linker length increases.

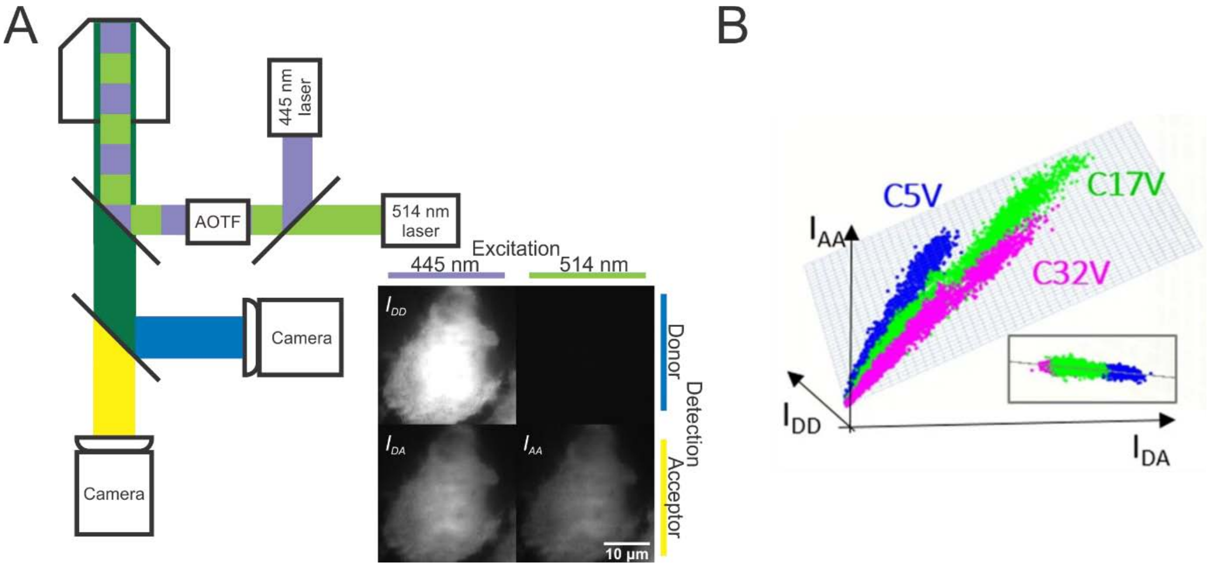

Figure 5.1. The QuanTI-FRET approach. (A) Schematic illustration of the widefield fluorescence microscopy setup used for image acquisition. A set of three images are acquired: donor emission after donor excitation ($I_{DD}$), acceptor emission after donor excitation ($I_{DA}$), acceptor emission after acceptor excitation ($I_{DD}$). The fourth channel, donor emission after acceptor excitation ($I_{AD}$) is discarded as it contains no relevant information. (B) A scatter plot of all pixel values from all cells imaged in dataset [A]. The three FRET standards form three distinct lines parallel to the plane defined by $\gamma^M$ and $\beta^X$ (grey) Inset: in-plane view of the same plot.

The FRET efficiencies obtained from the two independently acquired datasets, one from the primary authors of the paper (dataset [A]) and the other from the author of this thesis (dataset [B]), were in good agreement (Table 5.1). The crosstalk correction factors are close and reflect the same fluorophore pair and similar filter sets used. The difference between $\beta^X$ and $\gamma^M$ are larger, which are expected given the different illumination intensities and detection efficiencies of the two different setups.

Table 5.1. Comparison of correction factors and FRET efficiencies (in percentages) obtained by QuanTI-FRET method in two independently acquired datasets. For dataset [A], n = 10 cells for $\alpha^{BT}$, 12 cells for $\delta^{DE}$, 26 cells for C5V, 25 cells for C17V, 27 cells for C32V. For dataset [B], n = 12 cells for $\alpha^{BT}$, 12 cells for $\delta^{DE}$, 10 cells for C5V, 12 cells for C17V and 12 cells for C32V.

| | $\alpha^{BT}$ | $\delta^{DE}$ | $\beta^X$ | $\gamma^M$ | C5V | C17V | C32V |
|---|---|---|---|---|---|---|---|
| Dataset [A] | 0.421 ± 0.002 | 0.1100 ± 0.0008 | 1.167 ± 0.008 | 2.10 ± 0.02 | 50.3 ± 0.4 | 41.7 ± 0.8 | 35.1 ± 0.8 |
| Dataset [B] | 0.467 ± 0.001 | 0.101 ± 0.003 | 2.03 ± 0.07 | 1.35 ± 0.07 | 50.2 ± 1.7 | 43.0 ± 1.6 | 32.9 ± 1.5 |

The definitions of FRET efficiency and stoichiometry used here are mathematically equivalent to those previously introduced by Chen *et al.* [127] ($\gamma^M \equiv G$ and $\beta^X \equiv 1/(G \cdot k)$) and Lee *et al.* [34] ($\gamma^M \equiv \gamma$ and $\beta^X \equiv \beta$). Therefore, the robustness of QuanTI-FRET was compared to these two methods. In Chen *et al.*, $\gamma^M$ (or $G$) was determined from two constructs with defined and well-separated FRET efficiencies. The second parameter $k$ was calculated from a FRET standard with known stoichiometry in combination with G determined in the first step. For Lee et al., the raw FRET efficiency $E_{raw}$ and stoichiometry $S_{raw}$ are calculated with only spectral crosstalk corrections. The linear relationship between 1/ $S_{raw}$ and $E_{raw}$ was fitted to obtain $\gamma$ and $\beta$. When analyzing dataset [A], both methods yielded similar results to QuanTI-FRET. Chen *et al.* produced similar correction factors and FRET efficiencies to QuanTI-FRET. Lee *et al.*, on the other hand, produced similar correction factors but the resulting FRET efficiencies were systematically lower than those produced by QuanTI-FRET by 3%. However, analysis of dataset [B] saw Chen et al. producing different correction factors from QuanTI-FRET: $G = 3.63 \pm 1$ compared to $\gamma^M = 1.35 \pm 0.07$ and $1/(G \cdot k) = 1.02 \pm 7$ compared to $\beta^X = 2.03 \pm 0.07$. This yielded FRET probabilities that deviated from the expected values by 30%, 24% and 16% for C5V, C17V, and C32V respectively. The two-step calibration approach of Chen *et al.* appeared to be less robust when dealing with the smaller and less homogenous dataset [B], which had less cell-containing pixels for the calibration. Analysis of dataset [B] with the Lee *et al.* method also yielded FRET values that are lower by 8% compared to those obtained from QuanTI-FRET. Overall, it appears that the three methods can produce quantitative FRET efficiencies that are in good agreement with each other when dealing with ideal, homogenous data but only QuanTI-FRET produced consistent results when presented with a smaller and less homogenous dataset.

## 5.2. Outlook

QuanTI-FRET establishes a new framework for quantitative FRET imaging in live-cells that produces consistent results across two independently collected datasets in different microscopy systems. Although the microscopes used to produce the datasets seen here are relatively sophisticated, the imaging requirements can in principle be fulfilled on a simple multi-channel epifluorescence microscope. The calibration requirements are relatively simple, requiring measurements of donor-only, acceptor-only, and a minimum of two FRET samples with known stoichiometry and well-separated FRET efficiencies. The approach of obtaining correction factors by fitting a plane through the plotted pixel intensities is also straightforward and remains consistent even when dealing with inhomogeneous and limited calibration data. Overall, the method promises a widely applicable, robust and quantitative approach to performing live-cell FRET analysis.

# 6. Detection of CXCR4 and US28 heteromerization with Image Cross-Correlation Spectroscopy

Oligomerization of G-protein coupled receptors (GPCRs) have been reported to regulate ligand binding, signaling and receptor trafficking. The human cytomegalovirus (HCMV) encode viral GPCRs that interfere with cell signaling to facilitate the spread of the virus. Here, I determined the oligomerization between the human cytokine receptor CXCR4 and the HCMV-encoded GPCR US28 with image cross-correlation spectroscopy (ICCS).

## 6.1. Motivation and Introduction

GPCRs are the largest group of membrane receptors in eukaryotic cells and are involved in a diverse range of cellular functions. Structurally, they consist of 7 transmembrane α-helices (Figure 6.1). As the name implies, GPCRs interact with G proteins in the plasma membrane. Ligand binding to the receptor triggers a conformational change which subsequently activates the associated G protein. The activated G protein can then activate further downstream signaling pathways.

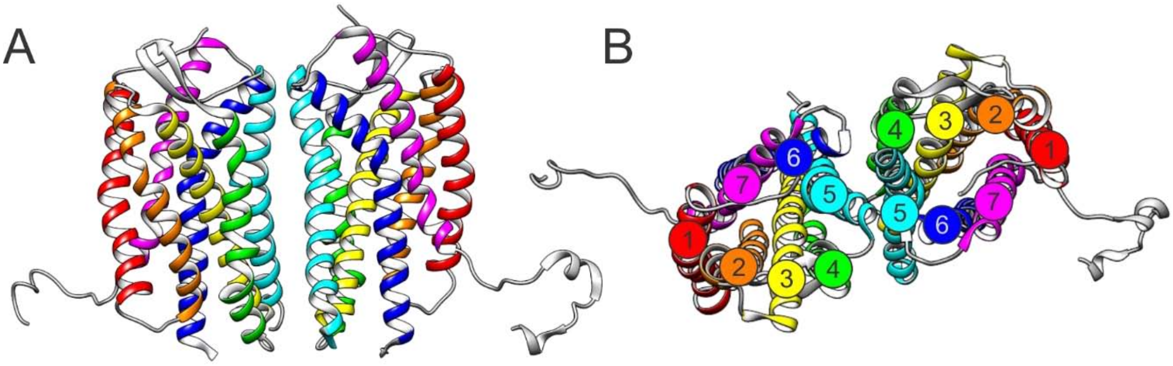

Figure 6.1. X-ray crystal structure of the human chemokine receptor CXCR4, a member of the GPCR family (PDB ID: 3ODU) [128]. The protein exists as a homodimer. (A) Side view showing the transmembrane helixes 1 to 7 colored red, orange, yellow, green, cyan, blue and magenta in that order. (B) Top view with labels indicating the position of each helix. Helices 4 and 5 form the dimerization interface.

Certain herpesviruses, such as HCMV, Epstein-Barr virus (EBV) and Kaposi's sarcoma associated herpesvirus (KSHV) express viral GPCRs [129, 130]. These GPCRs resemble human GPCRs in structure and function and are likely to have been derived from homologues within the human genome. Having acquired certain unique properties, such as constitutive activity and the ability to bind a wide range of human chemokines, these viral GPCRs are able to interfere with host cell signaling for the benefit of the virus, aiding in immune evasion and viral dissemination [131]. HCMV-encodes four GPCRs US28, US27, UL33 and UL78, of which US28 is the best characterized. US28 is constitutively active and binds a wide range of chemokines [132]. By doing so, it competes with human chemokine receptors for chemokine binding and potentially reduces immune responses at the site of inflammation [133]. The constitutive activity of US28 may also modulate intracellular signaling to aid in virus replication. One of its downstream effects is the activation of the HCMV immediate-early promoter/enhancer [134]. Additionally, US28 can act as a HIV coreceptor in certain cell types [135-138].

The human chemokine receptor CXCR4 is a promising target for manipulation by HCMV-encoded GPCRs as it is expressed on the target cells of HCMV infection [139]. CXCR4 activation is associated with cell migration and proliferation of non-hematopoietic cells [140]. It is also the principal HIV-1 entry coreceptor [141-144]. CXCR4 has been shown to form homodimers (Figure 6.1) [128, 145, 146] as well as various heterodimers [147, 148]. A study of US28 and CXCR4 by Frank *et al.* [149] showed that US28 attenuated CXCR4 receptor function and surface expression, but failed to conclusively show heteromerization between the two GPCRs using bioluminescence complementation (BiLC) and bioluminescence energy transfer (BRET) assays. These assays involved the use of *Renilla* luciferase to detect protein-protein interactions. In BiLC, the proteins-of-interest are tagged with split fragments of luciferase. Upon interaction of the tagged proteins, the luciferase fragments combine to form a functional luciferase, whose chemiluminescence can be measured [150, 151]. BRET involves a process similar to FRET, except the donor molecule is luciferase, a chemiluminescent molecule, rather than fluorophore. The acceptor is a fluorescent protein (YFP or GFP) [152]. Emission in the acceptor channel upon luciferase activation indicates binding between the two labeled species. For Frank *et al.*, BiLC suggested a weak interaction between US28 and CXCR4, but BRET did not detect an interaction [149]. However, it remains unclear if these assays are sensitive enough to detect an interaction between US28 and CXCR4, especially when it is in competition with the homodimerization of CXCR4.

Here, I measured the interaction between CXCR4 and US28 using ICCS. I optimized the exposure scheme for ICCS on a home-built TIRF microscope. Using this exposure scheme, I imaged the ventral plasma membrane of HEK293T cells expressing various combinations of GFP- or mCherry tagged CXCR4 and US28. ICCS analysis confirmed the homo-dimerization of CXCR4 as well as the heteromerization of US28 and CXCR4.

## 6.2. Key results

### 6.2.1. Optimization of exposure scheme for ICCS

In ICCS, images from two fluorescence channels are spatially cross-correlated. Interaction between two differently labeled species results in a non-vanishing cross-correlation amplitude. To avoid cross-correlation of the signals due to spectral crosstalk, the laser excitations must be alternated to obtain crosstalk-free images in both channels. This is achieved through ALEX on the millisecond timescale and a typical excitation/exposure scheme is shown in Figure 6.2A (*top panel*). However, ALEX was initially created for single-molecule FRET studies [33-35] and consequently both cameras are triggered together each time either one of the lasers are activated. This introduces a delay between the green and red exposures due to the time it takes for i) the exposure in a channel to complete and ii) the camera to readout the image recorded on its sensor. This delay decreases the spatial cross-correlation amplitude as the labeled species would move during this period. This was undesirable, especially since there were already other factors at play which would limit the potential cross-correlation amplitude, such as the potentially weak interaction between US28 and CXCR4, competition from CXCR4 homodimerization, as well as incomplete maturation of mCherry leading to a fraction of the labeled species existing in a dark state [123]. Therefore, to improve the sensitivity of ICCS, the time delay between the exposures in each color channel must be minimized.

To avoid crosstalk, the exposure in each channel to be completed before the exposure in the other channel can begin, so the green-red delay due to the exposure time of each frame is unavoidable. However, the delay introduced by the camera readout can be reduced. The Andor EMCCD cameras used in this project (see Section 6.4.3) feature a frame-transfer mode [153] in which, instead of directly reading out the charge from the sensor area, the accumulated charge on the sensor is rapidly shifted to a masked storage region that is then read out by the camera. This masked region therefore acts as a buffer, allowing the sensor to be cleared of accumulated charges and readied for the next exposure in a few milliseconds instead of having to wait for the readout to complete, which takes ~30 ms for a full-sized 512-by-512 pixel image. However, in this mode the minimum exposure time or repetition rate is still limited to the readout rate, as the camera must wait for the readout of the buffer region (the previous frame) to complete before transferring charges from the sensor region (the current frame).

We therefore created a modified ALEX scheme specifically optimized for ICCS. Unlike typical ALEX, the green and red cameras are not simultaneously exposed when either laser is triggered. Rather, the exposure of each camera was synchronized to its respective laser, so that the red laser and camera was triggered immediately after the green camera exposure was complete (Figure 6.2A). An additional delay was introduced between frames to allow for camera readout to be completed. This scheme allowed an arbitrarily low delay (as low as the green exposure time) between the green and red exposures to be achieved. Unlike ALEX with frame-transfer mode, arbitrarily low exposure times can be used regardless of the image size. The reduction in green-red delay improves the normalized cross-correlation amplitude (Figure 6.2B).

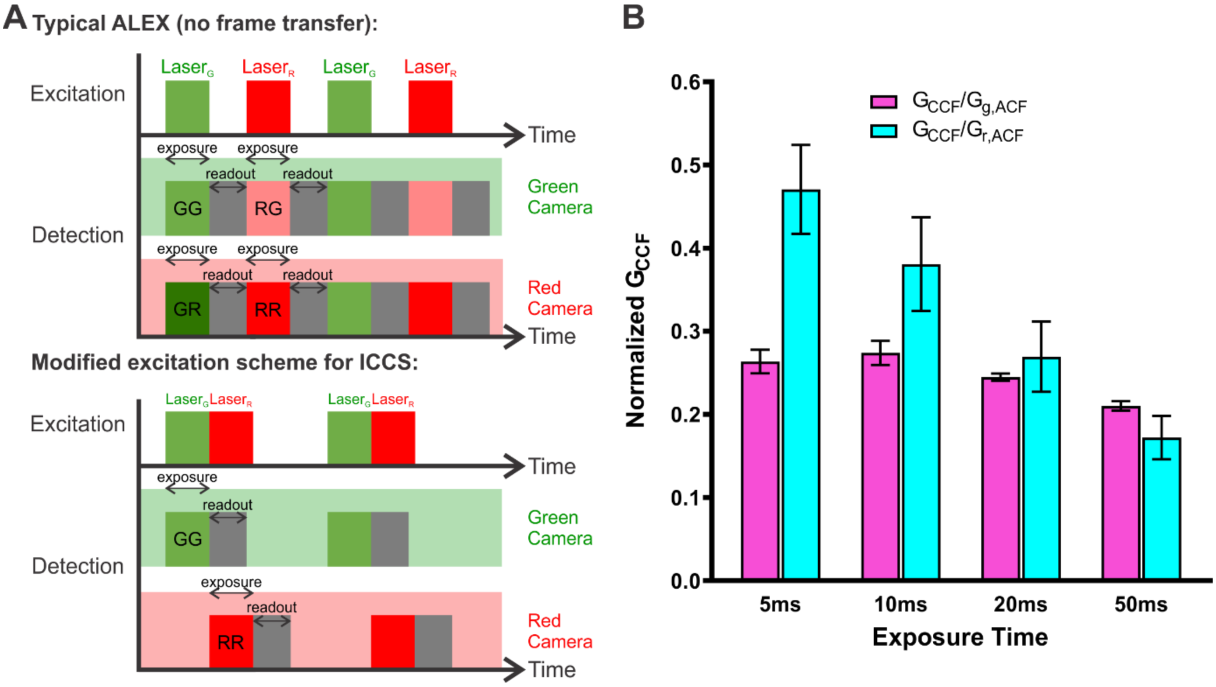

Figure 6.2. Optimization of the excitation scheme for ICCS. (A) Excitation and exposure schemes for typical ALEX (*top*) and the modified exposure scheme (*bottom*). For ALEX, the minimum delay between green and red exposures is the sum of the exposure time and readout time. In the modified scheme, red exposure begins immediately after green exposure is finished, without waiting for the readout of the green camera to finish. (B) Mean and SEM of the normalized spatial cross-correlation amplitude of HEK293T cells transfected with palm-GFP-mCherry at different exposure times using the modified excitation scheme. The spatial cross-correlation amplitude ($G_{CCF}$) was normalized against the spatial auto-correlation amplitudes in green ($G_{g,ACF}$) or red ($G_{r,ACF}$). n = 4 cells.

### 6.2.2. Detection of CXCR4 homo- and heteromerization using ICCS

To detect CXCR4 homo- and heteromerization, I performed ICCS on TIRF images of HEK293T cells co-expressing various combinations of CXCR4-GFP, CXCR4-mCherry US28-GFP and US28 mCherry fusion proteins. The cells were imaged at 37°C in Fluorobrite DMEM (Invitrogen). The cells co-transfected with CD86-GFP and CD86-mCherry were used as the negative control, as the protein is known to exist as a monomer [154, 155]. Cells transfected with palm-GFP-mCherry were used as the positive control. An example of each type of transfected cell is shown in Figure 6.3A. The fraction of the red and green fluorescent species involved in cross-correlation was calculated by normalizing the SCCF amplitude ($G_{CCF}$) against the SACF amplitude in green ($G_{g,ACF}$, Figure 6.3B) and red ($G_{r,ACF}$, Figure 6.3C) respectively (see equation (20), Chapter 3.1.2). Note that this was only done to account for variations in the expression levels of the GFP- and mCherry-tagged species across different cells and repeats. Quantification of the actual fraction of bound species would require knowing the relative fractions of the fluorescent and dark states of the fluorescent proteins [64], particularly that of mCherry, which is known to exhibit a dark state due inefficient maturation [123]. Determination of the fraction of the dark state was not feasible with our experimental setup, but the normalizations nevertheless facilitate comparisons across the different combinations of proteins.

A positive SCCF amplitude could be detected on cells co-transfected with CXCR4-GFP/CXCR4-mCherry, which confirmed its existence as a homodimer (Figure 6.3B and C). The negative control CD86-GFP/CD86-mCherry showed no detectable cross-correlation, suggesting that the image post-processing prior to ICS analysis (see Chapter 6.4.4) were effective. The positive control palm-GFP-mCherry showed a much higher amplitude. This is not surprising, as the control consisted of a covalently linked GFP-mCherry pair, while the CXCR4-GFP/CXCR4-mCherry homodimerization would inevitably be in competition against same-color homodimers (CXCR4-GFP/CXCR4-GFP and CXCR4-mCherry/CXCR4-mCherry). The calculation fraction of interacting species is much lower than 1 in all cases, including the positive control, which is expected due to incomplete maturation of mCherry and the green-red camera delay as discussed in the previous section.

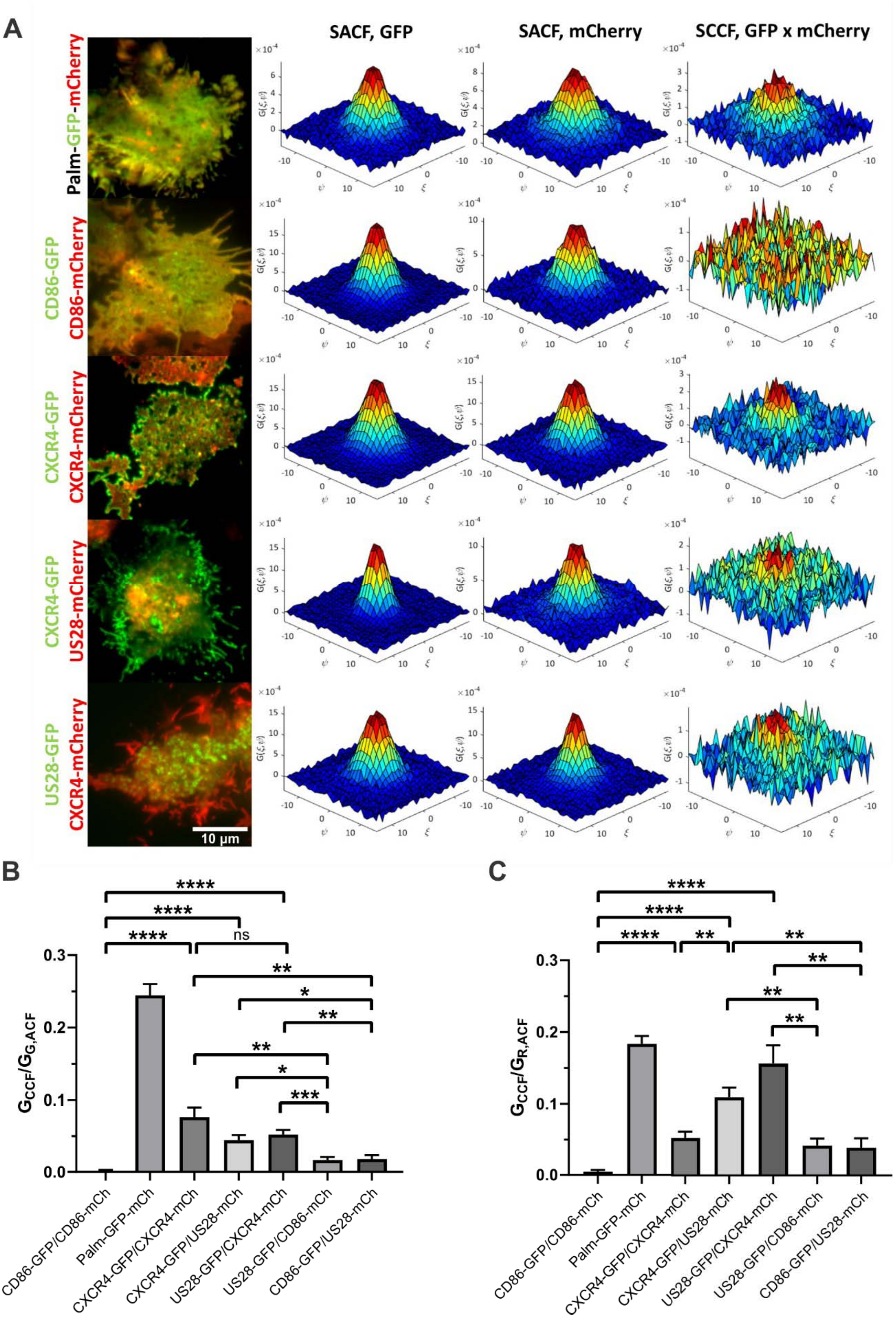

Figure 6.3. CXCR4 homo- and heteromerization detected by ICCS. (A) Examples of HEK293T cells transfected with (*from top to bottom*) palm-GFP-mCherry, CD86-GFP/CD86-mCherry, CXCR4-GFP/CXCR4-mCherry, CXCR4-GFP/US28-mCherry and US28-GFP/CXCR4-mCherry. For each example, (*from left to right*) the composite color image of the cell, the SACF in green (GFP), the SACF

in red (mCherry), and the SCCF are shown. (B) and (C) Plots of the mean and SEM of the spatial cross-correlation amplitude ($G_{CCF}$) normalized against the spatial auto-correlation amplitudes in (B) green ($G_{g,ACF}$) or (C) red ($G_{r,ACF}$). n = 16 for CD86-GFP/CD86-mCherry, 25 for palm-GFP-mCherry, 24 for CXCR4-GFP/CXCR4-mCherry, 25 for CXCR4-GFP/US28-mCherry, 21 for US28-GFP/CXCR4-mCherry, 8 for CD86-GFP/US28-mCherry and 8 for US28-GFP/CD86-mCherry. Dunnett's comparison test were performed between each protein pair involving at least one CXCR4 and the negative controls involving at least one CD86 (ns: $p > 0.05$; *: $p < 0.05$; **: $p < 0.01$; ***: $p < 0.001$; ****: $p < 0.0001$).

Cells co-transfected with US28-GFP/CXCR4-mCherry and CXCR4-GFP/US28-mCherry also showed an average normalized SCCF amplitude that was significantly higher than the negative control CD86-GFP/CD86-mCherry ($p < 0.0001$) as well as the additional controls pairing US28 with CD86 (p values range from $p < 0.001$ to $p < 0.05$ depending on the datasets compared). This suggests that US28 shows preferential binding to CXCR4 compared to the control partner CD86. The fraction of bound CXCR4 was comparable between US28-GFP/CXCR4-mCherry and CXCR4-GFP/CXCR4-mCherry homodimerization pair ($p > 0.05$, Figure 6.3B). For the reciprocal case of CXCR4-GFP/US28-mCherry, the average fraction of bound CXCR4 exceeded that of the CXCR4-GFP/CXCR4-mCherry ($p < 0.01$, Figure 6.3C). These results suggest that US28 is acting in competition against CXCR4 homodimerization, and has equivalent or higher binding affinity to CXCR4 than the homodimerization reaction.

## 6.3. Outlook

In this study, ICCS was used to perform interaction studies for viral and human GPCRs in the membrane of living cells. Despite the inherent inhomogeneity in the image data of membrane proteins, the image correction methods adapted from ARICS proved effective in removing correlation artefacts while preserving real interactions, as seen in the consistency of the results for the negative and positive controls. We were also able to detect CXCR4 homodimerization, which is consistent with the established literature for this protein [128, 145, 146]. In addition, our results also show that the viral GPCR US28 binds to CXCR4 in competition against the homodimerization reaction of the human GPCR. These results contradict the previous conclusions by Frank *et al.* that US28 does not directly bind to CXCR4 based on BRET assays

[145]. However, as the remainder of our results are consistent with the available literature, we argue that our data, obtained by direct imaging of individual living cells, are more likely to reflect the actual behavior of US28 than the bulk measurements by Frank *et al*. Our results are also more consistent with the track record of US28 in its prolific binding with other human chemokines [132]. ICCS here proves itself to be a capable technique for detecting protein interactions *in situ*. The image acquisition and processing techniques developed here are also widely applicable to other interaction studies, particularly those involving membrane proteins.

## 6.4. Methods

### 6.4.1. Plasmids

The palm-GFP-mCherry plasmid was created by subcloning the palmitoylation sequence of p63RhoGEF (coding sequence for amino acids 1-29) [156] into the AgeI site of the peGFP-mCherry plasmid, which was previously reported [31] and based on peGFP-C1 (Clontech, France). The CXCR4-GFP, CXCR4-mCherry, CD86-GFP, CD86-mCherry, US28-GFP and US28-mCherry fusion protein expression plasmids were based on the pcDNA5 backbone and provided by Nuska Tschammer.

### 6.4.2. Cell culture and transfection

HEK 293T cells were cultured in Dulbecco's modified Eagle's medium (DMEM GlutaMAX; Gibco) supplemented with 10 % fetal bovine serum (FCS; Thermo Fisher Scientific). Cells were seeded on Labtek II slides (Thermo Fisher Scientific) coated with poly-L-lysine at a density of $3 \times 10^4$ cells per well in 400 µl culture media 24 h prior to transfection. Xtreme-Gene 9 transfection reagent (Roche) was used for transfection according to the manufacturer's protocol. 20 ng of plasmid DNA was transfected for palm-GFP-mCherry and 100 ng for the CXCR4 constructs. For co-transfections a total of 200 ng of plasmid DNA was used per well at a 1:1 ratio. At 20-24 hpt, the culture media was replaced with FluoroBrite DMEM and the slides were transferred to the microscope for imaging.

### 6.4.3. Fluorescence imaging for ICCS

Images were acquired on a Nikon Eclipse Ti microscope with home-built excitation and detection pathways. A 100x oil immersion objective (Apo-TIRF 100x Oil/NA 1.49, Nikon) was used for all measurements. Samples were excited with 488 nm (MLD, Cobolt) and 561 nm (Jive, Cobolt) diode lasers coupled to an AOTF (PCAOM LFVIS5, Gooch & Housego) controlled by a FPGA unit (cRIO-9074, National Instruments). The fluorescence emission was separated from excitation pathway with a triple line 488/561/642 beamsplitter. The donor and acceptor emission were separated using an additional 561 longpass beamsplitter and were then spectrally filtered using 525/50 and 630/69 bandpass filters respectively before being detected on separate EMCCD cameras (DU-897, Andor). The camera exposure was synchronized to laser excitation through the FPGA unit and a self-written Labview program. The samples were excited for 20 ms at 488 nm followed immediately by 20 ms at 594 nm. An additional 40 ms delay was introduced between frames to allow camera readout to be completed. 300 frames were acquired in each color for each cell.

### 6.4.4. Image post-processing for ICCS

Cell membranes contain inherent inhomogeneity, which create artefacts on correlation functions. To minimize artefacts introduced by cellular inhomogeneity in the image, I adapted the ARICS approach (Chapter 3.2.3) to ICS. A 20-frame moving average correction was applied to remove relatively static structures in the image. In addition, a per-frame intensity threshold was applied to exclude the background as well as particularly bright or dark spots in the image of the cell. The frame range of 20 used for the moving average was larger than that of ARICS (typically 3) as the frame rate in these experiments (60 ms per frame) are much faster than that of typical CLSM frame rates (around 1 s per frame). In theory, what remains are the dynamic, fast fluctuations in the fluorescence signal as a result of diffusion or other dynamic processes (Figure 6.4). The post-processing and correlation spectroscopy was performed using the Microtime Image Analysis (MIA) module of the software package PIE analysis with MATLAB (PAM) [157].

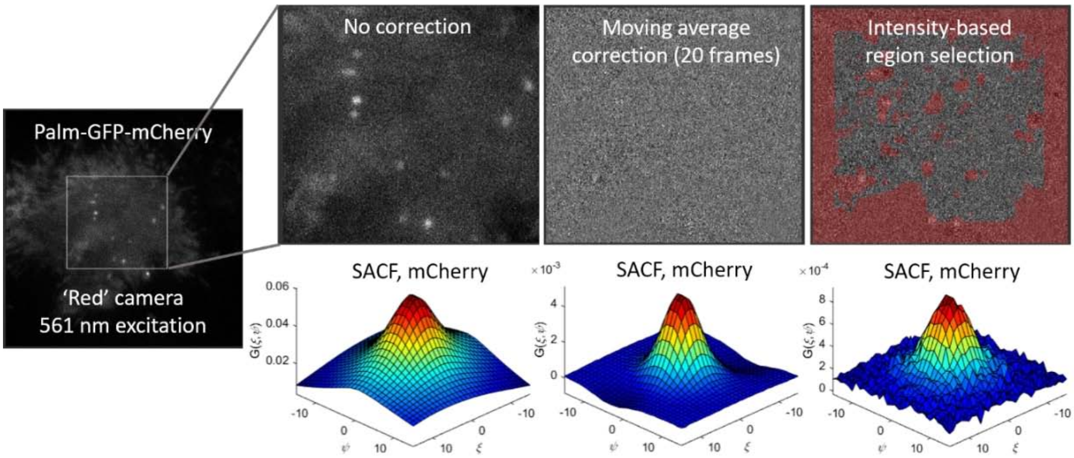

Figure 6.4. Effect of corrections on the SACF of the mCherry channel in a cell transfected with palm-GFP-mCherry.

# 7. Measuring histone diffusion in live mouse embryos using RICS

This project studies the phase separation of mouse heterochromatin in the early stages of mammalian embryogenesis. Together with Manuel Guthmann and Irene Gialdini, I performed live-cell imaging on fertilized mouse embryos at the 2-cell stage. Using ARICS analysis, we extracted the diffusion coefficient and concentration of histone H3.1 inside and outside pericentromeric heterochromatin, which was identified by tagging and imaging in a second color channel simultaneously. A copy of the submitted manuscript is included in Appendix III.

**A phase transition accompanies heterochromatin formation in mouse embryos** by Manuel Guthmann, Chen Qian, Irene Gialdini, Tsunetoshi Nakatani, Andreas Ettinger, Igor Kukhtevich, Robert Schneider, Don C. Lamb, Adam Burton & Maria-Elena Torres-Padilla. Manuscript submitted for publication. (2021)

## 7.1. Motivation and Key Results

The majority of eukaryotic genomes exist in the form of heterochromatin, a highly compacted structure that suppresses the expression and mutational potential of the genetic sequences within. In mammals, heterochromatin formation at pericentromeric regions of the chromosomes is accompanied by a spatial reorganization into domains containing multiple chromosomes, known as chromocenters. The major satellite repeats that constitute the pericentromeric heterochromatin in mice undergo a dramatic remodelling in their shape and nuclear positioning during the 2-cell stage, changing from a ring-like configuration around the nucleoli precursors into spherical chromocenters [158-160]. This organization persists subsequently throughout development and differentiation.

While several molecular pathways are known to contribute to heterochromatin formation, the potential contributions of its biophysical properties to this process is unknown. In *Drosophila* embryos, heterochromatin displays condensation behavior via liquid-liquid phase separation (LLPS) [161]. Whether mammalian heterochromatin displays similar properties has been debated [162-165]. In mouse embryos, the changes in the shape of heterochromatin during the formation of chromocenters result in the formation of spherical domains that are characteristic of LLPS. We thus sought to quantify the biophysical properties of pericentromeric chromatin after fertilization.

As part of the study, RICS was employed to measure the concentration and diffusion coefficients of histone H3.1, which is a component of pericentromeric chromatin [166]. Phase separation of embryonic heterochromatin should result in a distinct change in H3.1 concentration and diffusion coefficient within pericentromeric chromatin compared to the surrounding nucleoplasm [161, 167]. To distinguish pericentromeric chromatin from the surrounding nucleoplasm, TALE-MajSat-mClover was co-expressed with SNAP-H3.1 in 2-cell stage mouse embryos. SNAP-Cell 647-SiR (NEB) was used to label SNAP-H3.1 prior to imaging with CLSM. TALE-MajSat-mClover bound to the major satellite repeats (MajSat) in heterochromatin and provided a means of delimiting the heterochromatin domains using an intensity threshold (Figure 7.1A). The resulting masks were then used for the ARICS analysis of SNAP-H3.1 in the respective regions. We found that the SNAP-H3.1 diffusion coefficient is lower in the heterochromatin domain compared to the nucleoplasm (Figure 7.1B) and its concentration was higher inside the heterochromatin domain (Figure 7.1C). These results support the idea of pericentromeric heterochromatin being a phase-separated domain.

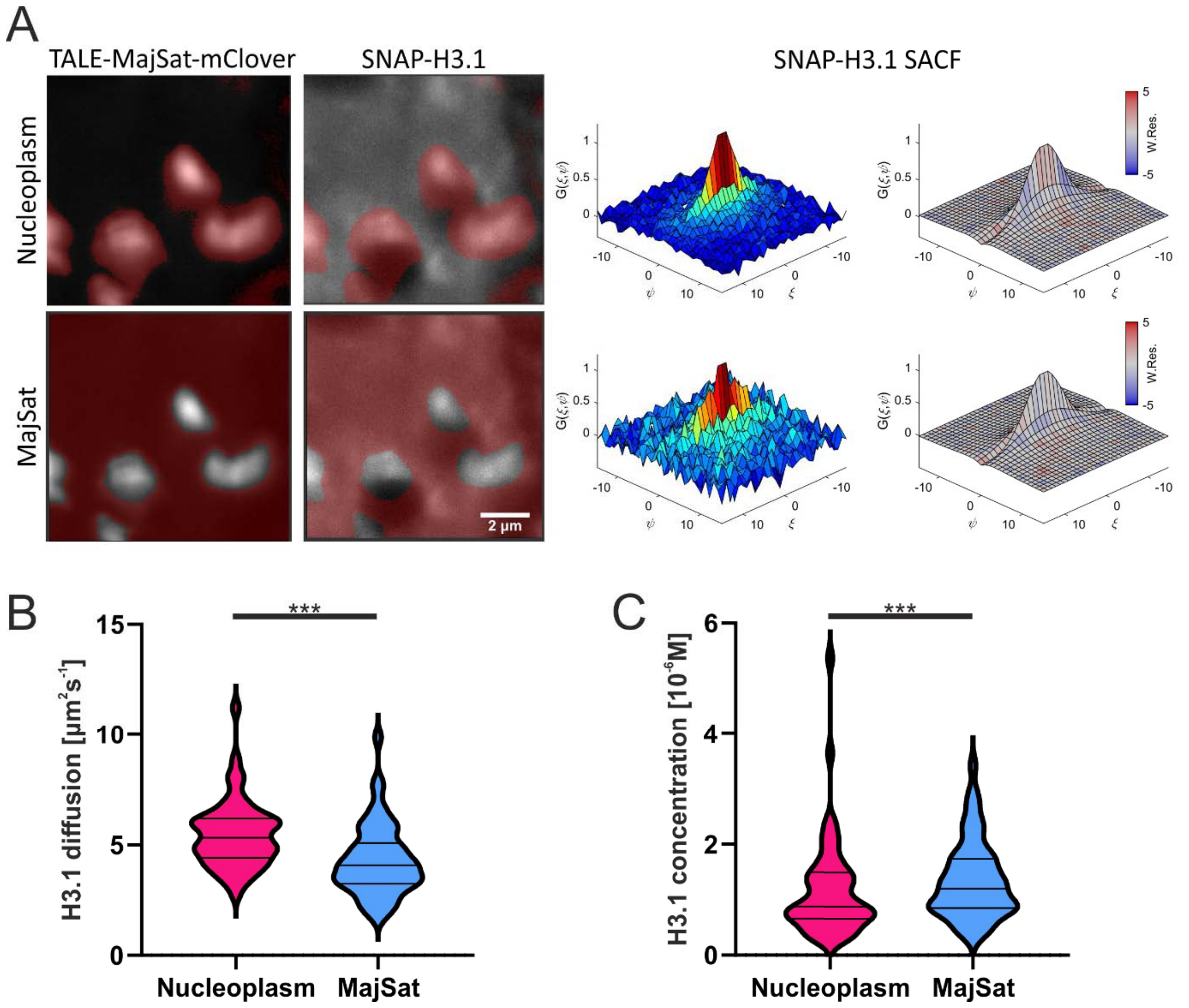

Figure 7.1. RICS analysis of histone H3.1 in 2-cell mouse embryos. (A) An example of the RICS analysis procedure on images of a mouse embryo. An exclusion mask (*red overlay*) was generated by intensity thresholding in the mClover channel (*left column*) and applied to the H3.1 channel (*right column*) for arbitrary-region RICS. Plots of the corresponding SACFs in the respective image regions and the fitted free-diffusion function are shown on the right. Violin plots of (B) SNAP-H3.1 diffusion coefficient and (C) concentration in the nucleoplasm and pericentromeric heterochromatin (MajSat) regions at the 2-cell stage. Horizontal lines indicate the 25th, 50th and 75th percentiles in the violin plots. n = 54 cells. Statistical analysis was performed using the two-sided Mann–Whitney U-test (***: $p < 0.001$).

The RICS data is also consistent with fluorescence recovery after photobleaching (FRAP) experiments conducted by our collaboration partners. Here, H3.1 showed slower recovery kinetics inside the pericentromeric heterochromatin region compared to the nucleoplasm, despite there being a similar mobile fraction of H3.1 in both regions. In combination with the RICS data, this suggested that embryonic heterochromatin forms a liquid phase-separated domain in the early stages of embryonic development.

## 7.2. Outlook

The study provided novel insights into chromatin organization in the early stages of embryogenesis. Arbitrary-region RICS provided a means to directly observe and quantify the diffusion and concentration of labelled histone H3.1 inside the nuclei of living mouse embryos, thereby giving information about the surrounding liquid environment with high spatial resolution. This observation would be otherwise difficult or impossible to achieve with other biochemical methods.

# 8. Summary and Conclusion

The central theme of this thesis is the application of quantitative fluorescence microscopy to follow dynamic processes in living cells. Living cells present a significant challenge for quantitative imaging in general, as the noisy, inhomogeneous and highly variable cellular background often masks the objects and signals that one is interested in. In addition, to reduce the effects of phototoxicity and photobleaching, live-cell fluorescence imaging is often performed with lower laser powers compared to *in vitro* equivalents, especially when imaging the same sample over extended periods of time. This reduces the signal-to-noise and a fine balance must be achieved to meet the requirements of both the cells and the methodology.

As a result of the complexities in live-cell imaging, we are often required to computationally process the images to extract the relevant regions for analysis. This is a common theme through all the projects in this thesis. In Chapter 4, I used a combination of FLIM and SPT to follow Gag processing and rearrangement in individual HIV-1 particles. It was necessary to track the HIV-1 assembly sites and nascent particles before extracting the fluorescence lifetime from the corresponding positions in the lifetime images. This gave us information about the behavior of individual particles as they journeyed through the various stages of assembly and release. Compared to the *in vitro* imaging of HIV-1 particles in the same project, where populations of mature and immature viruses were easily distinguishable, the live-cell experiments carried an additional layer of complexity. However, it was only through the live-cell experiments that we were able to obtain information regarding the timing and dynamics of Gag processing and rearrangement in an asynchronous virus population.

In Chapter 5, I helped to develop a method for quantitative FRET measurements in live-cells. The plethora of processing and corrections necessary for FRET quantification, as well as the additional complexities introduced by imaging fluorescent proteins in live-cells, make the comparison of results across different experiments, instruments, and laboratories difficult. A number of methods have been proposed to quantify FRET in live-cell imaging experiments, but there is no consensus on which method produces FRET efficiencies that are comparable across different instruments. By adapting the theory of single-molecule FRET studies, where a consensus exists on the method of correction, we introduced a FRET quantification method that has simple instrumentation and calibration requirements, is robust, and produces FRET efficiencies that are comparable across different setups.

In Chapters 6 and 7, ICS and RICS were used respectively for the analysis of live-cell images. In Chapter 6, I adapted previously established correction methods for ARICS to ICS, applying a moving average subtraction to remove static structures in the images as well as intensity thresholds to restrict the analysis to only the regions of interest. With this, I was able to measure the homodimerization of the human GPCR CXCR4 as well as its interaction with the viral GPCR US28. In particular, previous bulk biochemical assays failed to detect any interaction between US28 and CXCR4, but ICCS provided unambiguous proof that such an interaction exists in a live-cell environment. In Chapter 7, ARICS was applied to study histone diffusion in mouse embryos. The ability to segment the image by applying intensity thresholds in one channel and performing RICS on the resulting arbitrarily-shaped regions in a second channel was particularly useful here. It allowed us to identify the different diffusion behaviors of histones in- and outside of the heterochromatin regions, supporting the conclusion that embryonic heterochromatin is in a liquid phase-separated domain.

In summary, this thesis highlights the power of fluorescence microscopy in studying dynamic cellular processes and addresses some of the challenges posed by the complexities of a live-cell environment. Advanced fluorescence microscopy methods such as FLIM and RICS are combined with computational image processing and segmentation to extract quantitative information about the dynamic behavior of viruses and proteins in a wide range of cellular environments. As fluorescence technologies continue to develop alongside new biological and biochemical tools, fluorescence microscopy will no doubt continue to provide important and unique insights into the internal working of cells and viruses.

# References

1. Hooke, R., *Micrographia, or, some physiological descriptions of minute bodies made by magnifying glasses.* 1961.
2. Leeuwenhoek, A.V., *More observations from Mr. Leewenhook, in a letter of Sept. 7. 1674. sent to the publisher.* Philosophical Transactions of the Royal Society of London. **9**(108): p. 178-182.
3. Schleiden, M., *Arch Anat Physiol.* Wiss Med, 1838. **13**: p. 137-176.
4. Schwann, T., *Mikroskopische Untersuchungen über die Übereinstimmung in der Struktur und dem Wachsthum der Thiere und Pflanzen.* 1839.
5. Condon, E., *A theory of intensity distribution in band systems.* Physical Review, 1926. **28**(6): p. 1182.
6. Condon, E.U., *Nuclear motions associated with electron transitions in diatomic molecules.* Physical Review, 1928. **32**(6): p. 858.
7. Franck, J. and E. Dymond, *Elementary processes of photochemical reactions.* Transactions of the Faraday Society, 1926. **21**(February): p. 536-542.
8. Kasha, M., *Characterization of electronic transitions in complex molecules.* Discussions of the Faraday Society, 1950. **9**(0): p. 14-19.
9. Stokes, G.G., *XXX. On the change of refrangibility of light.* Philosophical Transactions of the Royal Society of London, 1852. **142**: p. 463-562.
10. Förster, T., *Zwischenmolekulare Energiewanderung und Fluoreszenz.* Annalen der Physik, 1948. **437**(1-2): p. 55-75.
11. Mau, A., et al., *Fast widefield scan provides tunable and uniform illumination optimizing super-resolution microscopy on large fields.* Nat Commun, 2021. **12**(1): p. 3077.
12. Voie, A.H., D.H. Burns, and F.A. Spelman, *Orthogonal-plane fluorescence optical sectioning: Three-dimensional imaging of macroscopic biological specimens.* Journal of Microscopy, 1993. **170**(3): p. 229-236.
13. Huisken, J., et al., *Optical Sectioning Deep Inside Live Embryos by Selective Plane Illumination Microscopy.* Science, 2004. **305**(5686): p. 1007-1009.
14. Planchon, T.A., et al., *Rapid three-dimensional isotropic imaging of living cells using Bessel beam plane illumination.* Nature methods, 2011. **8**(5): p. 417-423.
15. Ambrose, E.J., *A Surface Contact Microscope for the study of Cell Movements.* Nature, 1956. **178**(4543): p. 1194-1194.
16. Axelrod, D., *Cell-substrate contacts illuminated by total internal reflection fluorescence.* The Journal of cell biology, 1981. **89**(1): p. 141-145.
17. Foskett, J.K. and S. Grinstein, *Noninvasive techniques in cell biology*. 1990: Wiley-Liss.
18. Axelrod, D., *Total internal reflection fluorescence microscopy in cell biology.* Methods Enzymol, 2003. **361**: p. 1-33.
19. Zhuang, X., et al., *A Single-Molecule Study of RNA Catalysis and Folding.* Science, 2000. **288**(5473): p. 2048-2051.
20. Ha, T., et al., *Initiation and re-initiation of DNA unwinding by the Escherichia coli Rep helicase.* Nature, 2002. **419**(6907): p. 638-641.
21. Sako, Y., S. Minoghchi, and T. Yanagida, *Single-molecule imaging of EGFR signalling on the surface of living cells.* Nature Cell Biology, 2000. **2**(3): p. 168-172.
22. Ivanchenko, S., et al., *Dynamics of HIV-1 assembly and release.* PLoS Pathog, 2009. **5**(11): p. e1000652.
23. Minsky, M., *Microscopy apparatus*. 1961: United States Patent 3013467.

24. Airy, G.B., *On the diffraction of an object-glass with circular aperture.* Transactions of the Cambridge Philosophical Society, 1835. **5**: p. 283.
25. Rayleigh, L., *XXXI. Investigations in optics, with special reference to the spectroscope.* The London, Edinburgh, and Dublin Philosophical Magazine and Journal of Science, 1879. **8**(49): p. 261-274.
26. White, J.G., W.B. Amos, and M. Fordham, *An evaluation of confocal versus conventional imaging of biological structures by fluorescence light microscopy.* Journal of Cell Biology, 1987. **105**(1): p. 41-48.
27. Amos, W.B. and J.G. White, *How the confocal laser scanning microscope entered biological research.* Biol Cell, 2003. **95**(6): p. 335-42.
28. O'Connor, D.V. and D. Phillips, *Time-correlated single photon counting*. 1984, London ; Orlando: Academic Press. viii, 288 p.
29. Hendrix, J. and D.C. Lamb, *Pulsed interleaved excitation: principles and applications.* Methods Enzymol, 2013. **518**: p. 205-43.
30. Muller, B.K., et al., *Pulsed interleaved excitation.* Biophys J, 2005. **89**(5): p. 3508-22.
31. Hendrix, J., et al., *Pulsed interleaved excitation fluctuation imaging.* Biophys J, 2013. **105**(4): p. 848-61.
32. Hendrix, J. and D.C. Lamb, *Implementation and application of pulsed interleaved excitation for dual-color FCS and RICS.* Methods Mol Biol, 2014. **1076**: p. 653-82.
33. Kapanidis, A.N., et al., *Alternating-Laser Excitation of Single Molecules.* Accounts of Chemical Research, 2005. **38**(7): p. 523-533.
34. Lee, N.K., et al., *Accurate FRET Measurements within Single Diffusing Biomolecules Using Alternating-Laser Excitation.* Biophysical Journal, 2005. **88**(4): p. 2939-2953.
35. Kapanidis, A.N., et al., *Fluorescence-aided molecule sorting: Analysis of structure and interactions by alternating-laser excitation of single molecules.* Proceedings of the National Academy of Sciences, 2004. **101**(24): p. 8936-8941.
36. Schrimpf, W., *Development and Application of Software for Analyzing Advanced Fluorescence Spectroscopy Data*, in *Faculty of Chemistry and Pharmacy*. 2016, LMU Munich: Munich, Germany.
37. Danaf, N., *Advanced Fluorescence Methodologies for the Exploration of the Nanoworld*, in *Faculty of Chemistry and Pharmacy*. 2021, LMU Munich: Munich, Germany.
38. Chen, Y., et al., *Fluorescence fluctuation spectroscopy.* Methods, 1999. **19**(2): p. 234-52.
39. Chen, Y., et al., *The photon counting histogram in fluorescence fluctuation spectroscopy.* Biophys J, 1999. **77**(1): p. 553-67.
40. Magde, D., E. Elson, and W.W. Webb, *Thermodynamic Fluctuations in a Reacting System---Measurement by Fluorescence Correlation Spectroscopy.* Physical Review Letters, 1972. **29**(11): p. 705-708.
41. Magde, D., E.L. Elson, and W.W. Webb, *Fluorescence correlation spectroscopy. II. An experimental realization.* Biopolymers, 1974. **13**(1): p. 29-61.
42. Rigler, R. and E. Elson, *Fluorescence correlation spectroscopy : theory and applications*. Springer series in chemical physics,. 2001, Berlin ; New York: Springer. xx, 487 p.
43. Kimble, H.J., M. Dagenais, and L. Mandel, *Photon Antibunching in Resonance Fluorescence.* Physical Review Letters, 1977. **39**(11): p. 691-695.
44. Kask, P., P. Piksarv, and Ü. Mets, *Fluorescence correlation spectroscopy in the nanosecond time range: Photon antibunching in dye fluorescence.* European Biophysics Journal, 1985. **12**(3): p. 163-166.

45. Ehrenberg, M. and R. Rigler, *Rotational brownian motion and fluorescence intensity fluctuations.* Chemical Physics, 1974. **4**(3): p. 390-401.
46. Kask, P., et al., *Fluorescence correlation spectroscopy in the nanosecond time range: rotational diffusion of bovine carbonic anhydrase B.* Eur Biophys J, 1987. **14**(4): p. 257-61.
47. Sanborn, M.E., et al., *Fluorescence Properties and Photophysics of the Sulfoindocyanine Cy3 Linked Covalently to DNA.* The Journal of Physical Chemistry B, 2007. **111**(37): p. 11064-11074.
48. Oura, M., et al., *Polarization-dependent fluorescence correlation spectroscopy for studying structural properties of proteins in living cell.* Scientific Reports, 2016. **6**(1): p. 31091.
49. Widengren, J., R. Rigler, and U. Mets, *Triplet-state monitoring by fluorescence correlation spectroscopy.* J Fluoresc, 1994. **4**(3): p. 255-8.
50. Widengren, J., U. Mets, and R. Rigler, *Fluorescence correlation spectroscopy of triplet states in solution: a theoretical and experimental study.* The Journal of Physical Chemistry, 1995. **99**(36): p. 13368-13379.
51. Schönle, A., et al., *Monitoring triplet state dynamics with fluorescence correlation spectroscopy: Bias and correction.* Microscopy Research and Technique, 2014. **77**(7): p. 528-536.
52. Widengren, J., *Photophysical Aspects of FCS Measurements*, in *Fluorescence Correlation Spectroscopy*, R.E. Rigler, E.S., Editor. 2001. p. 276-301.
53. Schwille, P., F. Oehlenschlager, and N.G. Walter, *Quantitative hybridization kinetics of DNA probes to RNA in solution followed by diffusional fluorescence correlation analysis.* Biochemistry, 1996. **35**(31): p. 10182-93.
54. Chakraborty, S.K., et al., *Cholera toxin B conjugated quantum dots for live cell labeling.* Nano Lett, 2007. **7**(9): p. 2618-26.
55. Sabanayagam, C.R., et al., *Viral DNA packaging studied by fluorescence correlation spectroscopy.* Biophys J, 2007. **93**(4): p. L17-9.
56. Pramanik, A., et al., *Fluorescence correlation spectroscopy detects galanin receptor diversity on insulinoma cells.* Biochemistry, 2001. **40**(36): p. 10839-45.
57. Slaughter, B.D., J.W. Schwartz, and R. Li, *Mapping dynamic protein interactions in MAP kinase signaling using live-cell fluorescence fluctuation spectroscopy and imaging.* Proc Natl Acad Sci U S A, 2007. **104**(51): p. 20320-5.
58. Kapusta, P., et al., *Fluorescence lifetime correlation spectroscopy.* J Fluoresc, 2007. **17**(1): p. 43-8.
59. Felekyan, S., et al., *Filtered FCS and species cross correlation function*. SPIE BiOS. Vol. 7183. 2009: SPIE.
60. Felekyan, S., et al., *Filtered FCS: species auto- and cross-correlation functions highlight binding and dynamics in biomolecules.* Chemphyschem, 2012. **13**(4): p. 1036-53.
61. Schwille, P., F.J. Meyer-Almes, and R. Rigler, *Dual-color fluorescence cross-correlation spectroscopy for multicomponent diffusional analysis in solution.* Biophys J, 1997. **72**(4): p. 1878-86.
62. Bacia, K. and P. Schwille, *Practical guidelines for dual-color fluorescence cross-correlation spectroscopy.* Nat Protoc, 2007. **2**(11): p. 2842-56.
63. Weidemann, T. and P. Schwille, *Dual-color fluorescence cross-correlation spectroscopy with continuous laser excitation in a confocal setup.* Methods Enzymol, 2013. **518**: p. 43-70.
64. Foo, Y.H., et al., *Factors affecting the quantification of biomolecular interactions by fluorescence cross-correlation spectroscopy.* Biophys J, 2012. **102**(5): p. 1174-83.

65. Rappaz, B. and P.W. Wiseman, *Image correlation spectroscopy for measurements of particle densities and colocalization.* Curr Protoc Cell Biol, 2013. **Chapter 4**: p. Unit 4 27 1-15.
66. Wiseman, P.W., *Image correlation spectroscopy: mapping correlations in space, time, and reciprocal space.* Methods Enzymol, 2013. **518**: p. 245-67.
67. Wiseman, P.W., *Image correlation spectroscopy: principles and applications.* Cold Spring Harb Protoc, 2015. **2015**(4): p. 336-48.
68. Petersen, N.O., et al., *Quantitation of membrane receptor distributions by image correlation spectroscopy: concept and application.* Biophysical Journal, 1993. **65**(3): p. 1135-1146.
69. Srivastava, M. and N.O. Petersen, *Image cross-correlation spectroscopy: A new experimental biophysical approach to measurement of slow diffusion of fluorescent molecules.* Methods in Cell Science, 1996. **18**(1): p. 47-54.
70. Digman, M.A., et al., *Measuring Fast Dynamics in Solutions and Cells with a Laser Scanning Microscope.* Biophysical Journal, 2005. **89**(2): p. 1317-1327.
71. Digman, M.A., et al., *Fluctuation Correlation Spectroscopy with a Laser-Scanning Microscope: Exploiting the Hidden Time Structure.* Biophysical Journal, 2005. **88**(5): p. L33-L36.
72. Digman, M.A. and E. Gratton, *Analysis of diffusion and binding in cells using the RICS approach.* Microscopy Research and Technique, 2009. **72**(4): p. 323-332.
73. Digman, M.A., M. Stakic, and E. Gratton, *Raster Image Correlation Spectroscopy and Number and Brightness Analysis*, in *Methods in Enzymology*, S.Y. Tetin, Editor. 2013, Academic Press. p. 121-144.
74. Digman, M.A., et al., *Detecting Protein Complexes in Living Cells from Laser Scanning Confocal Image Sequences by the Cross Correlation Raster Image Spectroscopy Method.* Biophysical Journal, 2009. **96**(2): p. 707-716.
75. Hendrix, J., et al., *Arbitrary-Region Raster Image Correlation Spectroscopy.* Biophys J, 2016. **111**(8): p. 1785-1796.
76. BECKER, W., *Fluorescence lifetime imaging – techniques and applications.* Journal of Microscopy, 2012. **247**(2): p. 119-136.
77. Becker, W., et al., *Fluorescence lifetime imaging by time-correlated single-photon counting.* Microsc Res Tech, 2004. **63**(1): p. 58-66.
78. Chen, Y.C. and R.M. Clegg, *Fluorescence lifetime-resolved imaging.* Photosynth Res, 2009. **102**(2-3): p. 143-55.
79. Datta, R., et al., *Fluorescence lifetime imaging microscopy: fundamentals and advances in instrumentation, analysis, and applications.* Journal of Biomedical Optics, 2020. **25**(7): p. 071203.
80. van Munster, E.B. and T.W. Gadella, *Fluorescence lifetime imaging microscopy (FLIM).* Adv Biochem Eng Biotechnol, 2005. **95**: p. 143-75.
81. Digman, M.A., et al., *The phasor approach to fluorescence lifetime imaging analysis.* Biophys J, 2008. **94**(2): p. L14-6.
82. Redford, G.I. and R.M. Clegg, *Polar plot representation for frequency-domain analysis of fluorescence lifetimes.* Journal of fluorescence, 2005. **15**(5): p. 805-815.
83. Smal, I., et al., *Quantitative comparison of spot detection methods in fluorescence microscopy.* IEEE Trans Med Imaging, 2010. **29**(2): p. 282-301.
84. Olivo-Marin, J.C., *Extraction of spots in biological images using multiscale products.* Pattern Recognition, 2002. **35**(9): p. 1989-1996.
85. Messer, P.K., et al., *A Multiscale Wavelet Algorithm for Atom Tracking in STM Movies.* New Journal of Physics, 2022. **(In Press)**.

86. Starck, J., J. Fadili, and F. Murtagh, *The Undecimated Wavelet Decomposition and its Reconstruction.* IEEE Transactions on Image Processing, 2007. **16**(2): p. 297-309.
87. Sage, D., et al., *Automatic Tracking of Individual Fluorescence Particles: Application to the Study of Chromosome Dynamics.* IEEE Trans. Image Process., 2005. **14**: p. 1372.
88. Godinez, W.J., et al., *Deterministic and probabilistic approaches for tracking virus particles in time-lapse fluorescence microscopy image sequences.* Med Image Anal, 2009. **13**(2): p. 325-42.
89. Chenouard, N., et al., *Objective comparison of particle tracking methods.* Nat Methods, 2014. **11**(3): p. 281-9.
90. Reid, D., *An algorithm for tracking multiple targets.* IEEE Transactions on Automatic Control, 1979. **24**(6): p. 843-854.
91. Blackman, S.S., *Multiple hypothesis tracking for multiple target tracking.* IEEE Aerospace and Electronic Systems Magazine, 2004. **19**(1): p. 5-18.
92. Blackman, S. and R. Popoli, *Design and analysis of modern tracking systems*. Artech House. 1999, Norwood, MA: Artech House.
93. Genovesio, A., et al., *Multiple Particle Tracking in 3-D+T Microscopy: Method and Application to the Tracking of Endocytosed Quantum Dots.* IEEE Trans. Image Process., 2006. **15**: p. 1062.
94. Veenman, C.J., M.J. Reinders, and E. Backer, *Resolving Motion Correspondence for Densely Moving Points.* IEEE T. Pattern Anal., 2001. **23**: p. 54.
95. Jiang, S., et al., *Tracking Molecular Particles in Live Cells Using Fuzzy Rule-Based System.* Cytometry, Part A, 2007. **71**: p. 576.
96. Shafique, K. and M. Shah, *A Noniterative Greedy Algorithm for Multiframe Point Correspondence.* IEEE Trans. Pattern Anal. Mach. Intell., 2005. **27**: p. 51.
97. Jaqaman, K., et al., *Robust single-particle tracking in live-cell time-lapse sequences.* Nat Methods, 2008. **5**(8): p. 695-702.
98. Kuhn, H.W., *The Hungarian method for the assignment problem.* Naval Research Logistics Quarterly, 1955. **2**(1-2): p. 83-97.
99. Murray, P.S., et al., *Retroviral matrix domains share electrostatic homology: models for membrane binding function throughout the viral life cycle.* Structure, 2005. **13**(10): p. 1521-31.
100. Gamble, T.R., et al., *Structure of the carboxyl-terminal dimerization domain of the HIV-1 capsid protein.* Science, 1997. **278**(5339): p. 849-53.
101. Muriaux, D. and J.L. Darlix, *Properties and functions of the nucleocapsid protein in virus assembly.* RNA Biol, 2010. **7**(6): p. 744-53.
102. Sundquist, W.I. and H.G. Krausslich, *HIV-1 assembly, budding, and maturation.* Cold Spring Harb Perspect Med, 2012. **2**(7): p. a006924.
103. Erickson-Viitanen, S., et al., *Cleavage of HIV-1 gag polyprotein synthesized in vitro: sequential cleavage by the viral protease.* AIDS Res Hum Retroviruses, 1989. **5**(6): p. 577-91.
104. Tozser, J., et al., *Comparison of the HIV-1 and HIV-2 proteinases using oligopeptide substrates representing cleavage sites in Gag and Gag-Pol polyproteins.* FEBS Lett, 1991. **281**(1-2): p. 77-80.
105. Pettit, S.C., et al., *The p2 domain of human immunodeficiency virus type 1 Gag regulates sequential proteolytic processing and is required to produce fully infectious virions.* J Virol, 1994. **68**(12): p. 8017-27.
106. Hanne, J., et al., *Stimulated Emission Depletion Nanoscopy Reveals Time-Course of Human Immunodeficiency Virus Proteolytic Maturation.* ACS Nano, 2016. **10**(9): p. 8215-22.

107. Mattei, S., et al., *Induced maturation of human immunodeficiency virus.* J Virol, 2014. **88**(23): p. 13722-31.
108. Schimer, J., et al., *Triggering HIV polyprotein processing by light using rapid photodegradation of a tight-binding protease inhibitor.* Nat Commun, 2015. **6**: p. 6461.
109. Rizzo, M.A., et al., *An improved cyan fluorescent protein variant useful for FRET.* Nat Biotechnol, 2004. **22**(4): p. 445-9.
110. Grailhe, R., et al., *Monitoring protein interactions in the living cell through the fluorescence decays of the cyan fluorescent protein.* Chemphyschem, 2006. **7**(7): p. 1442-54.
111. Koushik, S. and S. Vogel, *Energy migration alters the fluorescence lifetime of Cerulean: implications for fluorescence lifetime imaging Forster resonance energy transfer measurements.* Journal of Biomedical Optics, 2008. **13**(3): p. 031204.
112. Kelly, D.J., et al., *Automated multiwell fluorescence lifetime imaging for Förster resonance energy transfer assays and high content analysis.* Analytical Methods, 2015. **7**(10): p. 4071-4089.
113. Muller, B., M. Anders, and J. Reinstein, *In vitro analysis of human immunodeficiency virus particle dissociation: gag proteolytic processing influences dissociation kinetics.* PLoS One, 2014. **9**(6): p. e99504.
114. Qu, K., et al., *Maturation of the matrix and viral membrane of HIV-1.* Science, 2021. **373**(6555): p. 700-704.
115. Carlson, L.A., et al., *Three-dimensional analysis of budding sites and released virus suggests a revised model for HIV-1 morphogenesis.* Cell Host Microbe, 2008. **4**(6): p. 592-9.
116. Jouvenet, N., P.D. Bieniasz, and S.M. Simon, *Imaging the biogenesis of individual HIV-1 virions in live cells.* Nature, 2008. **454**(7201): p. 236-40.
117. Rahman, S.A., et al., *Investigating the role of F-actin in human immunodeficiency virus assembly by live-cell microscopy.* J Virol, 2014. **88**(14): p. 7904-14.
118. Zeug, A., et al., *Quantitative intensity-based FRET approaches--a comparative snapshot.* Biophys J, 2012. **103**(9): p. 1821-7.
119. Gordon, G.W., et al., *Quantitative Fluorescence Resonance Energy Transfer Measurements Using Fluorescence Microscopy.* Biophysical Journal, 1998. **74**(5): p. 2702-2713.
120. Zal, T. and N.R.J. Gascoigne, *Photobleaching-Corrected FRET Efficiency Imaging of Live Cells.* Biophysical Journal, 2004. **86**(6): p. 3923-3939.
121. Hochreiter, B., et al., *Advanced FRET normalization allows quantitative analysis of protein interactions including stoichiometries and relative affinities in living cells.* Scientific Reports, 2019. **9**(1): p. 8233.
122. Hendrix, J., et al., *Dark states in monomeric red fluorescent proteins studied by fluorescence correlation and single molecule spectroscopy.* Biophysical journal, 2008. **94**(10): p. 4103-4113.
123. Wu, B., Y. Chen, and J.D. Muller, *Fluorescence fluctuation spectroscopy of mCherry in living cells.* Biophys J, 2009. **96**(6): p. 2391-404.
124. Hoppe, A., K. Christensen, and J.A. Swanson, *Fluorescence resonance energy transfer-based stoichiometry in living cells.* Biophys J, 2002. **83**(6): p. 3652-64.
125. Thaler, C., et al., *Quantitative Multiphoton Spectral Imaging and Its Use for Measuring Resonance Energy Transfer.* Biophysical Journal, 2005. **89**(4): p. 2736-2749.
126. Koushik, S.V., et al., *Cerulean, Venus, and VenusY67C FRET Reference Standards.* Biophysical Journal, 2006. **91**(12): p. L99-L101.
127. Chen, H., et al., *Measurement of FRET Efficiency and Ratio of Donor to Acceptor Concentration in Living Cells.* Biophysical Journal, 2006. **91**(5): p. L39-L41.

128. Wu, B., et al., *Structures of the CXCR4 chemokine GPCR with small-molecule and cyclic peptide antagonists.* Science, 2010. **330**(6007): p. 1066-71.
129. Alcami, A., *Viral mimicry of cytokines, chemokines and their receptors.* Nature Reviews Immunology, 2003. **3**(1): p. 36-50.
130. Rosenkilde, M.M., *Virus-encoded chemokine receptors – putative novel antiviral drug targets.* Neuropharmacology, 2005. **48**(1): p. 1-13.
131. de Munnik, S.M., et al., *Modulation of cellular signaling by herpesvirus-encoded G protein-coupled receptors.* Front Pharmacol, 2015. **6**: p. 40.
132. Kledal, T.N., M.M. Rosenkilde, and T.W. Schwartz, *Selective recognition of the membrane-bound CX3C chemokine, fractalkine, by the human cytomegalovirus-encoded broad-spectrum receptor US28.* FEBS Lett, 1998. **441**(2): p. 209-14.
133. Vomaske, J., et al., *Differential ligand binding to a human cytomegalovirus chemokine receptor determines cell type-specific motility.* PLoS Pathog, 2009. **5**(2): p. e1000304.
134. Boomker, J.M., et al., *The human cytomegalovirus-encoded receptor US28 increases the activity of the major immediate-early promoter/enhancer.* Virus Res, 2006. **118**(1-2): p. 196-200.
135. Rucker, J., et al., *Utilization of chemokine receptors, orphan receptors, and herpesvirus-encoded receptors by diverse human and simian immunodeficiency viruses.* J Virol, 1997. **71**(12): p. 8999-9007.
136. Pleskoff, O., C. Tréboute, and M. Alizon, *The cytomegalovirus-encoded chemokine receptor US28 can enhance cell-cell fusion mediated by different viral proteins.* J Virol, 1998. **72**(8): p. 6389-97.
137. Pleskoff, O., et al., *Identification of a chemokine receptor encoded by human cytomegalovirus as a cofactor for HIV-1 entry.* Science, 1997. **276**(5320): p. 1874-8.
138. Ohagen, A., et al., *Cell-dependent mechanisms restrict the HIV type 1 coreceptor activity of US28, a chemokine receptor homolog encoded by human cytomegalovirus.* AIDS Res Hum Retroviruses, 2000. **16**(1): p. 27-35.
139. Choi, W.-T. and J. An, *Biology and clinical relevance of chemokines and chemokine receptors CXCR4 and CCR5 in human diseases.* Experimental Biology and Medicine, 2011. **236**(6): p. 637-647.
140. Bianchi, M.E. and R. Mezzapelle, *The Chemokine Receptor CXCR4 in Cell Proliferation and Tissue Regeneration.* Front Immunol, 2020. **11**: p. 2109.
141. Feng, Y., et al., *HIV-1 entry cofactor: functional cDNA cloning of a seven-transmembrane, G protein-coupled receptor.* Science, 1996. **272**(5263): p. 872-7.
142. Maddon, P.J., et al., *The T4 gene encodes the AIDS virus receptor and is expressed in the immune system and the brain.* Cell, 1986. **47**(3): p. 333-48.
143. McDougal, J.S., et al., *Binding of HTLV-III/LAV to T4+ T cells by a complex of the 110K viral protein and the T4 molecule.* Science, 1986. **231**(4736): p. 382-5.
144. Berger, E.A., et al., *A new classification for HIV-1.* Nature, 1998. **391**(6664): p. 240.
145. Babcock, G.J., M. Farzan, and J. Sodroski, *Ligand-independent dimerization of CXCR4, a principal HIV-1 coreceptor.* J Biol Chem, 2003. **278**(5): p. 3378-85.
146. Iliopoulou, M., et al., *A dynamic three-step mechanism drives the HIV-1 pre-fusion reaction.* Nat Struct Mol Biol, 2018. **25**(9): p. 814-822.
147. Watts, A., et al., *Identification and profiling of CXCR3–CXCR4 chemokine receptor heteromer complexes.* British Journal of Pharmacology, 2013. **168**(7): p. 1662-1674.
148. Décaillot, F.M., et al., *CXCR7/CXCR4 heterodimer constitutively recruits beta-arrestin to enhance cell migration.* J Biol Chem, 2011. **286**(37): p. 32188-97.
149. Frank, T., et al., *Attenuation of chemokine receptor function and surface expression as an immunomodulatory strategy employed by human cytomegalovirus is linked to vGPCR US28.* Cell Commun Signal, 2016. **14**(1): p. 31.

150. Misawa, N., et al., *Rapid and high-sensitivity cell-based assays of protein-protein interactions using split click beetle luciferase complementation: an approach to the study of G-protein-coupled receptors.* Anal Chem, 2010. **82**(6): p. 2552-60.
151. Takakura, H., et al., *Visualization and quantitative analysis of G protein-coupled receptor-β-arrestin interaction in single cells and specific organs of living mice using split luciferase complementation.* ACS Chem Biol, 2012. **7**(5): p. 901-10.
152. Pfleger, K.D.G. and K.A. Eidne, *Illuminating insights into protein-protein interactions using bioluminescence resonance energy transfer (BRET).* Nature Methods, 2006. **3**(3): p. 165-174.
153. Andor. *CCD Architecture: Full Frame CCD, Frame Transfer and Interline CCD*. 2021 [cited 2021 20/12/2021]; Available from: https://andor.oxinst.com/learning/view/article/ccd-sensor-architectures.
154. Collins, A.V., et al., *The Interaction Properties of Costimulatory Molecules Revisited.* Immunity, 2002. **17**(2): p. 201-210.
155. Zhang, X., et al., *Crystal structure of the receptor-binding domain of human B7-2: Insights into organization and signaling.* Proceedings of the National Academy of Sciences, 2003. **100**(5): p. 2586-2591.
156. Souchet, M., et al., *Human p63RhoGEF, a novel RhoA-specific guanine nucleotide exchange factor, is localized in cardiac sarcomere.* J Cell Sci, 2002. **115**(Pt 3): p. 629-40.
157. Schrimpf, W., et al., *PAM: A Framework for Integrated Analysis of Imaging, Single-Molecule, and Ensemble Fluorescence Data.* Biophysical Journal, 2018. **114**(7): p. 1518-1528.
158. Casanova, M., et al., *Heterochromatin reorganization during early mouse development requires a single-stranded noncoding transcript.* Cell Rep, 2013. **4**(6): p. 1156-67.
159. Probst, A.V., et al., *A strand-specific burst in transcription of pericentric satellites is required for chromocenter formation and early mouse development.* Dev Cell, 2010. **19**(4): p. 625-38.
160. Jachowicz, J.W., et al., *Heterochromatin establishment at pericentromeres depends on nuclear position.* Genes Dev, 2013. **27**(22): p. 2427-32.
161. Strom, A.R., et al., *Phase separation drives heterochromatin domain formation.* Nature, 2017. **547**(7662): p. 241-245.
162. Larson, A.G., et al., *Liquid droplet formation by HP1alpha suggests a role for phase separation in heterochromatin.* Nature, 2017. **547**(7662): p. 236-240.
163. Strickfaden, H., et al., *Condensed Chromatin Behaves like a Solid on the Mesoscale In Vitro and in Living Cells.* Cell, 2020. **183**(7): p. 1772-1784 e13.
164. Huo, X., et al., *The Nuclear Matrix Protein SAFB Cooperates with Major Satellite RNAs to Stabilize Heterochromatin Architecture Partially through Phase Separation.* Mol Cell, 2020. **77**(2): p. 368-383 e7.
165. Erdel, F., et al., *Mouse Heterochromatin Adopts Digital Compaction States without Showing Hallmarks of HP1-Driven Liquid-Liquid Phase Separation.* Mol Cell, 2020. **78**(2): p. 236-249 e7.
166. Santenard, A., et al., *Heterochromatin formation in the mouse embryo requires critical residues of the histone variant H3.3.* Nat Cell Biol, 2010. **12**(9): p. 853-62.
167. Frank, L. and K. Rippe, *Repetitive RNAs as Regulators of Chromatin-Associated Subcompartment Formation by Phase Separation.* J Mol Biol, 2020. **432**(15): p. 4270-4286.

# List of Abbreviations

| | |
|---|---|
| ACF | autocorrelation function |
| ADC | analog-to-digital converter |
| ALEX | alternating laser excitation |
| AOTF | acousto-optic tunable filter |
| APD | avalanche photodiode |
| ARICS | arbitrary-region raster image correlation spectroscopy |
| BRET | bioluminescence energy transfer |
| CA | HIV Gag capsid domain |
| CCF | cross-correlation function |
| CFD | constant-fraction discriminator |
| CLSM | confocal laser scanning microscope |
| FCCS | fluorescence cross-correlation spectroscopy |
| FCS | fluorescence correlation spectroscopy |
| FFS | fluorescence fluctuation spectroscopy |
| FLIM | fluorescence lifetime imaging microscopy |
| FPGA | field programmable gate array |
| FRAP | fluorescence recovery after photobleaching |
| FRET | Förster resonance energy transfer |
| GPCR | G-protein coupled receptor |
| HIV-1 | human immunodeficiency virus type 1 |
| ICCS | image cross-correlation spectroscopy |
| ICS | image correlation spectroscopy |
| IUWT | isotropic undecimated wavelet transform |
| LAP | linear assignment problem |
| LLPS | liquid-liquid phase separation |
| LPV | lopinavir |
| MA | HIV Gag matrix domain |
| MHT | multiple-hypothesis tracking |
| PI | protease inhibitor |
| PIE | pulsed interleaved excitation |
| PMT | photomultiplier tube |
| PR | HIV protease |
| PSF | point spread function |
| RICS | raster image correlation spectroscopy |
| RT | HIV reverse transcriptase |
| SD | standard deviation |
| SEM | standard error of the mean |
| SPT | single particle tracking |
| TAC | time-to-amplitude converter |
| TCSPC | time correlated single photon counting |
| TIRFM | total internal reflection fluorescence microscopy |
| VLP | virus-like particle |

# Acknowledgements

It has been a long time coming, but here I am, at the end of a long journey. It hasn't exactly been what I expected when I first began, but I am grateful for every bit of it and for everyone whom I met along the way.

I would like to express my deepest gratitude to **Don**, who has wholeheartedly supported me and my research throughout my time here. Thank you for all the encouragement, advice and feedback – I have learnt a lot both as a scientist and as a person. May the Packers reign supreme on the field in the seasons to come.

**Philip**, thank you for agreeing to be the second examiner of this thesis. I am grateful for your scientific input and will miss the insightful discussions during our joint Monday seminars.

**Barbara**, thank you so much for your guidance and input on the HIV project, and for joining my thesis committee. I hope the maturation paper will be published soon, after all the twists and turns.

**Jelle**, I would like to thank you not just for being part of my thesis committee, but also for all the advice regarding RICS whenever I ran into a problem.

My heartfelt thanks also go out to **Prof. Achim Hartschuh** and **Prof. Christian Ochsenfeld** for joining the thesis committee.

The works in this thesis could not have been possible without the efforts all the wonderful people whom I have had the pleasure to work with over the years. For the HIV project, I would like to thank **Annica** for preparing particles and cells needed for our experiments and for subsequently taking on the arduous task of tracking the particles on Imaris. For the embryo project I would like to thank **Manuel** for providing the mouse embryos, which are a really interesting to work on. Also thank you **Irene** for taking over some of the experiments and analysis in the embryo project – I was pleasantly surprised by how quickly you learned all the esoteric quirks of the RICS setup and analysis. I would also like to thank **Dr. Aurélie Dupont** for offering the opportunity to collaborate in the QuanTI-FRET project.

My thanks also go to **Moritz** for guiding me through the maze of German bureaucracy and even providing personal help on a few occasions.

I would like to express my appreciation and gratitude for the networking opportunities and financial supported provided by CeNS and SFB1032.

I would like to thank all members of AK Lamb, both past and present: **Waldi, Wehne, Lena, Jens, Daniela, Alex, Anders, Kira, Alvaro, Sushi, Bässem, Philipp, Viola, Evelyn, Nader, Ivo, Maria, Ganesh, Vanessa, Adrian, Frank, Damir, Fabian, Pooyeh, Priyanshi, Ecenasz**. Especially the 3c-RICS crew **Waldi** and **Nader** for fixing the RICS setup every time it broke!

Finally, I would like to thank **my parents** and **my brother Qian Yi** for supporting and encouraging me despite all these years that I am away from home. And last but not least, thank you **Chenzhi**♥ **.** You light up my world with your smile. Thank you for keeping me company and lifting my spirits whenever I was down. I am so happy to have met you and am excited to see what the future has in store for us.

# Appendix I

## Dynamics of HIV-1 Gag Processing as Revealed by Fluorescence Lifetime Imaging Microscopy and Single Virus Tracking

Reprinted from *Viruses* **14**(2), 340 (2022) in accordance with the Creative Commons Attribution 4.0 International License.

viruses

MDPI

*Article*

# Dynamics of HIV-1 Gag Processing as Revealed by Fluorescence Lifetime Imaging Microscopy and Single Virus Tracking

**Chen Qian [1,2,†], Annica Flemming [3,†], Barbara Müller [3,*] and Don C. Lamb [1,2,4,5,*]**

[1] Department of Chemistry, Ludwig Maximilians-Universität München, Butenandtstraße 5-13, 81377 München, Germany; chen.qian@lmu.de
[2] Center for Nano Science (CeNS), Ludwig Maximilians-Universität München, Butenandtstraße 5-13, 81377 München, Germany
[3] Center for Integrative Infectious Diseases Research (CIID), Universitätsklinikum Heidelberg, Im Neuenheimer Feld 344, 69120 Heidelberg, Germany; annica.flemming@gmx.de
[4] Nanosystems Initiative München (NIM), Ludwig Maximilians-Universität München, Butenandtstraße 5-13, 81377 München, Germany
[5] Center for Integrated Protein Science (CIPSM), Ludwig Maximilians-Universität München, Butenandtstraße 5-13, 81377 München, Germany
* Correspondence: Barbara.Mueller@med.uni-heidelberg.de (B.M.); d.lamb@lmu.de (D.C.L.)
† These authors contributed equally to this work.

**Abstract:** The viral polyprotein Gag plays a central role for HIV-1 assembly, release and maturation. Proteolytic processing of Gag by the viral protease is essential for the structural rearrangements that mark the transition from immature to mature, infectious viruses. The timing and kinetics of Gag processing are not fully understood. Here, fluorescence lifetime imaging microscopy and single virus tracking are used to follow Gag processing in nascent HIV-1 particles in situ. Using a Gag polyprotein labelled internally with eCFP, we show that proteolytic release of the fluorophore from Gag is accompanied by an increase in its fluorescence lifetime. By tracking nascent virus particles in situ and analyzing the intensity and fluorescence lifetime of individual traces, we detect proteolytic cleavage of eCFP from Gag in a subset (6.5%) of viral particles. This suggests that for the majority of VLPs, Gag processing occurs with a delay after particle assembly.

**Keywords:** HIV; maturation; gag processing; fluorescence lifetime; single virus tracking

check for updates

**Citation:** Qian, C.; Flemming, A.; Müller, B.; Lamb, D.C. Dynamics of HIV-1 Gag Processing as Revealed by Fluorescence Lifetime Imaging Microscopy and Single Virus Tracking. *Viruses* **2022**, *14*, 340. https://doi.org/10.3390/v14020340

Academic Editor: Gregory B. Melikian

Received: 17 January 2022
Accepted: 6 February 2022
Published: 8 February 2022

## 1. Introduction

Assembly, release and maturation are critical steps in the late phase of the HIV-1 replication cycle. The viral structural polyprotein Gag plays an important role throughout the entire process. Independently folded domains of Gag are required for membrane targeting (matrix, MA), protein-protein interactions (capsid, CA), packaging of the viral RNA genome (nucleocapsid, NC), and recruitment of ESCRT machinery components that facilitate virion release (p6) [1–3]. Gag also recruits the GagProPol polyprotein, which is expressed by ribosomal frameshifting and comprises the viral enzymes PR, reverse transcriptase (RT) and integrase (IN) into the nascent particle. During or shortly after virus release, the mature form of PR generated by autoprocessing from GagProPol mediates proteolytic cleavage of GagProPol and Gag, triggering the morphological rearrangements that yield the characteristic cone-shaped capsid core of the infectious virus [4].

Productive maturation relies on coordination of Gag proteolysis and assembly and on sequential cleavage of specific sites within Gag and GagProPol in an ordered processing cascade [5]. The timing and kinetics of this process are not fully understood. In vitro processing of Gag or virus-like particles using purified PR identified the order of proteolytic events [5–7], but does not faithfully recapitulate processing by the endogenous viral PR in situ. Protease inhibitor (PI) wash out of photodestructible PI has been employed to synchronize Gag processing within the context of virus-like particles (VLPs) [8–10]. However, this approach uncouples proteolytic maturation from assembly.

Here, we describe the application of fluorescence lifetime imaging microscopy (FLIM) and single virus tracking (SVT) to the analysis of the assembly and maturation of HIV-1. Inserting the fluorophore eCFP as an additional domain into the Gag polyprotein allowed us to monitor changes in its fluorescence lifetime as a readout for proteolytic release. This enabled us to detect Gag processing in relation to the assembly process with high time resolution. We employed confocal laser scanning microscopy (CLSM) with time-correlated single photon counting (TCSPC) to image the assembly and maturation of eCFP-tagged HIV-1 VLPs. Increase of fluorescence intensity was used as a readout to monitor recruitment of Gag.eCFP to nascent assembly sites at the plasma membrane, as described earlier for eGFP [11]. In addition, we exploited sensitivity of the eCFP fluorescence lifetime to the close proximity of other eCFP molecules [12–15]. By tracking individual assembly sites and VLPs, we show that both incorporation of eCFP into the Gag lattice during assembly and its subsequent cleavage from the lattice during maturation result in measurable changes in the fluorescence lifetime of the fluorophore. Using this method, we were able to observe the timing and kinetics of Gag processing and rearrangement in relation to the assembly process in individually tracked VLPs.

## 2. Materials and Methods

### *2.1. Compounds and Antibodies*

Lopinavir was obtained through the AIDS Research and Reference Reagent Program, Division of AIDS, NIAID, National Institutes of Health. Sheep polyclonal anti-CA antiserum was raised against recombinant HIV-1 CA and rabbit polyclonal anti-GFP antiserum was raised against recombinant GFP (both in house).

### *2.2. Plasmids*

All HIV-1 plasmids used in this study were based on the non-replication competent derivative pCHIV, which expresses all HIV-1 NL4-3 proteins except for Nef under the control of a CMV promotor and lacks the viral long terminal repeat regions [16]. Plasmids pCHIV$^{eCFP}$ and pCHIV$^{ieCFP}$ are fluorescently tagged derivatives with the eCFP coding sequence inserted between the MA and CA region of the *gag* ORF. pCHIV$^{eCFP}$ has been described previously [17]. pCHIV$^{ieCFP}$ is a derivative of the previously reported pCHIV$^{iSNAP}$ [18]. It was generated by replacing the MluI/XbaI fragment encoding the SNAP-tag by a PCR fragment encoding eCFP flanked by two SQNYPIV protease recognition sites (primer sequences: ggcgc cACGC GTatg gtgag caagg gcgag gagc, cgggc ctcta gactt gtaca gctcg tccat gccga g).

peCFP, eCFP on a pcDNA 3.1 mammalian expression vector was purchased from Invitrogen (Carlsbad, CA, USA). pMA-eCFP was generated by inserting the MA sequence of pCHIV in the NheI/XhoI restriction sites (underlined in the primer sequence) of the peCFP multiple cloning site (MCS) (primer sequences: GATAT AGCTA GCATG GGTGC GAGAG CGTCG G, GGTGC TCGAG TCACT TGTAC AGCTC GTCCA TGCCG).

### *2.3. Cell Lines*

HEK293T and HeLa Kyoto cells were cultured in Dulbecco's modified Eagle's medium (GlutaMAX, Invitrogen) supplemented with 10% fetal calf serum (FCS; Biochrom), 100 IU/mL penicillin and 100 μg/mL streptomycin at 37 °C and 5%. The HeLa$_{rCDS}$ cell line was generated by Mücksch, et al. [19]. The medium for cultivation of HeLa$_{rCDS}$ cells was supplemented with 2 μg/mL Puromycin and 5 μg/mL Blasticidin. Identity of all cell lines has been authenticated using STR profiling (Promega PowerPlex 21 Kit; carried out by Eurofins Genomics, Ebersberg, Germany). Cells were monitored regularly for mycoplasma contamination using the MycoAlert mycoplasma detection kit (Lonza Rockland, MA, USA).

### 2.4. HEK293T Cell Transfection and Virus Particle Production

HEK293T cells (4 × $10^5$ cells per well) were seeded on a six-well plate 24 h before transfection with the indicated plasmids using a standard polyethyleneimine (PEI) transfection procedure, using 2 µg DNA per well of equimolar mixtures of pCHIV and its labeled derivative (pCHIV$^{eCFP}$ or pCHIV$^{ieCFP}$) and 6 µL 1µg/µL PEI. A final concentration of 2 µM lopinavir (LPV; 10mM) was added to the tissue culture medium at the time of transfection for production of immature particles. At 44 h post transfection (h.p.t.), tissue culture supernatant was collected and cleared via a 0.45 µm nitrocellulose filter. Particles were concentrated from the filtrate by ultracentrifugation through a 20% (*w/w*) sucrose cushion (TL-100 Ultracentrifuge with TLA 45 rotor (Tabletop), Beckman Coulter, Brea, CA, USA, 44.000 rpm for 45 min). Pelleted particles were resuspended in phosphate-buffered saline (PBS). and stored in aliquots at −80 °C.

### 2.5. Quantitative Immunoblot Analysis

Samples were separated by SDS-PAGE (17.5% acrylamide, acrylamide:bisacrylamide 200:1) and transferred to a nitrocellulose membrane by semi-dry blotting. Membranes were blocked with Li-Cor blocking buffer diluted 1:3 in tris-buffered saline with 0.05% (m/V) Tween 20 (TBS-T) and incubated with in-house polyclonal sheep antisera raised against recombinant HIV-1 CA or against recombinant GFP, respectively. Bound antibodies were detected with an Odyssey infrared scanner (Li-Cor, Lincoln, NE, USA), using secondary antibodies, protocols and ImageStudio software provided by the instrument manufacturer. For quantitation of anti-CA reactive bands, purified recombinant HIV-1 CA protein (kindly provided by R. Sahm, University Hospital Heidelberg) was analyzed in parallel.

### 2.6. Virus Particle Preparation for Microscopy

For imaging of free VLPs, 20 µL of HIV-1 particles in PBS were transferred onto the coverslip (Labtek II chambered coverglass, Thermo Scientific, Waltham, MA, USA) and incubated at 23 °C for 15 min. The samples were then washed carefully by removing the storage buffer, adding 20 µL of Dulbecco's phosphate-buffered saline (DPBS, Gibco) and incubating for 10 min. The wash buffer was then replaced by fresh DPBS for imaging at 23 °C.

### 2.7. Live Cell Sample Preparation

For microscopy experiments, HeLa Kyoto cells (2 × $10^4$ per well) were seeded on 8-well Lab-Tek II chambered coverslides (Thermo Scientific) and incubated at 37 °C for 24 h. Cells were then transfected using Fugene HD DNA transfection reagent (Roche) according to manufacturer's instructions. An equimolar mixture of pCHIV and its labeled derivative pCHIV$^{ieCFP}$ (in total 70 ng DNA per well) was transfected. The plasmids pMA-eCFP (70 ng DNA per well) or peCFP (20 ng DNA per well) were transfected in a similar manner. Where indicated, a final concentration of 2 µM LPV (kindly provided by Jan Konvalinka) was added at the time of transfection.

To synchronize the start of HIV-1 particle assembly, we used HeLa$_{rCDS}$ cells [19]. HeLa$_{rCDS}$ cells are modified HeLa Kyoto cells in which the concentration of phosphoinositide phosphatidylinositol 4,5-bisphosphate (PI(4,5)$P_2$) in the plasma membrane can be controlled via a modified form of the phosphatase 5Ptase. Using a reversible chemical dimerizer, rCD1, 5Ptase is recruited to the plasma membrane where it dephosphorylates PI(4,5)$P_2$. The depletion of PI(4,5)$P_2$ in the plasma membrane inhibits the assembly of HIV-1 and also leads to the dissociation of pre-assembled Gag lattices at the plasma membrane. By competing out the dimerizer with FK506, cellular hemostasis quickly restores PI(4,5)$P_2$ in the plasma membrane and HIV-1 assembly begins almost immediately. HeLa$_{rCDS}$ cells were seeded and transfected as described above with the additional treatment of 1 µM rCD1 (kindly provided by Carsten Schultz, EMBL Heidelberg) 6 h post transfection (hpt) to inhibit assembly. Prior to imaging, culture medium of transfected cells was replaced with imaging medium (DMEM Fluorobrite, Thermo Fisher Scientific) 20–22 h post transfection. Imaging was performed at 37 °C. For HeLa$_{\mathrm{rCDS}}$ cells, 1μM FK506 (kindly provided by Carsten Schultz, EMBL) was added to induce virus assembly immediately before image acquisition.

### 2.8. Fluorescence Imaging

Fluorescence imaging was performed on a home-built confocal laser scanning microscope, as described elsewhere [20]. A NA = 1.49 oil immersion objective (Apo-TIRF 100x Oil/NA 1.49, Nikon, Tokyo, Japan) was used for all measurements. A 440 nm pulsed diode laser (LDH-P-C-440, PicoQuant, Berlin, Germany) was used for excitation at a laser power of between 1–2 μW before objective. Fluorescence emission was detected using a single photon avalanche diode (PDM series, PicoQuant) after a 480/40 nm emission filter. A 30 × 30 μm area divided into 500 lines was scanned over 5 s for each frame. An additional delay of 5 s between each frame was introduced for some cells to reduce photobleaching and phototoxicity over the imaging time.

Raw photon data was processed and analyzed with the software package PIE analysis with MATLAB (PAM) [21]. The pixelwise decay data were transformed using the phasor approach [22,23] (see Text S1). An aqueous solution of Atto425-COOH was measured at 23 °C and used as a reference to correct for the instrument response function of the system. To simplify representation and analysis, the phase and modulation-derived lifetimes ($\tau_P$ and $\tau_M$ respectively) were averaged to produce a single lifetime value.

### 2.9. Single Virus Tracing and Analysis

Raw data was processed by FIJI [24] with a 1-pixel median filter and a 50-pixel rolling ball background subtraction prior to analysis. Particle detection and tracking was performed using Imaris' Spot detection module (Bitplane AG, Zurich, Switzerland). Within this process, the background was not subtracted and the estimated diameter for spot detection was set to 360 nm. The quality parameter for spot detection was set to 1. Tracking was performed using the Autoregressive Motion algorithm, assuming a maximum distance between frames of 60 nm, allowing for a maximum gap size of 1 and a track duration above 600 s. Filling gaps was disabled. Positions of each detected particle over time were exported to Excel. Exported particle coordinates were subsequently imported into the PAM software to generate image subregions containing each particle, from which the particle-wise phasor values and lifetimes could be extracted.

Mean assembly kinetics were calculated from a selected subset of particle traces. For each trace, the starting point of assembly was manually identified from the intensity increase and fitted with a saturating exponential function. Tracks that can be satisfactorily fitted were selected and synchronized at the starting point of assembly. To obtain the mean assembly kinetics, the mean intensity and lifetime at each frame were calculated and again fitted with the saturating exponential function,

$$y = (A_{max} - A_0)[1 - \exp(-kt)] + A_0, \tag{1}$$

where $A_{max}$ is the maximum fluorescence intensity, $A_0$ is the initial fluorescence intensity, $k$ is the rate of fluorescence increase and $t$ is the amount of time that has passed since the start of assembly.

## 3. Results

We first set out to show that the fluorescence lifetime of eCFP can be used to monitor the status of the Gag lattice. For this, we used virus variants carrying an eCFP moiety inserted between the MA and CA domains of Gag. HIV-1 derivatives carrying a fluorophore at this position have been employed previously to track assembly of viral budding sites at the plasma membrane [25]. In HIV$^{\mathrm{eCFP}}$ [17], the fluorophore is flanked by a single PR cleavage site (amino acid sequence SQNY↓PIV) at its C-terminus, so that the label will remain attached to the lipid envelope bound MA domain in the mature form of the virus. HIV$^{\mathrm{ieCFP}}$ comprises a duplication of this processing site at the N-terminus of eCFP, allowing for release of the free fluorophore upon processing. In both cases, proteolytic processing would result in a change of the environment of the fluorophore from its packed arrangement within the immature shell. Since mature MA remains associated with the viral membrane and was recently observed to retain a modified lattice arrangement [26], the change in the local microenvironment of eCFP is expected to be less pronounced for HIV$^{eCFP}$ compared to HIV$^{ieCFP}$, where the released fluorophore would be able to distribute within the particle volume (Figure 1A). To maintain wild-type assembly properties, eCFP-tagged HIV-1 plasmids were co-transfected with their untagged counterpart (pCHIV) in an equimolar ratio [27]. To determine the effect of virion maturation on the fluorescence lifetime of the particle associated fluorophore, we produced eCFP-labeled viral particles in the presence or absence of the PI lopinavir (LPV). Mature and immature VLPs were purified from the supernatant of transfected HEK293T cells and analyzed by immunoblot with antisera raised against GFP and CA to confirm the inhibition of Gag.eCFP processing by LPV (Figure S1).

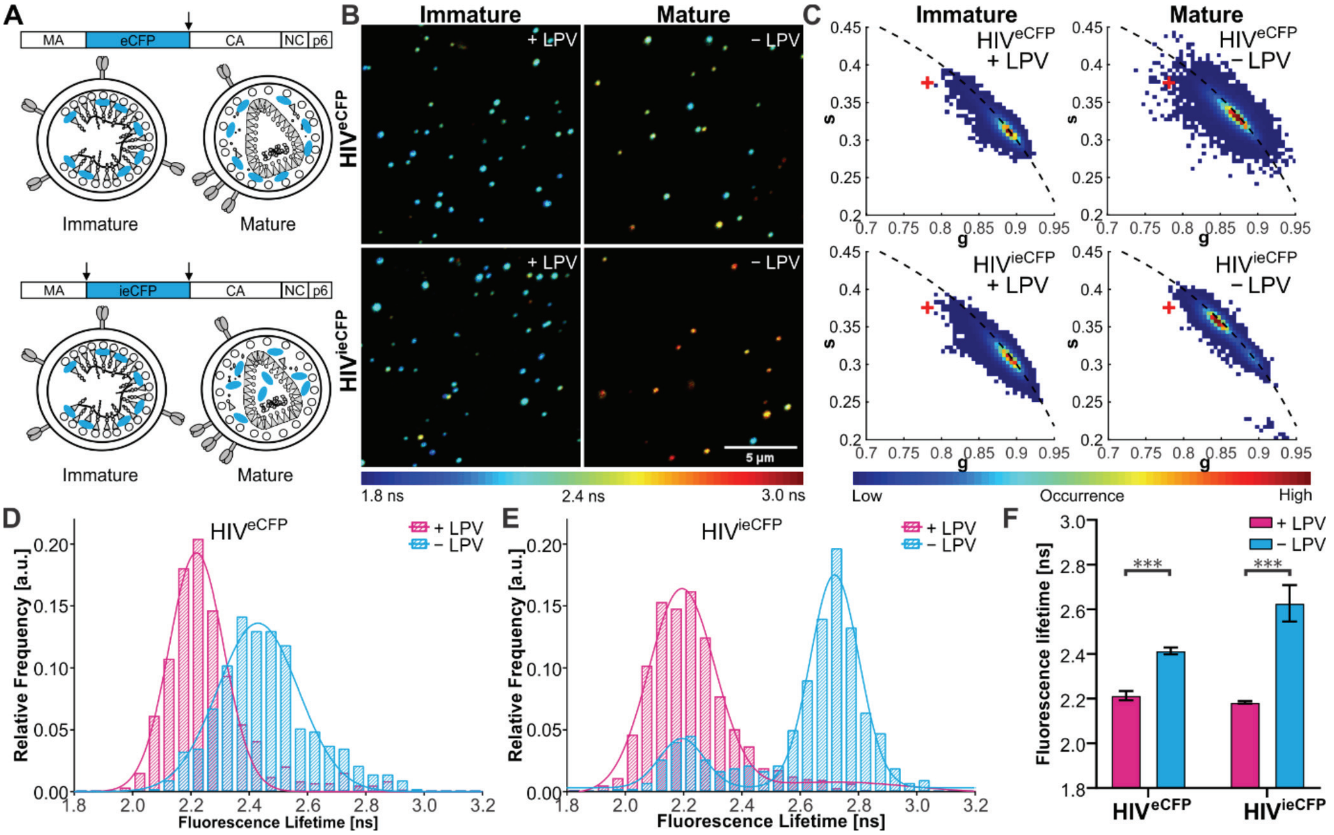

**Figure 1.** Fluorescence lifetime of eCFP in purified VLPs. (**A**) Scheme of the HIV-1 Gag polyprotein, with eCFP inserted between the MA and CA domains and flanked by one (eCFP, top) or two (ieCFP, bottom) PR cleavage sites. Arrows indicate PR cleavage sites flanking the eCFP domain. Schematic drawing of immature and mature HIV$^{eCFP}$ and HIV$^{ieCFP}$ particles. (**B**) Fluorescence lifetime images and (**C**) phasor plots of immature and mature HIV$^{eCFP}$ or HIV$^{ieCFP}$ particles. A '+' indicates the lifetime of free ECFP measured on the same setup. VLPs were produced in transfected HEK293T cells grown in the presence (immature) or absence (mature) of 2 µM LPV as described in materials and methods and Text S1. Particles were adhered to borosilicate coverslips and imaged by CLSM with TCSPC. Measurements were conducted at 23 °C. The lifetime determined for individual VLPs is represented according to the indicated color scale. Scale bar 5 µm. (**D**,**E**) Histograms of fluorescence lifetimes of the immature (*cyan*) and mature (*magenta*) particle populations extracted from the phasor analysis. Lines show the fit of the lifetime distributions to the sum of two Gaussians. $n = 500$ particles each. (**F**) Mean and SD of fluorescent lifetime distribution peak from three independent experiments. Statistical analysis was performed using a Welch's *t*-test (***: $p < 0.001$).

Particle preparations were then analyzed by FLIM at room temperature using a home-built CLSM (described elsewhere) [20] (Figure 1B) and fluorescence lifetimes were extracted from the TCSPC photon data using the phasor approach [22,23]. An averaged fluorescence lifetime was calculated for each particle. Two distinct populations were observed based on the eCFP fluorescence lifetime, which we assigned to the mature and immature populations (Figure 1C–E). Immature particles showed comparable eCFP fluorescence lifetimes for both virus derivatives (2.21 (±0.02) ns for $\text{HIV}^{\text{eCFP}}$ and 2.18 (±0.01) ns for $\text{HIV}^{\text{ieCFP}}$). Mature $\text{HIV}^{\text{ieCFP}}$ particles in which the eCFP moiety should be completely released from Gag showed an average increase of 0.45 ns to 2.63 (±0.07) ns compared to immature particles. For the $\text{HIV}^{\text{eCFP}}$ variant, where the eCFP moiety remains associated with the MA layer, the difference between immature and mature particles was smaller (0.20 ns), with an average lifetime of 2.43 (±0.01) ns for mature particles (Figure 1F). The lifetime of eCFP in the $\text{HIV}^{\text{ieCFP}}$ particles is still lower than that of free eCFP (3.34 ns, Figure 1C), suggesting that the lifetime of eCFP is sensitive to the high density of protein within the mature virus (based on an average number of 2400 Gag molecules per virion [28], the estimated concentration of eCFP is in the range of ~0.5 mM for an equimolar ratio of Gag and Gag.eCFP).

We also repeated the FLIM experiments on $\text{HIV}^{\text{ieCFP}}$ VLPs produced in cells transfected with different ratios of $\text{pCHIV}^{\text{ieCFP}}$ to pCHIV DNA. When the protein density of eCFP within the VLPs was changed by altering the ratio of Gag.ieCFP to unlabeled Gag, we observed a corresponding change the fluorescence lifetime (Figure S2). The mean ratio of labeled to unlabeled Gag protein in VLPs was assessed by immunoblot (Figure S2A,B). Mean eCFP lifetimes of the major VLP population determined for immature $\text{HIV}^{\text{eCFP}}$ and $\text{HIV}^{\text{ieCFP}}$, as well as mature $\text{HIV}^{\text{ieCFP}}$ increased with decreasing proportions of Gag.ieCFP:Gag (Figure S2C,D). Therefore, in addition to the Gag processing state, eCFP lifetime is sensitive to the eCFP molecule density within the particles.

To establish the suitability of $\text{HIV}^{\text{ieCFP}}$ as a detection system for Gag processing in situ, we characterized the effect of temperature on the fluorescence lifetime of eCFP. We measured a set of $\text{HIV}^{\text{eCFP}}$ and $\text{HIV}^{\text{ieCFP}}$ particles at two different temperatures, 23 °C and 37 °C (Figure S3). The fluorescence lifetime of eCFP showed a general decrease when the temperature was increased from 23 °C (Figure S3A,B) to 37 °C (Figure S3C,D), with the effect being greater for mature particles ($\Delta\tau \approx -0.3$ ns) than for immature ones ($\Delta\tau \approx -0.2$ ns). Nevertheless, the mature and immature populations could still be clearly distinguished for $\text{HIV}^{\text{ieCFP}}$ particles at 37 °C (Figure S3D). We also measured the fluorescence lifetime of eCFP alone and attached to MA in the cytosol of live cells at 37 °C (Figure S4). The lifetime of MA-eCFP (2.51 ± 0.04 ns) was lower than that of eCFP (2.70 ± 0.13 ns), suggesting an influence of the matrix domain on the lifetime of eCFP.

We now focus on the $\text{HIV}^{\text{ieCFP}}$ variant for live-cell imaging experiments as it provides higher contrast in the lifetime changes between immature and mature virions. FLIM of nascent $\text{HIV}^{\text{ieCFP}}$ particles was conducted in HeLa Kyoto cells transfected with an equimolar mixture of $\text{pCHIV/pCHIV}^{\text{ieCFP}}$ (Figure 2A). The coexpression of labeled and non-labeled Gag was confirmed by immunoblot (Figure S5). We first determined the fluorescence lifetime of the particle assemblies at the ventral plasma membrane. The distribution of lifetimes of membrane localized assemblies in cells grown in the absence of LPV was not notably different from the LPV+ condition (Figure 2B,C). In contrast, cell-free particles observed in the vicinity of the producing cells did display the difference in average lifetime as expected for immature vs. mature VLPs (Figure 2D–F). This observation suggests that maturation occurs relatively late in the assembly process such that potential signals corresponding to maturing VLPs at the plasma membrane is obscured by the immature background of nascent or newly assembled VLPs in these still images.

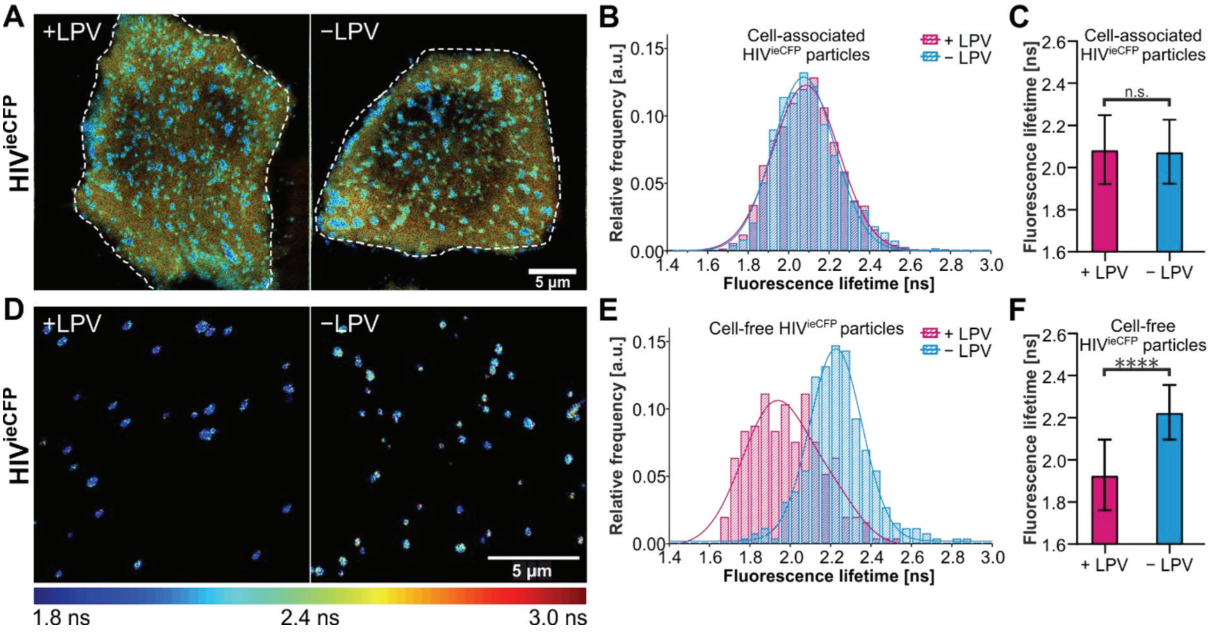

**Figure 2.** Measurements of the fluorescence lifetime of eCFP in HeLa Kyoto cells. HeLa Kyoto cells were transfected with an equimolar mixture of pCHIV/pCHIV$^{\mathrm{ieCFP}}$ and grown in the presence or absence of 2 µM LPV. Cells were imaged 24 hpt at 37 °C by CSLM. (**A**) Fluorescence lifetime images of assembly sites and trapped particles of HIV$^{\mathrm{ieCFP}}$ in cells measured in the absence or presence of LPV. (**B**) Histogram of fluorescence lifetime of trapped or cell-associated HIV$^{\mathrm{ieCFP}}$ particles and a fit to a single Gaussian distribution (solid lines). $n = 3196$ particles from 7 cells treated with LPV and $n = 2999$ particles from 9 non-treated cells. (**C**) Mean and SD of the fitted Gaussian functions in (**D**). (**D**) Fluorescence lifetime images of released HIV$^{\mathrm{ieCFP}}$ particles detected adjacent to transfected cells (cell-free particles). (**E**) Histogram of fluorescence lifetime of cell-free HIV$^{\mathrm{ieCFP}}$ particles and a fit to a sum of two Gaussians (solid lines). $n = 250$ particles each from LPV-treated and non-treated cells. (**F**) Mean and SD of the fitted Gaussian functions in (E). The peak of the major species was used. The fluorescence lifetime images are colored according to the 'jet' colormap with a range of 1.8 ns–3.0 ns. Scale bars 5 µm. Statistical analysis was performed using a Welch's *t*-test (n.s.: non-significant, $p > 0.05$; ****: $p < 0.0001$).

We proceeded to apply single virus tracing (SVT) to follow the assembly of individual VLPs at the plasma membrane (Figure 3A). The combination of SVT with FLIM allowed us to monitor both the fluorescence intensity and lifetime of individual nascent virus buds during assembly of HIV$^{\mathrm{ieCFP}}$ in Hela Kyoto cells. From a set of 489 traces with a minimum length of 60 frames (corresponding to 10 min), 354 traces showed an increase in fluorescence intensity over time, as expected for nascent assembly sites [11]. As the number of eCFP incorporated in a VLP increases, we anticipate a decrease in the fluorescence lifetime as observed for immature particles. Indeed, 170 out of the 354 traces displayed a decrease in fluorescence lifetime within the time window of observation.

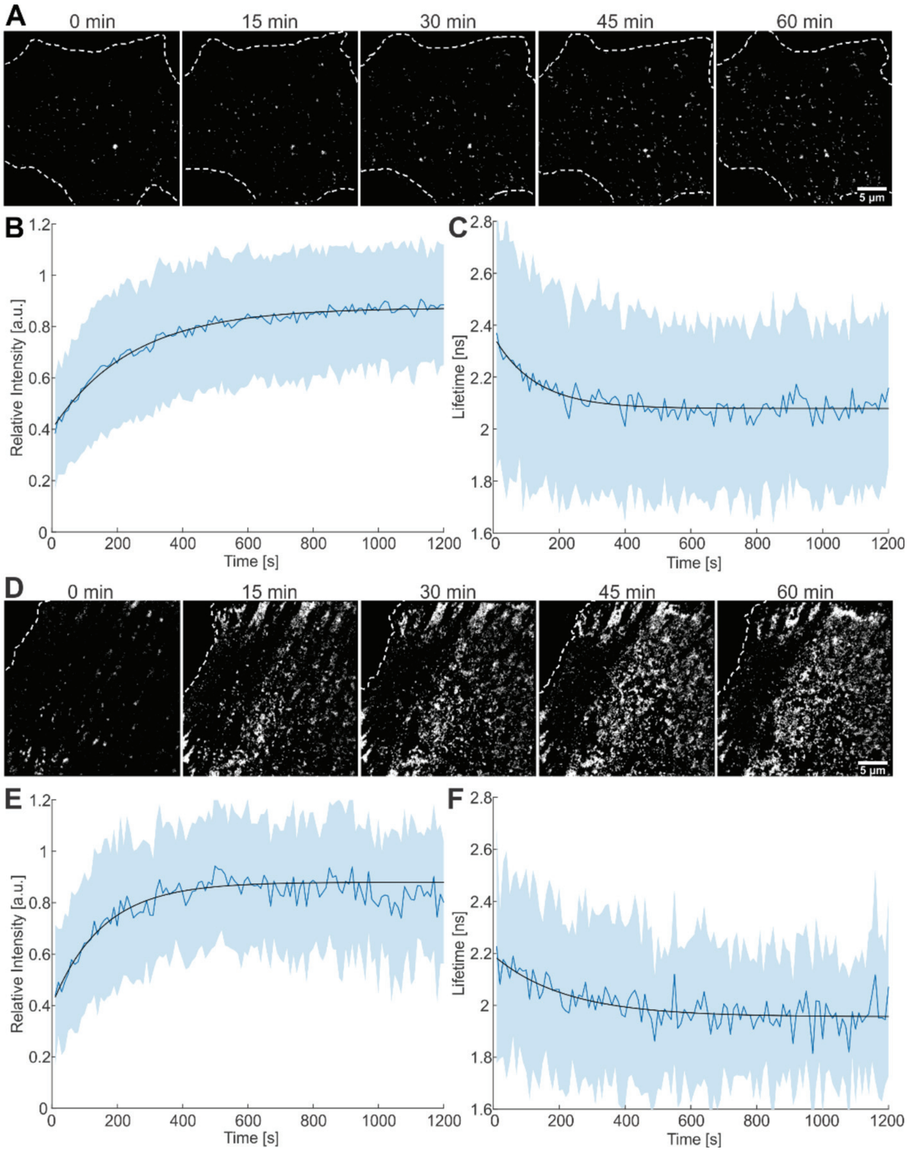

**Figure 3.** Live-cell imaging of the assembly process at the plasma membrane of HeLa Kyoto cells. (**A**) Time lapse images of Gag-ieCFP assembly recorded at the plasma membrane of a transfected HeLa Kyoto cell grown in the absence of LPV recorded at the indicated times after onset of microscopic observation. Plots of (**B**) fluorescence intensity and (**C**) fluorescence lifetime measured at individual assembly sites as detected in (**A**). Mean values and SD are shown ($n$ = 170 sites from 4 cells); black lines represent fits to single exponential equations. (**D**) Time lapse images recorded at the plasma membrane of a transfected HeLa Kyoto cell grown in the presence of 2 µM LPV. Plot of (**E**) fluorescence intensity and (**F**) fluorescence lifetime measured at individual assembly sites as detected in (**D**). Mean values and SD are shown ($n$ = 51 sites from 2 cells); black lines represent fits to single exponential equations. HeLa Kyoto cells were co-transfected with equimolar amounts of pCHIV wt and pCHIV$^{\text{ieCFP}}$ and imaged at 16 hpt. Cells were imaged every 5 s for 1–2 h. Scale bars: 5 µm.

For analysis, we averaged fluorescence intensities as well as fluorescence lifetimes from these 170 traces upon alignment to the onset of intensity increase and fitted the average intensity and lifetime with a saturating exponential function. The rate of assembly, determined from fitting the plot of the average intensity versus time, was 4.1 (±0.3) × $10^{-3}$ $s^{-1}$, yielding a half time, $\tau_{1/2}$, of 169 s (Figure 3B). The average lifetime decreased with a rate of 7.9 (±1.9) × $10^{-3}$ $s^{-1}$ ($\tau_{1/2}$ = 88 s, Figure 3C), i.e., similar to the rate extracted from the average intensity. The same analysis procedure was applied to 105 traces from $HIV^{ieCFP}$ expressing cells grown in the presence of LPV during transfection and imaging (Figure 3D). Of these, 86 traces showed an intensity increase indicative of assembly. Out of the 86 traces, 51 also showed a concomitant decrease in fluorescence lifetime. The rate of assembly determined by fitting the average intensity of the 51 traces for fluorescence intensity was 6.5 (±2.2) × $10^{-3}$ $s^{-1}$ ($\tau_{1/2}$ = 106 s, Figure 3E); fluorescence lifetime decreased with a similar rate of 4.6 (±3.6) × $10^{-3}$ $s^{-1}$ ($\tau_{1/2}$ = 151 s, Figure 3F). The assembly kinetics as measured here by CLSM are consistent with previously reported values recorded using other microscopy techniques [11,29,30].

The remaining traces, which showed only an increase in intensity but not a concomitant decrease in lifetime, were analyzed in a similar way. The intensity-derived rate of assembly was 5.7 (±0.6) × $10^{-3}$ $s^{-1}$ for the 184 traces from cells grown in the absence of LPV, and 10.1 (±3.1) × $10^{-3}$ $s^{-1}$ for the 35 traces from cells grown in the presence of LPV (Figure S6). The mean lifetimes of the traces were 2.1 ns and 2.0 ns respectively. These are comparable to the lifetimes of cell-associated particles (Figure 2A–C), suggesting that the lifetime change was complete before these particles were detected.

Based on our comparison of immature and mature VLPs described above, we proposed that Gag processing and conformation changes in the virion by PR should lead to an increase in fluorescence lifetime in individual particles. Among the 170 traces used for the analysis of assembly kinetics in cells grown in the absence of LPV, 11 traces (6.5%) showed an increase of ~0.4 ns after assembly was complete. This change was similar to the mean shift of lifetime between mature and immature $HIV^{ieCFP}$ virions observed in purified VLPs. An exemplary trace is shown in Figure 4A and in Movie S1 (with additional examples shown in Figure S7). In contrast, no such increase in fluorescence lifetime after assembly was observed for traces from cells grown in the presence of LPV ($n$ = 51). The same held true when we ignored assembly and looked at the full set of 105 LPV+ traces. (Table S1). To exclude the possibility that the small number of LPV+ traces caused us to miss potential fluorescence lifetime increase events, we analyzed more cells grown in the presence of LPV. In addition, we applied a newly developed wavelet tracking algorithm [31,32] to generate a large number of traces. Even with the ~1700 traces analyzed using this new approach, we did not observe any traces that showed a lifetime change indicative of Gag in the presence of LPV, while 46 out of 1992 (2.3%) of the traces recorded in the absence of LPV displayed the characteristic increase in fluorescence lifetime (Table S2).

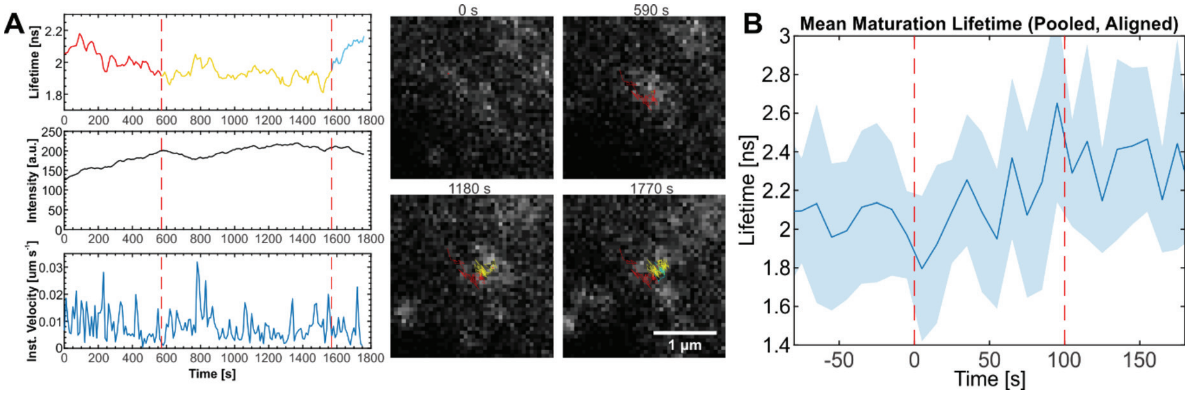

**Figure 4.** Particles showing eCFP lifetime changes indicative of maturation. (**A**) Lifetime, intensity, and velocity plots of an individual particle showing lifetime changes indicative of maturation following assembly. The lifetime plot is colored by the identifiable state of particle (red: assembly, yellow: plateau phase, blue: maturation). Still images from the movie analyzed for this graph recorded at the indicated times are shown. See Movie S1. (**B**) Mean and SD of fluorescence lifetime of maturing particles in pCHIV/pCHIV$^{\text{ieCFP}}$ (1:1) transfected HeLa Kyoto cells. The lifetime of each particle was aligned at the start point of maturation (Time = 0 s) for each trace before averaging. Dotted lines indicate the apparent time range over which the lifetime change occurs. $n$ = 11 traces from 4 cells. Scale bar: 1 µm.

To estimate the timescale of Gag processing, we analyzed the lifetime signal of the 11 traces identified above where the assembly process was observable. The starting points of the lifetime increase were aligned, and the average lifetime plotted at each time point. On average, the increase in lifetime indicative of Gag processing occurred over a period of ~100 s in an approximately sigmoidal fashion (Figure 4B). We note that the kinetics of Gag cleavage most likely depends on the sequence and surrounding context of the cleavage site.

The mean delay between the start of assembly and maturation as detected by FLIM was 837 (±542) s. However, it is likely that for the majority of VLPs Gag processing is further delayed with respect to viral assembly. The lifetime measurements on VLPs isolated from the tissue culture supernatant (Figure 1E) and recently released VLPs detected in the vicinity of particle producing cells (Figure 2D–F) indicated that the vast majority of VLPs produced eventually underwent Gag processing under the conditions of our experiments. Nevertheless, a distinct shift in lifetime indicative of processing was observed only for a minority of nascent assembly traces during the observation period in the live measurements. Based on this, we can infer that for most VLPs, Gag processing is delayed with respect to viral assembly and occurred beyond the period of observation in our SVT experiments.

## 4. Discussion

We have thus successfully generated and established a system to follow Gag processing in the relation to particle assembly in a live-cell environment. Our results show that the assembly and proteolytic maturation of HIV-1 VLPs induce changes in the fluorescence lifetime of eCFP when it is integrated as part of the Gag lattice. During assembly, the fluorescence lifetime of eCFP decreased concomitantly with the increase in fluorescence intensity, corresponding to an increase in the packing density of eCFP as more and more Gag molecules are recruited to the assembly site. We were also able to detect an increase in lifetime when viral particles transitioned from the immature to the mature state in live-cell SVT experiments. The magnitude of the lifetime change corresponded well with the lifetime difference of 0.4–0.5 ns between immature and mature HIV-1 VLPs measured in vitro.

In our SVT experiments, a small portion of assembly traces (6.5%) showed lifetime changes that indicate maturation, whereas imaging of virions in the vicinity of virus producing cells indicates that the vast majority of virions would eventually mature under our measurement conditions. This is consistent with many EM studies where mature HIV VLPs are observed near the plasma membrane or even in synapses [33–35]. The low proportion of maturation associated lifetime changes observed in the SVT experiments suggests that Gag processing primarily occurs after release of the viral particles, which was observed to occur 20–45 min after the onset of assembly in similar experimental setups [11,25]. Due to a combination of several factors such as photobleaching, viral particles moving into regions with dense particle concentrations (Figure 2A) and increased particle mobility following release [11], the tracking algorithm loses the majority of individually tracked particles before or shortly after release. Hence, only the particles that rapidly undergo Gag processing will be detected. The average delay between the onset of assembly and Gag processing for these traces (837 s or 14 min) is biased towards short time scales. However, the low fraction of traces showing maturation suggests that the actual average delay between assembly and maturation is longer.

The increase of lifetime ascribed to proteolytic eCFP release was observed to occur in a relatively short timeframe (~100 s). This is considerably faster than processing kinetics analyzed previously using in vitro systems or purified VLPs [5,8–10,36]. However, these measurements employed recombinant Gag or cell free particles, and the readout was completion of the final processing event within Gag (processing at the CA-Sp1 processing site) in the bulk population. In contrast, the proteolytic release of eCFP from Gag monitored here represents a single step in a complex processing cascade and the subsequent redistribution of the marker protein, representing only a part of the overall process.

In summary, we show that the fluorescence lifetime of eCFP can be used in conjunction with SVT to detect viral polyprotein processing in real-time in situ in an asynchronous virus population. As fluorescence imaging and SVT techniques continue to develop, we believe our approach has the potential for further applications in studying the kinetics of viral protease cascades.

**Supplementary Materials:** The following supporting information can be downloaded at: https://www.mdpi.com/article/10.3390/v14020340/s1, Text S1: Description of the phasor approach to analyzing FLIM data. Figure S1: Analysis of the processing status of Gag.eCFP and Gag.ieCFP by immunoblot; Figure S2: Effect of ratio of wild-type to eCFP-labelled Gag on eCFP fluorescence lifetime in VLPs; Figure S3: Effect of temperature on eCFP fluorescence lifetime in VLPs; Figure S4: Effect of the matrix domain on the fluorescence lifetime of eCFP. Figure S5: Coexpression of Gag and Gag.ieCFP in HeLa Kyoto cells verified by immunoblot. Figure S6: Mean intensity and lifetime of assembly traces that did not show a lifetime decrease corresponding to the intensity increase; Figure S7: Additional examples of particles showing eCFP lifetime changes indicative of maturation; Table S1: Summary of particle traces used for analysis; Table S2: Additional single virus tracing analysis using wavelet tracking method; Movie S1: Movie of maturing VLP shown in Figure 4A; Movies S2–S4: Movies of maturing VLPs shown in Figure S7.

**Author Contributions:** Conceptualization, B.M. and D.C.L.; Data curation, C.Q.; Funding acquisition, D.C.L.; Investigation, C.Q. and A.F.; Methodology, C.Q., A.F., B.M. and D.C.L.; Supervision, B.M. and D.C.L.; Visualization, C.Q. and A.F.; Writing—original draft, C.Q. and A.F.; Writing—review & editing, C.Q., Barbara Müller and D.C.L. All authors have read and agreed to the published version of the manuscript.

**Funding:** This research was funded by Deutsche Forschungsgemeinschaft (DFG, German Research Foundation)—Project-ID 201269156—SFB 1032 Project B03 as well as the LMU via the Center for NanoScience (CeNS) and the BioImaging Network (BIN).

**Institutional Review Board Statement:** Not applicable.

**Informed Consent Statement:** Not applicable.

**Data Availability Statement:** FLIM and SVT data have been deposited in Zenodo (DOI: 10.5281/zenodo.5564327). The PAM software package is available from https://gitlab.com/PAM-PIE/PAM, accessed on 7 January 2022.

**Acknowledgments:** We thank Philipp Messer for implementation of the wavelet tracking method in the PAM software package.

**Conflicts of Interest:** The authors declare no conflict of interest.

## References

1. Murray, P.S.; Li, Z.; Wang, J.; Tang, C.L.; Honig, B.; Murray, D. Retroviral matrix domains share electrostatic homology: Models for membrane binding function throughout the viral life cycle. *Structure* **2005**, *13*, 1521–1531. [CrossRef]
2. Gamble, T.R.; Yoo, S.; Vajdos, F.F.; von Schwedler, U.K.; Worthylake, D.K.; Wang, H.; McCutcheon, J.P.; Sundquist, W.I.; Hill, C.P. Structure of the carboxyl-terminal dimerization domain of the HIV-1 capsid protein. *Science* **1997**, *278*, 849–853. [CrossRef]
3. Muriaux, D.; Darlix, J.L. Properties and functions of the nucleocapsid protein in virus assembly. *RNA Biol.* **2010**, *7*, 744–753. [CrossRef]
4. Sundquist, W.I.; Krausslich, H.G. HIV-1 assembly, budding, and maturation. *Cold Spring Harb. Perspect. Med.* **2012**, *2*, a006924. [CrossRef]
5. Pettit, S.C.; Moody, M.D.; Wehbie, R.S.; Kaplan, A.H.; Nantermet, P.V.; Klein, C.A.; Swanstrom, R. The p2 domain of human immunodeficiency virus type 1 Gag regulates sequential proteolytic processing and is required to produce fully infectious virions. *J. Virol.* **1994**, *68*, 8017–8027. [CrossRef] [PubMed]
6. Erickson-Viitanen, S.; Manfredi, J.; Viitanen, P.; Tribe, D.E.; Tritch, R.; Hutchison, C.A., 3rd; Loeb, D.D.; Swanstrom, R. Cleavage of HIV-1 gag polyprotein synthesized in vitro: Sequential cleavage by the viral protease. *AIDS Res. Hum. Retrovir.* **1989**, *5*, 577–591. [CrossRef] [PubMed]
7. Tozser, J.; Blaha, I.; Copeland, T.D.; Wondrak, E.M.; Oroszlan, S. Comparison of the HIV-1 and HIV-2 proteinases using oligopeptide substrates representing cleavage sites in Gag and Gag-Pol polyproteins. *FEBS Lett.* **1991**, *281*, 77–80. [CrossRef]
8. Hanne, J.; Gottfert, F.; Schimer, J.; Anders-Osswein, M.; Konvalinka, J.; Engelhardt, J.; Muller, B.; Hell, S.W.; Krausslich, H.G. Stimulated Emission Depletion Nanoscopy Reveals Time-Course of Human Immunodeficiency Virus Proteolytic Maturation. *ACS Nano* **2016**, *10*, 8215–8222. [CrossRef] [PubMed]
9. Mattei, S.; Anders, M.; Konvalinka, J.; Krausslich, H.G.; Briggs, J.A.; Muller, B. Induced maturation of human immunodeficiency virus. *J. Virol.* **2014**, *88*, 13722–13731. [CrossRef]
10. Schimer, J.; Pavova, M.; Anders, M.; Pachl, P.; Sacha, P.; Cigler, P.; Weber, J.; Majer, P.; Rezacova, P.; Krausslich, H.G.; et al. Triggering HIV polyprotein processing by light using rapid photodegradation of a tight-binding protease inhibitor. *Nat. Commun.* **2015**, *6*, 6461. [CrossRef]
11. Ivanchenko, S.; Godinez, W.J.; Lampe, M.; Krausslich, H.G.; Eils, R.; Rohr, K.; Brauchle, C.; Muller, B.; Lamb, D.C. Dynamics of HIV-1 assembly and release. *PLoS Pathog.* **2009**, *5*, e1000652. [CrossRef] [PubMed]
12. Grailhe, R.; Merola, F.; Ridard, J.; Couvignou, S.; Le Poupon, C.; Changeux, J.P.; Laguitton-Pasquier, H. Monitoring protein interactions in the living cell through the fluorescence decays of the cyan fluorescent protein. *ChemPhysChem* **2006**, *7*, 1442–1454. [CrossRef]
13. Kelly, D.J.; Warren, S.C.; Alibhai, D.; Kumar, S.; Alexandrov, Y.; Munro, I.; Margineanu, A.; McCormack, J.; Welsh, N.J.; Serwa, R.A.; et al. Automated multiwell fluorescence lifetime imaging for Förster resonance energy transfer assays and high content analysis. *Anal. Methods* **2015**, *7*, 4071–4089. [CrossRef]
14. Rizzo, M.A.; Springer, G.H.; Granada, B.; Piston, D.W. An improved cyan fluorescent protein variant useful for FRET. *Nat. Biotechnol.* **2004**, *22*, 445–449. [CrossRef] [PubMed]
15. Koushik, S.; Vogel, S. Energy migration alters the fluorescence lifetime of Cerulean: Implications for fluorescence lifetime imaging Forster resonance energy transfer measurements. *J. Biomed. Opt.* **2008**, *13*, 031204. [CrossRef] [PubMed]
16. Lampe, M.; Briggs, J.A.; Endress, T.; Glass, B.; Riegelsberger, S.; Krausslich, H.G.; Lamb, D.C.; Brauchle, C.; Muller, B. Double-labelled HIV-1 particles for study of virus-cell interaction. *Virology* **2007**, *360*, 92–104. [CrossRef]
17. Muller, B.; Anders, M.; Reinstein, J. In vitro analysis of human immunodeficiency virus particle dissociation: Gag proteolytic processing influences dissociation kinetics. *PLoS ONE* **2014**, *9*, e99504. [CrossRef]
18. Eckhardt, M.; Anders, M.; Muranyi, W.; Heilemann, M.; Krijnse-Locker, J.; Muller, B. A SNAP-tagged derivative of HIV-1–a versatile tool to study virus-cell interactions. *PLoS ONE* **2011**, *6*, e22007. [CrossRef]
19. Mucksch, F.; Laketa, V.; Muller, B.; Schultz, C.; Krausslich, H.G. Synchronized HIV assembly by tunable PIP2 changes reveals PIP2 requirement for stable Gag anchoring. *Elife* **2017**, *6*, e25287. [CrossRef]
20. Hendrix, J.; Schrimpf, W.; Holler, M.; Lamb, D.C. Pulsed interleaved excitation fluctuation imaging. *Biophys. J.* **2013**, *105*, 848–861. [CrossRef]
21. Schrimpf, W.; Barth, A.; Hendrix, J.; Lamb, D.C. PAM: A Framework for Integrated Analysis of Imaging, Single-Molecule, and Ensemble Fluorescence Data. *Biophys. J.* **2018**, *114*, 1518–1528. [CrossRef] [PubMed]
22. Digman, M.A.; Caiolfa, V.R.; Zamai, M.; Gratton, E. The phasor approach to fluorescence lifetime imaging analysis. *Biophys. J.* **2008**, *94*, L14–L16. [CrossRef] [PubMed]

23. Ranjit, S.; Malacrida, L.; Jameson, D.M.; Gratton, E. Fit-free analysis of fluorescence lifetime imaging data using the phasor approach. *Nat. Protoc.* **2018**, *13*, 1979–2004. [CrossRef] [PubMed]
24. Schindelin, J.; Arganda-Carreras, I.; Frise, E.; Kaynig, V.; Longair, M.; Pietzsch, T.; Preibisch, S.; Rueden, C.; Saalfeld, S.; Schmid, B.; et al. Fiji: An open-source platform for biological-image analysis. *Nat. Methods* **2012**, *9*, 676–682. [CrossRef]
25. Baumgartel, V.; Ivanchenko, S.; Dupont, A.; Sergeev, M.; Wiseman, P.W.; Krausslich, H.G.; Brauchle, C.; Muller, B.; Lamb, D.C. Live-cell visualization of dynamics of HIV budding site interactions with an ESCRT component. *Nat. Cell Biol.* **2011**, *13*, 469–474. [CrossRef]
26. Qu, K.; Ke, Z.; Zila, V.; Anders-Osswein, M.; Glass, B.; Mucksch, F.; Muller, R.; Schultz, C.; Muller, B.; Krausslich, H.G.; et al. Maturation of the matrix and viral membrane of HIV-1. *Science* **2021**, *373*, 700–704. [CrossRef]
27. Muller, B.; Daecke, J.; Fackler, O.T.; Dittmar, M.T.; Zentgraf, H.; Krausslich, H.G. Construction and characterization of a fluorescently labeled infectious human immunodeficiency virus type 1 derivative. *J. Virol.* **2004**, *78*, 10803–10813. [CrossRef]
28. Carlson, L.A.; Briggs, J.A.; Glass, B.; Riches, J.D.; Simon, M.N.; Johnson, M.C.; Muller, B.; Grunewald, K.; Krausslich, H.G. Three-dimensional analysis of budding sites and released virus suggests a revised model for HIV-1 morphogenesis. *Cell Host Microbe* **2008**, *4*, 592–599. [CrossRef]
29. Rahman, S.A.; Koch, P.; Weichsel, J.; Godinez, W.J.; Schwarz, U.; Rohr, K.; Lamb, D.C.; Krausslich, H.G.; Muller, B. Investigating the role of F-actin in human immunodeficiency virus assembly by live-cell microscopy. *J. Virol.* **2014**, *88*, 7904–7914. [CrossRef]
30. Jouvenet, N.; Bieniasz, P.D.; Simon, S.M. Imaging the biogenesis of individual HIV-1 virions in live cells. *Nature* **2008**, *454*, 236–240. [CrossRef]
31. Messer, P.K.; Henß, A.-K.; Lamb, D.C.; Wintterlin, J. A Multiscale Wavelet Algorithm for Atom Tracking in STM Movies. *New J. Phys.* 2022; *in press*.
32. Olivo-Marin, J.C. Extraction of spots in biological images using multiscale products. *Pattern Recognit.* **2002**, *35*, 1989–1996. [CrossRef]
33. Jolly, C.; Kashefi, K.; Hollinshead, M.; Sattentau, Q.J. HIV-1 cell to cell transfer across an Env-induced, actin-dependent synapse. *J. Exp. Med.* **2004**, *199*, 283–293. [CrossRef] [PubMed]
34. Do, T.; Murphy, G.; Earl, L.A.; Del Prete, G.Q.; Grandinetti, G.; Li, G.H.; Estes, J.D.; Rao, P.; Trubey, C.M.; Thomas, J.; et al. Three-dimensional imaging of HIV-1 virological synapses reveals membrane architectures involved in virus transmission. *J. Virol.* **2014**, *88*, 10327–10339. [CrossRef] [PubMed]
35. Rudnicka, D.; Feldmann, J.; Porrot, F.; Wietgrefe, S.; Guadagnini, S.; Prevost, M.C.; Estaquier, J.; Haase, A.T.; Sol-Foulon, N.; Schwartz, O. Simultaneous cell-to-cell transmission of human immunodeficiency virus to multiple targets through polysynapses. *J. Virol.* **2009**, *83*, 6234–6246. [CrossRef]
36. Konnyu, B.; Sadiq, S.K.; Turanyi, T.; Hirmondo, R.; Muller, B.; Krausslich, H.G.; Coveney, P.V.; Muller, V. Gag-Pol processing during HIV-1 virion maturation: A systems biology approach. *PLoS Comput. Biol.* **2013**, *9*, e1003103. [CrossRef]

# Appendix II

## QuanTI-FRET: a framework for quantitative FRET measurements in living cells

Reprinted from *Sci Rep* **10**, 6504 (2020) in accordance with the Creative Commons Attribution 4.0 International License.

www.nature.com/scientificreports

SCIENTIFIC REPORTS

natureresearch

OPEN

# QuanTI-FRET: a framework for quantitative FRET measurements in living cells

**Alexis Coullomb[1], Cécile M. Bidan[1], Chen Qian[2], Fabian Wehnekamp[2], Christiane Oddou[3], Corinne Albigès-Rizo[3], Don. C. Lamb[2] & Aurélie Dupont[1]***

**Förster Resonance Energy Transfer (FRET) allows for the visualization of nanometer-scale distances and distance changes. This sensitivity is regularly achieved in single-molecule experiments *in vitro* but is still challenging in biological materials. Despite many efforts, quantitative FRET in living samples is either restricted to specific instruments or limited by the complexity of the required analysis. With the recent development and expanding utilization of FRET-based biosensors, it becomes essential to allow biologists to produce quantitative results that can directly be compared. Here, we present a new calibration and analysis method allowing for quantitative FRET imaging in living cells with a simple fluorescence microscope. Aside from the spectral crosstalk corrections, two additional correction factors were defined from photophysical equations, describing the relative differences in excitation and detection efficiencies. The calibration is achieved in a single step, which renders the Quantitative Three-Image FRET (QuanTI-FRET) method extremely robust. The only requirement is a sample of known stoichiometry donor:acceptor, which is naturally the case for intramolecular FRET constructs. We show that QuanTI-FRET gives absolute FRET values, independent of the instrument or the expression level. Through the calculation of the stoichiometry, we assess the quality of the data thus making QuanTI-FRET usable confidently by non-specialists.**

The theory behind Förster Resonance Energy Transfer (FRET) was first successfully described in 1946 but its application to biological systems, particularly in living cells, has only become popular in the late 1990s with the cloning of fluorescent proteins. Since the first cloning of the Green Fluorescent Protein (GFP), fluorescence microscopy has rapidly become a standard tool in cell biology. Fluorescence labelling allows the localization of a protein of interest in space and time in a biological specimen, from cells to animals. The labelling of several proteins in the same sample has been used to address protein-protein interactions in terms of colocalization. However, using standard fluorescence microscopy, determination of protein-protein distance is limited by the diffraction of light i.e., to hundreds of nanometers. Förster Resonance Energy Transfer (FRET) methods circumvent this barrier by allowing the detection of distances below 10 nanometers between a donor fluorophore and an acceptor through non-radiative energy transfer mediated by dipole-dipole interactions. FRET measurements can distinguish between two proteins being in the same compartment or in direct contact. Moreover, the ability to measure nanometric variations allows for the detection of protein conformational changes[1–3]. A large class of fluorescent biosensors have been engineered based on FRET to monitor protein function (kinase[4,5], GTPase[6]), calcium signals[7], or more recently, forces on the molecular scale[8–10]. The most common design relies on a molecular recognition element coupled with two fluorescent proteins (FPs) expressed in the same amino-acid sequence (intramolecular FRET sensor). An intermolecular FRET design is also possible where the FPs are inserted on two independent moieties. In this case, the apparent stoichiometry can strongly vary, which makes a quantitative analysis much more difficult.

There are two main approaches for measuring FRET in living cells: one is based on the change in fluorescence intensity and the other on the change in the donor fluorescence lifetime[11]. Fluorescence Lifetime Imaging Microscopy (FLIM) requires sophisticated instrumentation and analysis, and is often recognized as a quantitative method for live-cell measurements. Different strategies have been developed to measure FRET efficiency via the

[1]Univ. Grenoble Alpes, CNRS, LIPhy, Grenoble, F-38000, France. [2]Department of Chemistry, Center for Nano Science (CENS), Center for Integrated Protein Science Munich (CIPSM) and Nanosystems Initiative Munich (NIM), Ludwig Maximilians-Universität München, Munich, Germany. [3]Institute for Advanced Biosciences, Université Grenoble Alpes, INSERM U1209, UMR5309, F38700, La Tronche, France. *email: aurelie.dupont@univ-grenoble-alpes.fr

**Figure 1.** The QuanTI-FRET approach. (**A**) A schematic of a widefield epifluorescence setup used for the validation of the framework is shown. Three images are acquired in two snapshots by automatically alternating the laser excitation and splitting the camera in two detection channels corresponding the donor and acceptor channels. (**B**) Framework for quantitative FRET analysis. The analysis requires three images combining the detection in the donor and the acceptor channels with the excitation of the donor and the acceptor. A calibration step allows the determination of four factors correcting for the crosstalks and the relative excitation and detection efficiencies of the donor and acceptor fluorophores. As a result, instrument-independent FRET probabilities and stoichiometries are calculated. Scale bar: 20 $\mu$m.

fluorescence intensity of the donor and/or of the acceptor, some involving the total photobleaching of one fluorophore or specific instruments for spectral imaging[12–14]. The most compatible method with dynamic quantitative FRET imaging and live-cell imaging is based on the sensitized-acceptor emission. Because the collected fluorescence intensity depends strongly on numerous instrumental factors (excitation, filter set, camera sensitivity etc), this approach requires several corrections to calculate an instrument-independent FRET efficiency. The literature is rich of different correction factors and mathematical expressions of FRET indices[15,16]. The idea of correcting for spectral crosstalks and at least for the difference in detection efficiency between donor and acceptor channels emerged concomitantly in the single-molecule[17,18] and in the live-cell imaging fields[19–21]. It is now generally accepted that bleedthrough of the donor emission in the acceptor channel and direct excitation of the acceptor by donor excitation channel must be corrected by substracting their contributions. This requires the acquisition of three different signals, also called 3-cube strategy in live-cell imaging[20]. As such, the apparent FRET index varies with the fluorophore concentration and, even with additional normalization, the direct comparison of FRET values obtained independently is not possible[22]. To account for photophysical artifacts, we need to go back to physical equations and determine the origin of the signal in each channel. The next obstacle is the experimental determination of the correction factors. Existing methods require samples with known FRET efficiency[23] or known concentration[24] or even an additional experiment using acceptor photobleaching[21].

In this work, we clarify the theory coming from single-molecule studies[25] and adapt it to live-cell imaging. We present a new method to determine all the correction factors in a robust manner without any additional photobleaching experiment or external calibration of the FRET efficiency. The only requirement for calibration is knowledge of the donor:acceptor stoichiometry, which is in general known by construction. The calibration can thus be achieved directly on the sample of interest or with FRET standards[26]. While the stoichiometry can be accurately measured in the last case, this information can always be used as a quality factor to discard aberrant pixels. No specialized microscope is required as the QuanTi-FRET (Quantitative Three-Image) method can be applied to any epifluorescence triplet of images acquired with commercial instruments. Here, we demonstrate that QuanTI-FRET allows for absolute FRET measurements that are independent of the instrumental setup and of the fluorophore concentration. Being robust and including an inherent data quality check, the method can be used confidently by non-specialists, especially for FRET-based biosensors applications.

## Theory

The FRET efficiency, E, is defined as the percentage of energy transferred from the donor fluorophore to the acceptor fluorophore and increases as the donor-acceptor distance decreases. To properly calculate E from the images, factors influencing the relative excitation and detection efficiencies need to be taken into account. To determine the correction factors and obtain as much information as possible from the sample, we follow a multiple excitation scheme as introduced by Kapanidis and colleagues for single molecule spectroscopy[18] and close to the three-cube method in live-cell imaging[19]. Here, we used a rather sophisticated setup (Fig. 1). But, the only requirement is the capability to excite separately the donor and the acceptor fluorophores and to image both channels, preferably with an image splitting device for highly dynamic samples. This requirement also applies to three-cube imaging approaches. By switching rapidly between both excitation sources, and splitting the emission into two channels on the camera, we acquire in two successive snapshots four images:

$I_{DD}$: the detected signal in the donor channel after excitation at the donor wavelength,
$I_{DA}$: the detected signal in the acceptor channel after excitation at the donor wavelength,
$I_{AA}$: the detected signal in the acceptor channel after excitation at the acceptor wavelength.

The fourth image $I_{AD}$ contains no information, only noise, and is discarded. In principle, only $I_{DD}$ and $I_{DA}$ are sufficient to calculate the transfer efficiency. That would be the case if the photons coming from the donor and the acceptor had the same detection efficiency. In practice, it is not possible to have such an instrument and, several corrections must be considered to get unbiased quantitative FRET efficiencies. The third image, $I_{AA}$, is independent from the FRET efficiency but is required to calculate all the necessary correction factors.

One can write the intensity of the three types of signals as a function of the photophysical and instrumental parameters, the number of donor, $n^D$, and acceptor, $n^A$, fluorophores in the considered pixel and the FRET probability, $E$:

$$I_{AA} = n^A L_A \sigma^A_{Aex} \phi_A \eta^{Aem}_{Adet} \tag{1}$$

$$I_{DD} = n^D L_D \sigma^D_{Dex} (1 - E) \phi_D \eta^{Dem}_{Ddet} \tag{2}$$

$$I_{DA} = n^D L_D \sigma^D_{Dex} E \phi_A \eta^{Aem}_{Adet} + n^D L_D \sigma^D_{Dex} (1 - E) \phi_D \eta^{Dem}_{Adet} + n^A L_D \sigma^A_{Dex} \phi_A \eta^{Aem}_{Adet} \tag{3}$$

where $L_i$ is the excitation intensity at the wavelength chosen for excitation of fluorophore $i$, $\sigma_i^j$ is the absorption cross section of $j$ at the excitation wavelength of $i$, $\phi_i$ is the quantum yield of $i$ and $\eta_i^j$ is the detection efficiency of photons emitted by $j$ in the detection channel $i$. The expression of $I_{AA}$ is the simplest as it only depends on species $A$ (acceptor). For $I_{DD}$, one has to take into account the probability to transfer energy to the acceptor, $E$, as acceptor photons are not detected in this channel. Finally, to express $I_{DA}$, the FRET image, not only the signal coming from FRET events must be taken into account but also the two crosstalk terms: (i) the bleedthrough of photons emitted by the donor into the acceptor channel and (ii) the direct excitation of acceptor molecules with the donor specific wavelength. Some of the parameters in the above equations are difficult to measure. We follow a pragmatical approach and avoid the systematic determination of all twelve unknowns. First, we can simplify the expressions by defining a bleedthrough correction factor as $\alpha^{BT}$ and a direct excitation correction factor as $\delta^{DE}$. Additionally, a correction factor for the different detection efficiencies in both channels is defined as $\gamma^M$, and similarly a correction factor for the different excitation efficiencies in both channels is defined as $\beta^X$

$$\alpha^{BT} = \frac{\eta^{Dem}_{Adet}}{\eta^{Dem}_{Ddet}} \quad \delta^{DE} = \frac{L_D \sigma^A_{Dex}}{L_A \sigma^A_{Aex}} \quad \gamma^M = \frac{\phi_A \eta^{Aem}_{Adet}}{\phi_D \eta^{Dem}_{Ddet}} \quad \text{and} \quad \beta^X = \frac{L_A \sigma^A_{Aex}}{L_D \sigma^D_{Dex}} \tag{4}$$

Hence, the notation is simplified and by inverting the previous set of equations (see Supplementary Information), we obtain the FRET probability:

$$E = \frac{I_{DA} - \alpha^{BT} I_{DD} - \delta^{DE} I_{AA}}{I_{DA} - \alpha^{BT} I_{DD} - \delta^{DE} I_{AA} + \gamma^M I_{DD}} \tag{5}$$

In addition, as in Lee *et al.*[25], we define the stoichiometry as the relative amount of donor molecules with respect to the total number of fluorophores in each pixel:

$$S = \frac{n^D}{n^D + n^A} \tag{6}$$

From Eqs. (1) and (2), we derive expressions for $n^D$ and $n^A$ and insert them into Eq. (6). By simplifying with the excitation correction factor $\beta^X$ defined in Eq. (4), Eq. (6) reduces to:

$$S = \frac{1}{1 + \frac{I_{AA}}{I_{DD}} \frac{1}{\beta^X \gamma^M} (1 - E)} \tag{7}$$

To decouple stoichiometry and FRET probability, we replace $E$ by the expression given in Eq. (5). Finally the stoichiometry reads:

$$S = \frac{I_{DA} - \alpha^{BT} I_{DD} - \delta^{DE} I_{AA} + \gamma^M I_{DD}}{I_{DA} - \alpha^{BT} I_{DD} - \delta^{DE} I_{AA} + \gamma^M I_{DD} + I_{AA}/\beta^X} \tag{8}$$

By including the crosstalk corrections into a corrected FRET image, $I^{corr}_{DA} = I_{DA} - \alpha^{BT} I_{DD} - \delta^{DE} I_{AA}$, we obtain two master equations defining the FRET probability and the stoichiometry in each pixel:

$$E = \frac{I_{DA}^{corr}}{\gamma^M I_{DD} + I_{DA}^{corr}} \tag{9}$$

$$S = \frac{\gamma^M I_{DD} + I_{DA}^{corr}}{\gamma^M I_{DD} + I_{DA}^{corr} + I_{AA}/\beta^X} \tag{10}$$

Both E and S can be calculated from the three experimental images, $I_{DD}$, $I_{DA}$ and $I_{AA}$, and the four parameters, $\alpha^{BT}$, $\delta^{DE}$, $\gamma^M$ and $\beta^X$. All four correction factors are derived from the detailed expressions of the collected fluorescence intensities in the three different channels. The notations were chosen according to the consensus in the single-molecule field[27] with a supplemental superscript for a direct understanding of the role of each correction factor. The crosstalk correction factors are already widely used in the 3-cube approaches[21] and are straightforward to calibrate. Imaging a donor-only sample, in vitro or in cellulo, provides $\alpha^{BT}$; similarly, imaging an acceptor-only sample provides $\delta^{DE}$. $\alpha^{BT}$ depends only on the donor emission spectrum, the filter set and the spectral response of the camera. $\delta^{DE}$ depends on the acceptor excitation spectrum but also on the ratio of the illumination power in the two channels. Under the same experimental conditions (same fluorophores, same filter set and illumination intensities), the crosstalk corrections to be brought to $I_{DA}$ depend only on the quantity of both fluorophores, given by $I_{DD}$ and $I_{AA}$ while $\alpha^{BT}$ and $\delta^{DE}$ are unchanged.

The two other correction factors, $\gamma^M$ ("M" for Emission) and $\beta^X$ ("X" for Excitation), are more difficult to determine. $\gamma^M$ accounts for the difference in the measured fluorescence emission when the same number of donor or acceptor molecules are excited. Hence, it is related to the quantum yield and to the detection efficiency of the setup in each channel. $\beta^X$ accounts for the difference in energy absorption for each channel. Hence, it is related to the illumination intensity and the absorption cross-section of each fluorophore. $\gamma^M$ has already been described, in single molecule[17] and in live-cell imaging[21]. Several indirect strategies have been developed to determine the value of $\gamma^M$: acceptor photobleaching[21–28], the use of a FRET sample with known FRET efficiency[23], an interpolation from two constructions with very different FRET values[29] or a fit of the relation between $1/S$ and $E$[25]. $\beta^X$ has been introduced by Lee *et al.*[25] for single molecule experiments and a similar parameter has also been empirically introduced by Chen *et al.* for cellular experiments[29]. If $\beta^X$ and $\gamma^M$ are determined independently, $\beta^X$ has no effect on the FRET efficiency but just on the stoichiometry (see Eqs. (9) and (10)). Since the stoichiometry in single molecule studies is often limited to donor only, acceptor only and donor:acceptor complexes, S does not need to be known accurately and $\beta^X$ is not necessary. On the other hand, we will show that $S$ can be very useful in live-cell experiments even when the FRET construction has a well-defined stoichiometry.

**Calibration of the correction factors.** Having described the theory directly from the physical parameters of the fluorophores and of the experimental setup, the difficult part to achieve the calculation of quantitative FRET is to determine the four correction factors. As mentioned previously, the crosstalk correction factors are measured from donor-only and acceptor-only cells, and calculated as the ratios

$$\alpha^{BT} = \frac{I_{DA}^{donor\text{-}only}}{I_{DD}^{donor\text{-}only}} \quad \text{and} \quad \delta^{DE} = \frac{I_{DA}^{acceptor\text{-}only}}{I_{AA}^{acceptor\text{-}only}} \tag{11}$$

These ratios are calculated in each pixel of all the imaged cells and the median value is taken. The correction factors $\gamma^M$ and $\beta^X$ cannot be determined from the donor-only or acceptor-only samples where the FRET probability is equal to zero (or not defined). Another piece of information is necessary and is found in the stoichiometry. Equation (10) can be rewritten as

$$\beta^X \gamma^M I_{DD} + \beta^X I_{DA}^{corr} = \frac{S}{1 - S} I_{AA}, \tag{12}$$

which is the equation of a plane in the 3D space defined by $\{I_{DD}, I_{DA}^{corr}, I_{AA}\}$. If the stoichiometry is known, the strategy is to fit the experimental data $\{I_{DD}, I_{DA}^{corr}, I_{AA}\}$ to a plane and thereby determine $\beta^X\gamma^M$ and $\beta^X$. If the FRET sample of interest has an unknown stoichiometry, another calibration experiment has to be made with a defined stoichiometry FRET probe. Practically, the pixel values of a whole dataset (N cells) are gathered in the vectors $X = [I_{DD}, I_{DA}^{corr}]$ and $Y = [I_{AA}]$ and the matrix $A = [\gamma^M\beta^X, \beta^X]$ is determined using $XA = Y$ by a least-square fitting approach. If the sample shows only one FRET value $E$ with different fluorescence intensities (i.e. fluorophore concentrations), the pixel values will form a straight line in the 3D space $\{I_{DD}, I_{DA}^{corr}, I_{AA}\}$ (Fig. 2). As a result, an infinite number of planes can fit the dataset. For a good determination of $\beta^X$ and $\gamma^M$, it is therefore necessary that the FRET values of the dataset are sufficiently spread. The visualization and the calculation of the correction factors in the 3D space $\{I_{DD}, I_{DA}^{corr}, I_{AA}\}$ is the originality of this work. We compare our approach with the two other related methods in the last section.

## Results

### Validation of QuanTI-FRET using FRET standards.

To test the proposed method in live-cell experiments, we utilized the FRET standards developed by Thaler *et al.*[24] and Koushik *et al.*[26]. The FRET standards consist of a pair of fluoroscent proteins, a donor (Cerulean) and an acceptor (Venus), separated by an amino-acid sequence of variable length. Three standards were used in the present work to calibrate the experimental setup: C5V, C17V and C32V, where the linker between donor and acceptor consisted of 5, 17 and 32 amino-acids

**Figure 2.** FRET measurements on the three FRET standards, C5V, C17V and C32V. (**A**) Triplet fluorescence images are shown for exemplary cells transfected with the three FRET standards: C5V (short linker), C17V (medium linker) and C32V (long linker). The calculated FRET maps for the individual cells are shown on the right plotted using the same color scale. The highest FRET is observed for the shortest linker construct C5V and decreases to the lowest FRET construct C32V. Scale bar: 20 $\mu$m. Color bar: FRET efficiency in %. (**B**) A scatter plot of all pixels values from all cells imaged in the $\{I_{DD}, I_{DA}^{corr}, I_{AA}\}$ 3D-space and the fitted plane, side view as inset. The three FRET standard populations forming three distinct clouds are all lying in the plane defined by $\beta^X$ and $\gamma^M$. (**C**) Boxplot gathering cellwise FRET values of C5V, C17V and C32V measured independently in two different labs ([A] and [B]). After calibration, the same FRET median values were obtained.

respectively. The construct with the shortest linker, C5V, was expected to exhibit the highest FRET efficiency and the FRET efficiency to decrease as the linker length increases[26]. The FRET standards were expressed in Hela cells and imaged on the setup described in Fig. 1.

As a first step for the calibration, the crosstalk corrections corresponding to the donor, Cerulean, and the acceptor, Venus, must be determined. Hence, Cerulean-only cells and Venus-only cells were imaged. Using Eq. (11), the bleedthrough for Cerulean was calculated as $\alpha^{BT} = 0.421 \pm 0.002$ (10 cells) and the direct excitation of Venus as $\delta^{DE} = 0.1100 \pm 0.0008$ (12 cells). Here, with about 10 cells, a very good uncertainty was obtained. As a rule of thumb, one should at least consider 5 different cells and verify on the pixelwise distribution of the correction factors values that a single peak is well-defined. The pixelwise distributions of $\alpha^{BT}$ and $\delta^{DE}$ obtained in this work are shown in Supplementary Information (Fig. S1). The second step consists in the determination of $\gamma^M$ and $\beta^X$, the factors correcting for the difference in detection and excitation efficiencies in the different channels. The three necessary fluorescence images, $I_{DD}$, $I_{DA}$ and $I_{AA}$, of three exemplary cells transfected with C5V, C17V and C32V are shown in Fig. 2A. All the pixel values $\{I_{DD}, I_{DA}, I_{AA}\}$ of all cells expressing the three constructs were gathered as one dataset and fitted with the plane Eq. (12) (Fig. 2B). A mask of each cell was obtained and only the pixels coming from within the cells were kept. This equation has an additional unknown, S. An assumption on S is necessary at this step. By design, the CxV constructs should have on average one donor for one acceptor, *i.e.* $S = 0.5$. This assumes the maturation efficiency of the donor and the acceptor are close to 1. We will discuss the influence of maturation in the next section. For S = 0.5, the plane equation reduces to:

$$\beta^X \gamma^M I_{DD} + \beta^X I_{DA}^{corr} = I_{AA}. \tag{13}$$

A given set of experimental conditions (laser power, filter set, fluorophores, stoichiometry) corresponds to one plane, and in this plane, a given FRET efficiency corresponds to a line. As seen in Fig. 2B, the scatter plots of the three standards appear as linear clouds lying on the same plane defined by $\beta^X$ and $\gamma^M$ and the assumed stoichiometry $S$ ($S = 0.5$, 1 donor:1 acceptor). Here, the least squares fitting of the plane yielded $\beta^X = 1.167 \pm 0.008$ and $\gamma^M = 2.10 \pm 0.02$ with a coefficient of determination $R^2 = 0.995$.

Once all the correction factors are determined, the FRET probability can be measured. Since this dataset was used for calibration with the hypothesis of $S = 0.5$, the stoichiometry cannot be an output for this calibration dataset. Nevertheless, no assumption was made concerning $E$, and therefore, the FRET probability can be calculated on the same dataset as the one used for calibration. If the experiment of interest presents a sufficiently broad distribution of FRET probabilities to determine the plane in 3D, there is no need for a different experiment with FRET standards for calibration. Hence, calibration can be achieved on-the-fly on samples with known stoichiometry.

More than 25 Hela cells expressing one CxV construct were measured. The median FRET probability was $E_{C5V} = 51.1$ ($s.\ d = 12.2$, 26 cells) for C5V, $E_{C17V} = 43.1$ ($s.\ d = 11.8$, 25 cells) for C17V and $E_{C32V} = 35.1$ ($s.\ d = 11.5$, 27 cells) for C32V, calculated over more than $3 \cdot 10^6$ pixels. The uncertainty comes rather from the cell to cell variability than from the pixel statistics. Hence, the median FRET value per cell was taken (Fig. 2C, dataset [A]) and the uncertainty calculated as the standard error of the mean yielding: $E_{C5V} = 50.3 \pm 0.4$, $E_{C17V} = 41.7 \pm 0.8$ and $E_{C32V} = 35.1 \pm 0.8$. To verify that the FRET probability was independent of the fluorescence intensity, the Spearman's rank correlation coefficient was calculated between $E$ and $I_{AA}$, the only channel not affected by FRET and just related to the fluorophore concentration. Gathering the data from all three standards ($N = 5 \cdot 10^6$), the resulting Spearman's coefficient was $\rho = 0.04$, confirming the absence of a correlation between the fluorescence intensity and the calculated FRET probability. This is also true pixelwise on a single cell basis (see Supplementary Fig. S2) and cellwise comparing all cells expressing one FRET standard (see Supplementary Fig. S3). Similarly, we questioned the effect of the correction factor $\gamma^M$ by calculating the Spearman's coefficient between $E$ and the total donor fluorescence intensity ($\gamma^M I_{DD} + I_{DA}^{corr}$) without the correction, $\rho = 0.111$ ($\gamma^M = 1$, $N = 5 \cdot 10^6$), and with the correction $\rho = 0.045$ ($\gamma^M = 2.10$, $N = 5 \cdot 10^6$). Hence, correcting for the different detection efficiencies decreases the correlation by a factor 2.5 between the donor fluorescence intensity and the calculated FRET probability.

The goal of the QuanTI-FRET method is to enable the comparison of FRET-based experiments from different studies *i.e.*, obtained independently in different laboratories in the world. To test this, we performed the same experiments a second time in a completely independent way: with a different instrument, in a different country, by a different team on another cell culture with fresh constructs ordered directly from Addgene. Compared to the setup described in Fig. 1, the second setup used a larger magnification objective (100x versus 40x), a different laser source (two continuous-wave lasers versus a supercontinuum white light laser) and used two EMCCD cameras instead of a sCMOS camera for detection. The experimental data was analyzed with the exact same procedure. The calibration gave the following correction factors $\alpha^{BT} = 0.467 \pm 0.001$ (12 cells) and $\delta^{DE} = 0.101 \pm 0.003$ (12 cells) for the crosstalks and $\beta^X = 2.03 \pm 0.07$ and $\gamma^M = 1.35 \pm 0.07$ ($R^2 = 0.82$) for the excitation and emission correction factors. The FRET probability was measured for the three FRET standards giving $E_{C5V} = 50.2 \pm 1.7$ (10 cells), $E_{C17V} = 43.0 \pm 1.6$ (12 cells) and $E_{C32V} = 32.9 \pm 1.5$ (12 cells) (Fig. 2C, dataset [B]). For an easier comparison, correction factors and FRET probabilities from lab [A] and [B] are gathered in Supplementary Materials (Table S1). The variability in this second dataset was larger as seen by the smaller coefficient of determination ($R^2 = 0.82$) of the 3D fitting and the standard deviation of the FRET probability for each construct. Nevertheless, the FRET values obtained were in excellent agreement with the first dataset ([A]). Hence, we show that measuring FRET with the QuanTI-FRET method is quantitative: the absolute FRET values are meaningful and can be compared from one lab to another.

**Taking advantage of S.** So far, the stoichiometry value was used only to calibrate the system. However, once the experimental system has been calibrated, the QuanTI-FRET analysis can determine both E and S independently. In this case, additional information can be extracted from S. As in single molecule studies, the 2D histogram combining the stoichiometry and FRET probability histograms (Fig. 3A) is a useful tool. In theory, the standard constructs with 1 donor for 1 acceptor should appear as a cloud corresponding to their average FRET efficiency, $E_0$, and $S = 0.5$. A known stoichiometry of 1:1 donor:acceptor is also reasonable for a biosensor construct that contains both donor and acceptor fluorescent proteins that fold and mature with high efficiency. However, when looking for interactions between different proteins, a fraction of donor only and/or acceptor only constructs are expected. If free acceptors are also present in the image, the apparent FRET probability stays constant but the stoichiometry drops (Fig. 3A). On the contrary, if free donor is present with the 1:1 construct, both S and E are affected. This variation can be described theoretically. If a solution containing a donor-acceptor construct, $n_D^0$, with an average FRET efficiency of $E_0$ is mixed with free donor, $n_D^{free}$, the apparent FRET probability and the apparent stoichiometry are given by (see Supplementary Information):

$$E_{app} = \frac{1}{1 + \frac{1 - E_0 + n_{free}^D / n_0^D}{E_0}} \quad \text{and} \quad S_{app} = \frac{1 + n_{free}^D / n_0^D}{1/S_0 + n_{free}^D / n_0^D} \tag{14}$$

We can now write an analytical formula describing this mix in the E-S histogram:

$$S_{app} = \frac{E_0 / E_{app}}{1/S_0 + E_0 / E_{app} - 1}, \tag{15}$$

which is sketched in Fig. 3A. In Eqs. (2) and (3), we assumed that all donors were able to FRET *i.e.*, had an acceptor partner. If this is not the case and free donors exist, then E becomes an apparent FRET probability $E_{app}$ as in Eq. (14). If the experimental E-S histogram can be fitted to Eq. (15), the FRET probability, $E_0$ of the 1:1 construct can be extracted. The presence of free donors can result from the poor efficiency of the acceptor fluorophore to fold. As demonstrated above, this case can easily be seen and treated with the QuanTI-FRET method. The presence of free acceptors does not affect the FRET efficiency once the system is calibrated. If free acceptors are present in the calibration samples, one should at least evaluate and take into account the effective stoichiometry in order to obtain a reliable calibration and avoid the propagation of biases to the measurements of interest. If both free donors and free acceptors are present, the situation is more complicated due the ensemble measurement made in each pixel. But fortunately, most of FRET-based biosensors are formed with variants of GFP, in particular of the pair CFP/YFP, which fold well[30,31].

The observation of the E-S 2D histogram gives a hint about the quality of the calibration. In theory, for a sample with a fixed stoichiometry, the FRET probability and the stoichiometry should be uncorrelated resulting in horizontal clouds in the 2D histogram. Figure 3B shows the experimental data from this work with crosstalk

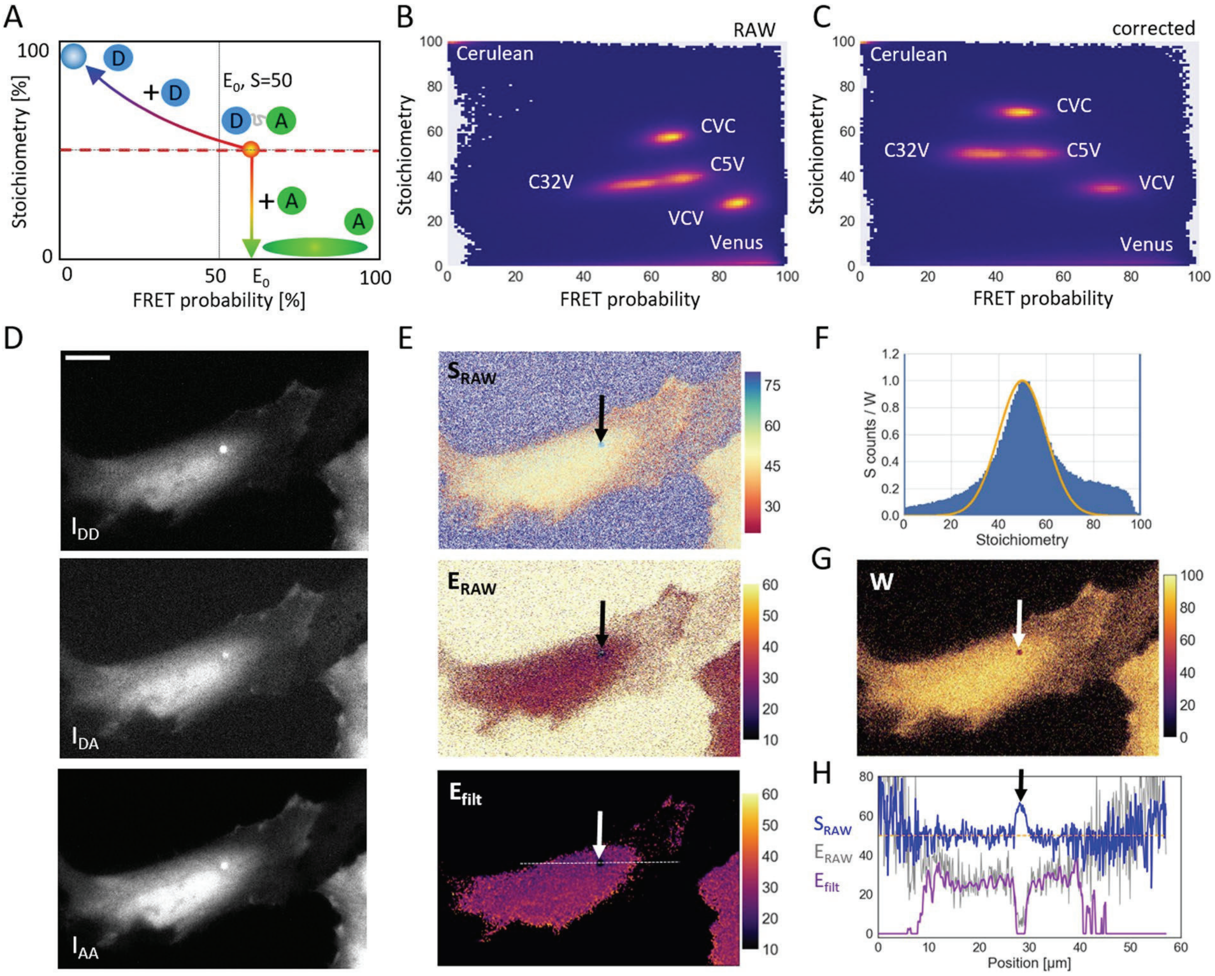

**Figure 3.** The influence of free donor or free acceptor in the sample. (**A**) A theoretical S-E histogram with trajectories corresponding to the addition of free donor or free acceptor to a construct with 1:1 donor to acceptor ratio. The blue disk represents the area where pure donor samples would appear, whereas the green ellipse is where free acceptor samples would appear. (**B**) Experimental histogram of S versus E for constructs showing different FRET values (C32V and C5V) or different stoichiometries (CVC and VCV) as well as pure donor (Cerulean) and pure acceptor (Venus). This histogram was calculated using only the crosstalk correction factors and concatenating results from different experiments. (**C**). The same experimental E-S histogram with the complete calibration including $\gamma^M$ and $\beta^X$. In the completely corrected 2D histogram, the stoichiometry and FRET probability are uncorrelated ($\rho = 0.02$, $N = 5 \cdot 10^6$). (**D**) An exemplary triplet of images showing a cell expressing C32V with a low signal-to-noise ratio, Scale bar 15 $\mu$m. (**E**) The corresponding RAW E and S maps and the FRET map for the images in panel **D** after filtering with a weigthed gaussian filter. (**F**) The corresponding stoichiometry histogram and the weights (W) as a function of the stoichiometry (line). For the weighting function, we used a Gaussian with a mean stoichiometry of $S = 0.5$ and a variance $\sigma_S = 0.1$ (Eq. 16). The corresponding map of weights W is shown in (**G**). (**H**) Line profiles corresponding to the three maps shown in panel (**E**). Due to high intensity background in an endosome, the FRET efficiency drops (thin grey line). This anomaly is also observable in the stoichiometry (blue). By weighting the image with the measured stoichiometry, such artifacts can be recognized (magenta).

correction but with $\beta^X$ and $\gamma^M$ both set equal to 1. The constructs C5V and C32V do not lie on a horizontal line whereas they should have the same stoichiometry. On the contrary, with the complete calibration of $\beta^X$ and $\gamma^M$ (Fig. 3C), the two clouds lie on a horizontal line corresponding to $S = 0.5$ (Spearman's correlation coefficient between E and S: $\rho = 0.02$, $N = 5 \cdot 10^6$ for C5V-C17V-C32V).

Once the system has been calibrated with FRET probes with a known stoichiometry, the stoichiometry becomes an output of the QuanTi-FRET analysis. Two additional FRET standards were imaged under the same conditions as before, CVC (2 donors:1 acceptor) and VCV (1 donor:2 acceptors)[24]. As these two constructs were not used to determinate $\gamma^M$ and $\beta^X$, no assumption was made with respect to their stoichiometry. Both constructs were built with the same fluorophore pair and imaged using the same conditions (filter set, laser power, camera), hence, the calibration was still valid. Practically, the experimental results gave $S = 68.9 \pm 0.2$ for CVC (24 cells), with an expected value of 66%, and $S = 35.1 \pm 0.2$ for VCV (9 cells), with an expected value of 33%

(Supplementary Fig. S4). Importantly, CVC and VCV experiments are well calibrated, appearing as horizontal clouds in the E-S histogram (Fig. 3C). On the same histogram, the acceptor-only (Venus) population was found at a very low stoichiometry value ($S = 7 \pm 2$, 10 cells, Supplementary Fig. S4) as expected and the donor-only population is also found where it is expected with a stoichiometry close to 1 ($S = 98.7 \pm 0.4$, 10 cells, Supplementary Fig. S4).

In the case of a fixed stoichiometry sample, as is the case for most FRET-based biosensors, S can still bring an important piece of information about the confidence. The usual way to determine the uncertainty about a pixel is to rely on the photon statistics: if the fluorescence signal is high, then a high confidence is assumed. This is certainly true for pure fluorescence imaging but, in the case of FRET, there are cases where a high fluorescence intensity occurs in pixels where the FRET is biased. For instance, FRET can be affected by the local chemical environment (pH), the local crowding or by any unequal effect on the fluorescence of the donor and acceptor. An example is shown on Fig. 3D where a lower-than-expected FRET efficiency was observed in certain bright intracellular vesicles. The corresponding raw results of the pixel-based analysis is shown in Fig. 3E ($S_{raw}$ and $E_{raw}$) and line profiles are plotted (Fig. 3H). For this example, the spot pointed to by the arrow has a high fluorescence intensity in the three channels but the stoichiometry differs from the expected 50% (close to 65%). Similarly, dark, out-of-cell regions of the image also show deviations from the expected stoichiometry. We define a confidence index $W$ as:

$$W = e^{-\frac{(S-S_0)^2}{2\sigma_S^2}}, \tag{16}$$

where $S_0$ is the expected S and $\sigma_S$ is a parameter to tune the sensitivity. $W$ renders the deviation from an expected stoichiometry as a score between 0 and 1 ($S = S_0$) with a gaussian shape (Fig. 3F). This confidence index can be used directly to display FRET maps with color-coded FRET values and brigthness-coded $W$. To go one step further, the confidence index can be inserted in a spatial filter. Indeed, FRET maps often need to be spatially averaged, the actual resolution being limited by the diffusion of the FRET species and is typically larger than the pixel size. A weighted gaussian filter was therefore designed where the effect of a Gaussian kernel, G (typically $7 \times 7$ pixels$^2$) was locally weigthed with $W$ (Fig. 3G) as follows:

$$E_{filt} = \frac{(W \circ E) * G}{W * G}, \tag{17}$$

where * denotes a convolution and ° the Hadamard product, $E$ and $W$ are dealt as matrices corresponding to the raw FRET image and the weights as defined in Eq. (16), $E_{filt}$ being the filtered FRET map. As the gaussian distribution never reaches zero, an additional threshold was applied based on the local weight of the considered pixel. An example is shown on Fig. 3E, the application of the weighted gaussian filter ($\sigma_S = 0.1$, $\sigma_{Gauss} = 1.5$ and threshold on W, $W_{th} = 0.5$) totally eliminates the background around the cells and also very dim areas inside cells as well as the bright vesicle with anomalous stoichiometry (Fig. 3H).

## Discussion

The definitions of FRET probability and stoichiometry used in QuanTI-FRET are mathematically equivalent to what was introduced previously by Chen *et al.*[20] ($\gamma^M \equiv G$ and $\beta^X \equiv 1/(G \cdot k)$) and Lee *et al.*[25] ($\gamma^M \equiv \gamma$ and $\beta^X \equiv \beta$). Therefore, we compared the performances of QuanTI-FRET to these two particular other methods. In the work by Chen *et al.*[29], the physical origin of the parameters was not described in detail as $\gamma^M$ was already introduced by Zal and Gascoigne[21] and the second parameter, $k$, was rationally defined from the $\gamma^M$-corrected intensities to account for the stoichiometry. The proposed calibration was achieved in two separated steps. First, two constructs with defined and well-separated FRET efficiencies were needed to determine $\gamma^M$ (a.k.a $G$). Second, a FRET standard with known stoichiometry was measured to calculate the other parameter, $k$, using $G$ determined in step 1. In Chen's work, the calibration was achieved by imaging the FRET standards C5V and CTV, where the linker $T$ is the 229 amino-acid TRAF domain of the TRAF2 protein[24]. However, the observation of the 3D representation of all the standards, including CTV, imaged in the present work, shows that CTV does not lie on the same plane as C5V, C17V and C32V (Supplementary Fig. S5). This is also visible in the E-S 2D histogram where the CTV cloud is tilted (Supplementary Fig. S5). These observations are in agreement with the later work of Koushik and Vogel[32] and demonstrate the utility of the 3D representation of the fluorescence intensities as well as the E-S 2D histogram to proofread the quality of the experimental data. The analysis of the experimental dataset [A] with Chen's method gave results close to the QuanTI-FRET method: $G = 2.19 \pm 0.02$ to compare with $\gamma^M = 2.10 \pm 0.02$ and $1/(G \cdot k) = 1.135 \pm 0.005$ to compare with $\beta^X = 1.167 \pm 0.008$ (see Table 1). However, the analysis of the second dataset [B] gave different results between the two methods: $G = 3.63 \pm 1$ to compare with $\gamma^M = 1.35 \pm 0.07$ and $1/(G \cdot k) = 1.02 \pm 7$ to compare with $\beta^X = 2.03 \pm 0.07$ yielding less reliable FRET probabilities (respectively 16%, 24% and 30% for C32V, C17V and C5V). This discrepancy results from the dataset being less homogeneous and the limited number of cell-containing pixels where the two-step calibration of $G$ and $k$ is less robust than the single-step fit of the QuanTi-FRET method. In the work of Lee *et al.*[25], the calibration consists of first calculating $E_{raw}$ and $S_{raw}$ with only spectral crosstalk corrections and then fitting the linear relation between $1/S_{raw}$ and $E_{raw}$, while assuming a 1:1 stoichiometry (see Supplementary Information). This method yielded very similar results to QuanTI-FRET: $\gamma = 2.37 \pm 0.05$ to compare with $\gamma^M = 2.10 \pm 0.02$ and $\beta = 1.13 \pm 0.01$ to compare with $\beta^X = 1.167 \pm 0.008$, resulting in FRET values slightly lower for the FRET standards ($\Delta E = 3\%$). The second dataset ([B]) was also used to test Lee's method leading to a decrease in the

| | $\beta^X$ | $\gamma^M$ | **C5V** | **C17V** | **C32V** |
|---|---|---|---|---|---|
| QuanTI-FRET | 1.167 ± 0.008 | 2.10 ± 0.02 | 50.3 ± 0.4 | 41.7 ± 0.8 | 35.1 ± 0.8 |
| Lee *et al.*[25] | 1.13 ± 0.01 | 2.37 ± 0.05 | 47.5 ± 0.4 | 38.9 ± 0.8 | 32.4 ± 0.8 |
| *Chen at al.*[29] | 1.135 ± 0.005 | 2.19 ± 0.02 | 49.4 ± 0.4 | 40.8 ± 0.8 | 34.2 ± 0.8 |

**Table 1.** Systematic comparison of QuanTI-FRET method with previous work from Lee *et al.*[25] and Chen *et al.*[29] Dataset [A] was analyzed with the three methods, the resulting correction factors and FRET probabilities for C5V, C17V and C32V are given in this table, with the uncertainty on $\beta^X$ and $\gamma^M$ resulting from a different bootstrap analysis.

FRET values of $\Delta E = 8\%$ with a relative difference of 11% for $\beta^X$ and 28% for $\gamma^M$. The correction factors and resulting FRET values for the three FRET standards are summarized in Table 1. The average FRET probabilities are in very good agreement between QuanTI-FRET and Chen's methods, a systematic difference of about 3% is observed with Lee's method. The three methods can all be considered as quantitative.

To further test the relative robustness of the three methods, a systematic bootstrap testing on experimental data ([A] with C5V, C17V and C32V) was performed. The whole experimental dataset was randomly divided to produce artificially smaller datasets and give access to statistical errors on the correction factors determination (as given so far). The standard deviation of $\gamma^M$ was around 0.12 (QuanTI-FRET and Chen's) and 0.23 (Lee's) for the minimum tested sample sizes between 1000 and 1300 points. The standard deviation of $\beta^X$ was found to be around 0.04 (QuanTI-FRET and Chen's) and 0.07 (Lee's) for the same range of sample sizes. Over the whole range of sample sizes (from $10^3$ to $10^5$ pixels), the standard deviation of both correction factors obtained by Lee's method remained larger than the ones obtained by Chen's and QuanTI-FRET (see Supplementary Fig. S6). This analysis demonstrates that Lee's method is less robust to dataset length, probably due to the fitting of $1/S$, which diverges for small $S$ values.

A different test was performed by reducing the FRET range of the calibration dataset by taking alternatively only two of the three standards (C5V-C17V, C17V-C32V and C5V-C32V) into account. In this case, Chen's method was not valid anymore for the C5V-C17V and C17V-C32V pairs resulting in relative variations of 76% for $G$ and 38% for $\beta^X$ (see Supplementary Fig. S6). Indeed, as Chen's method relies purely on the comparison between the average intensities of two populations, the uncertainty grows as the FRET distance decreases. QuanTI-FRET and Lee's methods, by fitting the total distribution, perform well in this bench test (relative variations of 14% and 22% for $\gamma^M$ respectively with QuanTI-FRET and Chen's, and 7% and 12% respectively for $\beta^X$, see Supplementary Fig. S5).

All in all, even if the three methods are quantitative in the best case scenario, QuanTI-FRET was demonstrated to be more robust to dataset dispersity, length and FRET range. The single-step calibration in a 3D $I_{DD}$, $I_{DA}^{corr}$, $I_{AA}$ representation, on a continuous distribution of FRET efficiencies allows for the calibration on-the-fly of the sample of interest itself, provided a defined stoichiometry and a distribution of FRET efficiencies in the range of the bench test (at least 5%). Taking inspiration from single-molecule literature, we can further exploit stoichiometry to provide a quality check of the experimental data and thereby filter the resulting FRET images.

## Conclusion

Building upon the previous contributions from live-cell and single-molecule FRET experiments, we present a new framework allowing for quantitative FRET imaging in living cells with a simple multi-channel epifluorescence microscope. Here, we demonstrated the consistency of the method on two different microscopy systems in different laboratories. The QuanTI-FRET method does not require specific instrumentation for determining spectra or lifetime nor specific hardware development. Image-splitting devices and LED excitation are now commercially available and allow for the same image acquisition protocols as the experimental system used in this work. The QuanTI-FRET calibration does not require acceptor photobleaching, purified proteins or known FRET samples. The only requirement is a known stoichiometry sample (as other quantitative methods) with a broad FRET distribution, which can be obtained directly from the FRET construct of interest (intramolecular-FRET-based biosensors for instance). Nevertheless, an independent calibration using FRET standards is recommended as it allows one to evaluate FRET efficiency and stoichiometry independently. The QuanTI-FRET method was demonstrated to be quantitative and robust, with the additional benefit of having an inherent data quality check.

## Methods

**Cells and plasmids.** All plasmids were gifts from Steven Vogel: C5V (Addgene plasmid # 26394), C17V (Addgene plasmid # 26395), C32V (Addgene plasmid # 26396), mVenus N1 (Addgene plasmid # 27793), mCerulean C1 (Addgene plasmid # 27796), VCV (Addgene plasmid # 27788), CVC (Addgene plasmid # 27809) and CTV (Addgene plasmid # 27803). Plasmids were amplified in *E.Coli* (DH5$\alpha$) and purified using the NucleoBond Xtra kit from Macherey-Nagel GmbH (http://www.mn-net.com). Hela cells were cultured in high glucose Dulbecco's Modified Eagle Medium supplemented with Foetal Bovine Serum (10%), GlutaMAX (Gibco) and Penicillin/ Streptomycin (1%). Cells were transfected with Lipofectamine 2000 (Invitrogen) and Opti-MEM (Gibco), then incubated in Fluorobrite DMEM medium (Gibco) overnight and finally imaged in Leibovitz's L-15 medium (Gibco) without phenol red.

**Microscopic image acquisition, Grenoble, setup [A].** Imaging was done with a widefield imaging system based on an Olympus IX83 inverted microscope body equipped with a home-made image splitter coupled to a sCMOS camera (ORCA Flash V2, Hamamatsu) as sketched in Fig. 1. Excitation was done in epifluorescence mode by a supercontinuum white light laser (Fianium) coupled to a high power AOTF (Fianium), which was controlled through an FPGA-RT unit (National Instruments) coded with Labview. This unit synchronized the alternated laser excitation with the camera acquisition. Images were acquired at 37 °C with Micromanager and a 40x objective. The donor fluorophore was excited at 442nm (power 200 *mu*W), the acceptor at 515nm (power 240 *mu*W). The fluorescence emission was first separated from the excitation via a triple line beamsplitter (Brightline R442/514/561 Semrock) in the microscope body. The fluorescence emission was further splitted with a beamsplitter at 510nm (Chroma) and filtered with a 475/50 filter (BrightLine HC, Semrock) for the donor channel and a 519/LP long-pass filter (BrightLine HC, Semrock) for the acceptor channel. Hence, in two camera snapshots, four images were obtained with all combinations of donor/acceptor excitation and donor/acceptor emission.

**Microscopic image acquisition, Munich, setup [B].** Images were acquired on a Nikon Eclipse Ti inverted microscope with home-built epifluorescence excitation and widefield detection pathways. A 100x oil immersion objective (Apo-TIRF 100x Oil/NA 1.49, Nikon) was used for all measurements. Samples were excited with 445nm (MLD, Cobolt) and 514nm (Fandango, Cobolt) diode lasers coupled to an AOTF (PCAOM LFVIS5, Gooch & Housego) controlled by a FPGA unit (cRIO-9074, National Instruments). The fluorescence emission was separated from the excitation pathway with a triple line 445/514/594 beamsplitter. The donor and acceptor emission were separated using an additional 514LP beamsplitter and were then spectrally filtered using 480/40 and 555/55 bandpass filters respectively before being detected on separate EMCCD cameras (DU-897, Andor). Each cell was excited for 300 ms at 445 nm (power 340 *mu*W) followed by 300 ms at 514 nm (power 139 *mu*W). The camera exposure was synchronized to laser excitation through the FPGA unit and a self-written Labview program. This produced four images over two exposure periods capturing donor and acceptor emissions at each excitation wavelength.

**Image analysis.** All the image analysis calculations were coded in Python, figures and plots were done in Python except for the boxplots obtained with PlotofPlots[33]. Raw fluorescence images were pre-treated by substracting the dark count of the camera and flattened by dividing with a fluorescence image obtained from a uniform fluorescent sample (Chroma slide). An essential step is then the registration between the two channels obtained on each half of the camera or between cameras. Brightfield images of beads randomly and densely spread on a coverslip were used for calibration. By calculating the image cross-correlations in local regions of the image between the two channels, a displacement map was obtained and hence a transformation matrix was calculated (accounting for translation, rotation, shear and magnification). This transformation matrix was systematically applied to $I_{DD}$ to match $I_{DA}$ and $I_{AA}$ before any calculation. Calibration of the system with QuanTI-FRET was done as explained in the main text. Visualization of the 3D fit was done in Paraview to explore all view angles. All calculations were done pixelwise. Parameters for the weighted gaussian filter are chosen as for standard gaussian filtering. Here, the spatial filtering is principally used to filter out pixels with an aberrant stoichiometry, *i.e.* $S$ larger than 0.6 or smaller than 0.4 as estimated from the S-E histograms. The spatial gaussian enveloppe is designed to avoid adding noise in this operation, as $S$ is subjected to stochastic pixel-to-pixel noise just as $E$ is.

The data that support the findings of this study are available from the corresponding author upon request.

Received: 13 December 2019; Accepted: 17 March 2020;

## References

1. Ha, T. *et al.* Single-molecule fluorescence spectroscopy of enzyme conformational dynamics and cleavage mechanism. *Proc. Natl. Acad. Sci. USA* **6** (1999).
2. Weiss, S. Fluorescence Spectroscopy of Single Biomolecules. *Science* **283**, 1676–1683, https://doi.org/10.1126/science.283.5408.1676 (1999).
3. Erickson, M. G., Alseikhan, B. A., Peterson, B. Z. & Yue, D. T. Preassociation of calmodulin with voltage-gated Ca 2+ channels revealed by FRET in single living cells. *Neuron* **31**, 973–985, https://doi.org/10.1016/S0896-6273(01)00438-X (2001).
4. Zhang, J., Ma, Y., Taylor, S. S. & Tsien, R. Y. Genetically encoded reporters of protein kinase A activity reveal impact of substrate tethering. *Proc. Natl. Acad. Sci.* **98**, 14997–15002, https://doi.org/10.1073/pnas.211566798 (2001).
5. Ting, A. Y., Kain, K. H., Klemke, R. L. & Tsien, R. Y. Genetically encoded fluorescent reporters of protein tyrosine kinase activities in living cells. *Proc. Natl. Acad. Sci.* **98**, 15003–15008, https://doi.org/10.1073/pnas.211564598 (2001).
6. Pertz, O., Hodgson, L., Klemke, R. L. & Hahn, K. M. Spatiotemporal dynamics of RhoA activity in migrating cells. *Nature* **440**, 1069–72, https://doi.org/10.1038/nature04665 (2006).
7. Miyawaki, A. *et al.* Fluorescent indicators for Ca2+ based on green fluorescent proteins and calmodulin. *Nature* **388**, 882–887 (1997).
8. Grashoff, C. *et al.* Measuring mechanical tension across vinculin reveals regulation of focal adhesion dynamics. *Nature* **466**, 263–6, https://doi.org/10.1038/nature09198 (2010).
9. Meng, F., Suchyna, T. M. & Sachs, F. A fluorescence energy transfer-based mechanical stress sensor for specific proteins in situ: Mechanical stress sensor. *FEBS J.* **275**, 3072–3087, https://doi.org/10.1111/j.1742-4658.2008.06461.x (2008).
10. Ringer, P. *et al.* Multiplexing molecular tension sensors reveals piconewton force gradient across talin-1. *Nat. Methods* **14**, 1090–1096, https://doi.org/10.1038/nmeth.4431 (2017).
11. Padilla-Parra, S. & Tramier, M. FRET microscopy in the living cell: different approaches, strengths and weaknesses. *Bioessays* **34**, 369–76, https://doi.org/10.1002/bies.201100086 (2012).
12. Chen, Y., Mauldin, J. P., Day, R. N. & Periasamy, A. Characterization of spectral FRET imaging microscopy. *J. Microsc.* **228**, 139–152 (2007).
13. Wlodarczyk, J. *et al.* Analysis of FRET Signals in the Presence of Free Donors and Acceptors. *Biophys. J.* **94**, 986–1000, https://doi.org/10.1529/biophysj.107.111773 (2008).
14. Arsenovic, P. T., Mayer, C. R. & Conway, D. E. SensorFRET: A Standardless Approach to Measuring Pixel-based Spectral Bleed-through and FRET Efficiency using Spectral Imaging. *Sci. Reports* **7**, 15609, https://doi.org/10.1038/s41598-017-15411-8 (2017).
15. Berney, C. & Danuser, G. FRET or no FRET: a quantitative comparison. *Biophys. J.* **84**, 3992–4010, https://doi.org/10.1016/S0006-3495(03)75126-1 (2003).
16. Zeug, A., Woehler, A., Neher, E. & Ponimaskin, E. G. Quantitative intensity-based FRET approaches - A comparative snapshot. *Biophys. J.* **103**, 1821–1827, https://doi.org/10.1016/j.bpj.2012.09.031 (2012).

17. Dahan, M. *et al*. Ratiometric measurement and identification of single diffusing molecules. *Chem. Phys.* **247**, 85–106, https://doi.org/10.1016/S0301-0104(99)00132-9 (1999).
18. Kapanidis, A. N. *et al*. Fluorescence-aided molecule sorting: analysis of structure and interactions by alternating-laser excitation of single molecules. *Proc. Natl. Acad. Sci. U. S. A.* **101**, 8936–8941, https://doi.org/10.1073/pnas.0401690101 (2004).
19. Youvan, D. C. *et al*. Fluorescence Imaging Micro-Spectrophotometer (FIMS). *Biotechnol. et alia* **1**, 1–16 (1997).
20. Gordon, G. W., Berry, G., Liang, X. H., Levine, B. & Herman, B. Quantitative fluorescence resonance energy transfer measurements using fluorescence microscopy. *Biophys. J.* **74**, 2702–2713, https://doi.org/10.1016/S0006-3495(98)77976-7 (1998).
21. Zal, T. & Gascoigne, N. R. J. Photobleaching-corrected FRET efficiency imaging of live cells. *Biophys. J.* **86**, 3923–39, https://doi.org/10.1529/biophysj.103.022087 (2004).
22. Hochreiter, B., Kunze, M., Moser, B. & Schmid, J. A. Advanced FRET normalization allows quantitative analysis of protein interactions including stoichiometries and relative affinities in living cells. *Sci. Reports* **9**, 8233, https://doi.org/10.1038/s41598-019-44650-0 (2019).
23. Hoppe, A., Christensen, K. & Swanson, J. A. Fluorescence resonance energy transfer-based stoichiometry in living cells. *Biophys. J.* **83**, 3652–64, https://doi.org/10.1016/S0006-3495(02)75365-4 (2002).
24. Thaler, C., Koushik, S. V., Blank, P. S. & Vogel, S. S. Quantitative Multiphoton Spectral Imaging and Its Use for Measuring Resonance Energy Transfer. *Biophys. J.* **89**, 2736–2749, https://doi.org/10.1529/biophysj.105.061853 (2005).
25. Lee, N. K. *et al*. Accurate FRET measurements within single diffusing biomolecules using alternating-laser excitation. *Biophys. J.* **88**, 2939–53, https://doi.org/10.1529/biophysj.104.054114 (2005).
26. Koushik, S. V., Chen, H., Thaler, C., Iii, H. L. P. & Vogel, S. S. Cerulean, Venus, and VenusY67c FRET Reference Standards. *Biophys. J.* **91**, L99–L101, https://doi.org/10.1529/biophysj.106.096206 (2006).
27. Hellenkamp, B. *et al*. Precision and accuracy of single-molecule FRET measurements—a multi-laboratory benchmark study. *Nat. Methods* **15**, 669–676, https://doi.org/10.1038/s41592-018-0085-0 (2018).
28. Ha, T. *et al*. Probing the interaction between two single molecules: fluorescence resonance energy transfer between a single donor and a single acceptor. *Proc. Natl. Acad. Sci.* **93**, 6264–6268, https://doi.org/10.1073/pnas.93.13.6264 (1996).
29. Chen, H., Puhl, H. L., Koushik, S. V., Vogel, S. S. & Ikeda, S. R. Measurement of FRET Efficiency and Ratio of Donor to Acceptor Concentration in Living Cells. *Biophys. J.* **91**, L39–L41, https://doi.org/10.1529/biophysj.106.088773 (2006).
30. Frommer, W. B., Davidson, M. W. & Campbell, R. E. Genetically encoded biosensors based on engineered fluorescent proteins. *Chem. Soc. Rev.* **38**, 2833, https://doi.org/10.1039/b907749a (2009).
31. Sizaire, F. & Tramier, M. FRET-based biosensors: genetically encoded tools to track kinase activity in living cells. In *Protein phosphorylation*, 179 (IntechOpen, 2017).
32. Koushik, S. V. & Vogel, S. S. Energy migration alters the fluorescence lifetime of Cerulean: implications for fluorescence lifetime imaging Forster resonance energy transfer measurements. *J. Biomed. Opt.* **13**, 031204, https://doi.org/10.1117/1.2940367 (2008).
33. Postma, M. & Goedhart, J. PlotsOfData—A web app for visualizing data together with their summaries. *PLOS Biol.* **17**, e3000202, https://doi.org/10.1371/journal.pbio.3000202 (2019).

## Acknowledgements

The authors are grateful to S. Pinel and N. Scaramozzino (M2Bio platform) for advices and help in plasmid amplification and purification. We thank B. Arnal and I. Wang for fruitful discussions and helpful suggestions regarding the code of the analysis. P. Moreau is acknowledged for his technical participation in building and maintaining the setup. This work was funded by the Agence Nationale de la Recherche (ANR, grant no. ANR-13-PDOC-0022-01), and supported by the Université Grenoble Alpes (UGA, AGIR-POLE program 2015, project ACTSUB). C.M.B., A.C. and A.D. are part of the GDR 3070 CellTiss. D.C.L. gratefully acknowledges the financial support of the Deutsche Forschungsgemeinschaft (DFG) via the collaborative research center (SFB1035, Project A11) and the Ludwig-Maximilians-Universität through the Center for NanoScience (CeNS) and the BioImaging Network (BIN). CAR and CO are supported by FRM and ANR (CE17 CE13 0022 01).

## Author contributions

A.D. conceived the experiments and the theory. D.C.L. contributed to the concept. C.O. and C.A.-R. contributed to the design of the biological protocols. A.C., C.M.B., C.Q. conducted the experiments. A.D. and A.C. analyzed the results. F.W. and C.M.B. built and interfaced the hardware. A.D. drafted the manuscript. All authors reviewed the manuscript and approved the final version.

## Competing interests

The authors declare no competing interests.

## Additional information

**Supplementary information** is available for this paper at https://doi.org/10.1038/s41598-020-62924-w.

**Correspondence** and requests for materials should be addressed to A.D.

# Appendix III

## A phase transition accompanies heterochromatin formation in mouse embryos

Latest manuscript draft.

# A phase transition accompanies heterochromatin formation in mouse embryos

Manuel Guthmann[1], Chen Qian[2], Irene Gialdini[2], Tsunetoshi Nakatani[1], Andreas Ettinger[1], Igor Kukhtevich[3], Robert Schneider[3], Don C. Lamb[2], Adam Burton[1] & Maria-Elena Torres-Padilla[1,4] *

[1]*Institute of Epigenetics and Stem Cells (IES), Helmholtz Zentrum München D-81377 München, Germany*
[2]*Department of Chemistry and Center for NanoScience (CeNS), Ludwig Maximilians-Universität München, Butenandtstraße 5-13, 81377 München, Germany*
[3]*Institute of Functional Epigenetics (IFE), Helmholtz Zentrum München, D-85764 Neuherberg, Germany*
[4]*Faculty of Biology, Ludwig-Maximilians Universität, München, Germany.*

* Correspondence: torres-padilla@helmholtz-muenchen.de

## Abstract

The majority of our genome is composed of repeated DNA sequences, which assemble into heterochromatin, a highly compacted structure that constrains their mutational potential. How heterochromatin forms during development and how its structure is maintained is not fully understood. Here, we show that mouse heterochromatin phase separates after fertilization, during the earliest stages of mammalian embryogenesis. Using high resolution, quantitative imaging and molecular biology approaches we show that pericentromeric heterochromatin displays liquid-like properties at the 2-cell stage, but it transitions into a more solid-like or gel-like state at the 4-cell stage, when chromocenters mature and heterochromatin becomes silent. Disrupting the condensates results in altered transcript levels of pericentromeric heterochromatin, suggesting a functional role for phase separation in heterochromatin integrity. Thus, our work shows that mouse heterochromatin forms membrane-less compartments with biophysical properties that change during development and provides new insights into the self-organization of chromatin domains during mammalian embryogenesis.

## Main text

Mammalian development starts upon fertilization of an oocyte by the sperm. Following fertilization, the two parental genomes undergo a major process of epigenetic reprogramming, which involves the establishment of chromatin domains *(1)*. How chromatin forms at the beginning of development remains a fundamental question in biology. In particular, how heterochromatin acquires its silencing signatures is poorly understood. Several molecular pathways contribute to the establishment of heterochromatin, however, the potential contribution of its biophysical properties to this process remains completely unknown.

In mammals, heterochromatin formation at pericentromeric regions of the chromosomes is accompanied by a spatial reorganization into multichromosomal domains, the chromocenters. The major satellite repeats that constitute the pericentromeric heterochromatin in mice undergo a dramatic remodelling in their shape and nuclear positioning during the 2-cell stage, changing from a ring-like configuration around the nucleoli precursors into spherical chromocenters (*Fig. 1A*) (*2-4*). This organization persists subsequently throughout development and differentiation. Functionally, silencing of pericentromeric heterochromatin occurs concomitantly with chromocenter formation and requires changes in nuclear organization (*2-4*).

In *Drosophila* embryos*,* heterochromatin displays condensation behaviour via liquid-liquid phase separation (LLPS)(*5*). Whether mammalian heterochromatin displays similar properties has been debated (*6-9*). Differences in the cellular systems used may explain some of the apparent discrepancies observed, but also, studying the biophysical properties of chromatin in a cellular environment remains technically challenging. Notwithstanding, the dynamic properties of mammalian embryonic heterochromatin *in vivo* have not been studied. Whether state transitions of heterochromatin occur in the mammalian embryo and whether such transitions are required for heterochromatin formation remains unknown.

Considering the significant changes in the shape of heterochromatin leading to the formation of chromocenters (*Fig. 1A*), we reasoned that large scale changes in their biophysical properties may take place after fertilization. Indeed, these morphological changes result in the formation of spherical domains (*Fig. 1A*)(*3*), a hallmark of LLPS (*10, 11*). We thus established imaging conditions with high spatial and temporal resolution to investigate and quantify the biophysical properties of pericentromeric chromatin after fertilization and verified that these do not impair development (*Fig. 1B and Fig. S1A-B*).

We focused on five key features to determine the biophysical state of pericentromeric domains: i) events of fusion and fission; changes in ii) sphericity and iii) volume over time; iv) the diffusion coefficients of its components inside and outside the domain, and v) the presence of a boundary constraining the diffusion of its components. To image pericentromeric heterochromatin in embryos, we used the TALE-based Genome Visualization (TGV) system that we developed previously, which uses fluorescent TALEs to specifically visualise the major satellites (*12*).We visualised nuclei by co-injection of mRNA for histone H2B and imaged heterochromatin for ~24 hours in more than 90 embryos (*Fig. 1B and S1C*). Over this time period, we observed the formation of bright, condensed pericentromeric foci, reflecting chromocenter formation (*Fig. S1C*)(*3, 13*). We then performed quantitative image analysis in 3D by implementing a segmentation and denoising pipeline (*Fig. S1D* and Methods). We observed both fusion and fission of pericentromeric domains in 2-cell stage embryos (*Fig. 1C* top and bottom panels, respectively) and an increase in their sphericity over time (*Fig. 1D*). Interestingly, pericentromeric domains initially increased in volume, but then started to decrease in size prior to a sharp increase in sphericity (*Fig. 1E and 1F*). This is not due to our long-term imaging, as we reproduced this result when imaging embryos during the late 2-cell stage only (*Fig. S2A-B*). We also validated the increase in volume at early stages using DNA FISH for major satellites (*Fig. S2C-D*). This suggests that events of fusion and fission underlie the changes in shape undergone by pericentromeric chromatin. Indeed, volume changes were consistently related to changes in sphericity, with most pericentromeric domains shifting from larger and less spherical to smaller domains of higher sphericity towards the end of the 2-cell stage (*Fig. 1G*), indicating partitioning of heterochromatin domains into smaller, more rounded clusters.

Interestingly, we did not observe the dynamic changes in volume and sphericity of pericentromeric chromatin at the 4-cell stage when chromocenters are already formed (*Fig. S2E-G*), indicating that such changes specifically accompany the period of heterochromatin maturation into chromocenters. To address whether the progressive changes in sphericity that we observed are a general feature of other nuclear bodies in early embryos, we imaged the embryonic nucleoli (referred to as nucleolar-like bodies or NLBs)(*14, 15*) (*Fig. 1H, I* and *Fig. S1E*). Nucleoli are known to undergo LLPS in other developmental settings and correspondingly, display highly spherical shapes (*10, 16*). As expected, NLBs exhibited high sphericity, but their sphericity remained relatively constant throughout the 2-cell stage (*Fig. S2H*). Thus, pericentromeric chromatin undergoes fission and fusion and displays specific changes in shape in early mouse embryos, which are consistent with condensate properties.

If embryonic heterochromatin is in a phase-separated state, we would expect distinct diffusion of its internal components within the condensate compared to the surrounding nucleoplasm (*5, 17*). To address this, we adapted RICS (Raster Image Correlation Spectroscopy)(*18*) to mouse embryos to measure diffusion coefficients inside and outside pericentromeric heterochromatin (*Fig. 2A*). We performed RICS for H3.1, which is a component of pericentromeric chromatin in 2-cell stage embryos (*Fig. S3A*)(*19*). To distinguish pericentromeric chromatin in live embryos, we co-expressed TALE-MajSat-mClover to delimit the heterochromatin domains (*Fig. 2A*). We found that the H3.1 diffuses at a significantly different rate in the pericentromeric domain compared to the nucleoplasm (*Fig. 2A*), suggesting that embryonic heterochromatin is phase-separated. In agreement, the concentration of H3.1 was significantly higher inside the heterochromatin domain (*Fig. S3B*). Next, we reasoned that if heterochromatin is in a liquid-like state, a boundary that partitions heterochromatin and the nucleoplasm should be present, resulting in different recovery kinetics of its internal components compared to the surrounding nucleoplasm. To test this, we performed FRAP (Fluorescence Recovery After Photobleaching) inside and outside heterochromatin at the 2-cell stage. For the former we measured H3.1 dynamics at both, NLB-associated and chromocenter domains as a mixture of both are present at this timepoint (*Fig. 2B*). H3.1 displayed high mobility in the nucleoplasm of 2-cell stage embryos (*Fig. 2C, D* and *Table S1*), consistent with previous work (*20, 21*). In addition, H3.1 was also highly mobile inside the pericentromeric domains, both when associated to the NLBs or in chromocenters (*Fig. 2C, D* and *Table S1*), in line with the RICS data. While the H3.1 mobile fraction did not differ significantly between the nucleoplasm and the pericentromeric domains (*Fig. 2D* and *Table S1*), the recovery kinetics at heterochromatin were significantly slower, particularly at NLBs (*Fig. 2E* and *Table S1*). Remarkably, at the 4-cell stage, when chromocenters are fully matured (*3, 13*), both the mobility and recovery kinetics of H3.1 are similar between heterochromatin domains and the surrounding nucleoplasm (*Fig. S3C-E* and *Table S1*). Thus, all the above support the interpretation that embryonic heterochromatin displays condensate properties that change during development. Initially heterochromatin displays liquid-like features during the process of chromocenter formation, including high sphericity, fusion/fission, and distinct recovery kinetics and diffusion of its internal components. However, the similar recovery kinetics inside and outside the heterochromatin domains when chromocenters are fully mature suggest a transition into a more solid-like or gel-like state. Overall, we conclude that pericentromeric chromatin forms membrane-less compartments with evolving biophysical properties during this time of development.

The formation of membrane-less compartments is promoted by weak hydrophobic interactions, which are primarily characteristic of LLPS (*11, 22*). Thus, we next probed whether weak hydrophobic interactions are necessary for chromocenter integrity and their biophysical properties by exposing embryos to 1,6-Hexanediol (*23*). Because NLBs displayed LLPS features in mouse embryos (*Fig. 1I, S3F-H*), we first identified conditions in which 1,6-Hexanediol disrupted the number of NLBs (*Fig. S4A*). To address whether 1,6-Hexanediol disrupts the pericentromeric compartment, we measured H3.1 mobility, as above. FRAP analysis after 1,6-Hexanediol treatment showed that the recovery kinetics of H3.1 in and outside of the pericentromeric domains became equalised (7.7±2.4 and 7.8±1.88, respectively), in contrast to the controls (6.2±1.6 at pericentromeric domain versus 10.4±3 in the nucleoplasm) (*Fig. 2F* and *Table S1*). These data suggest that liquid-liquid demixing of pericentromeric heterochromatin at the 2-cell stage is enabled through weak hydrophobic interactions. In line with this, DNA FISH for major satellites revealed a severe alteration in the nuclear localization of pericentromeric heterochromatin after 1,6-Hexanediol treatment, which led to the dispersion of the heterochromatin domains (*Fig. 2G*). Live imaging of pericentromeric domains recapitulated this observation (*Fig. 2H*). This behaviour was similar to that observed for the NLBs (*Fig. 2I*). Notably, 1,6-Hexanediol treatment at the 4-cell stage did not affect major satellite localization (*Fig. S4B*), suggesting that mature, fully formed chromocenters do not depend upon weak hydrophobic interactions. These observations, together with our findings showing that H3.1 kinetics are similar between the pericentromeric domains and the surrounding nucleoplasm at the 4-cell stage point towards a transition of heterochromatin from a liquid-like state to a more gel- or solid-like state during this early developmental period.

To examine the functional consequences of perturbing condensate integrity upon 1,6-Hexanediol treatment, we measured the transcript levels of major satellite repeats as a proxy for heterochromatin silencing. Pericentromeric heterochromatin is actively transcribed in zygotes and 2-cell stage embryos (*3*) and this transcriptional activity is thought to promote heterochromatin formation and chromocenter formation (*2, 19*). Treatment with 1,6-Hexanediol led to a significant reduction of major satellite transcripts as detected by RNA FISH and RT-qPCR (*Fig. 2J,K*), but not of control, β-actin transcripts (*Fig. S4C*), suggesting defective heterochromatin integrity.

Next, to investigate the molecular basis of our observations, we screened for proteins expressed in embryos with a potential to phase separate and a functional role in heterochromatin(*24, 25*). Of note HP1α is not expressed prior to the blastocyst stage (*26*).

Our previous work identified ATRX as a protein with a potential to phase separate (*24*). ATRX is required for heterochromatin integrity in oocytes and lack of ATRX in female gametes leads to chromosomal instability in pre-implantation embryos (*27-30*). ATRX contains a large intrinsically disordered domain (IDR) and a C-terminal prion-like domain (PLD)(*24*) which, are commonly found in proteins that promote or are enriched in phase separated compartments (*22, 31-36*). Immunostaining for ATRX revealed enrichment in foci at the pericentromeric chromatin around the NLBs in zygotes (*Fig. 3A)*, in agreement with previous work (*28, 29*). At the 2-cell stage ATRX displayed a marked pericentromeric heterochromatin enrichment, exclusively at chromocenters but not around NLBs (*Fig. 3A*).

To address whether ATRX is involved in the biophysical and morphological changes of the pericentromeric heterochromatin during this time of development, we performed acute protein depletion of ATRX using Trim-away (*37*), which led to efficient ATRX degradation in 2-cell stage embryos (*Fig. S5*). Depletion of ATRX did not affect the early changes in volume of heterochromatin domains (*Fig. 3B*). However, depletion of ATRX completely prevented the partitioning into smaller rounded heterochromatin domains observed in control embryos at the late 2-cell stage (*Fig. 3B*). This data suggests that the initial heterochromatin phase transition is independent of ATRX function, but that ATRX is required for later maturation into chromocenters. In agreement, ATRX depletion did not affect the recovery kinetics of H3.1 inside the heterochromatin domains or in the nucleoplasm (*Fig. 3C*), suggesting that ATRX is not required for the integrity of the pericentromeric condensate. Phase separated condensates rely on scaffold proteins for the integrity of the condensate, and on client proteins, which interact with the components of the condensate through low valency interactions (*38*). Because our data indicate that ATRX is not required for the condensate integrity, we thus tested whether ATRX acts as a client protein in the process of heterochromatin formation in the early embryo. Indeed, we found the specific localization of ATRX at chromocenters at the 2-cell stage was highly sensitive to 1,6-Hexanediol treatment (*Fig. 3D*). Overall, our data suggest that ATRX recruitment to heterochromatin depends on weak hydrophobic interactions, and that ATRX is subsequently required for the morphological and biophysical changes that lead to chromocenter formation.

The lack of partitioning into smaller heterochromatin domains in the absence of ATRX that we observed is in line with the known defects in aneuploidy resulting from maternal depletion of ATRX (*27, 28*). While all our observations are compatible with embryonic heterochromatin displaying condensate features, it is also plausible that ATRX may contribute additional roles through its ability to bind and remodel chromatin (*39-41*) by biochemical, rather than biophysical means. However, we note that the contribution of both is plausible and in line with the complexity of in vivo, cellular developmental systems.

Our work suggests a model whereby dynamic changes in biophysical properties underlie heterochromatin formation at the beginning of mammalian development (*Fig. 4*). While heterochromatin displays properties of a liquid-like state initially during development, heterochromatin maturation into chromocenters is accompanied by a phase transition into a more solid- or gel-like state. These data imply that the phase separation features of heterochromatin are cell-type variable and could potentially be linked to cellular plasticity, in this case in a developmental setting.

Overall, our data provide novel insights into self-organization of chromatin domains at the beginning of mammalian development and indicates that the physical state of heterochromatin may change depending on the biological cellular context.

## Acknowledgments

We thank F. Danner, F. Erdel and S. Bultmann for helpful discussions. M.E.T.-P. acknowledges funding from the Helmholtz Association and the German Research Foundation (DFG) Project-ID 213249687 (SFB 1064.

## Figure Legends

**Fig. 1. Live imaging of pericentromeric heterochromatin in mouse embryos.**

(**A**) DAPI stained nuclei of the corresponding mouse preimplantation embryo stage to visualise the nucleolar-like bodies and chromocenters. Right: schematic representation of the centromeric regions of a typical mouse chromosome. Scale bars, 10µm.

(**B**) Experimental design for visualising pericentromeric heterochromatin in live embryos.

(**C**) Still images of a single Z-plane of one nucleus from live imaging of a 2-cell stage embryo in the major satellite channel at the corresponding time in minutes. Arrows point to events of fusion (top row, cyan) and fission (bottom row, magenta). The black square in the 2-cell schematic depicts the imaged area. Scale bars, 5µm.

(**D**) Mean sphericity of major satellite regions in one nucleus represented with a dotplot and a locally estimated scatterplot smoothing (LOESS) curve (left) or a boxplot (right) .

(**E**) Z-scores of the volume of pericentromeric domains per nucleus during the 2-cell stage plotted as in Fig1.D.

(**F**) LOESS curves for the z-scores of sphericity and volume of major satellites per nucleus across the 2-cell stage.

(**G**) Density plot showing the sphericity and volume of individual pericentromeric domains across 4 different time windows covering the 2-cell stage. The small schematic shows the expected position of small spherical versus large irregular objects.

(**H**) Experimental design for live imaging of nucleolar-like bodies at the 2-cell stage.

(**I**) Still images of a single Z-plane from live imaging of one 2-cell stage nucleus in the NPM2 channel at the corresponding time in minutes. The black square in the 2-cell schematic depicts the imaged area. Scale bars, 10µm.

**Fig. 2. Pericentromeric heterochromatin phase separates in mouse embryos.**

(**A**) Experimental design of Raster Image Correlation Spectroscopy (RICS) of histone H3.1 at pericentromeric heterochromatin. Representative confocal microscopy images of TALE-MajSat and SNAP-H3.1 used for RICS analysis. Box plot of diffusion coefficients for H3.1-mRFP in the nucleoplasm (Nuc.) and at major satellites (MajSat) where each dot represents one nucleus. Mean±SEM values are 5.5±0.21 in the nucleoplasm versus 4.3±0.22 at pericentromeric domain. The black square in the 2-cell schematic depicts the imaged area. Scale bar, 5µm.

(**B**) Experimental design for Fluorescent Recovery After Photobleaching (FRAP) analysis of histone H3.1 at the 2-cell stage. Schematics and still images of FRAP performed in the nucleoplasm or inside pericentromeric heterochromatin, either when around the NLBs or at chromocenters. The black square in the 2-cell schematic depicts the imaged area. Bleach regions are represented by a red circle. Scale bars, 8µm.

(**C**) Recovery curves of H3.1-mRFP in the specified regions. The individual points are the mean±SEM. The curve is a double exponential fit of all individual points for each region.

(**D**) Mean±SEM of the estimated H3.1-mRFP mobile fraction from fitting a double exponential to each individual FRAP experiment.

(**E**) Mean±SEM of estimated H3.1 fast recovery kinetics from fitting a double exponential to each individual FRAP experiment.

(**F**) Experimental design, mobile fraction and fast recovery kinetics of H3.1-mRFP in the nucleoplasm or at pericentromeric heterochromatin after 1,6-Hexanediol treatment, measured by FRAP.

(**G**) Experimental design and representative images of major satellite DNA FISH after 1,6-Hexanediol treatment at the 2-cell stage. The panels show the DAPI and the major satellite channels, a merge of both channels and an inset with a higher magnification of one of the two nuclei in the major satellite channel. White dashed lines demarcate the nuclear membrane. Scale bars, 5µm.

(**H**) Experimental design and still images from live imaging of pericentromeric heterochromatin with 1,6-Hexanediol. Images show the major satellite and H2B channels at the corresponding timepoints in minutes. The black square in the 2-cell schematic depicts the imaged area. Scale bars, 15µm.

(**I**) Experimental design and still images from live imaging of nucleolar-like bodies (NLB) with 1,6-Hexanediol. Images show the merge of the NPM2 and H2B channels at the corresponding timepoints in minutes. The black square in the 2-cell schematic depicts the imaged area. Scale bars, 15µm.

(**J**) Experimental design and results of quantification of major satellite transcripts by RNA FISH after 1,6-Hexanediol treatment. Mean, intensity, volume and number of FISH foci per nucleus are shown.

(**K**) RT-qPCR analysis of major satellite transcripts after 1,6-Hexanediol treatment. Data are normalized against *Gapdh* mRNA and shown as log2 fold change to controls.

**Fig. 3. Liquid-like dependent ATRX recruitment to pericentromeric chromatin mediates chromocenter maturation.**

(**A**) Representative confocal section of ATRX immunostaining in zygotes and late 2-cell stage embryos.

(**B**) Experimental design for the analysis of pericentromeric heterochromatin in live embryos after ATRX depletion by Trim-Away. LOESS curves for the z-score of sphericity and volume of pericentromeric domains per nucleus across the 2-cell stage for control IgG and ATRX knockdown conditions.

(**C**) Experimental design and quantification of fast recovery kinetics of H3.1-mRFP in the in the specified regions after ATRX Trim-Away, measured by FRAP in late 2-cell stage embryos.

(**D**) Experimental design and representative confocal section of ATRX immunostaining after 1,6-Hexanediol treatment. The panels show the results of untreated embryos and 2 types of phenotypes observed after 1,6-Hexanediol treatment and their frequency.

Scale bars, 10µm.

**Fig. 4 Model summarizing our findings on the phase state transition of embryonic heterochromatin and the role of ATRX in this process.** Pericentromeric heterochromatin transitions from a liquid-like to a more solid or gel-like state during the process of chromocenter formation. ATRX is required for chromocenter formation but not for the initial heterochromatin phase transition.

## Supplementary Figure Legends

**Fig. S1. Live imaging protocol and pipeline to study the dynamics and biophysical properties of pericentromeric heterochromatin in mouse embryos.**

(**A**) Experimental design and representative bright-field images of embryos 3 days after microinjection with *H2B-tdiRFP*, *TALEMajSat-mClover* and *mRuby-NPM2* mRNA. Scale bars, 100µm.

(**B**) Proportion of embryos that reached the blastocyst stage after 3 days of culture.

(**C**) Representative images of 3D-reconstructions of Z-stacks acquired during live imaging of a 2-cell stage embryo in the major satellite and H2B channels at the corresponding time in minutes. The black square in the 2-cell schematic depicts the imaged area. Scale bars, 15µm.

(**D**) Diagram of the image analysis pipeline developed to calculate the volume and sphericity of 3D-reconstructed pericentromeric heterochromatin domains and nucleolar-like bodies (NLBs) from live imaging. The major satellite channel is denoised with the Rudin-Osher-Fatemi algorithm and subsequently segmentation and calculation of volume and sphericity for major satellites and NPM2 was performed using Imaris software. The black square in the 2-cell schematic depicts the imaged area.

(**E**) Representative images of 3D-reconstructions of Z-stacks acquired from live imaging of a 2-cell stage embryo in the NPM2 and H2B channels at the corresponding time in minutes. The black square in the 2-cell schematic depicts the imaged area. Scale bars, 15µm.

**Fig. S2. Changes in volume and sphericity of heterochromatin domains are specific to the 2-cell stage.**

(**A**) Mean sphericity of pericentromeric regions per nucleus over time, as determined using live imaging in the late 2-cell stage plotted as in Fig. 1D.

(**B**) Volume analysis of pericentromeric heterochromatin per nucleus over time, as determined based on live imaging at the late 2-cell stage plotted as in Fig. 1E.

(**C**) Sphericity of individual pericentromeric heterochromatin regions at the corresponding timepoints, quantified using superresolution microscopy of major satellite DNA FISH with stimulated emission depletion microscopy (STED).

(**D**) Volume of individual pericentromeric heterochromatin regions at the corresponding timepoints, calculated from major satellite DNA FISH imaged with STED.

(**E**) Mean sphericity of pericentromeric heterochromatin domains per nucleus from live imaging in 4-cell stage embryos plotted as in Fig.1D.

(**F**) Volume of pericentromeric heterochromatin per nucleus, calculated from live imaging during the 4-cell stage plotted as in Fig. 1E.

(**G**) Density plot showing the sphericity and volume of individual pericentromeric domains across 4 different time windows during the 4-cell stage. The small schematic shows the expected position of small spherical versus large irregular objects.

(**H**) Sphericity of nucleolar-like bodies (NLBs) and pericentromeric heterochromatin obtained from live imaging in 2-cell stage.

**Fig. S3. The liquid properties of pericentromeric heterochromatin resemble those of nucleolar-like bodies and are specific to the 2-cell stage.**

(**A**) Representative confocal section of a single nucleus of a late 2-cell stage embryo after immunostaining for SNAP-H3.1 and H3K9me3 after Triton X-100 pre-extraction to detect chromatin bound H3.1. Scale bar, 10µm.

(**B**) SNAP-H3.1 concentration at nucleoplasm (Nuc.) and at pericentromeric heterochromatin (MajSat) at the 2-cell stage as measured by RICS. Mean±SEM is $1.17\text{x}10^{-6}$±$1.19\ \text{x}10^{-7}$ in the nucleoplasm and $1.35\ \text{x}10^{-6}$±$9.41\ \text{x}10^{-8}$ at pericentromeric domain.

(**C**) Experimental design and FRAP recovery curves of H3.1-mRFP at the 4-cell stage in the specified regions. The individual points are the mean± SEM. The curve is a double exponential fit of all individual points for each region.

(**D**) Mean±SEM of estimated H3.1 mobile fractions from fitting a double exponential to each individual FRAP experiment at the 4-cell stage.

(**E**) Mean±SEM of estimated H3.1 fast recovery kinetics from fitting a double exponential to each individual FRAP experiment at the 4-cell stage.

(**F**) Experimental design and still images of FRAP for NPM2 in the nucleolar-like bodies (NLBs) at the 2-cell stage. Bleach region is represented by a red circle. The black square in the 2-cell schematic depicts the imaged area. Scale bar, 8µm.

(**G**) Mean±SEM of NPM2 mobile fraction and recovery kinetics at the 2-cell stage.

(**H**) Experimental design and still images of photoconversion experiments for NPM2 in nucleolar-like bodies at the 2-cell stage. The black square in the 2-cell schematic depicts the imaged area. Scale bars, 8µm.

All statistical analysis was performed using the two-sided Mann–Whitney U-test.

**Fig. S4. Conditions for 1,6-Hexanediol at the 2-cell stage and effect of 1,6-Hexanediol on pericentromeric heterochromatin localization at the 4-cell stage.**

(**A**) Experimental design to determine the effective concentration of 1,6-Hexanediol in mouse embryos. Embryos were treated at the indicated concentrations of 1,6-Hexanediol, fixed and the number of nucleolar-like bodies was determined using confocal imaging of DAPI-stained embryos. The left SINA plot shows the number of nucleolar-like bodies per embryo under different 1,6-Hexanediol concentrations. The right SINA plot shows the area of the pronuclei, measured in the Z-section of their maximal diameter, after incubation with the indicated 1,6-Hexanediol concentrations.

(**B**) Experimental design and representative images of major satellite DNA FISH after 1,6-Hexanediol treatment at the 4-cell stage. White dashed lines demarcate the nuclear membrane. Scale bars, 10µm.

**(C**) RT-qPCR analysis of *Actb* transcripts after 1,6-Hexanediol treatment. Data are normalized against *Gapdh* mRNA and shown as log2 fold change to controls.

**Fig. S5. ATRX is efficiently degraded by Trim-Away at the 2-cell stage**.

Representative single confocal section of an embryo immunostained for ATRX after Trim-Away with anti-ATRX antibody or IgG control. Scale bars, 10µm.

## Material and Methods

### Plasmid construction and mRNA production

The TALEMajSat-mClover, H2B-tdiRFP and mGFP plasmids were previously characterised and are available in Addgene (*12, 42*); 47878, 47884). For the mRuby-NPM2 and mEOS3.2-NPM2 plasmids, we replaced eGFP for either mRuby or mEOS3.2, which was amplified from a plasmid obtained from the Burtscher lab (*43*) in a eGFP-NPM2 construct kindly provided by F. Aoki (*15*). The mCherry-Trim21 plasmid was obtained from Addgene (105522,(*37*)) and the pRN3P.Trim21 plasmid was generated by removing the mCherry sequence. The H3.1 plasmid was constructed from the pRN3P.H3.1.GFP plasmid (*19*) by replacing the GFP sequence by mRFP. The SNAP-H3.1 plasmid contains an N-terminal SNAP tag sequence. mRNAs were transcribed *in vitro* using either a T3 or a T7 mMESSAGE mMACHINE kit (Ambion) or mMESSAGE mMACHINE ultra kit (Ambion).

### Embryo collection, microinjection and culture

Animal experiments were carried out in compliance with local regulations (Government of Upper Bavaria). For the ATRX immunostainings, CD1 female mice (4–8 weeks old) were mated with CD1 male mice (3–6 months old), and zygotes and 2-cell stage embryos were collected at 17h and 40h post-coitum, respectively. For all other experiments, embryos were collected from 5–6-week-old F1 (C57BL/6J×CBA/H) females mated with F1 males (3–6 months old) after hormonal induction with pregnant mare serum gonadotropin (Intervet, 5 IU) and human chorionic gonadotropin (hCG; Intervet, 7.5 IU) 46–48-h later. Embryos were collected at the following time points after hCG injection: zygotes were collected between 18h and 21h post-hCG except for Fig. 3.A when it was collected at 25h post-hCG; 2-cell stage embryos were collected at 48h post-hCG for Fig. 3A. Zygotes were microinjected with 1–2pl of the indicated mRNA or antibody. Embryos were cultured in K-modified simplex optimized medium (KSOM) microdrops under paraffin oil at 37 °C, 5% $CO_2$. For the analysis of H3.1 localization in Fig. S3A, *in vitro*-transcribed mRNA of SNAP tagged H3.1 (50ng/µL) was injected into zygotes at 17-18hphCG. Injected embryos were cultured until 47.5hphCG and treated with 5µM SNAP-Cell Oregon Green (NEB, S9104S) for 30 min in KSOM. Embryos were subject to triton pre-extraction to detect incorporated SNAP tagged H3.1 (*44*).

### Immunostaining and confocal microscopy

Embryos were fixed as previously described (*45*). Briefly, the zona pellucida was removed with Acid Tyrode solution, followed by two washes in PBS and fixation for 20 min in 4% paraformaldehyde, 0.04% Triton, 0.3% Tween-20, 0.2% sucrose at 37 °C. Embryos were then washed with PBS and permeabilized with 0.05% Triton X-100 for 20min. After permeabilization, embryos were washed three times in PBST (0.1% Tween 20 in PBS), quenched in 2.6mg/ml freshly prepared ammonium chloride, washed three times in PBST, blocked for 3–4h at 4 °C in blocking solution (3% BSA in PBST) and incubated with primary antibodies in blocking solution. Antibodies used were as follows: anti-ATRX (Cell Signaling, 8729, 1:250 dilution). After overnight incubation at 4 °C, embryos were washed three times in PBST, blocked and incubated for 3h at room temperature in blocking solution containing secondary antibodies labelled with Alexa-488 fluorophore (Invitrogen A32731, 1:500 dilution). After washing, embryos were mounted in Vectashield (Vector Laboratories) containing DAPI. Confocal microscopy was performed using a plan-Apo 63x NA 1.4 oil immersion objective on a TCS SP8 inverted confocal microscope (Leica). Z-sections were taken every 0.5–1µm. Image analysis was performed using FIJI (*46*). For all experiments, acquisition parameters were set to obtain fluorescence intensity signals in the linear range of hybrid detectors. These detectors have negligible detector noise and linearly amplify incoming photons into photoelectrons, thereby allowing the counting of measured photons, provided the detector is not saturated. Hence, given identical acquisition settings, the recovered fluorescence signal accurately reflects the level of antigen present in the sample.

**Live imaging of Major Satellite (MajSat) regions and Nucleolar-Like Bodies (NLBs)**

For live imaging, embryos were microinjected with 1-2pl of the following combinations of mRNAs: 1) 600 ng/µl of TALEMajSat-mClover mRNA and 200 ng/µl of H2B-tdiRFP mRNA for MajSat visualization; 2) 600 ng/µl of TALEMajSat-mClover mRNA, 200 ng/µl of H2B-tdiRFP mRNA and 100 ng/µl of mRuby-NPM2 mRNA for imaging NLBs. Embryos were cultured in microdrops of KSOM until the start of the live imaging, when they were transferred to an imaging chamber containing micrometric wells with 1mL of in KSOM covered with 1mL of paraffin oil prior the beginning of the live imaging. We used either a custom-made chamber (for most imaging experiments) or the Embryo Immobilisation Chip (Dolomite Microfluidics). Each of our custom-made chamber consists of two functional elements: a layer with wells for single embryo isolation and imaging; a wall around the wells, which allows media keeping and exchange. The layer with wells was made as a sandwich of a coverslip and a layer of Ostemer 322 (Mercene Labs AB, Sweden) with holes, which was bonded on top of the coverslip. The holes in Ostemer 322 were formed using a polydimethylsiloxane (PDMS) master mold, which was produced using standard soft lithography. Briefly, a master mold for replication in PDMS was fabricated from SU-8 photoresist (MicroChem, USA) spin-coated on a Si wafer. The SU-8 master mold was then used to produce the PDMS master mold from Sylgard 184 (Dow Corning, USA). In total, there are 361 wells with 200 µm diameter and 110 µm height in each chamber. The wall was 3D printed from High Temp Resin (Formlabs, USA) using 3D printer Form 2 (Formlabs, USA). The outer diameter of the wall is 35 mm, the inner area is 16x16 mm, and the height is 10 mm. The layer with wells and the wall were centered to have the wells within the inner area of the wall and then bonded to each other using Ostemer 322. Each chamber was extensively washed in distilled water and under sonication to remove residual non-cross-linked materials. Live imaging experiments were performed using a plan-Apo 100x NA 1.35 silicon oil immersion objective on a dragonfly 304 spinning disc system attached to a Nikon Ti-2microscope. Images were acquired on a Andor iXon 888 live EMCCD camera. Temperature was maintained at 37 °C with a microscope enclosure incubator (Ololab, Italy) and 5% $CO_2$was supplied by a gas mixer into a stage-top chamber with magnetic holder for 35 mm dishes (Okolab, Italy). For imaging of MajSat and NPM2 in early and late 2-cell stage embryos, live imaging was started between 40 and 42 h or 48h post-hCG respectively. For the 4-cell stage imaging live imaging was started between 54 and 55h post-hCG. Note that live imaging procedure may result in some developmental delay and therefore the post-hCG timepoints should be considered relative. To generate the 2-cell and 4-cell stage datasets, Z-sections were taken every 3µm and for live imaging of NPM2, Z-sections were taken every 8.33µm. For all the live imaging experiments images were taken every 20 minutes.

### Image Analysis and Processing

The MajSat channel was first denoised using the Rudin-Osher-Fatemi algorithm (*47, 48*) with a denoising weight of 10. The NPM2 or MajSat channel was then segmented using Imaris software (Bitplane). For segmentation a smoothing parameter of 0.4µm was applied and a size threshold of 0.674$\mu m^3$ for the MajSat channel and of 10$\mu m^3$ for the NPM2 channel. The values of sphericity and volume of the different segmented objects were selected from Imaris. All statistical analysis was done using Rstudio.

### Fluorescence Recovery After Photobleaching (FRAP) and Photoconversion

For H3.1 FRAP at MajSat regions, zygotes were microinjected with 600ng/µl of TALEMajSat-mClover and 300ngµl of H3.1-mRFP mRNAs. For FRAP and photoconversion of NPM2 at the NLBs, zygotes were microinjected with 100ng/µl of mRuby-NPM2 or 100ng/µl of mEOS3.2-NPM2 mRNAs, respectively. FRAP and photoconversion was performed on a Nikon Ti-e microscope equipped with a Bruker Opterra 2 confocal system using a plan-Apo 100x NA 1.4 oil immersion objective. Images were acquired on a Photometrics EVO EMCCD camera. Temperature was maintained with a microscope enclosure incubator adjusted to 37°C at the sample (In Vivo Scientific). Embryos were placed in drops of KSOM medium on a glass-bottom dish covered with paraffin oil. A circular region of interest of 2.28$\mu m^3$ was selected either in the nucleoplasm or in the region comprising the MajSat domains as determined by the TALEMajSat-mClover signal, or inside the NLBs as determined using the NPM2 signal, and was subjected to FRAP or photoconversion. Acquisition was started with images taken every 0.1s for 4s during which bleach was performed. Subsequently, images were acquired every 1s for 10s and then every 5s for 50s.

## FRAP curve fitting and statistical analysis

The FRAP raw data were processed with FIJI (ImageJ). All analyses were done on background-subtracted values, which were normalized by the average H3.1 or total NPM2 fluorescence intensity in the nucleus or NLB respectively. The curves obtained were normalized using the full-scale normalization method so that the first post-bleach frame was set to 0. Normalized curves were then subjected to curve fitting. Experimentally obtained and normalized recovery curves were fit using Rstudio. A two-phase exponential association equation, $Y = \text{Ymax1} \times [1 - e(-\text{K1} \times X)] + \text{Ymax2} \times [1 - e(-\text{K2} \times X)]$, was used to obtain mobile fractions and reaction rates of H3.1, as this has been previously described to be appropriate for nuclear proteins (*20, 49*). A single exponential association equation $Y = \text{Ymax} \times [1 - e(-\text{K} \times X)]$ was used to obtain the mobile fraction and reaction rate of NPM2. Unpaired *wilcoxon*-tests were used for statistical comparisons. Ymax2 values were used for mobile fraction estimation of H3.1, as they reflect the steady-state protein pool, unless otherwise stated.

## DNA and RNA FISH

DNA FISH was performed as previously described (*50*), using a protocol that preserves the nuclear 3D structure of embryos. Briefly, the zona pellucida was removed with Acid Tyrode solution, followed by two washes in PBS and fixation in 4% paraformaldehyde, 0.05% Triton-X at RT for 15 min. Embryos were then permeabilised in 0.5% Triton-X 100, 0,02% RNAseA for 1h at RT and treated with HCl solution (0.1N HCl, 0.7 Triton-X 100 and 1 mg/ml PVP in water) for 3min at RT. Embryos were washed into prehybridization buffer (50% formamide, 2x SSC, 10% Dextran, 1 mg/ml PVP, 0.05% TritonX, 0.5 mg/ml BSA) and incubated at 55 °C for 3 h. Embryos were then incubated 10 min at 80 °C and transferred into drops of 0.2 µl hybridization buffer containing the MajSat probe (*4*) at 5 ng/µl, which was previously denatured at 80 °C for 10 min. After overnight hybridization at 42 °C, embryos were washed once in 2x SSC at room temperature followed by washing three times 10 min in in 0.1x SSC at 42 °C and transferred in drops of Vectashield containing DAPI. Super resolution STED microscopy was performed using a plan-Apo 100x NA 1.4 oil immersion objective on a TCS SP8 inverted confocal microscope (Leica). STED was performed with a 775 nm pulsed laser. Z-sections were taken every 0.1µm. For RNA FISH, the zona pellucida was removed with Acid Tyrode solution, followed by two washes in PBS and fixation in 4% paraformaldehyde, 0.05% Triton-X at RT for 15 min. Embryos were then permeabilised in

0.5% Triton-X 100 for 1h at RT. Embryos were washed into prehybridization buffer (50% formamide, 2x SSC, 10% Dextran,  1 mg/ml PVP, 0.05% TritonX, 0.5 mg/ml BSA) and incubated at 55 °C for 3 h before being transferred into drops of 0.2 µl hybridization buffer containing the MajSat probe at 5 ng/µl, which was previously denatured at 80 °C for 10 min under oil. After overnight hybridization at 42 °C, embryos were washed once in 2x SSC at room temperature followed by washing three times 10 min in in 0.1x SSC at 42 °C and mounted in Vectashield (Vector Laboratories) containing DAPI. Confocal microscopy was performed using a plan-Apo 63x NA 1.4 oil immersion objective on a TCS SP8 inverted confocal microscope (Leica). Z-sections were taken every 0.5–1µm. DNA and RNA FISH signals were analysed using Imaris software (Bitplane). The nucleus was first segmented based on the DAPI channel with a smoothing parameter of 0.6. The MajSat signal was then segmented with a smoothing parameter of 0.2 and a size threshold of 0.674$\mu m^3$. The values of sphericity, volume and intensity of the different segmented objects were obtained from Imaris. Statistical analyses were performed using Rstudio.

**Raster Image Correlation Spectroscopy (RICS)**

Zygotes were microinjected with 600ngµl of TALEMajSat-mClover and 20ngµl of SNAP-H3.1 mRNA. Embryos were cultured in microdrops of KSOM until the start of the SNAP tagging, at 44 h post-hCG, at which time embryos were first incubated with a tagging medium (100nM of SNAP-tagcell647 in KSOM) for 30 minutes followed by 2 washes and a 30 min incubation in KSOM without dye. Embryos were then washed 3 times in M2 medium (Sigma) and then transferred to an imaging chamber containing micrometric wells with 1mL of M2 covered with 1mL of paraffin oil. RICS measurements were performed at 37 °C on a home-built confocal laser scanning microscope (CLSM), as described elsewhere (*51*). 470 nm and 635 nm pulsed diode lasers (LDH-P-C-470 and LDH-P-C-635M, PicoQuant) were used for the pulsed-interleaved excitation (*52*) of TALEMajSat-mClover and H3.1-SNAP-647-SiR at a laser power of 10 µW before the objective. A 100x oil immersion objective (Apo-TIRF 100x Oil/NA 1.49, Nikon) was used for all measurements. The descanned fluorescence emission was separated from the excitation pathway with a quad-line 405/488/561/635 beamsplitter (Semrock). The fluorescence emission of TALEMajSat-mClover and H3.1-SNAP-647-SiR was then separated with a 565DCXR beamsplitter (AHF) and spectrally filtered with 420/40 nm bandpass (Chroma) and 635 nm longpass (AHF) emission filters respectively before being detected with avalanche photodiode detectors (Count® Blue and Count® Series, Laser Components).The alignment of the system was routinely checked by measuring an aqueous mixture of ATTO488-COOH and ATTO655-COOH with fluorescence correlation spectroscopy. Per each embryo, 300 frames of 12x12 µm, divided into 300 lines, were acquired with a frame time of $\tau_f = 1$ s, line time, $\tau_l = 3.33$ ms, pixel dwell time $\tau_p = 11.11$ µs, and pixel size $\delta r = 40$ nm. Image calculation from raw photon data and subsequent analyses were performed with PIE Analysis in MATLAB (PAM)(*53*). The RICS measurements were corrected for slow fluctuation and cellular movement by applying a moving average correction prior to image correlation (*51*). To analyse H3.1-SNAP-647-SiR fluctuations in different cellular regions we selected arbitrary ROI based on the TALEMajSat-mClover signal, to distinguish between inside and outside the chromocenters. Subsequently the correlation functions were determined using the Arbitrary RICS (ARICS) algorithm (*18*). The spatial autocorrelation functions (SACFs) were fitted with a one-component free diffusion model assuming a 3D Gaussian focal shape:

$$G(\xi,\psi) = \frac{\gamma}{\mathrm{N}}\left(1+\frac{4\mathrm{D}|\xi\tau_\mathrm{p}+\psi\tau_\mathrm{l}|}{\omega_\mathrm{r}^2}\right)^{-1}\left(1+\frac{4\mathrm{D}|\xi\tau_\mathrm{p}+\psi\tau_\mathrm{l}|}{\omega_\mathrm{z}^2}\right)^{-\frac{1}{2}}\exp\left(-\frac{\delta\mathrm{r}^2(\xi^2+\psi^2)}{\omega_\mathrm{r}^2+4\mathrm{D}|\xi\tau_\mathrm{p}+\psi\tau_\mathrm{l}|}\right)$$

in which ξ and ψ indicate the spatial lags in pixels along the fast and slow scanning axes, respectively, and $\omega_r$ and $\omega_z$ represent the lateral and axial focus sizes, respectively. The shape factor γ is $2^{-3/2}$ for a 3D Gaussian. D represents the diffusion coefficient and N the average number of fluorescent particles in the observation volume. The correlation at zero lag time was omitted from analysis due to the contribution of uncorrelated shot noise. The concentration (C) of H3.1 was calculated according to the equation:

$$C = \frac{1}{G_0 N_A V_{eff}}$$

With $G_0$ being the correlation amplitude and equal to γ/N, NA the Avogadro number and $V_{eff}$ the effective detection volume (*54*), equal to:

$$V_{eff} = \gamma\pi^{\frac{3}{2}}\omega_\mathrm{r}^2\omega_z$$

**1,6-Hexanediol Treatment**

To determine the effective concentration of 1,6-Hexanediol (Alfa Aesar, A12439) zygotes were incubated for 1h with 0.01% to 3.5% of 1,6-Hexanediol in KSOM prior to fixing and staining with DAPI. The number of NLBs and the pronuclear area was calculated in 3D using Imaris (Bitmap). For the DNA and RNA FISH experiments, embryos were incubated 1 hour in 3.5% 1,6-Hexanediol in KSOM prior to fixation. For the experiments in which embryos were analysed under live imaging, embryos were put in the imaging chamber containing micrometric wells with 1mL of 3.5% 1,6-Hexanediol in KSOM covered in oil and imaged directly. For FRAP, embryos were incubated for 10 minutes in 3.5% 1,6-Hexanediol in KSOM and then photobleached. For all the experiments at the 2-cell and 4-cell stage, embryos were incubated in KSOM until 48h and 54h post-hCG, respectively, prior to 1,6-Hexanediol treatment.

### Trim away for ATRX

For FRAP, zygotes were first microinjected with 1 mg/ml of either ATRX or IgG antibodies with 0.33% of Cascade blue (Invitrogen, D1976) or rhodamine B dextran (Invitrogen, D1841), to monitor the success of injection, at 18h pHCG. After 4 h, zygotes were microinjected a second time with the following mRNAs: 130 ng/ml Trim21 with 600ngµl of TALEMajSat-mClover and 300ngµl of H3.1-mRFP. Embryos were placed in a 37 °C and 5%$CO_2$ incubator until the beginning of the experiment at the 2-cell stage. For live imaging, the same procedure was followed, except that the second microinjection was done with the following mRNAs: 200 ng/ml mCherry-Trim21 with 600ngµl of TALEMajSat-mClover and 200 ng/µl of H2B-tdiRFP. For the RNA FISH and qPCR experiments, the second microinjection included 200 ng/ml mCherry-Trim21 and 200 ng/ml mRNA for mGFP as a positive control for microinjection.

### Quantitative RT-qPCR

Single embryo RTqPCR was performed as previously described (*55*). Control, 1,6-Hexanediol treated or ATRX and IgG Trim-away embryos were washed in PBS and snap frozen in 5 µl of 2x reaction buffer at -80°C (CellsDirect One-Step qRT–PCR kit, 11753100, ThermoFisher) at 49 h post-hCG. TaqMan Gene Expression assays (20× Applied Biosystems), were pooled to a final concentration of 0.2x for each of the 3 assays. To each of the single-cell samples in 2x reaction buffer, 2.5 µl of 0.2x assay pool, 0.5 µl RT/Taq enzyme (CellsDirect One-Step qRT-PCR kit, 11753100, ThermoFisher) and 2.3 µl of water were added. Cell lysis and sequence-specific reverse transcription were performed at 50 °C for 20 min. The reverse transcriptase was inactivated by heating to 95 °C for 2 min. The resulting cDNA was diluted tenfold before analysis with Universal PCR Master Mix and 1x TaqMan Gene Expression assays (Applied Biosystems). qPCR analysis was carried out with an initial denaturing at 95 °C for 5 min followed by 45 cycles of denaturing at 95 °C for 15 s and then annealing and amplification at 60 °C for 1 min. All raw Ct values were normalised to Gapdh for all conditions. The delta-delta Ct and then fold change were calculated compared to the mean of the control for the 1,6-Hexanediol experiment and to the mean of the IgG Trim-away for the Atrx Trim-away experiments. Box plots of the resulting dataset were generated using the ggplot2 R package.

### Statistical Analysis

Statistical significance based on the two-sided Mann–Whitney U-test was performed for all the analysis except for the RICS experiment where a two-sided Wilcoxon signed-rank test was performed. All data derive from at least 3 independent biological experiments. All boxplots show the median and interquartile range; whiskers span the range of the data, while extending no further than 1.5× the interquartile range. N corresponds to the number of independent experiments and n to the total number of embryos analyzed. *P* values are designated as *P < 0.05, **P < 0.01, and ***P < 0.001. Non-significant values are indicated as n.s.

## References.

1. A. Burton, M. E. Torres-Padilla, Epigenetic reprogramming and development: a unique heterochromatin organization in the preimplantation mouse embryo. *Brief Funct Genomics* **9**, 444-454 (2010).
2. M. Casanova *et al.*, Heterochromatin reorganization during early mouse development requires a single-stranded noncoding transcript. *Cell Rep* **4**, 1156-1167 (2013).
3. A. V. Probst *et al.*, A strand-specific burst in transcription of pericentric satellites is required for chromocenter formation and early mouse development. *Dev Cell* **19**, 625-638 (2010).
4. J. W. Jachowicz, A. Santenard, A. Bender, J. Muller, M. E. Torres-Padilla, Heterochromatin establishment at pericentromeres depends on nuclear position. *Genes Dev* **27**, 2427-2432 (2013).
5. A. R. Strom *et al.*, Phase separation drives heterochromatin domain formation. *Nature* **547**, 241-245 (2017).
6. A. G. Larson *et al.*, Liquid droplet formation by HP1alpha suggests a role for phase separation in heterochromatin. *Nature* **547**, 236-240 (2017).
7. H. Strickfaden *et al.*, Condensed Chromatin Behaves like a Solid on the Mesoscale In Vitro and in Living Cells. *Cell* **183**, 1772-1784 e1713 (2020).
8. X. Huo *et al.*, The Nuclear Matrix Protein SAFB Cooperates with Major Satellite RNAs to Stabilize Heterochromatin Architecture Partially through Phase Separation. *Mol Cell* **77**, 368-383 e367 (2020).
9. F. Erdel *et al.*, Mouse Heterochromatin Adopts Digital Compaction States without Showing Hallmarks of HP1-Driven Liquid-Liquid Phase Separation. *Mol Cell* **78**, 236-249 e237 (2020).
10. C. P. Brangwynne, T. J. Mitchison, A. A. Hyman, Active liquid-like behavior of nucleoli determines their size and shape in Xenopus laevis oocytes. *Proc Natl Acad Sci U S A* **108**, 4334-4339 (2011).
11. S. Alberti, A. Gladfelter, T. Mittag, Considerations and Challenges in Studying Liquid-Liquid Phase Separation and Biomolecular Condensates. *Cell* **176**, 419-434 (2019).
12. Y. Miyanari, C. Ziegler-Birling, M. E. Torres-Padilla, Live visualization of chromatin dynamics with fluorescent TALEs. *Nat Struct Mol Biol* **20**, 1321-1324 (2013).
13. M. Puschendorf *et al.*, PRC1 and Suv39h specify parental asymmetry at constitutive heterochromatin in early mouse embryos. *Nat Genet* **40**, 411-420 (2008).
14. K. H. Burns *et al.*, Roles of NPM2 in chromatin and nucleolar organization in oocytes and embryos. *Science* **300**, 633-636 (2003).
15. A. Inoue, F. Aoki, Role of the nucleoplasmin 2 C-terminal domain in the formation of nucleolus-like bodies in mouse oocytes. *FASEB J* **24**, 485-494 (2010).
16. D. L. J. Lafontaine, J. A. Riback, R. Bascetin, C. P. Brangwynne, The nucleolus as a multiphase liquid condensate. *Nat Rev Mol Cell Biol* **22**, 165-182 (2021).
17. L. Frank, K. Rippe, Repetitive RNAs as Regulators of Chromatin-Associated Subcompartment Formation by Phase Separation. *J Mol Biol* **432**, 4270-4286 (2020).
18. J. Hendrix, T. Dekens, W. Schrimpf, D. C. Lamb, Arbitrary-Region Raster Image Correlation Spectroscopy. *Biophys J* **111**, 1785-1796 (2016).
19. A. Santenard *et al.*, Heterochromatin formation in the mouse embryo requires critical residues of the histone variant H3.3. *Nat Cell Biol* **12**, 853-862 (2010).
20. A. Boskovic *et al.*, Higher chromatin mobility supports totipotency and precedes pluripotency in vivo. *Genes Dev* **28**, 1042-1047 (2014).
21. M. Ooga, H. Fulka, S. Hashimoto, M. G. Suzuki, F. Aoki, Analysis of chromatin structure in mouse preimplantation embryos by fluorescent recovery after photobleaching. *Epigenetics* **11**, 85-94 (2016).
22. J. R. Simon, N. J. Carroll, M. Rubinstein, A. Chilkoti, G. P. Lopez, Programming molecular self-assembly of intrinsically disordered proteins containing sequences of low complexity. *Nat Chem* **9**, 509-515 (2017).

23. S. Elbaum-Garfinkle, Matter over mind: Liquid phase separation and neurodegeneration. *J Biol Chem* **294**, 7160-7168 (2019).
24. M. Guthmann, A. Burton, M. E. Torres-Padilla, Expression and phase separation potential of heterochromatin proteins during early mouse development. *EMBO Rep* **20**, e47952 (2019).
25. T. L. McDowell *et al.*, Localization of a putative transcriptional regulator (ATRX) at pericentromeric heterochromatin and the short arms of acrocentric chromosomes. *Proc Natl Acad Sci U S A* **96**, 13983-13988 (1999).
26. T. Wongtawan, J. E. Taylor, K. A. Lawson, I. Wilmut, S. Pennings, Histone H4K20me3 and HP1alpha are late heterochromatin markers in development, but present in undifferentiated embryonic stem cells. *J Cell Sci* **124**, 1878-1890 (2011).
27. C. Baumann, M. M. Viveiros, R. De La Fuente, Loss of maternal ATRX results in centromere instability and aneuploidy in the mammalian oocyte and pre-implantation embryo. *PLoS Genet* **6**, e1001137 (2010).
28. R. De La Fuente, C. Baumann, M. M. Viveiros, ATRX contributes to epigenetic asymmetry and silencing of major satellite transcripts in the maternal genome of the mouse embryo. *Development* **142**, 1806-1817 (2015).
29. Z. Liu *et al.*, SUMOylated PRC1 controls histone H3.3 deposition and genome integrity of embryonic heterochromatin. *EMBO J* **39**, e103697 (2020).
30. R. De La Fuente, M. M. Viveiros, K. Wigglesworth, J. J. Eppig, ATRX, a member of the SNF2 family of helicase/ATPases, is required for chromosome alignment and meiotic spindle organization in metaphase II stage mouse oocytes. *Dev Biol* **272**, 1-14 (2004).
31. T. M. Franzmann, S. Alberti, Prion-like low-complexity sequences: Key regulators of protein solubility and phase behavior. *J Biol Chem* **294**, 7128-7136 (2019).
32. S. Hennig *et al.*, Prion-like domains in RNA binding proteins are essential for building subnuclear paraspeckles. *J Cell Biol* **210**, 529-539 (2015).
33. J. Wang *et al.*, A Molecular Grammar Governing the Driving Forces for Phase Separation of Prion-like RNA Binding Proteins. *Cell* **174**, 688-699 e616 (2018).
34. Y. Lin, S. L. Currie, M. K. Rosen, Intrinsically disordered sequences enable modulation of protein phase separation through distributed tyrosine motifs. *J Biol Chem* **292**, 19110-19120 (2017).
35. T. J. Nott *et al.*, Phase transition of a disordered nuage protein generates environmentally responsive membraneless organelles. *Mol Cell* **57**, 936-947 (2015).
36. C. W. Pak *et al.*, Sequence Determinants of Intracellular Phase Separation by Complex Coacervation of a Disordered Protein. *Mol Cell* **63**, 72-85 (2016).
37. D. Clift, C. So, W. A. McEwan, L. C. James, M. Schuh, Acute and rapid degradation of endogenous proteins by Trim-Away. *Nat Protoc* **13**, 2149-2175 (2018).
38. S. F. Banani *et al.*, Compositional Control of Phase-Separated Cellular Bodies. *Cell* **166**, 651-663 (2016).
39. Y. Xue *et al.*, The ATRX syndrome protein forms a chromatin-remodeling complex with Daxx and localizes in promyelocytic leukemia nuclear bodies. *Proc Natl Acad Sci U S A* **100**, 10635-10640 (2003).
40. S. Eustermann *et al.*, Combinatorial readout of histone H3 modifications specifies localization of ATRX to heterochromatin. *Nat Struct Mol Biol* **18**, 777-782 (2011).
41. S. Iwase *et al.*, ATRX ADD domain links an atypical histone methylation recognition mechanism to human mental-retardation syndrome. *Nat Struct Mol Biol* **18**, 769-776 (2011).
42. M. Borsos *et al.*, Genome-lamina interactions are established de novo in the early mouse embryo. *Nature* **569**, 729-733 (2019).
43. M. Zhang *et al.*, Rational design of true monomeric and bright photoactivatable fluorescent proteins. *Nat Methods* **9**, 727-729 (2012).
44. P. Hajkova *et al.*, Genome-wide reprogramming in the mouse germ line entails the base excision repair pathway. *Science* **329**, 78-82 (2010).

45. M. E. Torres-Padilla, A. J. Bannister, P. J. Hurd, T. Kouzarides, M. Zernicka-Goetz, Dynamic distribution of the replacement histone variant H3.3 in the mouse oocyte and preimplantation embryos. *Int J Dev Biol* **50**, 455-461 (2006).
46. J. Schindelin *et al.*, Fiji: an open-source platform for biological-image analysis. *Nat Methods* **9**, 676-682 (2012).
47. P. Getreuer, Rudin-Osher-Fatemi Total Variation Denoising using Split Bregman. *Image Processing On Line* **2**, 74-95 (2012).
48. S. O. Leonid I. Rudin, Emad Fatemi, Nonlinear total variation based noise removal algorithms. *Physica D: Nonlinear Phenomena* **60**, 259-268 (1992).
49. R. D. Phair, T. Misteli, High mobility of proteins in the mammalian cell nucleus. *Nature* **404**, 604-609 (2000).
50. Y. Miyanari, M. E. Torres-Padilla, Control of ground-state pluripotency by allelic regulation of Nanog. *Nature* **483**, 470-473 (2012).
51. J. Hendrix *et al.*, Live-cell observation of cytosolic HIV-1 assembly onset reveals RNA-interacting Gag oligomers. *J Cell Biol* **210**, 629-646 (2015).
52. B. K. Muller, E. Zaychikov, C. Brauchle, D. C. Lamb, Pulsed interleaved excitation. *Biophys J* **89**, 3508-3522 (2005).
53. W. Schrimpf, A. Barth, J. Hendrix, D. C. Lamb, PAM: A Framework for Integrated Analysis of Imaging, Single-Molecule, and Ensemble Fluorescence Data. *Biophys J* **114**, 1518-1528 (2018).
54. R. Rigler, U. Mets, J. Widengren, P. Kask, Fluorescence Correlation Spectroscopy with High Count Rate and Low-Background - Analysis of Translational Diffusion. *Eur Biophys J Biophy* **22**, 169-175 (1993).
55. A. Burton *et al.*, Single-cell profiling of epigenetic modifiers identifies PRDM14 as an inducer of cell fate in the mammalian embryo. *Cell Rep* **5**, 687-701 (2013).

# Figure 1

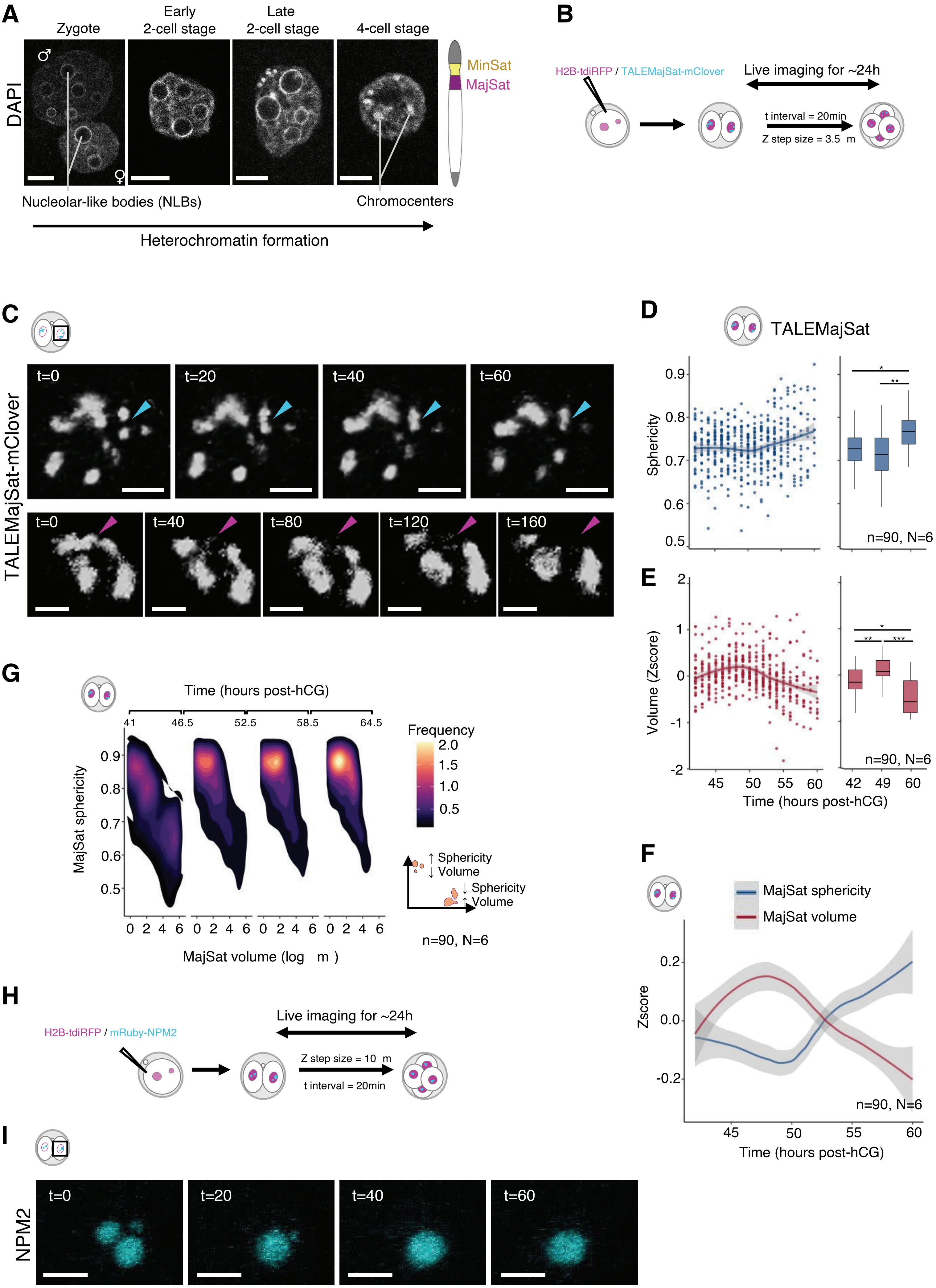
A
Zygote
Early
2-cell stage
Late
2-cell stage
4-cell stage
DAPI
♂
♀
MinSat
MajSat
Nucleolar-like bodies (NLBs)
Chromocenters
Heterochromatin formation
B
H2B-tdiRFP / TALEMajSat-mClover
Live imaging for ~24h
t interval = 20min
Z step size = 3.5 m
C
TALEMajSat-mClover
t=0
t=20
t=40
t=60
t=0
t=40
t=80
t=120
t=160
D
TALEMajSat
Sphericity
0.9
0.8
0.7
0.6
0.5
*
**
n=90, N=6
E
Volume (Zscore)
2
1
0
-1
-2
*
**
***
n=90, N=6
45
50
55
60
42
49
60
Time (hours post-hCG)
F
MajSat sphericity
MajSat volume
Zscore
0.2
0.0
-0.2
n=90, N=6
45
50
55
60
Time (hours post-hCG)
G
Time (hours post-hCG)
41
46.5
52.5
58.5
64.5
MajSat sphericity
0.9
0.8
0.7
0.6
0.5
0 2 4 6 0 2 4 6 0 2 4 6 0 2 4 6
MajSat volume (log m )
Frequency
2.0
1.5
1.0
0.5
↑ Sphericity
↓ Volume
↓ Sphericity
↑ Volume
n=90, N=6
H
H2B-tdiRFP / mRuby-NPM2
Live imaging for ~24h
Z step size = 10 m
t interval = 20min
I
NPM2
t=0
t=20
t=40
t=60

# Figure 2

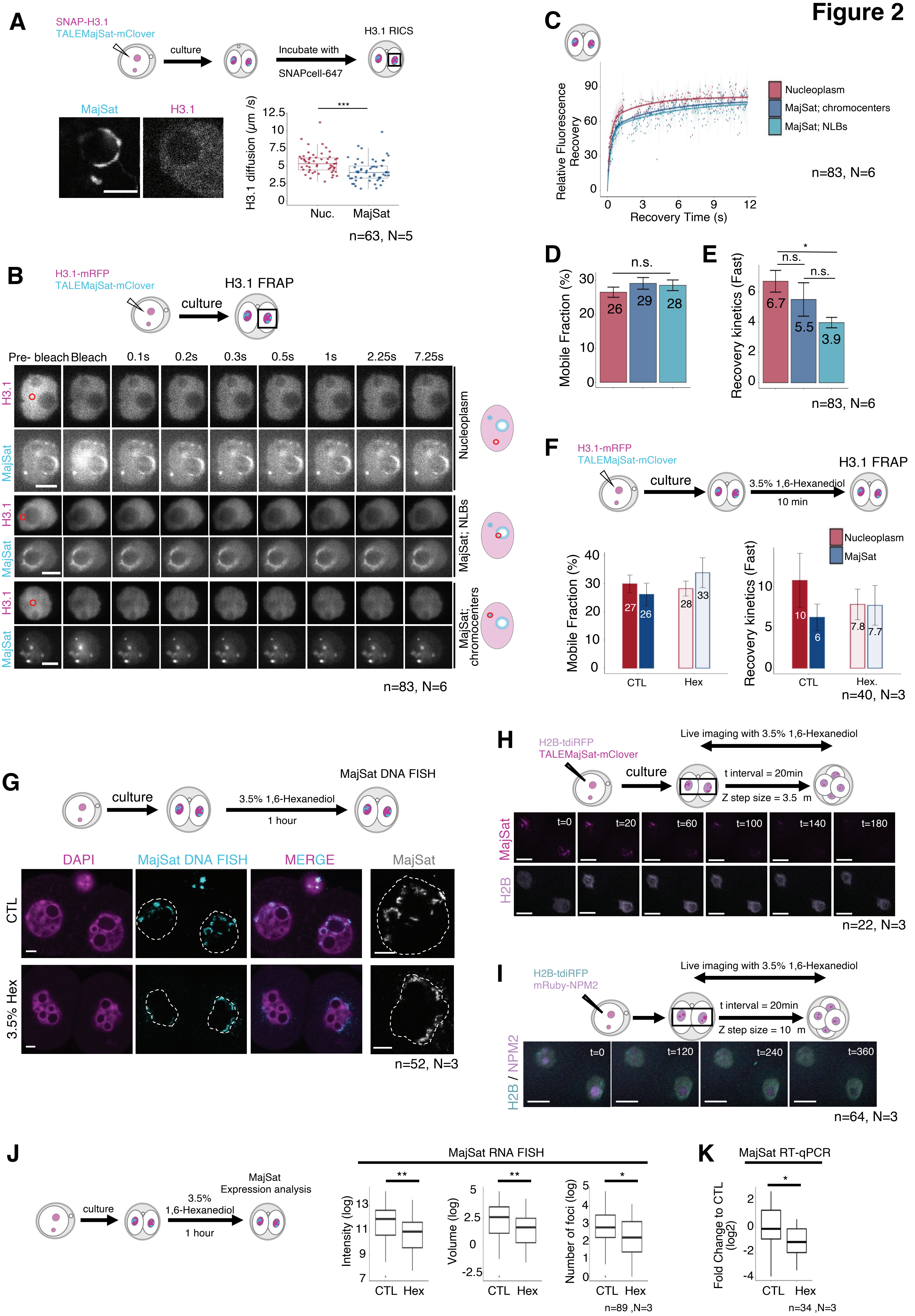
A
SNAP-H3.1
TALEMajSat-mClover
culture
Incubate with
SNAPcell-647
H3.1 RICS
MajSat
H3.1
H3.1 diffusion (μm /s)
12.5
10
7.5
5
2.5
0
***
Nuc.
MajSat
n=63, N=5
B
H3.1-mRFP
TALEMajSat-mClover
culture
H3.1 FRAP
Pre- bleach
Bleach
0.1s
0.2s
0.3s
0.5s
1s
2.25s
7.25s
H3.1
MajSat
Nucleoplasm
MajSat; NLBs
MajSat; chromocenters
n=83, N=6
C
Relative Fluorescence Recovery
90
60
30
0
Recovery Time (s)
0
3
6
9
12
Nucleoplasm
MajSat; chromocenters
MajSat; NLBs
n=83, N=6
D
Mobile Fraction (%)
n.s.
30
20
10
0
26
29
28
E
Recovery kinetics (Fast)
*
n.s.
n.s.
6
4
2
0
6.7
5.5
3.9
n=83, N=6
F
H3.1-mRFP
TALEMajSat-mClover
culture
3.5% 1,6-Hexanediol
10 min
H3.1 FRAP
Mobile Fraction (%)
40
30
20
10
0
27
26
28
33
CTL
Hex
Recovery kinetics (Fast)
10
5
0
10
6
7.8
7.7
CTL
Hex.
Nucleoplasm
MajSat
n=40, N=3
G
culture
3.5% 1,6-Hexanediol
1 hour
MajSat DNA FISH
DAPI
MajSat DNA FISH
MERGE
MajSat
CTL
3.5% Hex
n=52, N=3
H
H2B-tdiRFP
TALEMajSat-mClover
culture
Live imaging with 3.5% 1,6-Hexanediol
t interval = 20min
Z step size = 3.5 m
MajSat
H2B
t=0
t=20
t=60
t=100
t=140
t=180
n=22, N=3
I
H2B-tdiRFP
mRuby-NPM2
Live imaging with 3.5% 1,6-Hexanediol
t interval = 20min
Z step size = 10 m
H2B / NPM2
t=0
t=120
t=240
t=360
n=64, N=3
J
culture
3.5%
1,6-Hexanediol
1 hour
MajSat
Expression analysis
MajSat RNA FISH
Intensity (log)
13
11
9
7
**
Volume (log)
5
2.5
0
-2.5
**
Number of foci (log)
5
4
3
2
1
0
*
CTL
Hex
n=89 ,N=3
K
MajSat RT-qPCR
Fold Change to CTL (log2)
*
2
0
-2
-4
CTL
Hex
n=34 ,N=3

## Figure 3

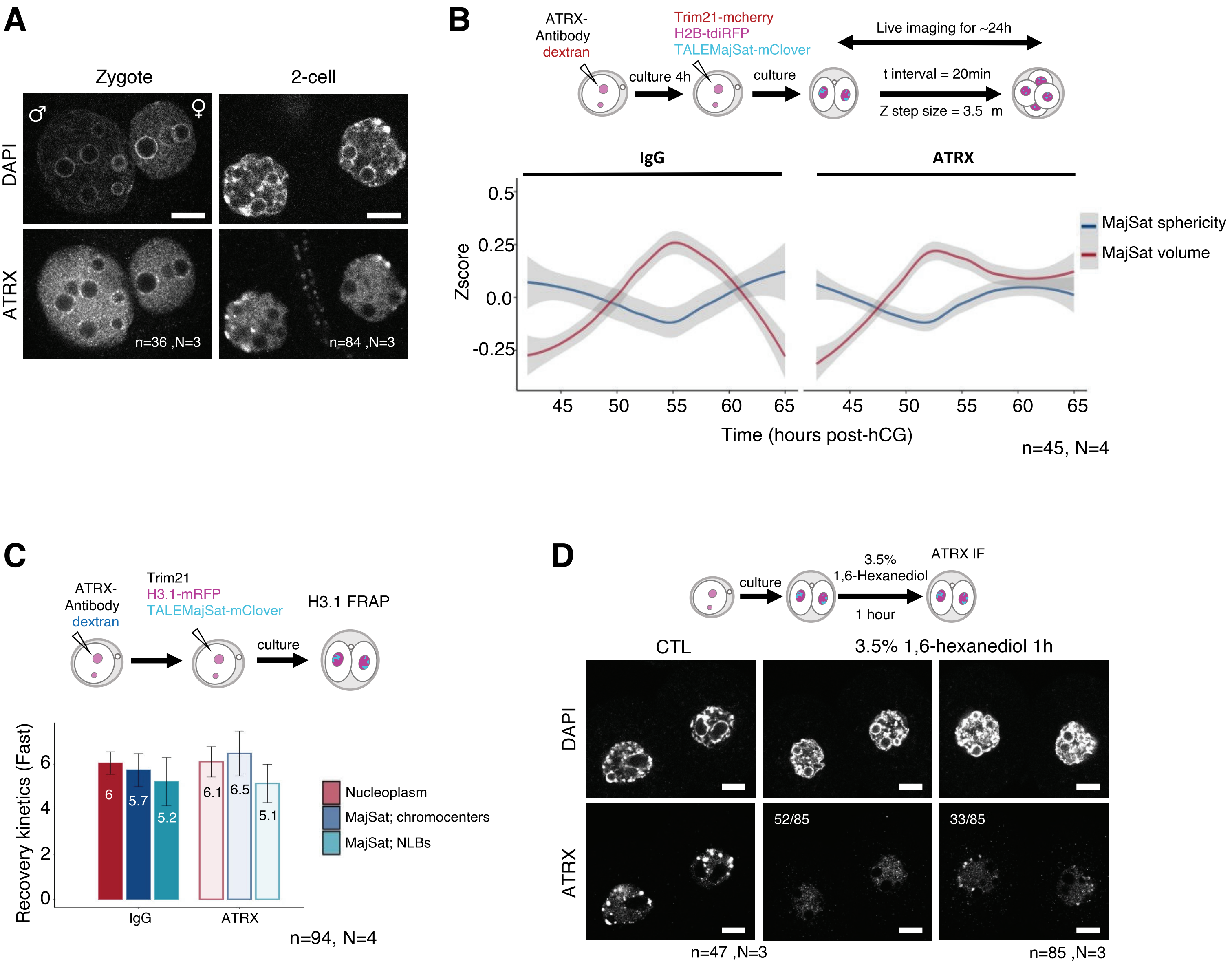
A
Zygote
2-cell
♂
♀
DAPI
ATRX
n=36 ,N=3
n=84 ,N=3
B
ATRX-
Antibody
dextran
culture 4h
Trim21-mcherry
H2B-tdiRFP
TALEMajSat-mClover
culture
Live imaging for ~24h
t interval = 20min
Z step size = 3.5 m
IgG
ATRX
Zscore
0.5
0.25
0.0
-0.25
45
50
55
60
65
Time (hours post-hCG)
MajSat sphericity
MajSat volume
n=45, N=4
C
ATRX-
Antibody
dextran
Trim21
H3.1-mRFP
TALEMajSat-mClover
culture
H3.1 FRAP
Recovery kinetics (Fast)
0
2
4
6
6
5.7
5.2
6.1
6.5
5.1
IgG
ATRX
Nucleoplasm
MajSat; chromocenters
MajSat; NLBs
n=94, N=4
D
culture
3.5%
1,6-Hexanediol
1 hour
ATRX IF
CTL
3.5% 1,6-hexanediol 1h
DAPI
ATRX
52/85
33/85
n=47 ,N=3
n=85 ,N=3

**Figure 4**

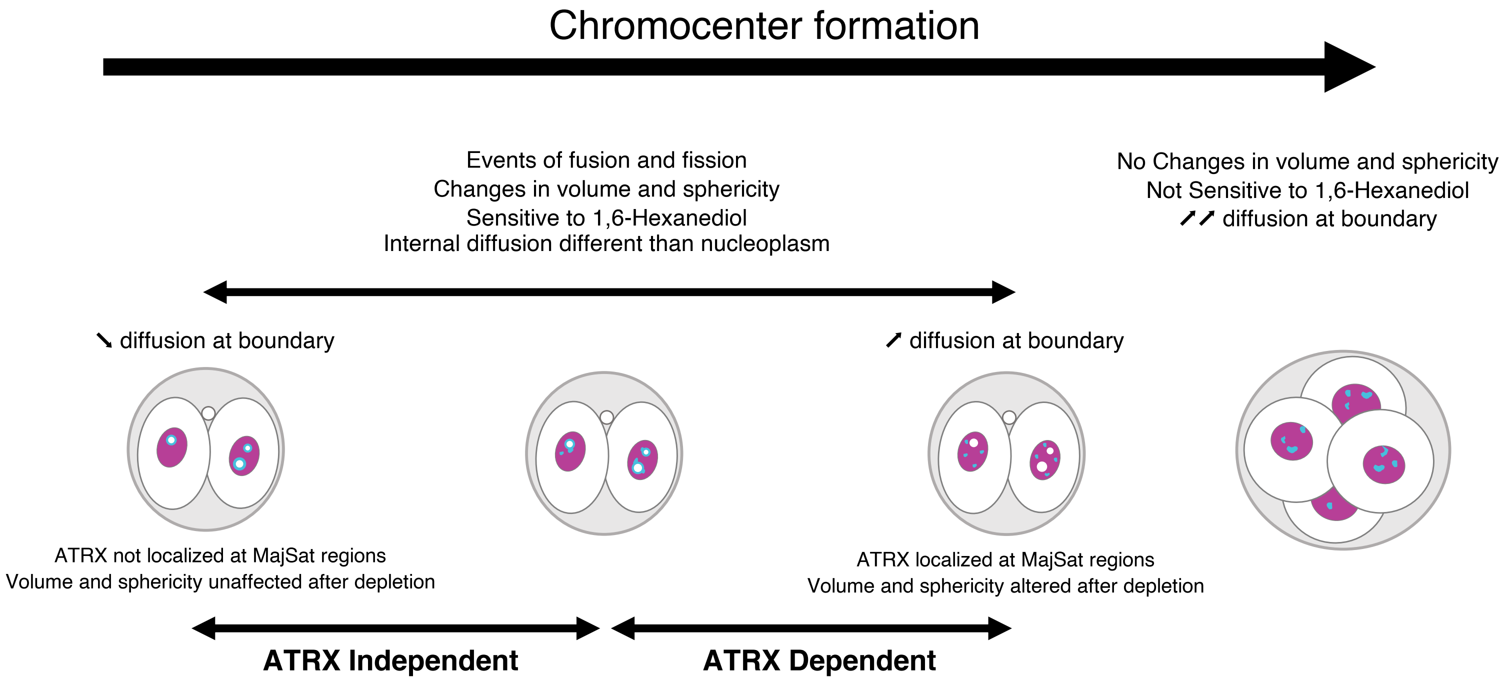
Chromocenter formation
Events of fusion and fission
Changes in volume and sphericity
Sensitive to 1,6-Hexanediol
Internal diffusion different than nucleoplasm
No Changes in volume and sphericity
Not Sensitive to 1,6-Hexanediol
↗↗ diffusion at boundary
↘ diffusion at boundary
↗ diffusion at boundary
ATRX not localized at MajSat regions
Volume and sphericity unaffected after depletion
ATRX localized at MajSat regions
Volume and sphericity altered after depletion
ATRX Independent
ATRX Dependent

# Figure S1

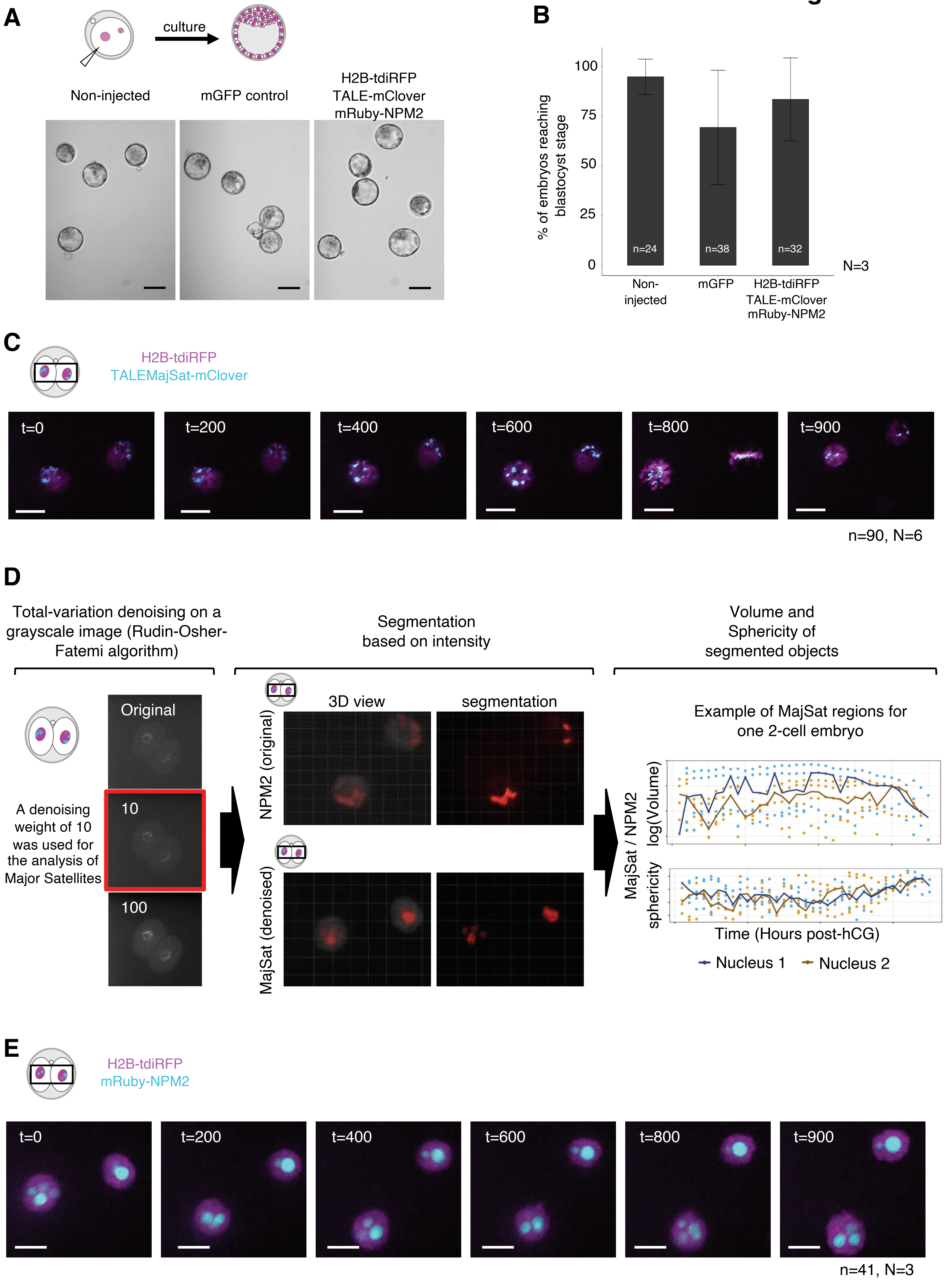
A
culture
Non-injected
mGFP control
H2B-tdiRFP
TALE-mClover
mRuby-NPM2
B
% of embryos reaching blastocyst stage
100
75
50
25
0
n=24
n=38
n=32
N=3
Non-injected
mGFP
H2B-tdiRFP
TALE-mClover
mRuby-NPM2
C
H2B-tdiRFP
TALEMajSat-mClover
t=0
t=200
t=400
t=600
t=800
t=900
n=90, N=6
D
Total-variation denoising on a grayscale image (Rudin-Osher-Fatemi algorithm)
Segmentation based on intensity
Volume and Sphericity of segmented objects
Original
10
100
A denoising weight of 10 was used for the analysis of Major Satellites
3D view
segmentation
NPM2 (original)
MajSat (denoised)
Example of MajSat regions for one 2-cell embryo
MajSat / NPM2
log(Volume)
sphericity
Time (Hours post-hCG)
Nucleus 1
Nucleus 2
E
H2B-tdiRFP
mRuby-NPM2
t=0
t=200
t=400
t=600
t=800
t=900
n=41, N=3

# Figure S2

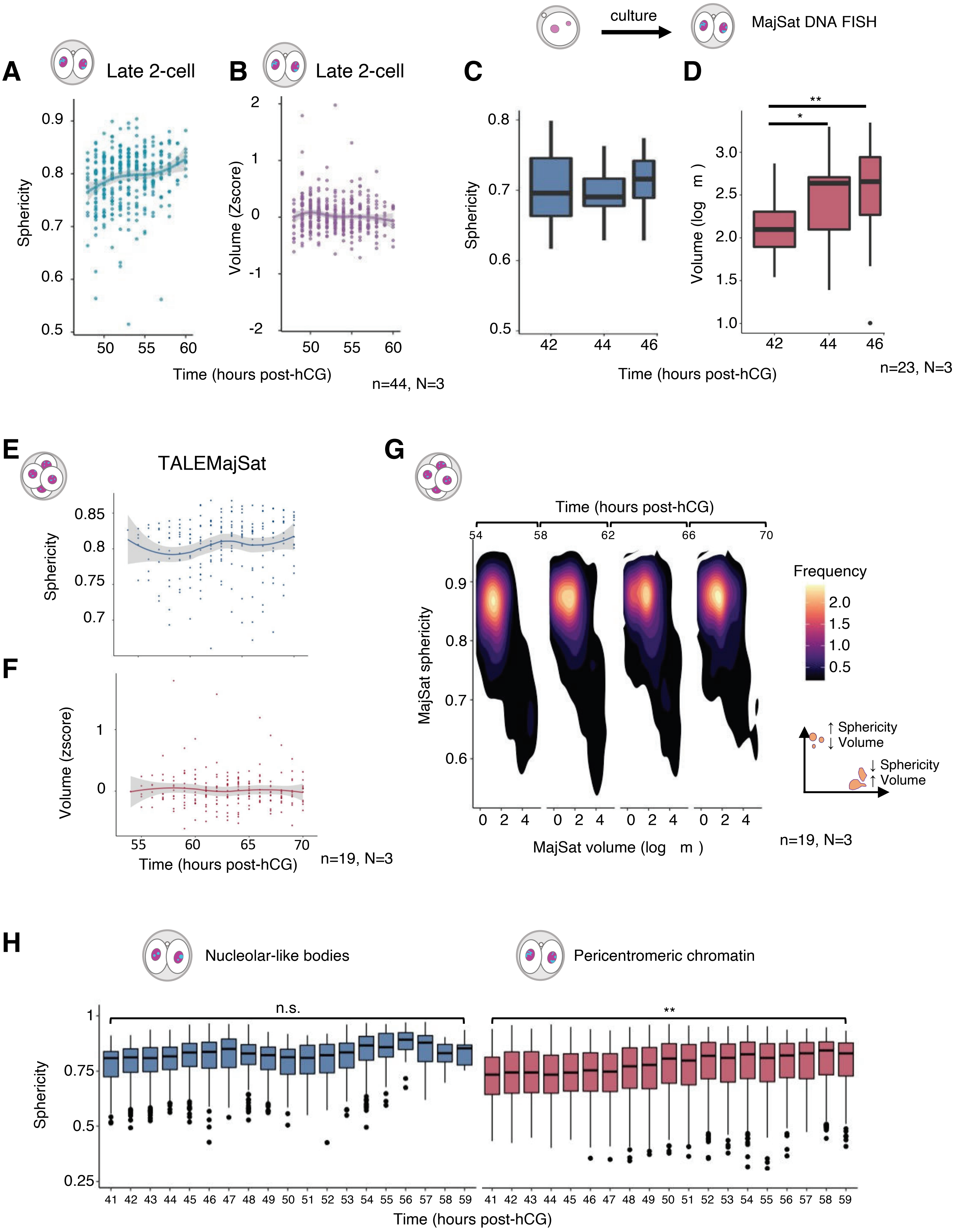

culture
MajSat DNA FISH
A
Late 2-cell
Sphericity
0.9
0.8
0.7
0.6
0.5
50
55
60
B
Late 2-cell
Volume (Zscore)
2
1
0
-1
-2
50
55
60
Time (hours post-hCG)
n=44, N=3
C
Sphericity
0.8
0.7
0.6
0.5
42
44
46
D
**
*
Volume (log m )
3.0
2.5
2.0
1.5
1.0
42
44
46
Time (hours post-hCG)
n=23, N=3
E
TALEMajSat
Sphericity
0.85
0.8
0.75
0.7
F
Volume (zscore)
1
0
55
60
65
70
Time (hours post-hCG)
n=19, N=3
G
Time (hours post-hCG)
54
58
62
66
70
MajSat sphericity
0.9
0.8
0.7
0.6
0 2 4
0 2 4
0 2 4
0 2 4
MajSat volume (log m )
Frequency
2.0
1.5
1.0
0.5
↑ Sphericity
↓ Volume
↓ Sphericity
↑ Volume
n=19, N=3
H
Nucleolar-like bodies
Pericentromeric chromatin
n.s.
**
Sphericity
1
0.75
0.5
0.25
41 42 43 44 45 46 47 48 49 50 51 52 53 54 55 56 57 58 59
41 42 43 44 45 46 47 48 49 50 51 52 53 54 55 56 57 58 59
Time (hours post-hCG)

# Figure S3

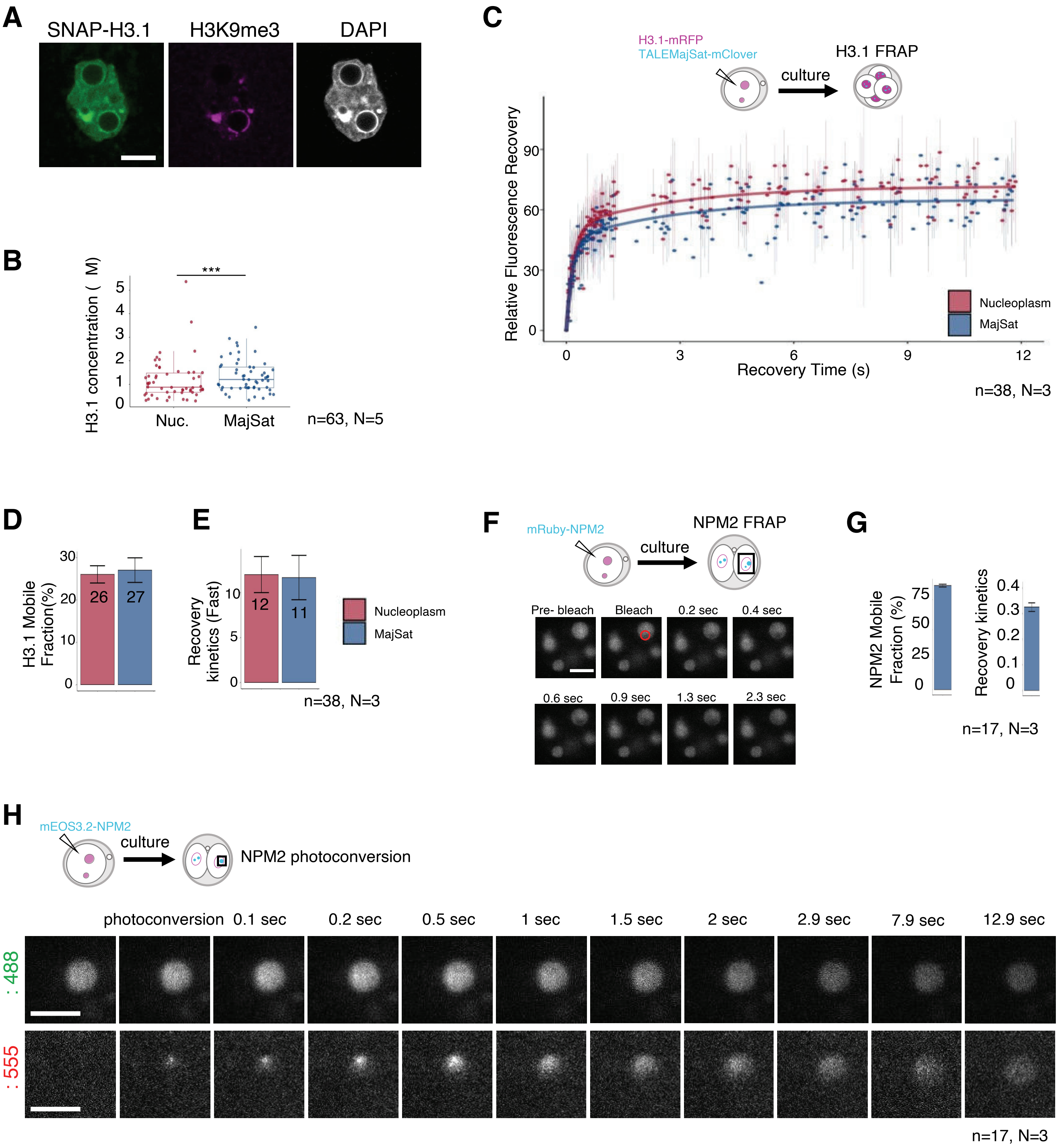
A
SNAP-H3.1
H3K9me3
DAPI
B
H3.1 concentration ( M)
0
1
2
3
4
5
***
Nuc.
MajSat
n=63, N=5
C
H3.1-mRFP
TALEMajSat-mClover
culture
H3.1 FRAP
Relative Fluorescence Recovery
0
30
60
90
0
3
6
9
12
Recovery Time (s)
Nucleoplasm
MajSat
n=38, N=3
D
H3.1 Mobile Fraction(%)
0
10
20
30
26
27
E
Recovery kinetics (Fast)
0
5
10
12
11
Nucleoplasm
MajSat
n=38, N=3
F
mRuby-NPM2
culture
NPM2 FRAP
Pre- bleach
Bleach
0.2 sec
0.4 sec
0.6 sec
0.9 sec
1.3 sec
2.3 sec
G
NPM2 Mobile Fraction (%)
0
25
50
75
Recovery kinetics
0
0.1
0.2
0.3
0.4
n=17, N=3
H
mEOS3.2-NPM2
culture
NPM2 photoconversion
photoconversion
0.1 sec
0.2 sec
0.5 sec
1 sec
1.5 sec
2 sec
2.9 sec
7.9 sec
12.9 sec
: 488
: 555
n=17, N=3

# Figure S4

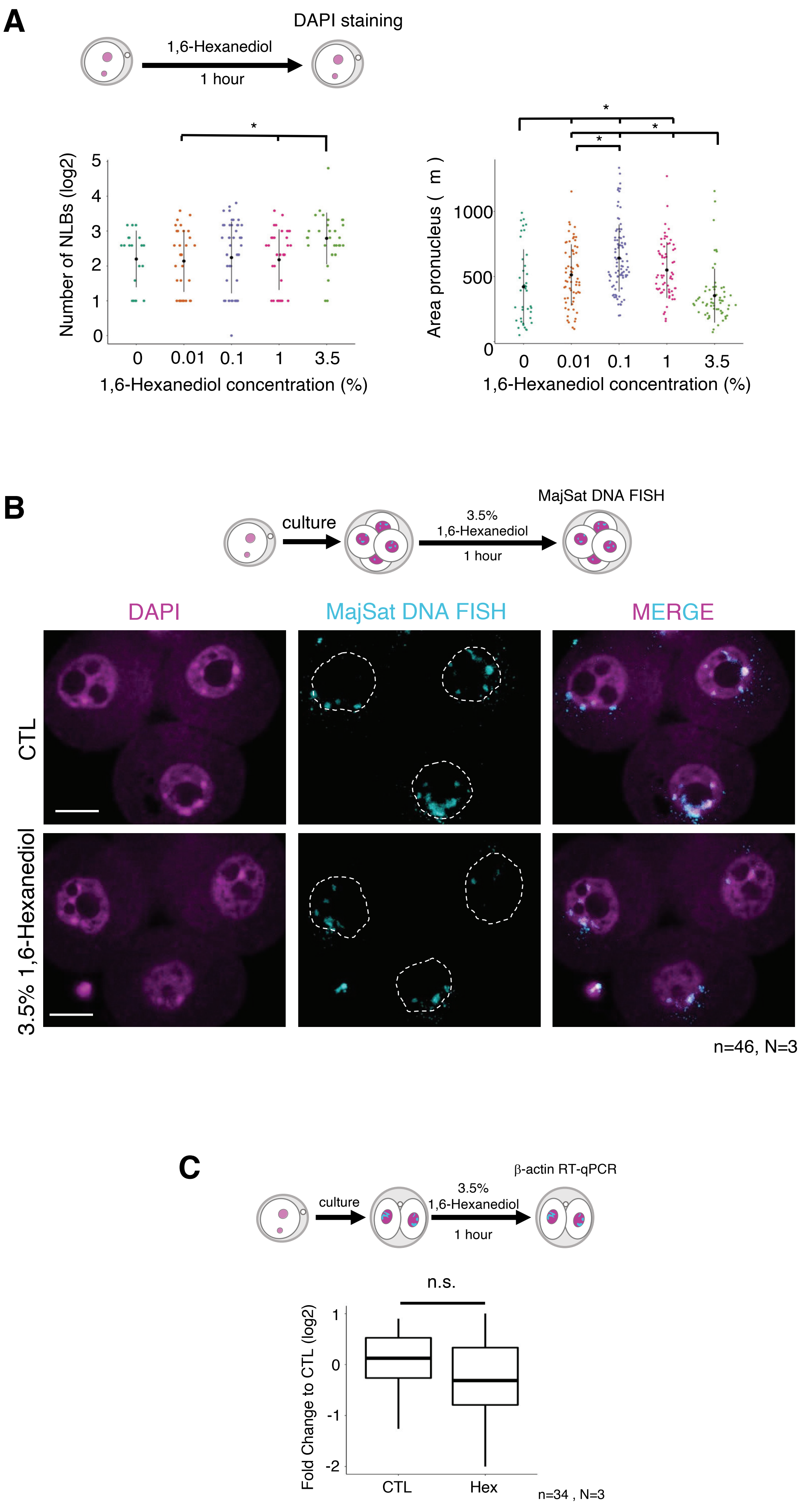
A
1,6-Hexanediol
1 hour
DAPI staining
*
Number of NLBs (log2)
5
4
3
2
1
0
0
0.01
0.1
1
3.5
1,6-Hexanediol concentration (%)
*
*
*
*
Area pronucleus ( m )
1000
500
0
0
0.01
0.1
1
3.5
1,6-Hexanediol concentration (%)
B
culture
3.5%
1,6-Hexanediol
1 hour
MajSat DNA FISH
DAPI
MajSat DNA FISH
MERGE
CTL
3.5% 1,6-Hexanediol
n=46, N=3
C
culture
3.5%
1,6-Hexanediol
1 hour
β-actin RT-qPCR
n.s.
Fold Change to CTL (log2)
1
0
-1
-2
CTL
Hex
n=34 , N=3

# Figure S5

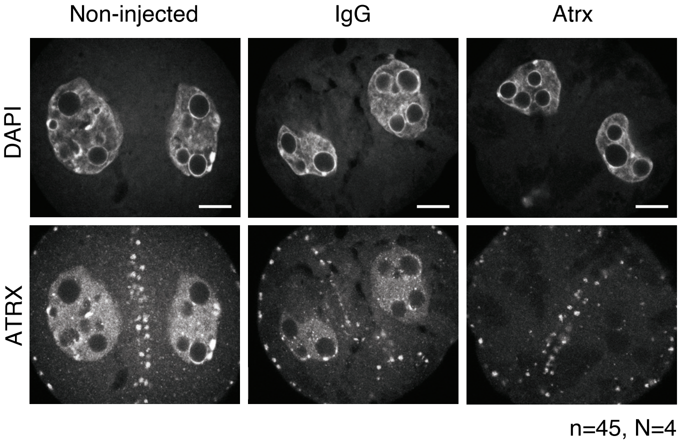

**Table S1. Estimated fractions and recovery kinetics of H3.1-mRFP obtained by FRAP in different conditions and compartments**

| Experi-ment | Treatment | Localization | Ymax1 | Ymax2 | K1 | K2 |
|---|---|---|---|---|---|---|
| 2-cell | CTL | Nucleoplasm | 56.27 ± 1.42 | 26.60 ± 1.50 | 6.70 ± 0.72 | 0.519 ± 0.061 |
| | | MajSat; chromocenters | 51.98 ± 1.59 | 29.21 ± 1.72 | 5.50 ± 1.10 | 0.338 ± 0.042 |
| | | MajSat; NLBs | 52.21 ± 1.95 | 28.64 ± 1.58 | 3.97 ± 0.34 | 0.1.87 ± 0.023 |
| 4-cell | CTL | Nucleoplasm | 46.62 ± 2.56 | 26.05 ± 2.04 | 12.02 ± 2.01 | 0.646 ± 0.107 |
| | | MajSat | 41.11 ± 2.47 | 27.05 ± 2.91 | 11.68 ± 2.47 | 0.481 ± 0.100 |
| 2-cell after 1,6-HD | CTL | Nucleoplasm | 51.36 ± 3.08 | 29.93 ± 3.14 | 10.80 ± 3.34 | 0.478 ± 0.138 |
| | | MajSat | 45.34 ± 3.98 | 26.19 ± 5.32 | 6.26 ± 1.63 | 0.443 ± 0.125 |
| | Hex | Nucleoplasm | 51.81 ± 3.03 | 28.25 ± 2.65 | 7.85 ± 1.88 | 0.463 ± 0.133 |
| | | MajSat | 43.35 ± 4.17 | 33.89 ± 5.32 | 7.73 ± 2.44 | 0.376 ± 0.117 |
| 2-cell after Trim-Away | IgG | Nucleoplasm | 58.16 ± 2.29 | 23.91 ± 2.60 | 6.05 ± 0.50 | 0.385 ± 0.071 |
| | | MajSat; chromocenters | 46.72 ± 4.25 | 28.84 ± 5.21 | 5.74 ± 0.73 | 0.353 ± 0.110 |
| | | MajSat; NLBs | 49.73 ± 3.24 | 29.90 ± 3.59 | 5.22 ± 1.07 | 0.329 ± 0.087 |
| | ATRX | Nucleoplasm | 56.99 ± 1.96 | 24.77 ± 1.96 | 6.11 ± 0.68 | 0.375 ± 0.073 |
| | | MajSat; chromocenters | 45.74 ± 2.20 | 27.79 ± 1.77 | 6.47 ± 1.00 | 0.324 ± 0.057 |
| | | MajSat; NLBs | 48.06 ± 2.10 | 31.22 ± 2.54 | 5.14 ± 0.85 | 0.294 ± 0.054 |

Mean ± SEM of the diffusive fraction (Ymax1), the mobile fraction (Ymax2), the fast kinetics (K1) and slow kinetics (K2) of H3.1-mRFP. The different experiments shown correspond to the FRAP experiments shown in Figs. 2B-E (2-cell), Figs.S3C-E (4-cell), Fig.2F (2-cell after 1,6-Hexanediol) and Fig.3C (2-cell After Trim-Away).